Geodätisch-geophysikalische Arbeiten in der Schweiz

(Fortsetzung der Publikationsreihe
«Astronomisch-geodätische Arbeiten in der Schweiz»)

herausgegeben von der

Schweizerischen Geodätischen Kommission
(Organ der Akademie der Naturwissenschaften Schweiz)

Zweiundneunzigster Band
Volume 92

Atmospheric Water Vapour Sensing By Means of Differential Absorption Spectrometry Using Solar And Lunar Radiation

Stefan Walter Münch

2014

Adresse der Schweizerischen Geodätischen Kommission:

Institut für Geodäsie und Photogrammetrie
Eidg. Technische Hochschule Zürich
ETH Zürich
8093 Zürich
Switzerland

Internet: http://www.sgc.ethz.ch

ISBN 978-3-908440-35-2

Redaktion des 92. Bandes:
Dr. Stefan W. Münch, J. Müller-Gantenbein, Prof. M. Rothacher
Druck: Print-Atelier ADAG, Zürich

VORWORT

Mit den modernen satellitengestützten Positionierungsmethoden sind die Anforderungen gewachsen, hochpräzise geodätische Anwendungen im cm- oder gar im mm-Genauigkeitsbereich zu realisieren. Ein zentrales Problem bleibt weiterhin der Störeinfluss der Troposphäre. Problematisch ist insbesondere die Korrektur des wasserdampfbedingten, sich örtlich und zeitlich oft schnell ändernden Fehlers an den Distanzmessungen zwischen Satellit und Empfänger. Der vorliegende SGK Band widmet sich der Entwicklung des neuen mobilen Messsystems SOLUSAR (Solar Lunar Spectrometer for Atmospheric Research), das auf Absorptionsmessungen mit einem hochauflösenden Sonnenspektrometer (SSM) beruht und genaue Daten über den troposphärischen Wasserdampfgehalt liefert. Die SOLUSAR-Messungen können zur Bestimmung von Korrekturwerten bei Satellitenbeobachtungen verwendet werden. Systematische Vergleiche mit anderen bodengestützten Verfahren, wie Wasserdampfradiometrie (WVR), GPS-Schätzung und Ballonsondierungen geben Aufschluss darüber, wie weit die Sonnenspektrometrie als zusätzliches Schätz- bzw. Kalibrationsverfahren eingesetzt werden kann.

Das Geodesy and Geodynamics Lab (GGL) der ETH Zürich blickt auf etliche Jahre Erfahrung im Bereich der Wasserdampfbestimmung zurück. Seit den 90er Jahren hat das GGL zusammen mit der working group Optical Spectroscopy des Leibniz-Instituts für Analytische Wissenschaften (ISAS), Berlin zwei dedizierte Messsysteme (SAMOS and GEMOSS) entwickelt, die ebenfalls auf dem Prinzip der Differential Optical Absorption Spectroscopy (DOAS) beruhen. Dazu erschienen in dieser Reihe bereits die zwei Bände 62, Bernd Sierk, 2001 und Band 68, Alexander Somieski, 2005. Das Projekt ‚Solar Lunar Spectrometer for Atmospheric Research' (SOLUSAR) wurde 2007 von der ETH Zürich, dem Leibniz-Institut für Analytische Wissenschaften - ISAS und dem Helmholtz-Zentrum Potsdam Deutsches GeoForschungsZentrum (GFZ) initiiert mit dem Ziel, ein Wasserdampfbestimmungsverfahren von hoher Präzision und hoher zeitlicher Auflösung zu entwickeln. Eine spezielle Herausforderung ergab sich durch die Zielvorgabe, auch Mondmessungen durchführen zu können. Zudem sollte das Gerät für mobile Feldeinsätze konzipiert werden. Die Zielvorgaben von Mobilität, Empfindlichkeit (Mondmessungen) und Genauigkeit stellten eine grosse Herausforderung dar, die Herr Münch, wie die vorliegende Arbeit zeigt, mit Bravur gelöst hat.

Die SGK dankt sowohl dem Autor für den wertvollen Beitrag zur geodätischen Meteorologie als auch der Schweizerischen Akademie für Naturwissenschaften (SCNAT) für die Übernahme der Druckkosten.

Prof. Dr. M. Rothacher
Institut für Geodäsie und Photogrammetrie
ETH Zürich

Prof. Dr. A. Geiger
ETH Zürich
Präsident der SGK

PREFACE

Avec l'apparition des méthodes modernes de positionnement par satellites la demande pour des applications géodésiques de hautes précisions, dans les gammes du centimètre et même du millimètre, a sensiblement augmenté. Cependant le problème central des effets perturbateurs des variations rapides tant spatiales que temporelles du contenu en vapeur d'eau de l'atmosphère demeure. Ces variations influencent les mesures de la distance entre le récepteur et les satellites. Le présent fascicule de la Commission Géodésique Suisse (SGK) est dédié au développement du nouveau système mobile de mesure, SOLUSAR, (Solar Lunar Spectrometer for Atmospheric Research) basé sur la mesure de l'absorption à l'aide d'un spectromètre solaire à haute résolution (SSM). Celui-ci délivre des données précises sur le contenu atmosphérique en vapeur d'eau. Les mesures SOLUSAR peuvent être utilisées pour déterminer les corrections applicables aux observations satellitaires.

Des comparaisons systématiques entre des méthodes au sol comme la radiométrie de vapeur d'eau (WVR) ou l'estimation des paramètres GNSS et les données des ballons sondes, fournissent des indications sur l'utilisation du spectromètre solaire comme outil additionnel de calibration.

Le laboratoire de géodésie et géodynamique de l'EPF-Z (GGL) a une expérience de plusieurs années dans le domaine de la détermination du contenu en vapeur d'eau de l'atmosphère. Depuis les années 90 le GGL, en coopération avec le groupe de travail de la spectrométrie optique de l'institut Leibnitz pour les sciences analytiques (SAS) de Berlin, a développé deux systèmes (SAMOS et GEMOSS) qui sont basés sur le principe de l'absorption optique différentielle (Differential Optical Absorption Spectroscopy ou DOAS). Des articles relatifs à ce sujet apparaissent déjà dans cette série au volume 62, Bernd Sierk, 2001 et au volume 68, Alexander Somieski, 2005.

Le projet, SOLUSAR (Differential Optical Absorption Spectroscopy) a été initié en 2007 par le GGL de l'ETH-Z, le Leibniz-Institut für Analytische Wissenschaften – ISAS, et le Helmholtz-Zentrum du Deutsches GeoForschungsZentrum de Potsdam (GFZ) avec comme objectif de concevoir une méthode permettant la détermination du contenue en vapeur d'eau de haute précision et d'une haute résolution temporelle. Le but fixé de pouvoir aussi exécuter des mesures lunaires et de plus d'avoir un équipement devant être conçu pour des mesures mobiles de terrain a été particulièrement un défi. Les buts de mobilité, de sensibilité (mesures lunaires) et de précision ont été des besognes que Monsieur Münch a superbement maitrisées.

La commission suisse de Géodésie (SGK) remercie l'auteur pour cette contribution de valeur à la métrologie géodésique.

Nos remerciements vont aussi à l'académie suisse des sciences naturelles pour avoir pris à sa charge les coûts d'impression du présent fascicule.

Prof. Dr. M. Rothacher
Institut de Géodésie et Photogrammetrie
ETH Zürich

Prof. Dr. A. Geiger
ETH Zürich
Président de la CGS

FORWORD

Conjointly with the advent of modern satellite based positioning methods the request has grown to implement high precision geodetic applications in the cm or even in the mm- range of precision. One central problem still persists: The tropospheric perturbation.

Particularly problematic are corrections due to atmospheric water vapour with its often rapid variations in space and time. The present SGC volume is dedicated to the development of the new mobile measurement system SOLUSAR (Solar Lunar Spectrometer for Atmospheric Research), which is based on absorption measurements by a high-resolution sun-spectrometer (SSM). It delivers precise data on the troposphere's content of water vapour. The SOLUSAR-measurements might be used to determine corrections for satelliteobservations. Systematic intercomparisons with other ground-based methods, like water vapour radiometry (WVR), GNSS-parameter estimation, and balloon soundings provide indications on the usability of the sun-spectrometry as an additional calibration tool.

The Geodesy and Geodynamics Lab (GGL) of ETH Zurich looks back on a number of years of experience in the domain of water vapour determination. Since the 90s GGL in cooperation with the working group Optical Spectroscopy of the Leibniz-Institut für Analytische Wissenschaften (ISAS), Berlin, has developed two dedicated systems (SAMOS and GEMOSS) which also were based on the principle of Differential Optical Absorption Spectroscopy (DOAS). Related publications appeared in this series as volume 62, Bernd Sierk, 2001 and volume 68, Alexander Somieski, 2005. The project ‚Solar Lunar Spectrometer for Atmospheric Research' (SOLUSAR) was initiated 2007 by ETH Zurich, the Leibniz-Institut für Analytische Wissenschaften – ISAS, and the Helmholtz-Zentrum Potsdam Deutsches GeoForschungsZentrum (GFZ) with the aim to devise a method of water vapour determination of high precision and high temporal resolution. Thereby, the set target to perform also lunar measurements was a special challenge. In addition the equipment had to be conceived for mobile fieldwork. The targets of mobility, sensitivity (lunar measurements), and accuracy were demanding tasks which Mr. Münch mastered superbly.

The SGC thanks the author for his valuable contribution to geodetic meteorology as well as the Swiss Academy of Sciences (SCNAT) for covering the printing costs of this volume.

Prof. Dr. M. Rothacher
Institut für Geodäsie und Photogrammetrie
ETH Zürich

Prof. Dr. A. Geiger
ETH Zürich
Präsident der SGK

Abstract

Tropospheric water vapour plays a crucial role in the understanding of a variety of different atmospheric processes, ranging from local weather phenomena to global climate change. Regarding satellite geodesy, water vapour acts as disturbing factor for various measurement methods, causing path delays of radio signals and consequently leads to considerable biases in the measurement results. The spatial and temporal concentration distribution can hardly be modelled and therefore has to be determined instrumentally to correct the influence computationally.

The application of the principle of "Differential Optical Absorption Spectroscopy" (DOAS) using the sun as radiation source to locally determine integrated water vapour concentrations (PW), has proven itself as a very potent methodology, with good relative and absolute accuracy, high temporal resolution and comparably low calibration efforts. It also seems especially well suited for validation purposes for independent measurement methods.

The intention of the presented project is to implement the findings from the development of earlier prototype instruments and to contemplate several further aspects related with the DOAS approach to determine atmospheric water vapour: Improved temporal coverage of the measurement method through inclusion of night time measurements with the help of moonlight, which are enabled by means of a massively increased system sensitivity to deal with the up to six orders of magnitude lower intensity of the background radiation with respect to solar measurements. Further it is to investigate, how reliable acquisitions of sun transmission spectra can be achieved, when deploying the system on moving platforms, for possible future validation measurements of satellite-borne radiometer data on satellite ground tracks on the open sea. The prototype instruments developed should particularly feature high field versatility, requiring eased transportability, resistance to weather and not least the possibility of a fully automatic measurement procedure, including instrument self-calibration.

For this purpose two identically constructed compact measurement systems were built. The instruments dispose of a custom-built telescope (heliostat principle) and an optically directly coupled spectrometer unit. The whole system is enclosed in a rugged aluminium hull, including most of the steering electronics. The motorized telescope is able to follow the moving light source fully autonomously, also with the platform moderately moving. A quasi-monochromator with an echelle grating as main dispersion element is used as spectrometer unit, allowing a compact architecture, a great spectral resolution and efficiency at the same time. Together with a back-thinned CCD detector highly resolved images of water vapour absorption lines can be obtained. The primary wavelength range lies between 789 nm and 802 nm, the reciprocal linear dispersion amounts to 7.3 pm/px at a focal length of just 400 mm. A motorized deflection mirror in the spectrometer allows the observation of adjacent spectral windows and serves for the highly precise position stabilization of the spectrum on the CCD sensor.

Test measurements with the sun and the moon as background radiation source show the extraordinarily high system light throughput and the high spectral resolving power of the apparatus. However illumination dependent interference structures on the detector (etaloning) prevent the deduction of usable transmission spectra from the measured raw data. For that reason a variety of optical measures to homogenize the radiation entering the spectrometer with respect to field and aperture are examined. As a feasible solution, with sufficient radiation distribution and a still acceptable intensity attenuation, a short quartz light guiding fibre with a hexagonal cross section has been found and implemented.

For instrumental control a software package has been developed, which autonomously handles the measurement process including the various calibration processes and the interaction of the various sensors and actuators. Additionally a variety of algorithms have been provided, helping to eliminate various defective influences in the raw data, as the correction of stray and false light portions or the elimination of interspersed beat structures in lunar spectra. Furthermore procedures which serve in spectrum processing have been supplied, as for the computation of a holistic intensity baseline or the

dynamic determination of apparatus profiles. For the determination of the water vapour concentrations from the measured spectroscopic data established computational procedures could be used mostly.

Various available spectroscopic databases have been analysed regarding the suitability of the listed absorption line parameters for the deduction of reliable water vapour concentrations. Comparison between the two identically built solar spectrometers yield considerable deviations of up to $1.5\,\mathrm{kg/m^2}$ in the zenith integral concentrations which are presumably ascribable to systematic influences likely caused by unrecognised stray light influence. The mean value of the stochastic deviations amounts to about 1.1 % of the slant PW concentration. The cross-comparison with an independent measurement method, in this case GPS meteorology, however also shows significant divergences and thus point to the various further systematic effects which have to be examined more closely, as e.g. the uncertainty of the published spectroscopic parameters regarding line strength and line broadening as well as the baseline determination in the measured spectra.

Despite the considerable sensitivity losses with respect to the originally planned design due to beam homogenization, the methodology has been successfully applied to lunar measurements, albeit with reduced accuracy as stated in stochastic appraisals and with considerably lower temporal resolution.

The project presented here confirms and clarifies the possibilities of the application of DOAS for ground-based remote sensing of integral water vapour concentrations, but also gives clear indication on the different systematic biases which have to be examined more closely, e.g. regarding the accuracy of the spectroscopic parameters (both, for line strength and line broadening), as well as the determination procedure of the baseline in the measured spectra. This work also points out the chances as well as the serious difficulties which arise from the design, construction and deployment of highly integrated DOAS spectrometers of high performance. Regarding the application of various optical components and detectors for the development of similar instruments valuable insights have been gathered.

Zusammenfassung

Troposphärischer Wasserdampf spielt als Einflussgrösse eine wichtige Rolle für das Verständnis einer Vielzahl atmosphärischer Vorgänge, von lokalen Wetterphänomenen bis hin zum globalen Klimawandel. Im Bereich der Satellitengeodäsie tritt Wasserdampf als schwer modellierbarer Störfaktor in Erscheinung, der bei verschiedenen Messsystemen Fehler durch Laufzeitverzögerungen von Radiosignalen verursacht. Die Störgrösse muss instrumentell bestimmt werden, um den Einfluss rechnerisch zu eliminieren.

Die Anwendung des Prinzips der *Differentiellen Optischen Absorptionsspektroskopie* (DOAS) mit Hilfe der Sonne als Hintergrundstrahler zur lokalen Bestimmung von integralen Wasserdampfkonzentrationen (PW) hat sich in der Vergangenheit als äusserst wirksamer Ansatz erwiesen, dies mit guter relativer und absoluter Genauigkeit bei gleichzeitig hoher zeitlicher Auflösung und verbunden mit einem vergleichsweise geringen Kalibrationsaufwand. Insbesondere auch als Validierungsmethode unabhängiger Messverfahren scheint diese Methode hervorragend geeignet zu sein.

Die Intention des vorliegenden Projektes liegt in der Umsetzung der Erkenntnisse, welche aus der früheren Entwicklung von Geräteprototypen gewonnen wurden und in der genaueren Untersuchung weiterer Aspekte der DOAS Methodik zur Wasserdampfbestimmung: Verbesserung der zeitlichen Einsatzfähigkeit der Messmethode durch Ermöglichung von Nachtmessungen mithilfe von Mondlicht, dies durch eine massive Verbesserung der Instrumentensensitivität, um im Vergleich zu Sonnenmessungen mit bis zu sechs Grössenordnungen schwächeren Intensitäten umgehen zu können. Weiter soll untersucht werden, wie eine zuverlässige Erfassung von Sonnentransmissionsspektren auf einer bewegten Plattform durchzuführen ist, zur möglichen Validierung von satellitengestützen Radiometermessungen auf Satelliten-Groundtracks auf offener See. Die zu entwickelnden Prototypen sollen sich insbesondere auch durch einfache Einsetzbarkeit im Feld auszeichnen, was neben einer erleichterten Transportfähigkeit und Witterungsbeständigkeit nicht zuletzt die Möglichkeit eines vollautomatisierten Messablaufs, inklusive Geräteselbstkalibrierung, umfasst.

Zu diesem Zweck wurden zwei baugleiche kompakte Messsysteme erstellt. Die Geräte verfügen über ein spezifisch für diese Aufgabe entwickeltes Teleskop (Heliostat-Prinzip) und ein optisch direkt angekoppeltes Spektrometer. Die gesamte Messeinheit ist wetterfest in einer robusten Aluminiumhülle eingeschlossen, einschliesslich der Steuerelektronik. Das Teleskop ist in der Lage, der bewegten Lichtquelle vollautomatisch zu folgen, dies auch bei moderater Bewegung des Untergrundes. Bei der Spektrometereinheit handelt es sich um einen Quasi-Monochromator mit einem Echelle-Gitter als Hauptdispersionselement, was eine kompakte Bauweise bei gleichzeitig hoher spektraler Auflösung und Lichtstärke erlaubt. Mithilfe eines rückseitig beleuchteten CCD-Sensors können hochaufgelöste Aufnahmen von Wasserdampf-Absorptionslinien erfasst werden. Der primäre Wellenlängenbereich liegt zwischen 789 und 802 nm, die reziproke Lineardispersion beträgt 7.3 pm/px bei einer Brennweite von nur 400 mm. Ein motorisierter Umlenkspiegel im Spektrometer ermöglicht zusätzlich das Anfahren benachbarter Wellenlängenregionen, sowie die hochpräzise Positionsstabilisierung des Spektrums auf dem Detektor.

Testmessungen mit der Sonne und dem Mond als Hintergrundstrahler zeigen die ausserordentliche Lichtstärke des Systems. Jedoch verwehren beleuchtungsabhängige Interferenzstrukturen (Etaloning) auf dem Detektor das Generieren von auswertbaren Transmissionsspektren aus den Messdaten. Unter diesem Aspekt wurde die Eignung verschiedener optischer Verfahren zur Homogenisierung der ins Spektrometer eingeleiteten Strahlung bezüglich Feld und Apertur untersucht. Als Lösung mit hinreichend guter Strahlungsumverteilung bei gleichzeitig hinnehmbarer Intensitätsreduktion hat sich der Einsatz von kurzen Quartzlichtleitfasern mit hexagonalem Querschnitt erwiesen.

Hinsichtlich des Messbetriebes wurde ein Softwarepaket entwickelt, welches den Messablauf inklusive der zahlreichen Kalibrationsvorgänge autonom steuert und das Zusammenspiel der verschiedenen Sensoren und Aktuatoren koordiniert. Es wurden zudem verschiedene Algorithmen entwickelt, welche der

Eliminierung von Fehleinflüssen in den Rohmessdaten dienen, wie die Korrektur von Streu- und Falschlicht oder Algorithmen zur Korrektur von eingestreuten Schwebungsstrukturen im Spektrenbild. Ebenso wurden Verfahren bereitgestellt, welche zur Weiterverarbeitung der erfassten Spektren dienen, wie für eine integrale Bestimmung der Intensitätsbasislinie oder die dynamische Bestimmung von Apparateprofilen. Für die Ermittlung der Wasserdampfkonzentrationen aus den gemessenen spektroskopischen Daten konnte weitgehend auf bekannte Rechenverfahren zurückgegriffen werden.

Verschiedene verfügbare Spektraldatenbanken wurden hinsichtlich der Eignung der Daten ihrer Absorptionslinien zur zuverlässigen Bestimmung der Wasserdampfkonzentrationen analysiert. Vergleichsmessungen zwischen den beiden baugleichen Sonnenspektrometern zeigen erhebliche Abweichungen von bis zu $1.5\,\mathrm{kg/m^2}$ der zenitalen Integralkonzentrationen, welche aber hauptsächlich auf systematische Einflüsse zurückzuführen sind, wahrscheinlich in erster Linie verursacht durch noch unerkannten Streulichteinfluss. Der Mittelwert der stochastischen Abweichungen beträgt etwa $1.1\,\%$ der Slant PW Konzentration. Quervergleiche mit Daten, die durch GPS-Meteorologie erhoben wurden, zeigen ebenfalls deutliche Abweichungen und weisen auf verschiedene weitere systematischen Effekte hin, welche noch genauer untersucht werden müssen, beispielsweise die Genauigkeit der spektroskopischen Parameter aus der Literatur bezüglich Linienstärke und Linienverbreiterung, wie auch die Basislinienbestimmung in den gemessenen Spektren.

Trotz der deutlichen Empfindlichkeitseinbusse gegenüber dem ursprünglich geplanten Konzept konnte die Methodik dennoch auch erfolgreich auf Mondmessungen angewandt werden, wenngleich mit verminderter Genauigkeit, wie mittels stochastischer Abschätzungen dargelegt, und mit deutlich reduzierter zeitlicher Auflösung.

Das vorliegende Projekt bestätigt und verdeutlicht die Möglichkeiten der Anwendung von DOAS auf die bodengestütze Bestimmung von integralen Wasserdampfkonzentrationen, gibt aber auch klare Hinweise bezüglich der noch eingehender zu betrachtenden systematischen Einflüsse. Mit dieser Arbeit werden sowohl die Chancen, als auch die erheblichen Schwierigkeiten aufgezeigt, mit denen das Design, die Konstruktion und der Einsatz von hochintegrierten DOAS-Spektrometern hoher Leistungsfähigkeit verbunden ist. Bezüglich des Einsatzes von verschiedenen optischen Komponenten und Detektoren konnten für die Entwicklung ähnlicher Instrumente wertvolle Erkenntnisse gewonnen werden.

Contents

Abbreviations & Nomenclature

CCD	Charge-Coupled Device
CMOS	Complementary Metal-Oxide Semiconductor
DIAL	Differential Absorption LIDAR (see LIDAR)
DOAS	Differential Optical Absorption Spectroscopy
FWHM	Full Width at Half Maximum
GEMOSS	Geodetic Mobile Solar Spectrometer
GFZ	Helmholtz-Zentrum Potsdam Deutsches GeoForschungsZentrum
GGL	Geodesy and Geodynamics Lab, ETH Zürich
GNSS	Global Navigation Satellite System
GPS	Global Positioning System (NAVSTAR-GPS)
ISAS	Leibniz-Institut für Analytische Wissenschaften - ISAS - e.V.
LIDAR	Light Detection and Ranging
LSQ	Method of Least Squares
MAX-DOAS	Scattered Light DOAS with Multi-Axis Viewing Geometry
MJD	Modified Julian Date
MOSFET	Metal-Oxide-Semiconductor Field-Effect Transistor
NA	Numeric Aperture
NIR	Near Infrared Radiation
OpAmp	Operational Amplifier
QE	Quantum Efficiency
PID	Proportional-Integral-Derivative Controller
POF	Polymer Optical Fibre
PW	Integrated Precipitable Water Vapour
PWM	Pulse Width Modulation
px	Picture Element (pixel)
rev	Revolution
RH	Relative Humidity
SAMOS	Solar Atmospheric Monitoring Spectrometer
SOLUSAR	Solar Lunar Spectrometer for Atmospheric Research
TTL	Transistor-Transistor Logic
UTC	Coordinated Universal Time
UV	Ultraviolet Radiation
VIS	Visible Light
VLBI	Very Long Baseline Interferometry
WVR	Water Vapour Radiometer
ZPD	Zenith Path Delay
ZPW	Zenith Integrated Precipitable Water Vapour
ZSL-DOAS	Zenith Scattered Light DOAS
ZWD	Zenith Wet Path Delay

1

Introduction

Water in the gaseous state of matter is involved in abundant processes in the earth's atmosphere. For many decades its influence in a vast number of chemical processes on a small scale has been a prime interest in the realm of atmospheric physics. In recent years a considerable shift of attention towards the manifestation of influence on larger scales is recognizable. The role of atmospheric water vapour as a greenhouse gas in the process of human-made global climate change is under close scrutiny. However its effects are still not fully understood as manifold positive and negative feedback loops have to be considered and the impacts are strongly dependent on different parameters like, e.g., its vertical distribution [Maurellis and Tennyson, 2003; Sherwood et al., 2010].

In the geodetic scientific community water vapour has caught constantly rising attention with the introduction of more and more satellite-based microwave measurement systems. Due to the ever increasing demands for higher measurement accuracy the efforts to determine and hence eliminate the disturbing influence of water vapour in the atmosphere has steadily risen and has lead to the definition of a whole new discipline within the geodetic sciences. A sizeable set of diverse methodological approaches with very different characteristics have been developed and deployed to obtain water vapour abundances and help to increase the reliability and accuracy of satellite systems for earth observation and surveying (see, e.g., [Niell et al., 2001] or [BKG, 2006]).

At the *Geodesy and Geodynamics Lab* of the *Institute of Geodesy and Photogrammetry IGP* at *ETH Zürich* the determination of atmospheric water vapour has been a research subject for nearly 20 years (see, e.g., Bürki and Kahle [1995], Sierk et al. [1997], Dodson et al. [1998]). Besides the extraction of information on water vapour abundances from GNSS data obtained by permanently installed receivers (GNSS meteorology, GNSS tomography), another focus has been laid onto the development of dedicated remote water vapour sensing instruments: Beginning with Water Vapour Radiometers (WVR) deriving water vapour concentrations from emitted thermal radiation; later on solar spectrometers measuring atmospheric absorption spectra with the sun as background illumination source and thus determining slant integral concentrations through the analysis of strength and shape of single water absorption lines.

The developed spectrometers ***S**olar **A**tmospheric **Mo**nitoring **S**pectrometer (SAMOS)* and ***Ge**odetic **Mo**bile **S**olar **S**pectrometer (GEMOSS)*, jointly conceived with the *Leibniz-Institut für Analytische Wissenschaften - ISAS - e.V.* in Berlin using the technique of *Differential Optical Absorption Spectroscopy (DOAS)*, have proven the possibility to retrieve highly accurate water vapour concentrations using said methodology. Its usefulness as a verification and calibration tool in support of other independent measurement techniques has been shown [Somieski et al., 2006]. The above named projects also lead to a clarification regarding the necessary instrument characteristics in order to guarantee highly precise and reliable measurement results, while keeping the complexity of the hardware and its handling at a reasonable level.

1.1 Goals of this work

The project ***So**lar **Lu**nar **S**pectrometer for **A**tmospheric **R**esearch (SOLUSAR)* was initiated in the year 2007 as a joint project of *ETH Zürich*, the *Leibniz-Institut für Analytische Wissenschaften - ISAS* and the *Helmholtz-Zentrum Potsdam Deutsches GeoForschungsZentrum (GFZ)* to take onward the development of spectrometers using DOAS to retrieve total column water vapour contents and to further explore certain related topics by building two instrument prototypes with identical design. This with the following main objectives:

- The new instruments should facilitate a prolongation of the possible measurement uptime with respect to the predecessor instruments. This should be achieved through the design of a telescope-spectrometer combination, with a markedly enhanced sensitivity, thus enabling night-time measurements using sunlight reflected by the moon surface and possibly direct sunlight at slightly cloudy conditions.
- The instruments ought to be considerably smaller, more compact and lightweight and thus easier to transport and deploy at remote measurement sites.
- For possible future validation campaigns of on-board WVR instruments of altimetry satellites (see Somieski et al. [2006]) the instrument should be capable to produce measurement data when applied on a vessel. Thus telescope mechanics (including gimbal mounting), electronics and software have to be designed allowing an automatic high-speed tracking of the moving radiation source.
- To reduce the instrument size and complexity and to shorten the spectra readout period, the simultaneously obtained wavelength range will be markedly narrowed to a spectral window promising the best possibilities for water vapour concentrations retrieval. The potential to use adjacent wavelength regions should be maintained however.
- For the first time two identical instrument prototypes are to be built and deployed in order to assess the inherent accuracy of the chosen measurement concept.

Various qualities also attributable to the predecessor instruments such as fully automated permanent deployment and a comparable final accuracy should also apply to the new systems.

1.2 Outline of the thesis

This thesis is structured in the following way: *Chapter 2* will give a broad overview on the relevance of atmospheric water vapour in various fields of science such as climatology and meteorology, but emphasizing the implications in the domain of geodesy and how the water vapour's disturbing influence does take effect and can be described. A non-comprehensive description of a number of retrieval methods applied nowadays is given, discussing also advantages and disadvantages of the various methodological approaches. *Chapter 3* explains the basic principles of absorption spectroscopy in general before focussing on the particularities of DOAS and its application for the sake of water vapour retrieval.

A detailed description of the SOLUSAR instrument's hardware and its features is given in *Chapter 4* covering the mechanical, optical and electronic design of the telescope and spectrometer unit. Major issues faced during the development are described specifically. Also the various adjunct hardware components are outlined. *Chapter 5* covers the algorithms applied during the measurement process, whereas *Chapter 6* deals with various aspects relevant in the preprocessing of the retrieved data, which are specific for the SOLUSAR measurement system.

Chapter 7 presents measurement results from the two measurement systems made under different circumstances and discusses their accuracy of the established instruments. *Chapter 8* sums up the gathered findings and gives an outlook on possible further developments.

Selected schemes and drawings concerning the electronic design can be found in *Appendix A*.

2

Atmospheric Water Vapour

Water in its different states of matter shapes the surface of the earth like no other chemical substance. Also the emergence and sustainment of all known forms of life are inseparably bound to the presence of water [Wozniak and Dera, 2007] and to a major part they consist of it. More than 70 % of the earth's surface is covered by liquid water, more than 6 % by ice or snow. The total quantity of water on earth amounts to 1.35×10^{21} kg [Roedel, 1994]. Of this amount only around 0.01 % can be found in the gaseous hull of the earth – the atmosphere. Uniformly distributed over the total surface of the earth this corresponds to an average condensed water column height of around 25 mm (corresponds to 25 kg/m^2).

The allocation of the atmospheric water vapour on a global scale is vastly uneven though. From the equator region, where the average water content reaches over 40 mm, it continuously drops in direction of the poles where mean abundances are usually between 5 mm and 10 mm as shown in Fig. 2.1(a).

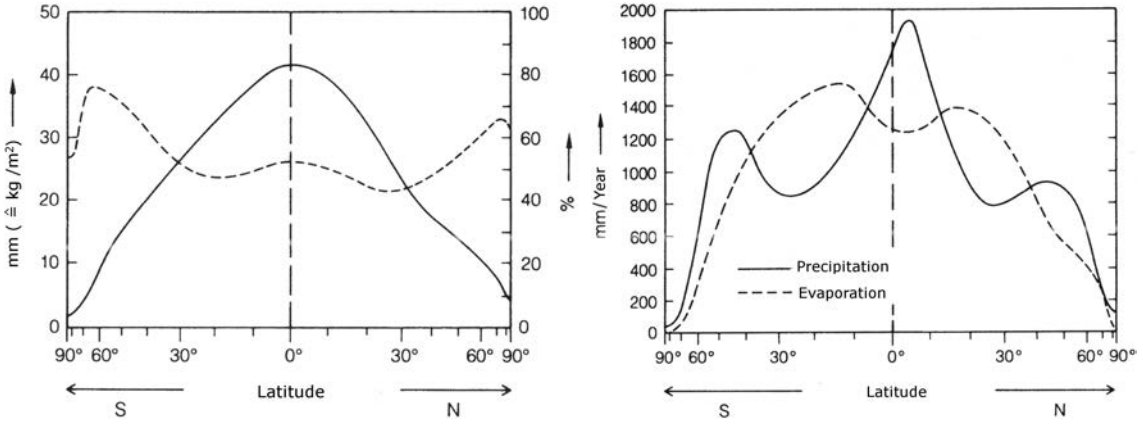

(a) Mean water vapour content expressed as condensed water column height (full line, left scale) and mean cloud coverage percentage (dashed line, right scale). Both with respect to latitude.

(b) Mean precipitation and evaporation rates per year on earth as a function of latitude.

Figure 2.1: Water vapour in the earth's atmosphere (adapted from Roedel [1994]).

As evident in Fig. 2.1(b), the meridional distributions of evaporation and precipitation also show a large latitudinal dependency. The evaporation rate of water is closely linked to the amount of incident radiation and to the local albedo (reflection coefficient). The greatest

evaporation rates can be found in the subtropics during summertime. The occurrence of precipitation is mainly determined by the amount of precipitable water vapour in the atmosphere and the occurrence of updraught and downdraught systems. The regional imbalances of precipitation and evaporation have to be compensated by means of transport of water (gaseous, liquid or solid) in the atmosphere. Large amounts of water are carried by winds from the zone between 10° and 35° of latitude in direction of the poles and to the Intertropical Convergence Zone (ITCZ) in the equator region. Apart from meridional transport, a net atmospheric transfer of water from sea areas to land masses is observable [Roedel, 1994]. On average a water molecule stays in the atmosphere for about 9 days which illustrates the swiftness of the atmospheric water transfer [Seidel, 2002].

The atmospheric water transporting process describes just one part of what is generally called the *hydrological cycle* wherein water in different phases is moved in and between oceans, atmosphere and continents [American Geophysical Union (AGU), 1995] by means of the processes of precipitation, vapour transport, evaporation, evapotranspiration, infiltration, groundwater flow and run-off [United Nations Environment Programme (UNEP), 2002] depicted in Fig. 2.2. The process of water transport in the atmosphere can also be seen as a displacement mechanism of energy in form of latent heat which is brought into the atmosphere through the process of evaporation.

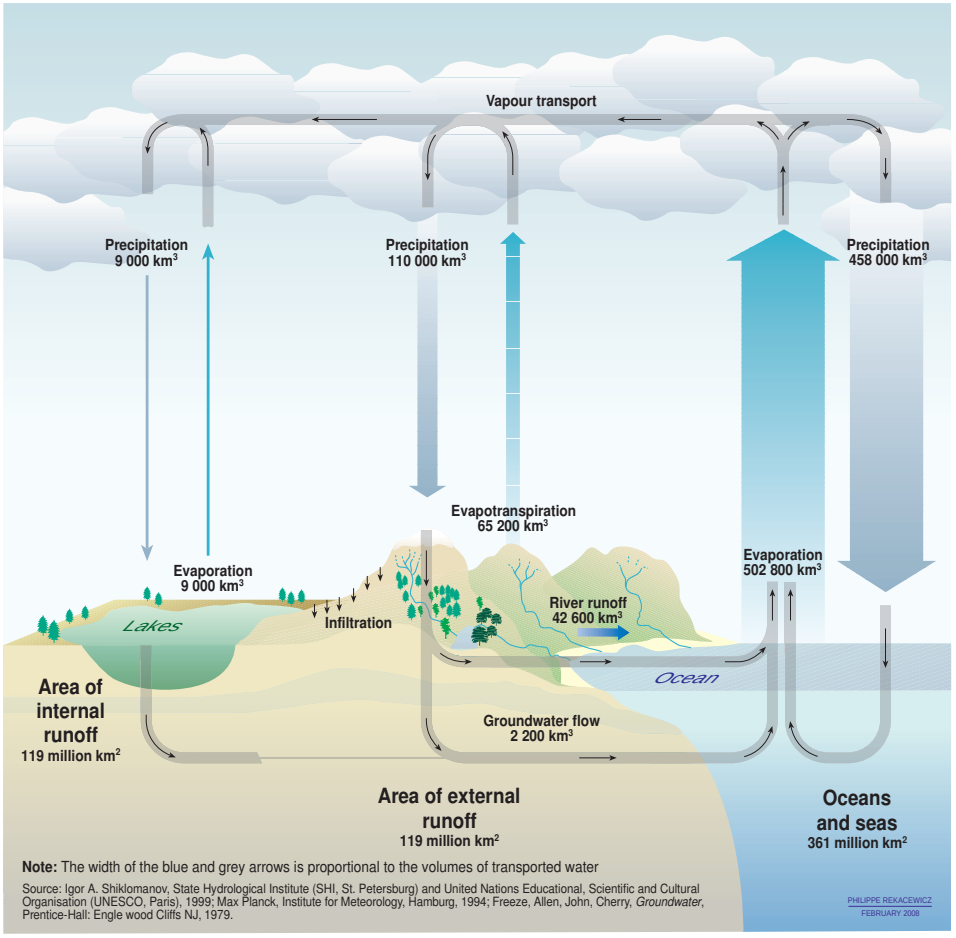

Figure 2.2: Processes belonging to the earth's hydrological cycle with estimated amounts of water involved [United Nations Environment Programme (UNEP), 2002].

The distribution of water vapour is not only horizontally uneven, it also shows a strong height dependency. The mean vertical distribution of water vapour is shaped to a large degree by the

occurring temperatures which determine the dew point and thus the storage capacity of water in its gaseous phase. A good approximation of the temperature dependency of the saturation pressure e_S of water vapour is based on the *August-Roche-Magnus approximation* given in Eq. 2.1, a simplification of the *Clausius-Clapeyron* relationship [Lawrence, 2005]:

$$e_S(T) = C \cdot \exp\left[\frac{A \cdot T}{B + T}\right] \tag{2.1}$$

with T the temperature in [°C] and the constant values $C = 6.1094\,\text{hPa}$, $A = 17.625$, $B = 243.04\,°\text{C}$. In the lower atmosphere mean temperatures gradually decrease with increasing height thus leading to lower water vapour abundances. Around 99 % of the atmospheric water vapour can be found in this lowest atmospheric part, called *troposphere*. The height of the tropospheric layer depends largely on the geographical latitude and the season. Around the equator the troposphere can reach up to 15 km but in direction of the pole regions it can decline to 7 km. The barrier defining the border between the upper troposphere and the lower stratosphere is called *tropopause* (see Fig. 2.3). It is mainly characterized by a temperature inversion. Within the troposphere 50 % of the water is found below heights of about 1.5 km, 95 % below 5 km.

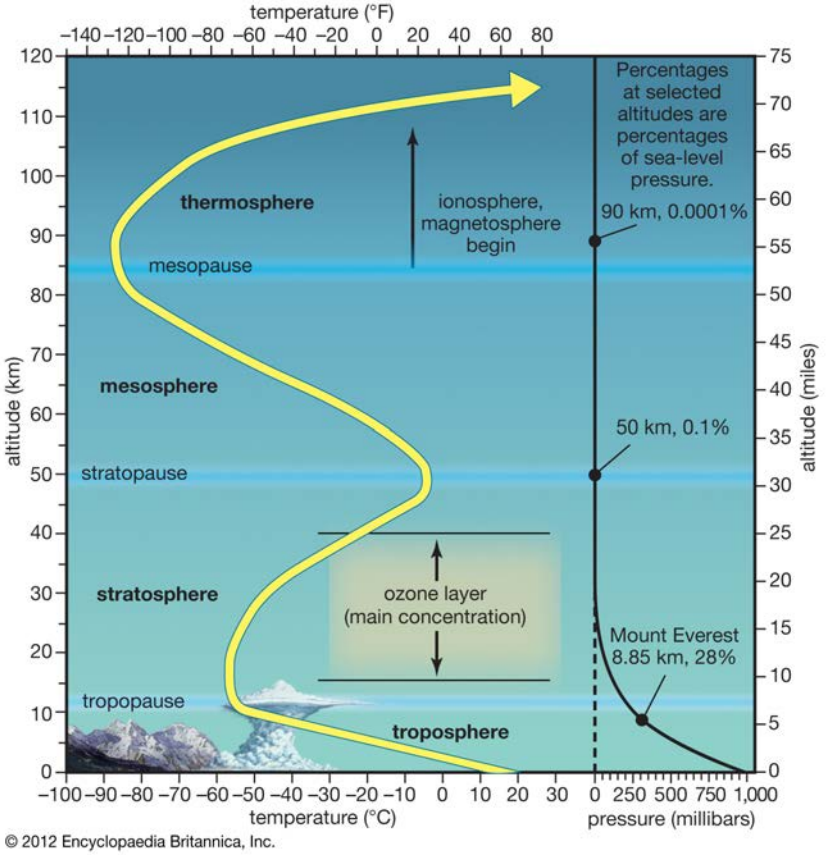

Figure 2.3: Vertical structure of the earth's atmosphere. The yellow line shows the temperature variation in different layers of the earth's gaseous envelope. At a height of around 10 km (tropopause) a reversal of the temperature trend is observable. Around 99 % of the atmospheric water vapour can be found beneath the tropopause [Encyclopedia Britannica, 2012].

Water vapour influences atmospheric processes in manifold ways. This work cannot provide a

comprehensive overview of the countless mechanisms taking place. But as water vapour plays a crucial role in the understanding of the causal relations both, in the fields of meteorology and climatology, some of the implications will be shortly outlined in the following sections.

2.1 Significance in Meteorology

Apart from the general distribution variability on a global scale and the dependence on seasonality described above, one of the major characteristics of water vapour in the earth's atmosphere is its tremendous variation in concentrations, spatially and temporally, also on very short scales. In this regard water substantially differentiates from the other major constituents of the atmosphere, which show a lot less distribution variations and whose occurrence thus is much more easily predictable using modelling approaches. The registration and understanding of the concentration distribution, the distributional changes and state of phase transitions of water on a short time scale are especially relevant in the field of meteorology. Dense monitoring networks with high temporal resolution can provide detailed information on the formation and development of small-scale meteorological phenomena, such as fronts or squall lines [Bevis et al., 1992].

The distribution of clouds or the occurrence of precipitation for instance are closely linked to the distribution of water vapour. These phenomena occur where air masses containing water vapour reach a temperature where saturation takes place and water forms droplets or snow flakes around condensation nuclei. The saturation point can be reached through different processes: Import of colder or moister air, thermal upwinds or uplift processes during passages of cold or warm fronts. In the process of condensation, energy is released which again leads to uplifts as the warming air becomes lighter. This procedure has a major impact on the development and intensification of thunderstorm systems. Perler [2012] emphasizes the potential of knowledge on the spatial distribution of water vapour, which for instance is obtainable by means of water vapour GNSS tomography (for a short description see Section 2.4.6), to considerably improve the initial state in numerical weather prediction models.

2.2 Significance in Climatology

As mentioned before, variations in the atmospheric water vapour field occur not only on short time scales. The long-term atmospheric characteristics regarding temperature, humidity and precipitation are of great importance because they basically determine the climate regimes prevailing in the different zones. The distribution of water vapour is closely linked to global circulation patterns defining global climate zones but also determined by local atmospheric structures leading to specific micro climates. Though, as described above, water vapour itself is alike involved in the process of building said circulation patterns.

Additionally a variety of seasonal distribution variations appear forced by temperature and circulations changes, especially in the northern hemisphere where the larger land fraction with lower heat capacity is susceptible to such variations. Furthermore the El-Niño-Southern Oscillation (ENSO) causing changes in the surface temperature in tropical pacific is an example of a dominant mechanism leading to distribution changes of water vapour on a even longer (multi-annual) time scale [American Geophysical Union (AGU), 1995].

Water vapour is one of various greenhouse gases in the atmosphere contributing to the process where short wave radiation of the sun is transmitted through the atmosphere whereas earth-emitted longer wave radiation is absorbed thus establishing a climate allowing large areas with

temperatures beyond freezing. In today's constitution of the atmosphere, water vapour is the most abundant and arguably most important greenhouse gas. Nearly two thirds of the whole natural greenhouse effect is caused by water vapour, whereas the much-discussed carbon dioxide accounts for about a quarter. As explained in Section 3.4, water vapour shows strong radiation absorption, e.g., at wavelengths between 5 µm and 8 µm.

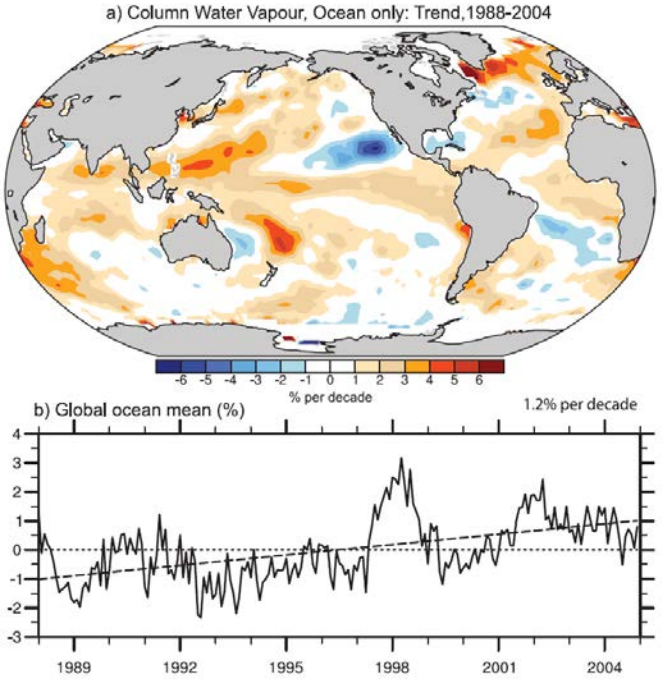

Figure 2.4: Regional changes of the total column water vapour over oceans in the time span between 1988 and 2004 (above) and monthly deviations from the 1988 to 2004 mean water vapour amount on a global scale with linear trend (below). (Adapted from Intergovernmental Panel on Climate Change [2007]).

Understanding the behaviour of water vapour in the atmosphere and especially its distribution in the various atmospheric layers is of great importance, because of its ascribed potential to amplify the human-caused climate change. The different and partly contradictory effects are still insufficiently understood to this day. Certain modelling approaches which include the amplification effects of atmospheric moisture, predict an increase of the surface temperature sensitivity to carbon dioxide input by up to a factor of three [Held and Soden, 2000]. According to these models a main positive feedback loop arises from the increased evaporation and the potential of the atmosphere to hold water vapour, if temperatures are rising through the human-made greenhouse effect. The additionally stored water in vapour phase could prevent even more radiation to escape into space thus leading to even higher temperatures. However the described mechanism is mitigated, if not broken, by the processes of condensation and precipitation of water.

Next to the above mentioned positive feedback loop, also potential negative feedback loops have to be considered. Emergence of larger amounts of atmospheric water vapour leads to stronger cloud building with the effect that greater parts of incoming solar radiation are reflected back to space. On the other hand clouds also trap portions of long-wave radiation emitted by the earth. Another aspect to be considered is that increased temperatures lead to a greater vertical atmospheric convection and to an uplift of the tropopause and freezing out of water vapour at the very low temperatures.

Water vapour also plays a role in countless chemical reactions taking place in the atmosphere, having an impact on air quality, influence on aerosol particle size, composition and their reaction with other gases [Kämpfer, 2012].

2.3 Influence on geodetic applications

Manifold geodetic applications such as the different GNSS entities, altimetry satellites or Very Long Baseline Interferometry (VLBI) are based on the measurement of the propagation time (or propagation time differences) of electromagnetic waves belonging to the microwave range. In absence of the earth atmosphere these signals would travel on a straight line from the emitting source to the receiver. In reality the propagation of these signals is considerably affected by the varying refractive indexes along the ray path: First, and more importantly, the signal is delayed due to the decreased speed of light compared to propagation in vacuum. Secondly the ray path is bent due to continuous incremental diffraction [Bevis et al., 1992].

2.3.1 Total Propagation Delay

According to the *Fermat Principle* radiation travelling in a refractive medium between two points follows the path S which produces the minimal travel time. The propagation time τ along said path is:

$$\tau = \int_S dt = \int_S \frac{1}{c_{medium}(s)}\, ds. \tag{2.2}$$

The speed of light $c_{medium}(s)$ depends on the refractive index n at a certain position s in the medium:

$$c_{medium}(s) = \frac{c_{vac}}{n(s)}. \tag{2.3}$$

c_{vac} denotes the speed of light in vacuum ($2.997\,924\,58 \times 10^8\,\mathrm{m\,s^{-1}}$). Combining Eq. 2.2 and Eq. 2.3, the electric path S_{el} of radiation travelling between two points along the ray path S becomes:

$$S_{el} = c_{vac} \cdot \tau = \int_S n(s)\, ds. \tag{2.4}$$

The electric path S_{el} is the travel distance of a signal propagating in vacuum for a travel time period of τ. The so-called path delay Δ^{PD} describes the difference between the electric path S_{el} and the straight euclidean distance S_g of the two points. The path delay includes both effects: geometric bending of the ray path as well as slower signal propagation:

$$\Delta^{PD} = \int_S n(s)\, ds - S_g = \underbrace{\int_S \Big(n(s) - 1\Big)\, ds}_{\text{slower propagation}} + \underbrace{\int_S ds - \int_{S_g} ds}_{\text{ray bending}}. \tag{2.5}$$

The smaller bending part becomes exceedingly important for observations at very low elevation angles. For observations with elevation angles greater 15° it normally amounts to less than 1 cm

and totally vanishes for zenith observations, if the atmospheric layers are perfectly horizontally stratified.

2.3.2 Wet and Dry Path Delay

Path delays are often described using the atmospheric refractivity N instead of the refraction index n:

$$N = 10^6 \cdot (n - 1). \tag{2.6}$$

Different estimations can be found in literature. Basically, refractivity is a function of the absolute temperature T, air pressure p and the partial pressure of water vapour p_{H_2O}. An often used formula for the total refractivity N_{tot} is provided by Essen and Froome [1951]:

$$N_{tot} = k_1 \frac{p_d}{T} + k_2 \frac{p_{H_2O}}{T} + k_3 \frac{p_{H_2O}}{T^2}. \tag{2.7}$$

In Eq. 2.7 p_d denotes the partial pressure of dry air. In the coefficients k_i compressibility factors describing the non-ideal behaviour of the atmospheric gas components are contained. The parameters k_1, k_2 and k_3 have been redetermined several times [Perler, 2012]. Below the parameter set proposed by Rüeger [2002] is given which applies for air with a CO_2 content of 300 ppm:

$$\begin{aligned} k_1 &= 77.6848\,\mathrm{K\,hPa^{-1}} \\ k_2 &= 71.2952\,\mathrm{K\,hPa^{-1}} \\ k_3 &= 375\,463\,\mathrm{K^2/hPa} \end{aligned}$$

The total refractivity N_{tot} can be partitioned. Two different distinction methods are commonly applied. Either N_{tot} can be partitioned into *dry refractivity* N_{dry}, denoting the influence of air in absence of water vapour, and *wet refractivity* N_{wet}, which produces a division of the total path delay Δ^{PD} into a *dry delay* Δ^{PD}_{dry} and *wet delay* Δ^{PD}_{wet}:

$$N_{tot} = \underbrace{k_1 \frac{p_d}{T}}_{N_{dry}} + \underbrace{k_2 \frac{p_{H_2O}}{T} + k_3 \frac{p_{H_2O}}{T^2}}_{N_{wet}} \tag{2.8}$$

$$\Delta^{PD}_{dry} = 10^{-6} \int_S N_{dry}\, ds \tag{2.9}$$

$$\Delta^{PD}_{wet} = 10^{-6} \int_S N_{wet}\, ds \tag{2.10}$$

Saastamoinen [1972] proposed a separation of the refractivity N_{tot} and, accordingly, of the total path delay, into a *hydrostatic refractivity* N_{hs} summing the influence of dry air and the contributions of water vapour not caused by its dipole moment and a *non-hydrostatic*

refractivity N_{n-hs} describing the influence of the water vapour dipole characteristics. By applying the ideal gas law:

$$p_i = \rho_i \frac{R}{M_i} T \tag{2.11}$$

with R the universal gas constant, ρ_i the density, M_i the molar mass and p_i the partial pressure of the gas i, Eq. 2.7 can be transformed into:

$$N_{tot} = \underbrace{k_1 \frac{R}{M_{dry}} \rho_{tot}}_{N_{hs}} + \underbrace{\left(k_2 - k_1 \frac{M_{H_2O}}{M_{dry}}\right) \frac{p_{H_2O}}{T} + k_3 \frac{p_{H_2O}}{T^2}}_{N_{n-hs}}. \tag{2.12}$$

Thus the *hydrostatic delay* Δ_{hs}^{PD} and *non-hydrostatic delay* Δ_{n-hs}^{PD} are:

$$\Delta_{hs}^{PD} = 10^{-6} \int_S N_{hs}\, ds \tag{2.13}$$

$$\Delta_{n-hs}^{PD} = 10^{-6} \int_S N_{n-hs}\, ds \tag{2.14}$$

The hydrostatic part of the delay is generally the much greater portion: In zenith direction at sea level it amounts to approximately 2.3 m. The very variable non-hydrostatic delay normally ranges between 1 cm to 40 cm in zenith direction [Elgered, 1993].

Path Delay Modelling

A reasonable estimation of the atmospheric refractivity along the ray path from sender to receiver is fairly difficult, especially when the influence of atmospheric moisture is included. Saastamoinen [1972] has proposed a model for Δ^{PD} , based on gas laws, which requires knowledge on the ground temperature T_{local}, local ground pressure p_{local}, local ground water vapour pressure $p_{H_2O,local}$ and the signal direction through elevation angle z:

$$\Delta_{Saas}^{PD} = \frac{a_1}{\cos z} \cdot \left[p_{local} + \left(\frac{a_2}{T_{local}} + a_3 \right) \cdot p_{H_2O,local} - B \tan^2 z + \right] + \delta_R \tag{2.15}$$

with the correction term B for pressure (depending on station height), δ_R for range (depending on observation angle and station height) and the constants $a_1 = 0.002\,279\,\mathrm{m\,hPa^{-1}}$, $a_2 = 1153\,\mathrm{K}$ and $a_3 = 0.074$ [Rüeger, 2002]. The values for B and δ_R are listed in tables, e.g. [Hofmann-Wellenhof et al., 2001]. Troller [2004] describes a split of Δ_{Saas}^{PD} into a dry delay Δ_{dry}^{PD} and wet delay Δ_{wet}^{PD}:

$$\Delta_{dry}^{PD} = \frac{a_1}{\cos z} \cdot \left(p_{local} - a_4 \cdot p_{H_2O,local} - B \cdot \tan^2 z \right) + \delta_R, \tag{2.16}$$

$$\Delta_{wet}^{PD} = \frac{a_1}{\cos z} \cdot \left(\frac{a_2}{T_{local}} + a_5 \right) \cdot p_{H_2O,local}. \tag{2.17}$$

The constants are: $a_4 = 0.155\,471$ and $a_5 = 0.205\,471$.

2.3.3 Path Delay and Precipitable Water Vapour

In some measurement methods, such as GNSS meteorology, estimates for path delays are computed. Other methods, as LIDAR or DOAS described in Chapter 3, are deriving water vapour abundances. In order to compare the results of different methods or to introduce values into weather models, Bevis et al. [1992] describe a procedure to convert the mentioned quantities.

The *Precipitable Water Vapour (PW)*, which is sometimes also called *Integrated Water Vapour (IWV)*, describes the total mass of water vapour of density ρ_{H_2O} [kg/m^3] along the ray path S with respect to an area of 1 m^2 at the ground in [kg/m^2]:

$$PW\,[\mathrm{kg/m^2}] = \int_S \rho_{H_2O}(s)\,ds \tag{2.18}$$

Often the water vapour amount is also expressed as liquid water column height $PW_{condensed}$:

$$PW_{condensed}\,[\mathrm{m}] = \frac{PW}{\rho_{H_2O,liquid}} \tag{2.19}$$

where $\rho_{H_2O,liquid}$ is the density of liquid water. The precipitable water vapour in zenith direction ZPW [m] between levels h_b and h_t is given by:

$$ZPW = \int_{h_b}^{h_t} \rho_{H_2O}(z)\,dz \tag{2.20}$$

To relate path delays and water vapour amounts, a conversion factor κ is introduced:

$$ZPW = \kappa \cdot ZWD \tag{2.21}$$

with ZWD being the *Zenith Wet Delay*, corresponding to the calculated value of Eq. 2.17 with $z = 0$. According to Elgered and Jarlemark [1998] for an effective mean temperature of 270 K a PW value of 1 kg/m^2 corresponds to a wet delay of 6.5 mm. For the computation of κ Davis et al. [1985] suggest the introduction of a weighted mean temperature T_m:

$$T_m = \frac{\int (p/T)\,dz}{\int (p/T^2)\,dz} \tag{2.22}$$

p and T denote the height-dependent total pressure and absolute temperature. κ according to Bevis et al. [1992] is then given by:

$$1/\kappa = 10^{-6}(k_3/T_m + k_2)R_{H_2O} \tag{2.23}$$

with R_{H_2O} being the specific gas constant for water vapour ($R_{H_2O} = \frac{R}{M_{H_2O}}$). If the vertical atmospheric temperature distribution cannot be obtained from numerical weather models or profiles from radiosondes, Bevis et al. [1992] suggest an estimation for T_m using ground temperatures T_s:

$$T_m = \tau_1 \cdot T_s + \tau_2 \tag{2.24}$$

with the constants $\tau_1 = 0.72$ and $\tau_2 = 70.2\,\mathrm{K}$.

2.3.4 Mapping Function

For the sake of comparability it is convenient to estimate path delays in direction of the zenith ZPD, using previously determined *slant path delays* $SPD(z)$ which describe the propagation error at a specific measurement site for observations with zenith directions z greater than 0°. The conversion between slant delays and zenith delays is carried out using *mapping functions* $m(z)$:

$$ZPD = \frac{SPD(z)}{m(z)} \tag{2.25}$$

A multitude of different mapping function approaches exist, the simplest being $m(z) = \frac{1}{\cos z}$. More accurate formulas include also the influence of the earth's curvature. An often used mapping function is proposed by Marini [1972]:

$$m(z) = \frac{1}{\cos z + \frac{a}{\cos z + \frac{b}{\cos z + \frac{c}{\cos z + \ldots}}}} \tag{2.26}$$

for which different sets of constants a, b, c exist [Troller, 2004]. Niell [1996] proposes a different approach which does not require any meteorological data, but only information on the receivers geographic location and the season. Also models taking care of the azimuthal anisotropy of the atmosphere exist.

2.4 Retrieval Methods

Direct observations play the most important role in the assessment of the atmospheric water vapour content. A large number of dedicated retrieval methods serving specific needs have emerged. In this section a few of the different approaches are shortly outlined, namely:

- In-situ measurement methods
- Water Vapour Radiometry (WVR)
- LIDAR
- Fourier Transform Infrared Spectrometry (FTIR)
- Sun Photometry
- GPS Meteorology

The listing above is by no means complete and the selection of the described methods or method groups is arbitrary, but does serve particular intentions: By describing the in-situ measurements nowadays deployed with their strengths and limitations the role of remote sensing techniques should be emphasized. Water Vapour Radiometry is maybe the most widely applied ground-based measurement technique for remote water vapour sensing and, in terms of instrumental effort, comparable to the method of Solar Lunar Spectrometry. The differential LIDAR approach (DIAL) shows certain similarities to Differential Optical Absorption Spectroscopy (DOAS) as it is applied in this work. However FTIR and Sun Photometry, measuring

direct light solar absorption as a water vapour signature, show even greater similarities. GPS Meteorology has been used in this work for validation purposes.

To this date no method for the determination of water vapour concentrations in the atmosphere has established itself as the clearly most advantageous procedure. The usefulness and accuracy of different approaches depend on many parameters, such as the observed atmospheric region, the demanded spatial (especially vertical) and temporal resolution, the mixing ratios or the atmospheric conditions. Intercomparison of the independent methodological approaches under different conditions are necessary to further assess the potentials of the different techniques.

This section focuses on measurement methods providing local humidity profiles or total column abundances. The vast field of satellite measurement systems which have been deployed will not be discussed in detail. Unlike ground-based instruments they can provide far greater spatial coverage: Sensors installed on geostationary satellites continuously provide observations of a certain area, whereas satellites orbiting the earth at heights below 1000 km, such as the weather satellites belonging to the TIROS series, have broad geographical coverage, but obtain only a few local water vapour profiles a day at a given location. The chosen instrumental approaches for satellites are mirroring the applied principles for ground-based instruments. Down-looking radiometers are measuring emitted radiation either in the infrared (e.g. High Resolution Infrared Radiation Sounder (HIRS)) or the microwave region. Other systems like SCIAMACHY (Scanning Imaging Absorption spectroMeter for Atmospheric CHartographY) are measuring differential optical absorption in back-scattered or emitted light in the UV, VIS and NIR. Besides many nadir-looking experiments, instruments analysing radiation transmitted through the atmospheric limb are providing information on the vertical distribution of humidity and with their long ray paths especially target higher altitudes with very low concentrations. Such occultation experiments can analyse sun or moonlight travelling laterally through the atmosphere, deriving the moisture from absorption strength [Rind et al., 1993]. Another possibility is the analysis of received radio signals from GNSS satellites with low elevations by an instrument mounted on a satellite on a low earth orbit track (e.g. CHAMP). A comprehensive overview on current satellite missions is, e.g., given by Kämpfer [2012].

2.4.1 In-situ measurements

The most common in-situ measurement method is the launch of balloon-borne radiosondes allowing the retrieval of vertical atmospheric profiles of different parameters, such as temperature, humidity, air pressure, wind speed and direction or concentrations of other atmospheric constituents (e.g. ozone) up to the height of around 30 km [Richner, 1999]. The mean height resolution for humidity measurements typically amounts to 50 m. Launching radiosondes is relatively expensive, hence 2 to 4 starts are ordinarily conducted per launch site a day. The data collected by the sensors is transmitted to the ground via radio signals. Compared to various remote sensing methods with measurement intervals of few minutes or even less, the temporal resolution is very low and does not allow monitoring of rapid changes in the atmospheric constitution.

Furthermore the distribution of launch sites is very sparse. In Switzerland only one permanent launching site exists run by *MeteoSwiss* in Payerne (VD), in Germany currently 16 stations are counted. The worldwide distribution of the over 800 routinely operated stations is very uneven and concentrated in the industrialized nations. Polar regions and oceans are largely unrepresented [Vey, 2007].

For the retrieval of water vapour profiles mostly capacitive humidity sensors are deployed nowadays. The water vapour is absorbed by a polymeric layer used as the dielectric of an

electric capacitor changing its capacity. The response time of the sensor ranges from a few seconds near ground-level to several minutes at heights with low temperatures [Kämpfer, 2012]. Besides the capacitive sensors measuring the relative humidity, also dew/frost-point hygrometers obtaining absolute water vapour concentrations are used. In such hygrometers the temperature of a sample of moist ambient air is adjusted until the point is reached where dew or frost is just forming [Vömel and Jeannet, 2012]. This equilibrium temperature of a 2-phase system vapour/liquid or vapour/solid is kept and measured. From this temperature the vapour pressure can be deduced using the Clausius Claperyon equation (see Eq. 2.1). A third sensor technique with a high dynamic range are fluorescence hygrometers, monitoring the intensity of emitted fluorescence due to relaxation of excited OH (produced by photodissociation of atmospheric H_2O with UV radiation) into the ground state.

The accuracy of the registered humidity profiles is largely determined by the calibration of the sensors before launch. After correction of several systematic biases relative uncertainties for relative humidity at temperatures above 20 °C of ± 3 % to 5 % can be reached [Kämpfer, 2012]. For the interpretation of the obtained measurements of the vertical water concentration profiles, it has to be taken into account that radiosondes are often affected by winds which can lead to horizontal deviations of up to 250 km from the launch site [McGrath et al., 2006].

Nonetheless balloon sondes still form an important tool in order to validate the remote water vapour sensing methods. They also provide information on specific weather phenomena (such as intra-tropospheric temperature inversions) which can consequently be taken into account in the modelling procedure for various measurement methods, such as GNSS tomography, Water Vapour Radiometry or solar photospectrometry.

In situ measurement methods can also be applied using drop-sondes or sondes attached to aircraft (e.g. EU-funded project “Measurement of ozone and water vapour by Airbus in-service aircraft (MOZAIC)”, [Marenco et al., 1998]).

2.4.2 Water Vapour Radiometry

Water Vapour Radiometers (WVR) are among the most commonly applied instruments for remote moisture sensing of the earth’s atmosphere. Especially they have been applied over decades to correct for the refractivity fluctuations of the neutral atmosphere disturbing very-long-baseline interferometry (VLBI) measurements used for the estimation of geodetic parameters [Elgered et al., 1991]. WVR measure the background radiation emitted by the water vapour molecules at specific microwave frequencies along the line of sight. The radiation is emitted due to thermal excitation. Various pressure-broadened emission lines belonging to rotational transitions can be used for the task. Ground-based WVR commonly measure at two different frequencies: On a primary frequency reacting more sensitively to water in its gaseous form, and on a secondary frequency used for the correction of the influence of liquid water. Often WVRs are using frequency pairs in the spectral vicinity of the water vapour line centred at 22.235 GHz which is a rather weak transition: Thus radiation emitted by water molecules at high altitudes is only slightly attenuated when arriving at the ground-based measurement site [Elgered, 1993]. Wu [1979] describes the process of finding optimal frequency pairs where “the thermal radiations due to liquid water at the two frequencies cancel one another when linearly combined” and where the degree of dependence on the circumstances such as measurement site, season or meteorological profiles is reduced or can be corrected by surface measurements. Single-channel WVRs can normally only provide accurate estimates when operating during clear-sky conditions. Jarlemark and Elgered [2003] describe a process where for single-channel

WVRs the disturbing influence of liquid water can be reduced through studies of the rapid brightness temperature fluctuations by application of a Kalman filter.

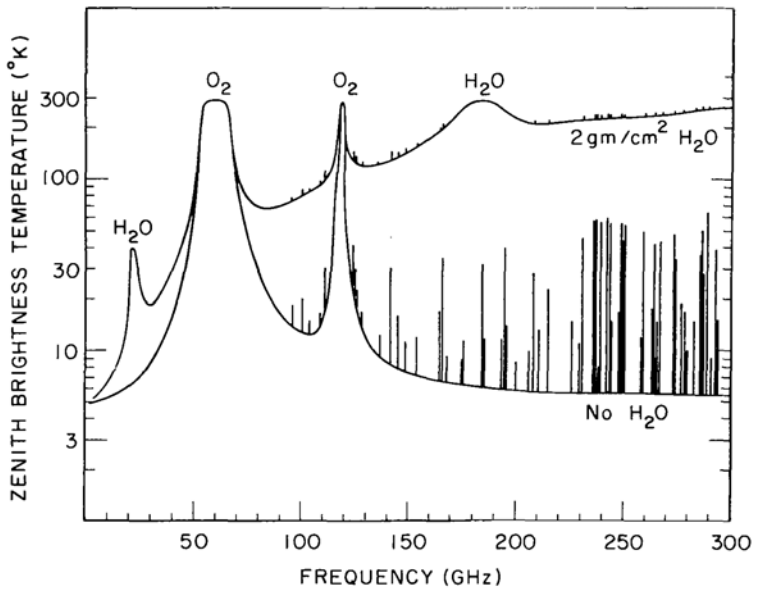

Figure 2.5: Computed brightness temperature spectrum of the atmosphere under different humidity conditions. The lower curve shows the emission spectrum in absence of water vapour, the upper curve at a total concentration of 20 kg/m^2. Prominent are the water vapour emission lines around 22 GHz and 183 GHz (adapted from Resch and Claflin [1979]).

The radiation emitted by an ideal blackbody is described by Planck's Law (see 3.8.1). For radiation with long wavelengths the Rayleigh-Jeans approximation describing the spectral radiance B_λ as a function of the temperature T and wavelength λ can be used:

$$B_\lambda(\lambda, T) = \frac{2 \cdot c \cdot k_B \cdot T}{\lambda^4} \tag{2.27}$$

where c is the speed of light and k_B the Boltzmann constant. In this approximation the spectral radiance B_λ of a black body is proportional to its absolute temperature T. Thus the spectral radiance of any origin can be directly attributed to the temperature T_b of a black body emitting the same spectral radiance. Used in this way as a measure for spectral radiance, T_b is called *brightness temperature* [Kruse, 2001]. The brightness temperature of a radiating grey body at a physical temperature T with an absorption factor α is $T_b = \alpha T \leq T$. This is the expression for the reduced grey body emission with respect to a blackbody of the same temperature T. For a blackbody $\alpha = 1$.

The frequency-dependent signal strength T_b at the measurement site s_0, which includes contributions of emissions at different altitudes can be written as [Kämpfer, 2012]:

$$T_b(\nu, s_0) = T_{b,BG} e^{-\tau(\nu, s_1)} + \int_{s_0}^{s_1} \underbrace{T(s)\alpha(\nu, s)}_{T_b(\nu, s)} e^{-\tau(\nu, s)}\, ds \tag{2.28}$$

with ν the frequency, s_1 the upper atmospheric boundary, $\alpha(\nu, s)$ the absorption coefficient (and likewise emission coefficient) depending on frequency and the local molecule concentration

along the ray path. $T_{b,BG}$ is the brightness temperature of the radiation background. $\tau(\nu, s)$, the the opacity, is:

$$\tau(\nu, s) = \int_{s_0}^{s} \alpha(\nu, s)\, ds \tag{2.29}$$

The computation of the emission spectrum is not possible without information on the atmospheric conditions as temperature, pressure and also density profile of water vapour. For reliable WVR measurements a great number of calibration procedures have to be conducted, especially brightness temperature calibration using targets of different temperatures (often referred to as cold and hot loads). Still WVR seem sometimes suffering from considerable systematic uncertainties. Especially the improperly modelled temperature and water vapour height profiles and the uncertainties of the absorption coefficients can lead to measurement errors [Elgered et al., 1991].

WVR can be operated from ground, measuring radiation emission against the cold background of space, or in down-looking mode from platforms, such as satellites, measuring the corresponding absorption lines in the background radiation from earth [Bevis et al., 1992; Somieski et al., 2006]. Reliability of space-based WVR is generally affected by the difficulty to model the background radiation of land masses. Also the occurrence of overcast sky generally degrades the utility of down-looking WVR. Ground-based WVR are less prone to cloudiness, but the occurrence of heavy rain-fall can also limit the accuracy. Compared with radiosondes, ground-based WVR have a far better temporal resolution. Space-based instruments show exactly the opposite characteristics, providing great spatial but limited temporal resolution. Increasingly dedicated WVR instruments able to determine water vapour and temperature profiles are deployed (compare, e.g., [Ware et al., 2003]). A fundamental description of the methodology to retrieve tropospheric path delays from microwave radiometry can be found at Elgered [1993].

2.4.3 LIDAR

LIDAR (Light Detection and Ranging) comprises various techniques allowing the characterisation of different physical properties of remote targets by studying the backscattered portion of light emitted in direction of the target. The measurement technique has numerous fields of application – among the most prominent geodesy, where ground- or space-based laser-scanners allow to derive 3-dimensional models of physical targets (buildings, topography) and atmospheric sensing. In atmospheric studies, physical properties of air masses can be measured, e.g. air density, wind speed, gas mixing ratios, temperature or aerosol characteristics [Leblanc et al., 2012]. LIDAR stations are often ground-based, but also air-borne platforms exist.

When applying this active measurement method for atmospheric sensing, typically monochromatic light from one or several lasers, emitted in form of short high-energy pulses, are used nowadays [Leblanc et al., 2012]. Different scattering processes are observable: Rayleigh scattering at molecules, Mie scattering at particles (both elastic scattering processes) or inelastic Raman scattering (compare, e.g., [Hinkley, 1976; Svanberg, 1994]). In a radar-like mode an optical telescope registers the fraction of the backscattered light (and its temporal intensity variations) gathered within the telescope's field of view. With the knowledge on the time difference between radiation emission and reception of the backscattered signal the obtained target characteristics can be related to the distance r of the scatterer from the instrument. Profile information with a spatial resolution ranging from several meters to several hundred meters are achieved depending on the application. With a series of measurements in different

directions also 3-dimensional concentration fields can be computed. The fundamental LIDAR equation, describing the relation between the number of emitted photons P_E and the received backscattered signal P_D of a volume element with thickness δr at the distance r can be written as follows, according to Leblanc et al. [2012]:

$$P_D(r, \lambda_D) = P_E(r, \lambda_E)\kappa_L(\lambda_D)\frac{O_L(r)A_L\delta_r}{r^2}\beta(r, \lambda_E \rightarrow \lambda_D)t_\uparrow(r, \lambda_E)t_\downarrow(r, \lambda_D) \tag{2.30}$$

Variable	Description
λ_E	Wavelength of the emitted light (laser wavelength)
λ_D	Detected wavelength of the backscattered radiation
κ_L	Optical transmittance and quantum efficiency of the receiver channel
O_L	Telescope field of view and laser beam overlap (between 0 and 1)
A_L	Telescope receiving area
β	Total backscatter coefficient for the observed scattering process (dependent on λ_E, λ_D)
$t_\uparrow$	Total atmospheric transmittance on the way up from emitter to the scattering volume
$t_\downarrow$	Total atmospheric transmittance on the way down from the scattering volume to the receiver

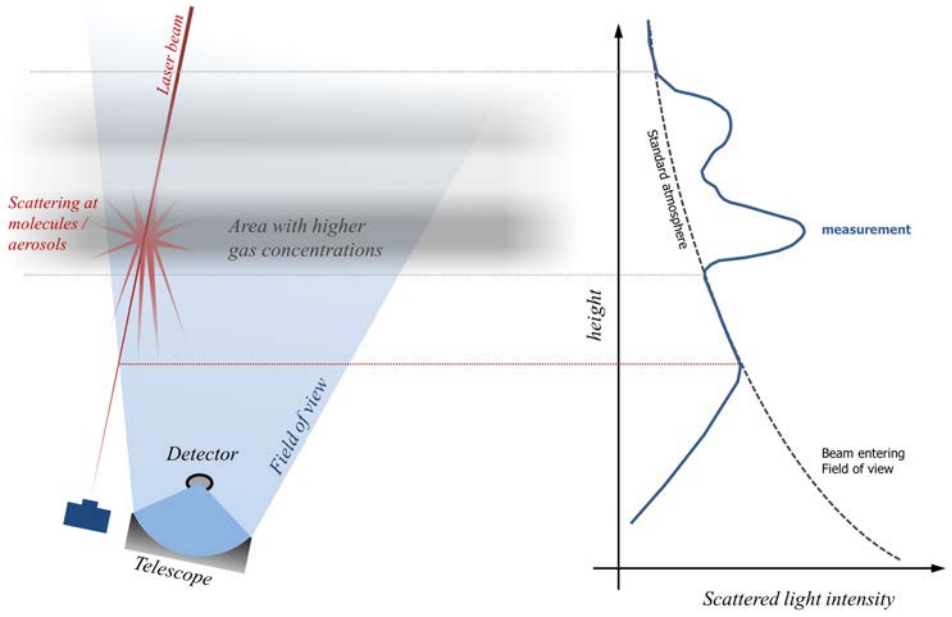

Figure 2.6: Principle of atmospheric sensing using LIDAR: A laser emits monochromatic light into the atmosphere. A fraction of the light is backscattered by the various atmospheric constituents. Radiation travelling back into the field of view of the receiver telescope can be registered by the detector unit. By analysis of the propagation time and the intensity of the backscattered signals, concentration profiles in direction of the laser can be obtained. With the laser beam meeting layers of higher concentrations the backscattered intensity increases with respect to a standard atmosphere. The backscattered intensity steadily decreases with increasing height of the scattering volume.

The transmittance values $t_\uparrow$ and $t_\downarrow$ are the integrated wavelength-dependent extinction coefficients (through scattering and absorption) along the ray path between the LIDAR system and the scattering volume. As shown in Fig. 2.6, in absence of a specific scattering species, P_D generally decreases with increasing distance to the LIDAR.

For atmospheric water vapour sensing generally two different LIDAR approaches are used:

Water Vapour Raman LIDAR and *Differential Absorption LIDAR (DIAL)*. Measurements of water vapour mixing ratios from ground up to 8 km have been executed successfully for more than 20 years [Leblanc et al., 2012]. Measurements at higher levels, especially above the tropopause, are far more difficult: Water vapour mixing ratios are around four orders of magnitude lower, which markedly raises the instrumental requirements (larger telescopes, more powerful lasers).

Water Vapour Raman LIDAR

Raman LIDAR does not register backscattered light which is spectrally close to the emitted radiation. It makes use of the much more selective inelastic Raman backscattering process. This technique has its limitations due to the much weaker Raman backscatter signal which is typically about 10^3 times weaker than Rayleigh scattering. Thus it is mostly applied for sensing of the main atmospheric constituents N_2 and O_2. But it has also been successfully applied for the determination of water vapour profiles (e.g Ansmann et al. [1992]).

In the case of Raman LIDAR, with well-selected emission and receiving wavelengths, the local backscattering coefficient β in Eq. 2.30 does include but the radiation caused by rotational Raman transition of a specific molecule:

$$\beta(r, \lambda_E \rightarrow \lambda_D) = \sigma_M(T(r), \lambda_E, \lambda_D) \cdot N_M(r) \tag{2.31}$$

with σ_M denoting the temperature dependent Raman backscattering cross section and N_M the sought molecule number density. By inserting Eq. 2.31 into Eq. 2.30 and solving the latter for N_M, the mixing ratio can be found. To estimate the influence of the remaining unknowns in the equation (e.g. extinction by particles, quantum efficiencies, overlap functions) a Raman signal of a reference molecule with a well-known mixing-ratio (mostly Nitrogen or Oxygen) is acquired using a secondary receiver channel. An extensive description can, e.g., be found in Weitkamp [2005].

Differential Optical Absorption LIDAR (DIAL)

An often applied technique, especially for the monitoring of human-made or natural emissions (as of volcanic and geothermal sources), but also for meteorological purposes is *Differential Optical Absorption LIDAR (DIAL)*. Unlike Raman LIDAR with only one emission wavelength, DIAL typically makes use of two lasers with close-by wavelengths. Similarly to the DOAS method, a wavelength λ_{on}, where the sought-after molecule is showing strong absorption (center of an absorption line), and another wavelength λ_{off}, where minimal absorption takes place, are observed. The number density of water vapour can be found using the so-called DIAL equation [Leblanc et al., 2012]:

$$N_{H_2O} = -\frac{1}{\Delta\sigma_{\uparrow}(r) + \Delta\sigma_{\downarrow}(r)} \frac{d}{dr}\left[\ln\left(\frac{P_{on}(r)}{P_{off}(r)}\right)\right] \tag{2.32}$$

with $\Delta\sigma_{\uparrow}(r)$ and $\Delta\sigma_{\downarrow}(r)$ being the absorption cross section differences between the on-band and off-band frequency on the way up and down, respectively. P_{on} and P_{off} are the distance-referenced detected intensities of the on- and off-band. DIAL, by taking the ratio of two backscatter signals (see Fig. 2.7), can be seen as a cognate method of DOAS, as many broad-band influences can be neglected. But unlike traditional DOAS, as described in Chapter

3, DIAL offers also the assessment of the spatial distribution of water vapour [Vogelmann, 2005].

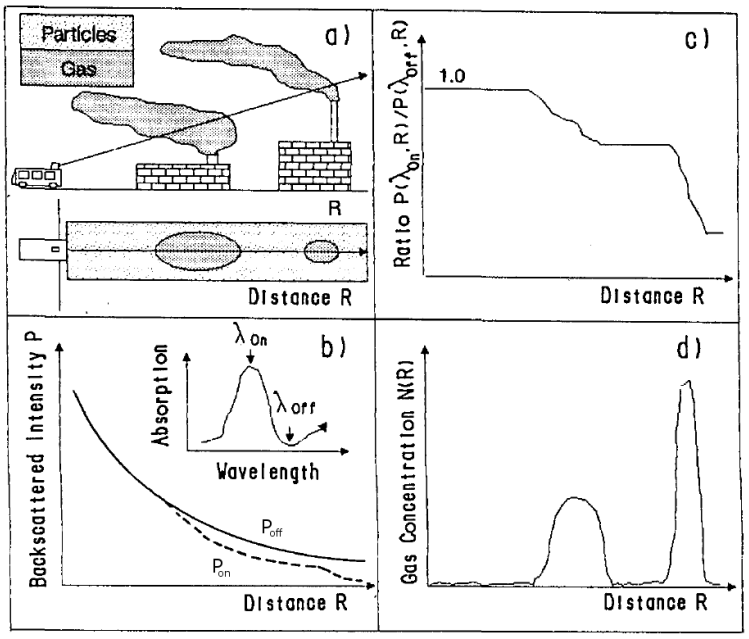

Figure 2.7: Principle of Differential Absorption LIDAR (DIAL) applied for air pollution sensing. Radiation is emitted on two close-by wavelengths, see (a) and the small graph in (b). The backscattered signals at both wavelengths is registered (b). By building the ratio (c) of the on- and off-band signals, spatially resolved information on the gas concentration can be obtained (adapted from Edner et al. [1987]).

2.4.4 Fourier Transform Infra-red Spectrometry (FTIR)

Besides the absorption in the VIS/NIR, water vapour and many other atmospheric constituents also cause strong absorption in the mid-infrared region. Studies of these absorption features in sun or moon light for water vapour determination are conducted using high-resolution Fourier-transform spectrometers, instead of a dispersive approach as used in this work. By analysing single lines in the range between wavelengths of 1 µm to 14.3 µm in the solar or lunar spectra, gathered by a sun-tracking telescope, total column concentrations can be obtained and, through analysis of the line profiles, low-resolution vertical profile information is retrievable. When measuring in spectral regions below wave numbers of $1000\,\mathrm{cm}^{-1}$ atmospheric emission contributions have to be considered.

The feasibility of FTIR for water vapour retrieval has long been hindered by the lack of sufficiently accurate spectral data [Sussmann et al., 2009]. To this date around 25 ground-based FTIR stations are installed around the world. Comparisons with radiosondes have shown very good agreements. For a detailed description see also Sussmann and Schäfer [1997].

2.4.5 Solar and Lunar Spectrophotometry

Unlike in the DOAS method applied here or the above described FTIR, in sun spectrophotometry the integrated spectrally broad absorption bands including a multitude of absorption lines are analysed, instead of distinct single absorption features. The methodology has lately

also been successfully applied using lunar light [Querel and Naylor, 2011]. As visible in Fig. 2.8, the wavelength region between 800 nm and 1050 nm is often analysed (e.g. Thome et al. [1994]).

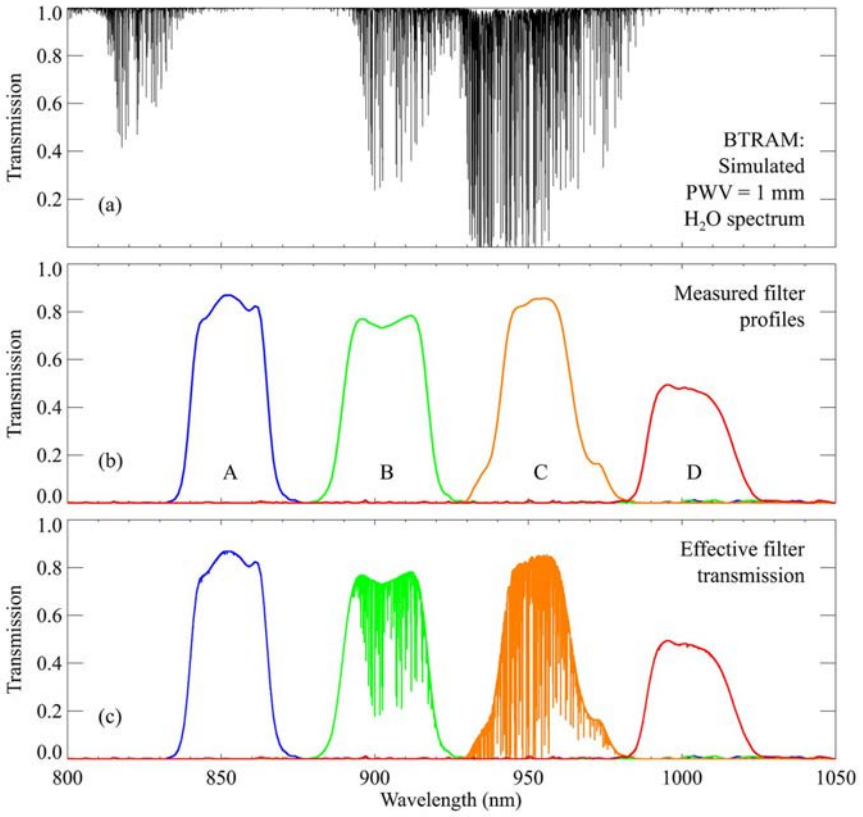

Figure 2.8: (a) shows a simulated transmission spectrum between 800 nm to 1050 nm. (b) shows the transmission spectrum of optical filters used for the different spectral channels. (c) displays the effective transmission through each spectral channel A to D (adapted from Querel and Naylor [2011]).

Spectrophotometers sequentially observe the intensity of different spectral bands using, e.g., band pass filters (see Fig. 2.8). As spectral bands wavelength regions with practically no absorption (off-band) and others including only water vapour transitions are chosen (on-band). The spectral windows are typically between 5 nm to 20 nm broad. The ratio between on- and off-band intensities, assuming no absorption lines are reaching saturation, is directly proportional to the amount of water vapour. "This ratio is compared to the transmission values in a precomputed look-up table constructed for the observation site" [Querel and Naylor, 2011] thus assigning it to absolute PW values. The calibration of this technique can either be supported using radiosondes or using radiation transfer models. The accuracy of the method therefore depends on the assumptions for the radiative transfer and the correct consideration of the spectral response of the instrument optics and the detector.

2.4.6 GNSS Meteorology

Today different Global Navigation Satellite Systems (GNSS) are fully or partly operational, such as GPS, GLONASS, BeiDou or GALILEO. Data from these systems can be altogether used to conduct GNSS meteorology as described by Bevis et al. [1992]. To shortly outline the underlying principle in this section, GPS will be used as a proxy for all GNSS systems.

The Global Positioning System GPS (officially NAVSTAR-GPS) has been developed by the Department of Defense (DoD) of the United States and has been fully operational since 1993 [Zogg, 2009]. The principle aim of the satellite system is to globally provide precise data on position and time. The system comprises a satellite segment with at least 24 satellites arranged in 6 tracks orbiting the earth in an altitude of 20 180 km with an orbit inclination of 55°. Each satellite orbits the planet twice every sidereal day. The constellation ensures the simultaneous visibility of at least four satellites at every point on the global sphere and thus the computation of a 3-dimensional position and the determination of the receiver clock error. The satellites transmit continuous radio signals on up to three carrier frequencies. Frequency stability is realized by use of on-board atomic clocks. A comprehensive description of the system can be found in Seeber [2003].

A measurement mode called *pseudo-ranging* takes advantage of the digital codes modulated onto the carrier signals. The code contains amongst other things information about the satellite clock time, satellite orbit and several correction data. By use of this so-called Navigation-Code the receiver is able to compute the transmission time of the signal from satellite to measurement site through autocorrelation with a receiver-generated code signal. The shift between the two signals in this process is a measure for the signal transmission time. Knowing the transmission time Δt_i of the signal from satellite i one can compute the so-called pseudo-range PSR_i:

$$PSR_i = \Delta t_i \cdot c = R_i + \Delta t_{clock} \cdot c \tag{2.33}$$

PSR_i does not exactly equal the geometrical distance R_i between satellite and receiver, as the receiver's clock, and also the satellite clock to a smaller degree, are affected by unknown clock errors (here summarized in Δt_{clock}) with respect to the GPS time. c is the speed of light. With data from at least four satellites the unknown distances R_i (or rather the three Cartesian coordinates of the receiver position) and the receiver clock error can be computed. Pseudo-ranging is mainly used for navigation purposes and applications with limited accuracy demands.

Since its introduction GPS and other services subsumed under *Global Navigation Satellite Services (GNSS)* have revolutionized geodesy due to their precision, weather independence and worldwide availability. Numerous geodetic and geophysical applications, such as research on crustal motion associated with earthquakes, monitoring of volcanic activity or plate tectonics are in need of position accuracy in the millimetre-range. This can only be achieved by performing a comparison of the carrier signal phase shifts between the receiver-generated wave and the received satellite wave.

The observation phase Φ_i^k in the case of phase measurements can be expressed as follows [Rothacher, 1992; Teunissen and Kleusberg, 1998]:

$$\begin{aligned}\Phi_i^k(t) = \rho_i^k(t, t-\tau_i^k) - I_i^k + T_i^k + r_i^k + m_i^k + c \cdot \left[dt_i(t) - dt^k(t-\tau_i^k)\right] \\ + c\left[\delta_i(t) + \delta^k(t-\tau_i^k)\right] + \lambda\left[\Phi_i(t_0) - \Phi^k(t_0)\right] + \lambda N_i^k + \epsilon_i^k\end{aligned} \tag{2.34}$$

The measurement of the signal phase Φ_i^k yields only a fragment of the signal wavelength. For a computation of the receiver coordinates at a particular time primarily the phase ambiguities N_i^k have to be determined. As described in Eq. 2.34 the observations are influenced by a large number of effects and errors which in the processing of the signals either have to be quantified or eliminated.

Symbols	Description
Φ_i^k	Observed phase from satellite k signal by the receiver i
t	Observation time
τ_i^k	Signal propagation time from satellite k to receiver i
$\rho_i^k(t, t-\tau_i^k)$	Geometric distance between electric phase-center of satellite k and receiver i
I_i^k	Signal delay due to ionospheric effects
T_i^k	Signal delay due to tropospheric effects
r_i^k	Relativistic effects
m_i^k	Multipath effects
c	Speed of light (vacuum)
$dt_i(t)$	Receiver clock error
$dt^k(t-\tau_i^k)$	Satellite clock error
$\left[\delta_i(t) + \delta^k(t-\tau_i^k)\right]$	Signal delay due to receiver i and satellite k hardware
λ	Wavelength of carrier waves
$\left[\Phi_i(t_0) - \Phi^k(t_0)\right]$	Phase difference between satellite i and receiver k at time t_o
N_i^k	Phase ambiguity (integer number of phase-cycles)
ϵ_i^k	Residual of phase observation

Table 2.1: Explanation of variables in Eq. 2.34

A number of procedures addressing and largely eliminating distinct errors exist. Some of the most important ones are [Dach et al., 2007]:

- **Single differences**
  Computing the difference of two phase observations of two different receivers to the same satellite serves to eliminate the satellite clock errors, satellite hardware effects and satellite start phase.
- **Double differences**
  Computing the difference of two single differences associated with two different satellites leads to thorough elimination of the receiver clock error, receiver hardware effects and receiver start phase.
- **Ionospheric Correction**
  Due to its dispersive characteristics regarding microwave signals the influence of the ionosphere can mostly be eliminated by computing a linear combination of the phase observations Φ for two carrier waves (here L_1 and L_2 with frequencies f_1 and f_2, respectively) at the same epoch. Different linear combinations are in use, the *ionospheric free linear combination* $\Phi(L_3)$ being one of the most prominent [Seeber, 2003]:

$$\Phi(L_3) = \frac{f_1^2}{f_1^2 - f_2^2} \cdot \Phi(L_1) - \frac{f_1 f_2}{f_1^2 - f_2^2} \cdot \Phi(L_2). \tag{2.35}$$

Unlike the ionospheric influence, the effects caused by the troposphere cannot be eliminated in a similar way since the troposphere is a non-dispersive medium for radio signals, and thus has to be approached using models and dedicated direct observations. As described above, the influence of the troposphere in absence of moisture can be modelled very accurately (2.3.2). The non-hydrostatic part of the delay cannot be modelled with an accuracy better than a few centimetres though [Mendes and Langley, 1995] and thus enters the GPS processing as an unknown variable, which is to be estimated [Vey, 2007].

Bevis et al. [1992] first described the possibility to reversely determine water vapour concentrations by estimating tropospheric path delays from fixed GPS receiver stations. The

translation from the estimated path delays to water abundances is carried out as described in Section 2.3.3.

One difficulty when estimating tropospheric path delays lies in its strong correlation with the station height, which is estimated simultaneously. This holds true at least for observations with great elevation angles [Vey, 2007]. This issue can be addressed by including observations of satellites with low elevation angles, but with an adjusted lower weighting due to their higher uncertainty levels (e.g. lower S/N ratio). Low-elevation observations on the other hand also increase the sensitivity to mapping function errors. Other effects lowering the accuracy of the estimated path delays are insufficient modelling of the antenna phase center and the antenna radome or station specific influences like multipath. Nevertheless the operation of dense permanent GNSS networks has proven to be valuable in delivering near-real time data supporting weather forecasting as well as to yield information on long-term spatial concentration development applicable in climate monitoring and for the evaluation of climate models [Elgered, 2013].

GNSS Tomography

Conventional GNSS meteorology produces total slant delays, which can be mapped onto other directions, foremost to the zenith. However, no information on the distribution of water vapour along the ray path can be deduced from GNSS observations. In recent years a large number of dense permanent GNSS receiver networks has emerged yielding the possibility to apply tomographic approaches in order to evaluate temporal and spatial distributions of water vapour in the atmosphere.

In GNSS tomography the space above the field of receivers is discretized with a 3-dimensional voxel model [Kruse, 2001]. For each of the voxel i a single refractivity N_i is assumed. The total slant path delay Δ_j^{PD} for a ray path j becomes.

$$\Delta_j^{PD} = 10^{-6} \cdot \sum_{i=1}^{k} N_i \Delta s_{j,i} \tag{2.36}$$

with k the number of voxels passed through by the ray, and $\Delta s_{j,i}$ the length of the ray path j inside the voxel i. A stack of observations can be written as a matrix equation [Troller, 2004]:

$$\boldsymbol{\Delta^{PD}} = \boldsymbol{A} \cdot \boldsymbol{N} \tag{2.37}$$

with $\boldsymbol{\Delta^{PD}}$ as vector including all path delay observations, $\boldsymbol{N}$ as refractivity vector and $\boldsymbol{A}$ as design matrix including the path length fragments. In order to make the design matrix $\boldsymbol{A}$ invertible and thus to be able to solve the equation system 2.37 many observations with different elevation angles, a sufficient height distribution of the receiver stations and the introduction of different constraints, as limits for neighbouring voxel refractivity differences, are necessary.

As observations in the tomographic adjustment process not only slant delays can be used (as e.g. described by Flores et al. [2000]) – often approaches using double difference residuals are pursued [Perler et al., 2011]. The potential of GNSS meteorology derived integrated water vapour concentrations and the thereof deduced three-dimensional distributions using tomographic approaches to validate or improve numerical weather prediction models (NWP) and to contribute to hydrological hazard assessment, has gained increasing evidence (Hurter

et al. [2012], Lutz et al. [2010]). Crucial for a good reconstruction of the three-dimensional water vapour field a is dense receiver network and a sufficient number of slant observations (preferably also at low elevation angles) [Bender et al., 2009].

3

Principle of Solar Lunar Spectrometry

3.1 Absorption Spectroscopy

Spectroscopic methods have played a crucial role in the research on the chemical constitution and physical properties of the earth's atmosphere for far more than a century. Especially analysis of atmospheric radiation absorption has been conducted for identification and quantification of trace gases thus contributing considerably to the understanding of manifold chemical and physical processes taking place in the various layers of the atmosphere. To this date absorption spectroscopy applications form powerful tools to derive information on the chemical composition of the open atmosphere and on the temporal and spatial variations of molecular concentrations [Platt and Stutz, 2008]. The importance of the named methodology is ever growing, especially in the context of global warming, due to the increasing input of trace gases and aerosols produced by human civilization, which disturbs the balance of the atmosphere on local and global scale and has to be understood more closely.

Measurement methods belonging to the realm of quantitative absorption spectroscopy are mostly based on *Lambert-Beer's law* which describes the absorption of collimated electromagnetic radiation travelling a distance L through a volume containing an absorber (gaseous or liquid) with a homogeneous concentration c. The gaugeable intensity I at a certain wavelength λ incident on the detector can be written as [Platt and Stutz, 2008]:

$$I(\lambda) = I_0(\lambda) \cdot e^{-(\sigma(\lambda) \cdot c \cdot L)}. \tag{3.1}$$

$I_0(\lambda)$ denotes the initial light intensity, while $\sigma(\lambda)$ stands for the wavelength-dependent absorption cross section, a characteristic for each molecular species. Hence the sought-after concentration of a specific species can be derived from the measured ratio $I(\lambda)/I_0(\lambda)$, the natural logarithm of which is called the optical density or absorbance D for a layer of a specific absorber:

$$c = \frac{\ln\left(\frac{I_0(\lambda)}{I(\lambda)}\right)}{\sigma(\lambda) \cdot L} = \frac{D}{\sigma(\lambda) \cdot L}. \tag{3.2}$$

If more than one species j is present, a superposition of the different absorption contributions takes place and Eq. 3.1 can be written as follows:

$$I(\lambda) = I_0(\lambda) \cdot \exp\left[-L \cdot \sum_j (\sigma_j(\lambda) \cdot c_j)\right]. \tag{3.3}$$

3.2 Differential Optical Absorption Spectroscopy (DOAS)

The direct application of Lambert-Beer's law as described above to measure concentrations of gaseous species in the open atmosphere in contrast to an enclosed terrestrial experiment has its limitations due to various reasons. The initial intensity $I_0(\lambda)$, which in a laboratory measurement can be determined by measuring of the intensity in absence of the absorber, is not known. This applies especially when celestial bodies are used as a light source. Additionally the light not only undergoes absorption by a large number of different species, but is also attenuated along the ray path due to scattering at air molecules (Rayleigh scattering) and aerosol particles (Mie scattering). Also a general transmissivity influence of the different optical elements in the measurement instrument has to be considered. This includes also the wavelength-dependent signal generation of the detector. Platt and Stutz [2008] suggest that Lambert-Beer's law for measurements in the open atmosphere can be rewritten as:

$$I(\lambda) = I_0(\lambda) \cdot \exp\left[-L \cdot \left(\sum_j (\sigma_j(\lambda) \cdot c_j) + \epsilon_R(\lambda) + \epsilon_M(\lambda)\right)\right] \cdot A(\lambda) \tag{3.4}$$

with ϵ_R and ϵ_M denoting the influence of Rayleigh-Scattering and Mie-Scattering, and $A(\lambda)$ describing the compound influence of instrumental and turbulence effects. ϵ_R and ϵ_M depend on the concentration and optical properties of the involved particles.

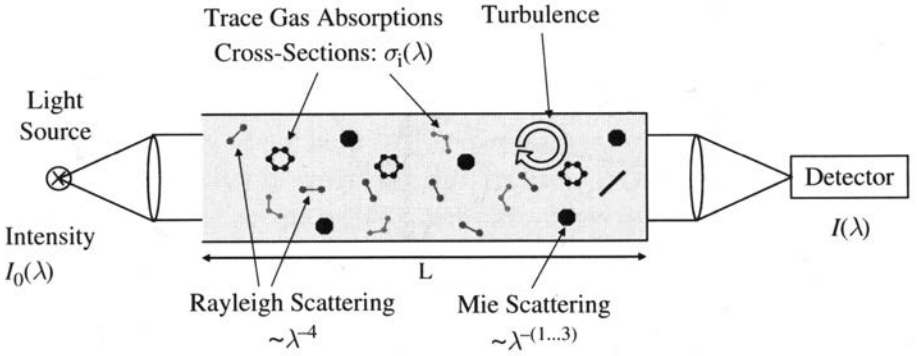

Figure 3.1: Schematic illustration of the various effects (and their wavelength-dependence) affecting the spectral composition of light beam emitted by a suited broadband light source which have to be considered in the application of absorption spectroscopy in the open atmosphere (from Platt and Stutz [2008]).

Conducting the described approach of classical absorption spectroscopy for atmospheric studies would afford to quantify said additional influences through modelling procedures or auxiliary measurements. While a fairly good modelling of the initial intensity of the sun would be possible (see, e.g., Krivova and Solanki [2013]), various other effects, such as the different scattering effects, cannot be determined with sufficient accuracy or only with tremendous effort.

Differential optical absorption spectroscopy (DOAS) addresses the aforementioned issues by obtaining spectrally resolved intensity measurements in a certain wavelength range (spectral channels obtained simultaneously or non-simultaneously) and by assuming that the scattering processes and instrument transmittance effects commonly only exhibit spectral structures which can be considered as being "*broadband*", whereas absorption structures, when measured with high-resolution spectrometers, yield comparatively "*narrowband*" line structures. This

allows a separation of the absorption cross section into a smooth, slowly-varying part σ_b and a rapidly changing part σ_n describing molecular absorption:

$$\sigma_j(\lambda) = \sigma_b(\lambda) + \sigma_n(\lambda). \tag{3.5}$$

Combining 3.4 and 3.5, yields:

$$I(\lambda) = I_0(\lambda) \cdot \underbrace{\exp\Big[-L \cdot \Big(\sum_j (\sigma_n(\lambda) \cdot c_j)\Big)\Big]}_{\text{narrowband absorption}} \cdot \underbrace{\exp\Big[-L \cdot \Big(\sum_j (\sigma_b(\lambda) \cdot c_j) + \epsilon_R(\lambda) + \epsilon_M(\lambda)\Big)\Big] \cdot A(\lambda)}_{\text{broadband absorption}}. \tag{3.6}$$

The second exponential function sums up all effects yielding broadband extinction patterns. Thus a new artificial reference intensity I_0^* in absence of narrowband absorption features is defined:

$$I_0^*(\lambda) = I_0(\lambda) \cdot \exp\Big[-L \cdot \Big(\sum_j (\sigma_b(\lambda) \cdot c_j) + \epsilon_R(\lambda) + \epsilon_M(\lambda)\Big)\Big] \cdot A(\lambda). \tag{3.7}$$

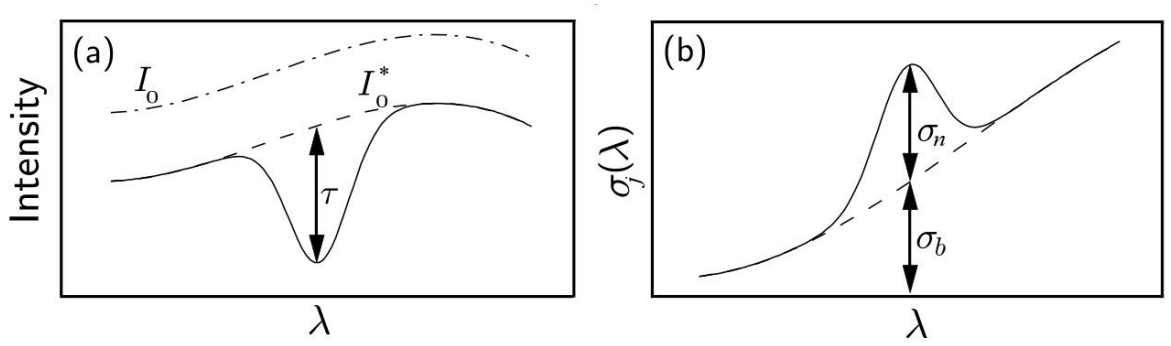

Figure 3.2: In *Differential Optical Absorption Spectroscopy (DOAS)* not the overall absorption is considered but the narrowband radiation attenuation τ with respect to a computed reference intensity I_0^* which represents the initial intensity distribution attenuated by a number of broadband effects (a). The total absorption cross section $\sigma_j(\lambda)$ thus can be divided into a slowly-varying part σ_b and a rapidly-varying part σ_n (adapted from Bösch [2002]).

The quantity described by Eq. 3.7 whose characteristic is its smooth wavelength-dependent intensity variation in a spectrally resolved measurement, will be named *baseline* onwards, as it acts as a new reference or base intensity to which again Lambert-Beer's law can be applied for occurring narrowband absorption features as illustrated in Fig. 3.2.

Thus the sought-after concentrations of a specific absorber can hence be determined by again

applying 3.2, substituting $\sigma_n(\lambda)$ for $\sigma(\lambda)$, and I_0^* for I_0:

$$c = \frac{\ln\left(\frac{I_0^*(\lambda)}{I(\lambda)}\right)}{\sigma_n(\lambda) \cdot L}. \tag{3.8}$$

The differential optical absorption cross section $\sigma_n(\lambda)$, necessary to derive c from Eq. 3.8, for the element whose concentration is sought is normally obtained from literature (for a short description of the spectroscopic databases used for this purpose, see 3.10).

3.3 Absorption Spectra

3.3.1 Absorption Process

Absorption of radiation by atoms or molecules is just one of different possible interactions of electromagnetic radiation with matter. In the case of absorption the atoms or molecules are excited through the energy of incident photons and thus reach higher energy levels. Below the dissociation boundary the energy levels of atoms and molecules are discrete and can be described by a set of quantum numbers [Platt and Stutz, 2008]. Molecules, as quantum mechanical multi-particle systems, dispose of far more energy states than single atoms, due to additional internal degrees of freedom coming from the ability of the molecule to rotate and vibrate inter-atomically [Welz et al., 2005]. The energy ΔE absorbed by atoms or molecules in a transition from energy level E_M to an upper lever $E_{M'}$ is equal to the energy of the photon with the frequency ν:

$$\Delta E = E_{M'} - E_M = h\nu \tag{3.9}$$

with h denoting the Planck constant. As energy level differences are also discrete, only photons of specific wavelengths ($\lambda = \frac{c}{\nu}$, c being the speed of light) can be absorbed. Hence if an amount of molecules of a certain species is illuminated by a light source emitting a continuous spectrum, it results in a full or partial attenuation of radiation at characteristic spectral positions leaving so-called *absorption lines* (for a description of the strength and shape of absorption lines see Section 3.5).

The total energy stored within a molecule can be described as a sum of different energy portions:

$$E_M(\Lambda, v, J) = E_{el}(\Lambda) + E_{vib}(v) + E_{rot}(J) + E_{tr} \tag{3.10}$$

where $E_{el}(\Lambda)$ is the energy of the electrons belonging to the molecule, $E_{vib}(v)$ the vibrational energy stored in the oscillations of its atoms around their equilibrium positions and $E_{rot}(J)$ the energy stored in the rotation of the molecule around its different axes of symmetry. Λ, v and J are the respective quantum numbers which can be used to describe the molecule's excitation state. The term E_{tr} stands for the energy stored in the translational motion of the particle depending on temperature [Wozniak and Dera, 2007].

The stored electronic energy $E_{el}(\Lambda)$ is determined through the location of electrons with respect to the nuclei. The spatial probability density of electron presence in atoms allowed by quantum mechanics, is described by so-called orbitals. The overlapping of atomic orbitals in molecules leads to molecular orbitals which can be occupied by electrons. Through excitation of a photon

an electron can transit to an orbital with a higher energy. As energy differences between different electronic energy levels are relatively high (as in the case of atoms), photons with higher frequency, belonging mainly to the UV (ultra-violet radiation) or VIS (visible radiation range), are needed to initiate such transitions.

Molecules can also absorb energy from photons by increasing their vibrational energy level. E_{vib} is typically one to two orders of magnitude lower than E_{el}. Hence pure vibrational transitions of molecules are mainly caused by lower energy IR (infra-red) radiation. The vibrational energy in case of a single 1-dimensional harmonic oscillator can be described as:

$$E_{vib} = h\nu\Big(v + \frac{1}{2}\Big). \tag{3.11}$$

with v, the vibrational quantum number, being a non-negative integer number.

Rotational energies E_{rot} are usually two to three orders of magnitude lower than E_{vib} and hence absorption lines are commonly exhibited in the far-infrared or microwave region [Welz et al., 2005]. E_{rot} is also quantized and in case of one rotational degree of freedom can be described as:

$$E_{rot} = B \cdot J(J+1) \text{ with } J = 0, 1, 2, \ldots \tag{3.12}$$

The rotational constant B depends on the moment of inertia of the molecule.

The pure transitions described above, affecting only single energy portions, are not the common case. In general a molecule changes from a quantum state $[(\Lambda, v, J)]$ to an upper state $([(\Lambda\prime, v\prime, J\prime)]$ in accordance with the allowed quantum mechanical selection rules [Wozniak and Dera, 2007] as schematically shown in Fig. 3.3 for a diatomic molecule. The change of the electronic state is commonly accompanied by a change in the vibrational and rotational states and thus gives rise to an *electronic-vibrational-rotational* spectrum, which exhibits complex structures of densely packed line clusters, often called absorption bands. If changes occur only regarding the vibrational and rotational energy this leads to *vibrational-rotational* spectra.

3.4 Water vapour absorption properties

The absorption of solar radiation by water in the atmosphere is very strong not only due to the abundance of the substance in all states of matter (gaseous, liquid an solid state), but also due to its optical properties. Wozniak and Dera [2007] estimate that around 70 % of the radiation energy is absorbed in the atmosphere by water vapour.

Since the project presented here deals with radiation belonging to the NIR (near-infrared), electronic transitions induced by higher energetic UV light will not be discussed. The interaction of radiation with water vapour molecules is determined by the geometrical structure and its constituent particles. The common water monomer molecule (H_2O) is a three-atomic non-linear compound. In the state of equilibrium the distances between the hydrogen atoms and the central oxygen atom d_{OH} is 9.57×10^{-11} m and the respective distance between hydrogen atoms d_{HH} is 1.54×10^{-10} m, with the angle α_{HOH} being 104.5°.

Water vapour exhibits fairly complex absorption spectra, conditioned mainly by the asymmetrical molecular structure and the prevailing high, permanent dipole moment. The intramolecular motions of the atoms under the influence of the interaction forces lead to changes of the inter-atomic distances and the angle α_{HOH}, which can be interpreted as vibrations

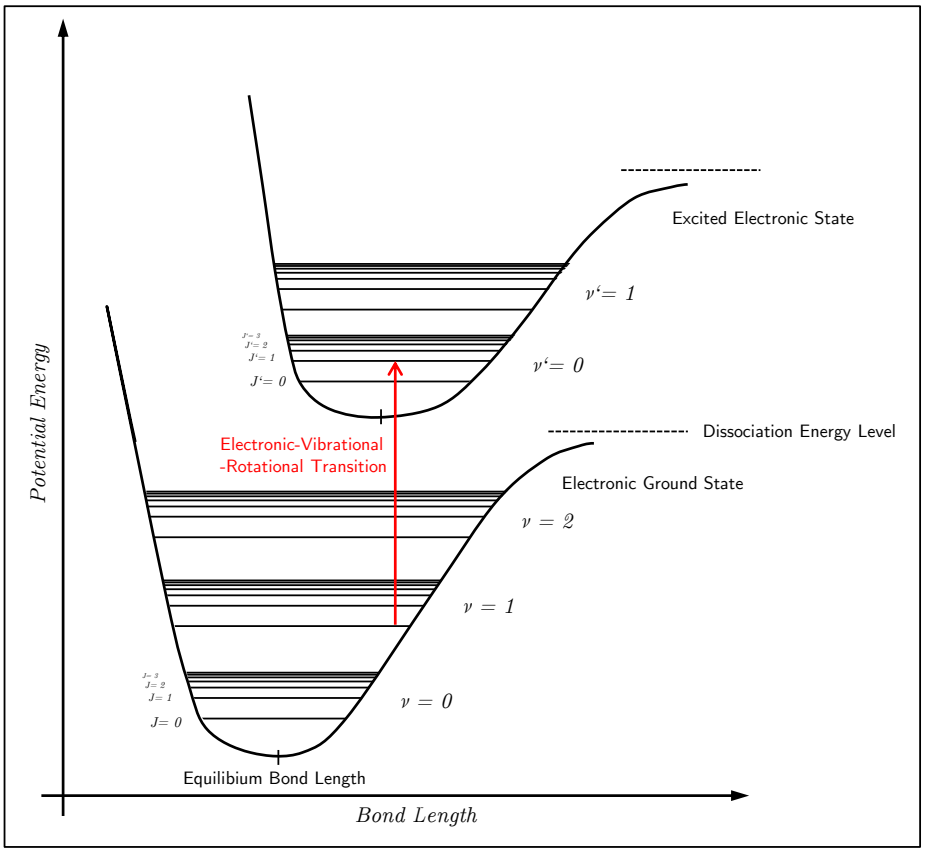

Figure 3.3: Schematic illustration of typical potential energy curves of a diatomic molecule in the electronic ground state and an excited electronic state as a function of the internuclear separation. At the equilibrium bond length the molecule has its energy minimum, given a specific electronic state. The horizontal lines denote the different rotational energy levels (J), which occur in groups according to their vibrational energy levels (v).

of a three-dimensional anharmonic oscillator [Wozniak and Dera, 2007]. Fig. 3.5 shows the three different vibration modes of water molecules: Mode I causes symmetrical stretching of the molecule, mode II is a bending of the molecule altering the angle and mode III can be described as asymmetrical stretch vibrations. All vibration modes occur within the molecule plane. Vibration modes can be described using a vibration quantum number triple (v_1, v_2, v_3). Especially excitation of mode I and III can absorb high energies.

The vibrational water vapour spectrum is hence a compound of different excitation processes. The strongest absorption bands can be seen for the fundamental transition from ground state $(0, 0, 0)$ to a the group of states $(1, 0, 0)$, $(0, 1, 0)$ and $(0, 0, 1)$, which cause absorption at wavelength 2.66 µm (mode III), 2.73 µm (mode I) and 6.27 µm (mode II) in the IR. Additionally, there are contributions from overtone transitions ($v_{1,2,3} = 2, 3, ...$) and combined transitions from the ground state (at least two vibrational quantum numbers becoming greater than 0). These (weaker) absorption bands reach from the VIS (blue) into the infra-red region. Absorption of even lower energy radiation can occur through transitions from an excited vibrational state to an even higher energetic state, but they are far less probable than the aforementioned transitions, as under normal atmospheric conditions the density of excited molecules is markedly less compared with molecules in the ground state.

The most common isotopologue of water under normal conditions consists of ^{1}H and ^{16}O. Molecules consisting of heavier isotopes of the respective atoms differ in their absorption properties. The energy of the excited vibrational states are generally lower, thus absorption

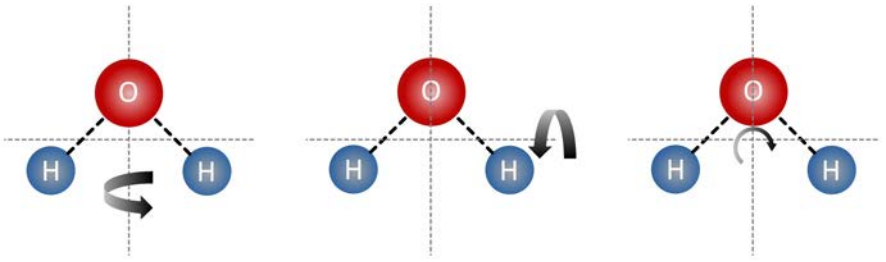

Figure 3.4: Possible rotation modes of a water molecule around the different axes of symmetry. Rotational-vibrational absorption bands occur both, on the long-wave and short-wave side of purely vibrational transitions, as the rotational energy part can either increase or decrease.

properties tend to be shifted to slightly longer wavelengths.

With the help of high-resolution spectroscopes it becomes apparent that the vibrational excitation of the water vapour molecules is accompanied by changes in the rotational energy, see Fig. 3.4. Vibrational-rotational lines can be found on either side of the purely vibrational transition, as ΔJ can either be negative or positive. Resolved rotational-vibrational lines, whose intensity sometimes exceeds the central vibrational transition, can only be observed for molecules in non-condensed state, with less predominant line broadening. Low energy purely rotational transitions are induced by far IR radiation or microwaves.

Fig. 3.6 provides a broad range low-resolution display of the vibrational-rotational absorption coefficients of water vapour ranging from the VIS to the IR. Beside the strong fundamental absorption bands, several overtone and combined transition bands with shorter wavelengths are visible. In the spectral vicinity of the primary SOLUSAR measurement range (790 nm to 802 nm) lies a compound band of different combined vibrational transitions. For the application of the DOAS procedure, as it is carried out in this work, the presence of a great number of distinct single lines is desirable: Lines showing considerable absorption by atmospheric water vapour, but which do not fully saturate at higher water vapour concentrations and low observation elevation angles.

Water Vapour Dimers

Water vapour molecules can form hydrated complexes by building up hydrogen bonds between a hydrogen atom and an oxygen atom of another water molecule. The most prominent thus formed molecules are water vapour dimers $(H_2O)_2$. Water vapour dimers are under suspicion of being considerable absorbers of solar radiation as their absorption spectrum could be shifted and broadened, thus possibly not overlapping with the absorption features of the water vapour monomer. They could also play an important role in the understanding of weather phenomena and chemical reactions in the atmosphere [Leforestier, 2012]. Also with respect to the application of the DOAS methodology for the determination of atmospheric humidity, the question has occasionally arisen, if water vapour dimer could influence the accuracy of the determined total column water vapour.

To assess the influence of water vapour clusters on the overall absorption budget of water vapour, the spectral features and the concentrations of these compounds have to be known. Considerable efforts, both experimentally and theoretically have been made to get such information.

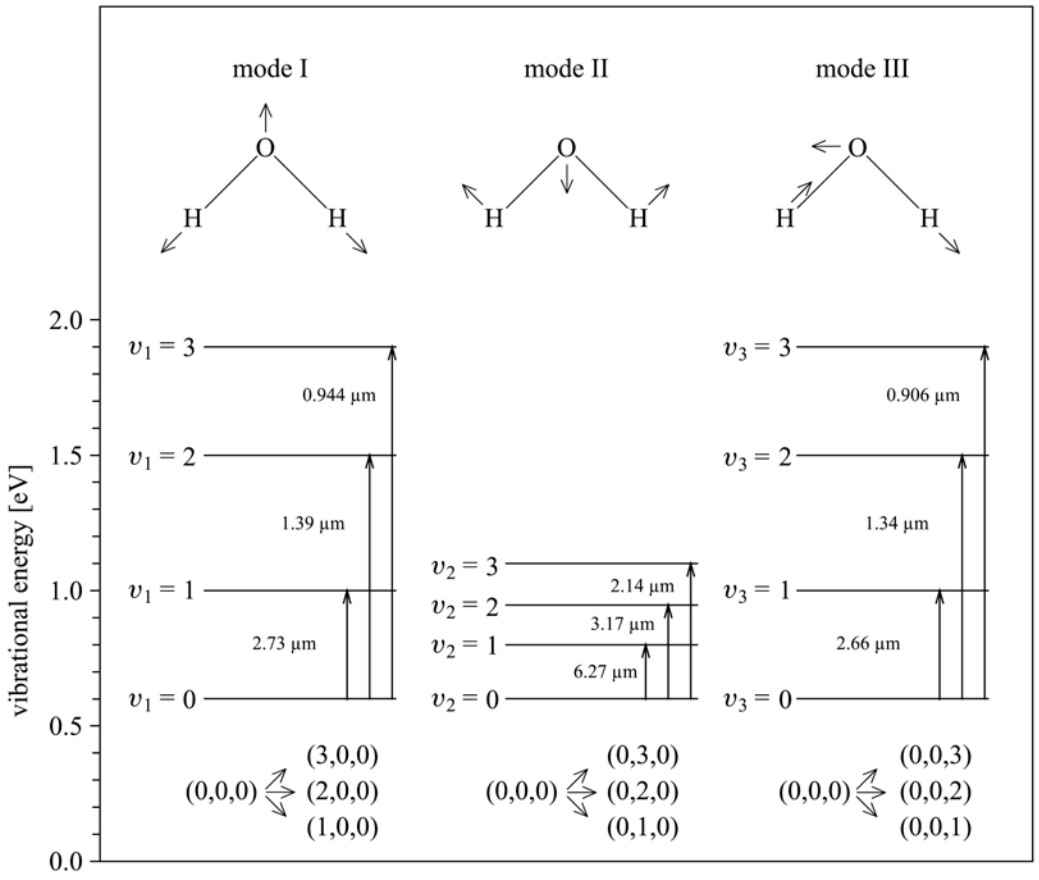

Figure 3.5: Different vibrational modes of water molecules and the corresponding fundamental and overtone transitions described by the set of vibrational quantum numbers (v_1, v_2, v_3). The figure includes the stored vibrational energy for the different excitation states and the photon wavelength necessary to induce transitions from ground state (0,0,0); (from Wozniak and Dera [2007]).

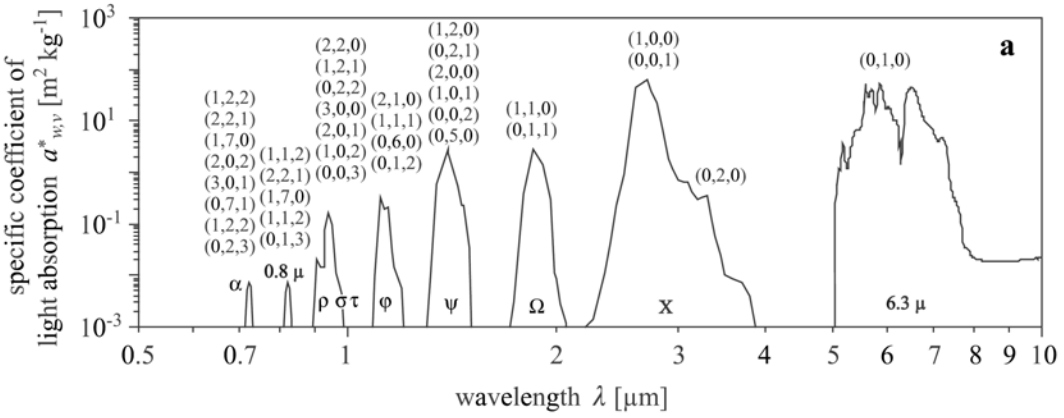

Figure 3.6: Water vapour vibrational-rotational absorption bands in the IR region with the associated vibrational state quantum numbers in parentheses after excitation from the ground state. The wavelength region in the vicinity of the SOLUSAR measurement range around 800 nm is populated with various combined transitions from ground state (adapted from Wozniak and Dera [2007]).

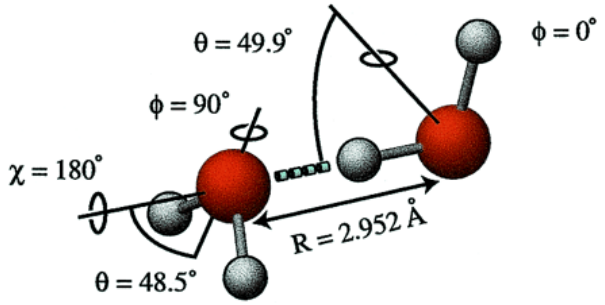

Figure 3.7: Equilibrium geometry of a water dimer. One hydrogen atom of the donor molecule interacts with the electronegative oxygen atom of a second water molecule (acceptor molecule); (from Keutsch and Saykally [2001]).

It is generally expected that the hydrogen bonding perturbs the electronic and rotational-vibrational states of the individual molecules thus inducing changes in the spectra. For instance stretching vibrations between the oxygen atom and the tightly bound hydrogen atom in the donor molecule should be red-shifted and increased in intensity for the fundamental transitions [Vaida et al., 2001]. Many spectroscopic experiments have been carried out in such directions, e.g., by Shillings et al. [2011] using broadband cavity ringdown spectroscopy (BBCRDS) to verify a dimer absorption band around 750 nm reported by Pfeilsticker et al. [2003], and possibly by Sierk et al. [2004]. BBCRDS provides measurements with an effective path length of 60 km in a 2 m high finesse cavity under reproducible conditions. Comparisons of measured spectra with synthetic data yielded no clear residual structures attributable to dimer absorption. That supports the hypothesis that if considerable dimer absorption is present it must exhibit very broad spectral structures, thus contributing to the overall continuum of water vapour absorption. Corresponding computational quantum-chemical modelling of the dimer behaviour are still so demanding that considerable simplifications are inevitable and therefore stringent result are difficult to achieve [Tennyson et al., 2012].

As direct atmospheric measurement of the water vapour dimer concentrations did not provide positive results (e.g. Daniel et al. [1999]), the question of dimer mixing ratios as a function of altitude, temperature and water vapour partial pressure has to be answered through laboratory experiments or models. The dimer molecule number density with respect to the monomer are estimated to be around three to five orders of magnitude smaller depending on altitude [Vaida et al., 2001].

With such low concentrations and the expectedly much broader absorption features, no noticeable influence on the DOAS measurement using distinct single-line monomeric absorption features is to be expected. With the presumed low abundance of water dimers in the atmosphere one may assume that their influence on the air's refraction index is extremely small and hence the impact on radio signal delaying negligible.

3.5 Spectral line characteristics

In the following sections we will conceptually distinguish between *absorption profile* and *line profile*. The former describes the likelihood for one or many atoms of a certain species to absorb a photon as a function of wavelength (or frequency), whereas the latter stands for the wavelength-dependent intensity distribution of an *observed* absorption line.

To describe the absorption profile a_{mn} for a transition of an atom or molecule from a lower state m to an upper state n a split into a quantity standing for the line strength S_{mn} and a

frequency-dependent function $g_{nm}(\nu)$ denoting the spectral shape of the absorption feature is convenient:

$$a_{mn}(\nu) = S_{mn} \cdot g_{mn}(\nu). \tag{3.13}$$

$g_{mn}(\nu)$ is the normalized profile function:

$$\int_{-\infty}^{+\infty} g(\nu)\, d\nu = 1. \tag{3.14}$$

Both, the line strength and the profile function are subject to variations depending on the ambient conditions, such as temperature and pressure. This has to be taken into account when computing synthetic absorption spectra. In the following section only the most important formulas for line strength and absorption profile used in processing algorithms are given. For more detailed derivations see Sierk [2001] and Somieski [2005].

3.5.1 Line Strength

The line strength is mainly determined by the radiation density at a certain frequency and the transition probabilities between different molecular states, often described by the Einstein parameters (measures for the probability of photon absorption, induced emission and spontaneous emission). To analytically determine the line strength S_{mn} for a certain central frequency of transition ν_{mn} at the reference temperature T_{ref}, following formula can be used [Rothman et al., 1998]:

$$S_{mn}(T_{ref}) = \frac{h}{c}\,\nu_{mn}\frac{I_a\, g_m\, e^{[-c_2\, E_m/T_{ref}]}}{Q(T_{ref})}\left[1 - e^{[-c_2\,\nu_{nm}/T_{ref}]}\right] \cdot B_{mn} \tag{3.15}$$

where I_a is the natural isotopic abundance, g_m the degeneration of the lower energy state, B_{mn} the Einstein coefficient for induced absorption, $Q(T)$ the total internal partition sum and c_2 the second radiation constant ($c_2 = \frac{hc}{k_B} = 1.4388 \times 10^{-2}\,\mathrm{m\,K}$). Using Eq. 3.15, the line strength can be computed if the different quantum mechanical parameters involved are known. In practice the line strength for different isotopes/isotopologues for the characteristic absorption lines is determined in laboratory experiments under fixed temperature conditions T_{ref} and are listed in spectral line catalogues. The line strength for a transition with the lower state energy E_m expressed in wave numbers, for a different ambient temperature can then be computed as follows:

$$S_{mn}(T) = S_{mn}(T_{ref}) \cdot \frac{Q(T_{ref})}{Q(T)} \cdot \frac{e^{[-c_2\, E_m/T]}}{e^{[-c_2\, E_m/T_{ref}]}} \cdot \frac{1 - e^{[-c_2\,\nu_{mn}/T]}}{1 - e^{[-c_2\,\nu_{mn}/T_{ref}]}}. \tag{3.16}$$

The total internal partition sum $Q(T)$, which allows to obtain the number density of molecules, each in a particular state for a system in thermodynamic equilibrium for a temperature T, can be modelled using a polynomial expression of third degree using parameters for the specific isotopologues (see, e.g., Gamache et al. [2000], Fischer et al. [2003]). Hence the line strength at different altitudes in the atmosphere with different prevalent temperatures can be computed.

3.5.2 Line Broadening

Absorption or emission lines are not infinitely narrow structures. A certain number of processes lead to a frequency-dependent redistribution of the radiation thus "broadening" the spectral lines. The integral intensity remains the same.

Natural Line Width

Excited atomic and molecular states have a finite life span, typically in the range of 1×10^{-9} s to 1×10^{-8} s for undisturbed excitation states [Welz et al., 2005]. The released energy E in case of relaxation, according to the energy-time uncertainty relation ($\Delta t \Delta E \geq \frac{1}{2}\hbar$), has an uncertainty ΔE, which also adds uncertainty to the frequency of the emitted photon. The frequency uncertainty is inversely proportional to the lifetime and produces a Lorentzian-like distribution of the energy around the center frequency ν_0. The area normalized intensity profile g_N as a function of frequency ν is given by:

$$g_N(\nu) = \frac{\gamma_N}{4\pi^2} \frac{1}{(\nu - \nu_0)^2 + (\gamma_N/4\pi)^2} \tag{3.17}$$

with γ_N being related to the transition-dependent spontaneous decay rates from the excited to the lower state.

The natural line broadening has a very weak influence on the spectral shape compared to broadening effects described in the following sections as they occur under atmospheric conditions on earth.

Doppler Broadening

Particles (atoms or molecules) are subject to thermal motion. The motion of the particles with respect to each other is described by the Gaussian *Maxwell-Boltzmann distribution*. As the particles move forth or back with respect to the observer's position, a slight shift of the absorbed frequency becomes noticeable. The compound influence of all absorbing particles leads to a (nearly) symmetrical broadening of the absorption line, called *(thermal) Doppler broadening*. Like the mentioned velocity field, the frequency distribution of the radiation around the central frequency ν_0 can be described using a Gaussian approach:

$$g_D(\nu) = \frac{1}{\sqrt{\pi}\gamma_D} \cdot \exp\left[-\left(\frac{\nu - \nu_0}{\gamma_D}\right)^2\right] \tag{3.18}$$

with the Doppler frequency half-width

$$\gamma_D = \frac{\nu_0}{c} \cdot \sqrt{\frac{2k_B \cdot T \cdot \ln 2}{m}}. \tag{3.19}$$

T stands for the absolute temperature, m is the molecule mass and k_B the Boltzmann constant. For measurements in the open atmosphere, Doppler broadening for a specific molecule at a specific wavelength is mainly a function of temperature and thus of altitude. In higher

atmospheric regions Doppler broadening decreases, but the relative influence on overall broadening rises due to the more rapidly decreasing effect of the subsequently described collision broadening.

Collision Broadening

When measuring radiation absorption which takes place in the lowest parts of the earth's atmosphere, so-called collision broadening (or pressure broadening) plays a far more dominant role than the thermal Doppler broadening described above. This applies especially to relatively short wavelengths [Schreier, 2009]. Water vapour molecules frequently undergo collisions with molecules of the same or different molecular species contained in the air. This leads to slight perturbations of the energy levels of the absorbing molecules and thus to a shifting of the absorbable photon frequency (to likewise lower and higher levels) and thus to absorption profile broadening. The magnitude of this broadening effect is determined by the frequency at which collision events occur. A comprehensive description of the various processes subsumed under collisional broadening is given by Allard and Kielkopf [1982].

For the processing of SOLUSAR spectra the following formula provided by Rothman et al. [1998] is used to describe the collision broadening. The pressure broadened line half-width γ_L as a function of pressure p [atm] and temperature T [K] is:

$$\gamma_L(p,T) = \Big(\frac{T_{ref}}{T}\Big)^n (\Gamma_{air}(p_{ref},T_{ref})(p-p_s) + \Gamma_{self}(p_{ref},T_{ref})p_s). \tag{3.20}$$

Γ_{air} [cm^{-1}/atm] and Γ_{self} [cm^{-1}/atm] describe the transition-dependent broadening half-widths for collision processes with various atmospheric molecules and water vapour molecules, respectively, under reference conditions ($T_{ref} = 296\,\mathrm{K}$ and $p_{ref} = 1\,\mathrm{atm}$). p_s [atm] denotes the water vapour partial pressure. n is a transition-dependent coefficient describing the temperature-dependence of the air-broadened half-width.

The Lorentz-distribution describing the collision broadening hence can be written as:

$$g_L(\nu,\nu_0,p,T) = \frac{1}{\pi}\frac{\gamma_L(p,T)}{\gamma_L(p,T)^2 + (\nu-\nu_0)^2} \tag{3.21}$$

Voigt Profile

Doppler broadening and collision broadening occur simultaneously depending on the prevalent conditions where absorption takes place. The two effects are considered to be largely independent. The overall broadening effect hence can be described as a convolution of the Gaussian-like intensity distribution of the Doppler broadening and the Lorentzian distribution evoked by collision broadening. The thus produced intensity distribution is called *Voigt profile*. With both portions showing comparable half-widths γ_D and γ_L, the center of the profile is dominated by the Gauss portion, whereas the wings are mainly shaped by the Lorentz function. The profile as a function of wavelength can be written as:

$$g_V(\nu) = \frac{g_0 \cdot A}{\pi} \cdot \int_{-\infty}^{+\infty} \frac{e^{-t^2}}{A^2 + (B-t)^2}\,dt \tag{3.22}$$

with

$$g_0 = \frac{1}{\gamma_D} \cdot \sqrt{\frac{\ln 2}{\pi}}, \qquad A = \frac{\gamma_L}{\gamma_D} \cdot \sqrt{\ln 2}, \qquad B = \frac{\nu - \nu_0}{\gamma_D} \cdot \sqrt{\ln 2}.$$

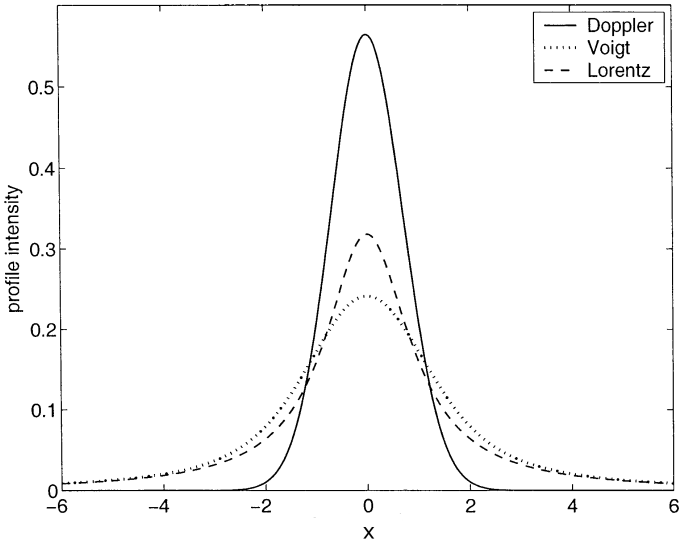

Figure 3.8: Lorentz profile and Doppler Profile with the same halfwidth ($\gamma_L = \gamma_D$). The convolution of these distribution functions yields a Voigt profile. x is defined as the normalized frequency deviation from the central frequency ν_0: $x \equiv (\nu - \nu_0)/\gamma_D$ (adapted from Huang and Yung [2004]).

Eq.3.22 is not solvable analytically. Humlícek [1982] provides a common approach for numerical computation of the Voigt profiles. For an approximation of the FWHM, the so-called Voigt line width $\Delta\lambda_V$ (expressed in wavelength), this empirical formula can be used [Welz et al., 2005]:

$$\Delta\lambda_V \approx \frac{\Delta\lambda_C}{2} + \sqrt{\left(\frac{\Delta\lambda_C}{2}\right)^2 + \Delta\lambda_D^2} \tag{3.23}$$

with $\Delta\lambda_C$ and $\Delta\lambda_D$ the FWHM of the collision and Doppler broadening distributions, respectively, also expressed in wavelengths. According to Ngo et al. [2012] there is evidence that in case of water vapour absorption the true line shape differs considerably from the Voigt profile. The Voigt profile is itself an approximation which does not include certain effects associated with Doppler broadening, e.g. the Dicke narrowing caused by the change of velocity of the radiating molecule due to collisions. What distribution function should better be used instead remains a matter of debate [Tennyson et al., 2012].

3.6 Apparatus Influcence on Spectra

The factor $A(\lambda)$ in Eq. 3.4 sums up manifold possible instrumental influences altering the spectral composition of the observed spectra on a broadband level, as, e.g., the intensity distribution within diffraction orders produced by echelle gratings (see Section 4.4.1), the wavelength dependent attenuation factor of optical filter elements or the likewise wavelength-dependent quantum efficiency of the detector recording the spectra. These effects, in general, can be comfortably handled when applying the DOAS method. Nonetheless one has also to

take into account the apparatus' influence on narrowband spectral features, leading to even broader line profiles. To quantify said influences the so-called *apparatus function* (also known as *instrument function* or *slit function*) is introduced.

The apparatus function describes the response of the measurement instrument to an ideally monochromatic input, thus taking into account "the limited resolution power of a non-ideal instrument" [Sierk, 2001]. The output $I_a(\lambda)$ of an arbitrary input signal $I(\lambda)$ is computed by a convolution of the input signal with the apparatus function F_A [Bösch, 2002]:

$$I_a(\lambda) = I(\lambda) * F_A = \int I(\lambda - \lambda') \cdot F_A(\lambda')\, d\lambda'. \tag{3.24}$$

In order to model the apparatus influence mathematically often a Voigt distribution is used. The apparatus function half-width is mainly determined by the width of the entrance slit. The procedure to obtain the apparatus function for the SOLUSAR instruments will be thoroughly described in the Section 5.4.

Furthermore, the spectrum undergoes alteration due to limited spatial resolution of the applied detector on which the spectrum is spread. Applied solid-state detectors are divided in a finite number of pixels (or pixel columns). Each pixel i is illuminated by radiation of wavelengths between $\lambda(i) \pm \frac{\Delta\lambda}{2}$. The wavelength range $\Delta\lambda$ covered by each pixel can vary considerably with wavelength. The recorded spectrum is generated by the accumulated intensities $R(i)$ at the discrete pixel positions i along the array, which are:

$$R(i) = \int_{\lambda(i)-\Delta\lambda/2}^{\lambda(i)+\Delta\lambda/2} QE(\lambda') \cdot I_a(\lambda')\, d\lambda'. \tag{3.25}$$

QE denotes the wavelength-dependent quantum efficiency of the detector. The mapping to attribute the pixel output at position i to the central wavelength $\lambda(i)$ can normally be achieved using a polynomial expression. In case of SOLUSAR with a relatively short wavelength range and a single simultaneously obtained diffraction order a polynomial of second degree produces a quite accurate mapping result (see Section 6.7).

3.7 DOAS Set-Up Characteristics

The DOAS measurement principle can be applied in a multitude of different set-ups, thus reflecting the diverse requirements met in the growing field of studying and monitoring the earth's atmosphere. In the following some of the major classification aspects of DOAS applications are shortly outlined. For a more detailed overview of the different DOAS set-ups, see Platt and Stutz [2008].

Active DOAS versus Passive DOAS

Detection of trace gas concentrations in the atmosphere can either be performed by *active DOAS* using artificial light sources or using *passive DOAS* with light emitted by natural radiators. Active DOAS is mainly implemented for trace gas detection in air masses near ground level. It puts high requirements regarding the optical set-up: The deployed light source has to emit light with a smooth spectral characteristic, high intensity as well as an excellent beam collimation. Commonly high-pressure arc lamps or broadband lasers are used. (A comprehensive list of different light sources can be found in Platt and Stutz [2008]). Main advantages

over passive measurement set-ups lie in the availability at any daytime and the possibility of UV-measurements. Passive DOAS applications usually have a much simpler set-up, benefiting from the already collimated incident beam and strong radiation intensities when using direct sunlight. Furthermore even the highest atmospheric layers can be covered.

Measurement Platforms

Along with the classical application with a receiving platform permanently installed at a specific ground-based measurement site, numerous applications with instrument mountings on a moving platform have emerged over the years. Aircraft-based experiments can provide a great spatial coverage and give access to otherwise uncovered areas. Balloon-borne measurements can provide information on the vertical distribution of trace gas concentrations either by measuring at different altitudes or through measurements from a higher altitude using light from an ascending or descending celestial body at different elevation angles.

Further there are multiple DOAS-like instruments installed on satellite platforms. Mostly they are mounted on satellites with geostationary orbits thus allowing steady monitoring of the air masses over a certain area. Other measurements are performed in low earth orbit (LEO), possibly on a sun-synchronous polar orbit, allowing coverage of nearly the whole planet within a few days time span.

Light Paths

The classical DOAS application uses radiation travelling directly from its source to the measurement site. But also set-ups using external ray paths folded by mirrors are possible. More demanding regarding the processing are applications using scattered light or tomographic approaches using various sources and measurement instruments thus providing spatially resolved concentration fields.

3.8 Passive DOAS

The following sections will provide information on the application of ground-based, direct light passive DOAS using the sun and the moon as radiation source as it is applied in this project.

3.8.1 Solar Irradiance

The optical radiation emitted by the sun is mainly generated in the solar photosphere, a layer which lies underneath the 10 000 km thick chromosphere. The exhibited spectrum is a superposition of spectra emitted by distinct photospheric layers with different temperatures and pressure. The electromagnetic radiation emitted ranges from x-rays to the long radio wavelength range. Between wavelength of 140 nm to 10 cm the solar spectrum closely resembles the intensity distribution of a black-body with a temperature of 5700 K to 6000 K. The spectral radiance B emitted by a black body in thermal equilibrium with a temperature T as a function of wavelength λ is described by *Planck's Law*:

$$B(\lambda) = \frac{2hc^2}{\lambda^5} \frac{1}{\exp\left[\frac{hc}{\lambda k_B T}\right] - 1} \tag{3.26}$$

As visible in Fig. 3.9 the radiation undergoes several alterations as it passes the atmosphere: Light with wavelengths below 300 nm is absorbed by the atmospheric ozone layer. Different atmospheric constituents (especially ozone, oxygen, carbon-dioxide and water) cause large absorption bands. There remain some atmospheric windows where absorption is particularly small. Additionally, scattering processes also lead to attenuation of the overall intensity.

Solar irradiance is well suited for DOAS applications due to its high brightness thus enabling measurements with a low detection limit and high spectral resolution. Due to the large distance between the radiation source and the measurement site the beam is perfectly collimated. The sunlight shows an overall smooth spectral characteristic which is only disturbed by the occurrence of Fraunhofer lines. Fraunhofer lines themselves are absorption lines originating from resonance absorption in the solar photosphere by its constituent gases. These lines show quite similar line-widths as spectral features coming from absorption in the earth's atmosphere.

Drawbacks when using sunlight are the restrictions to daytime measurements and periods of time with limited cloud coverage. The great dynamic range of the incident intensity has also to be taken into account. The influence of the atmospheric thickness which the radiation has to traverse, often described by the so-called direct light airmass factor (AMF, practically equivalent to the mapping function described in Section 2.3.4), leads to an intensity attenuation between zenith observation angles z of 0° and 85° of more than an order of magnitude, when applying the simplest wavelength-independent AMF model: $AMF = \frac{1}{cosz}$. This dynamic range is further widened by the different occurring atmospheric conditions with changing concentrations of straying particles and water droplets.

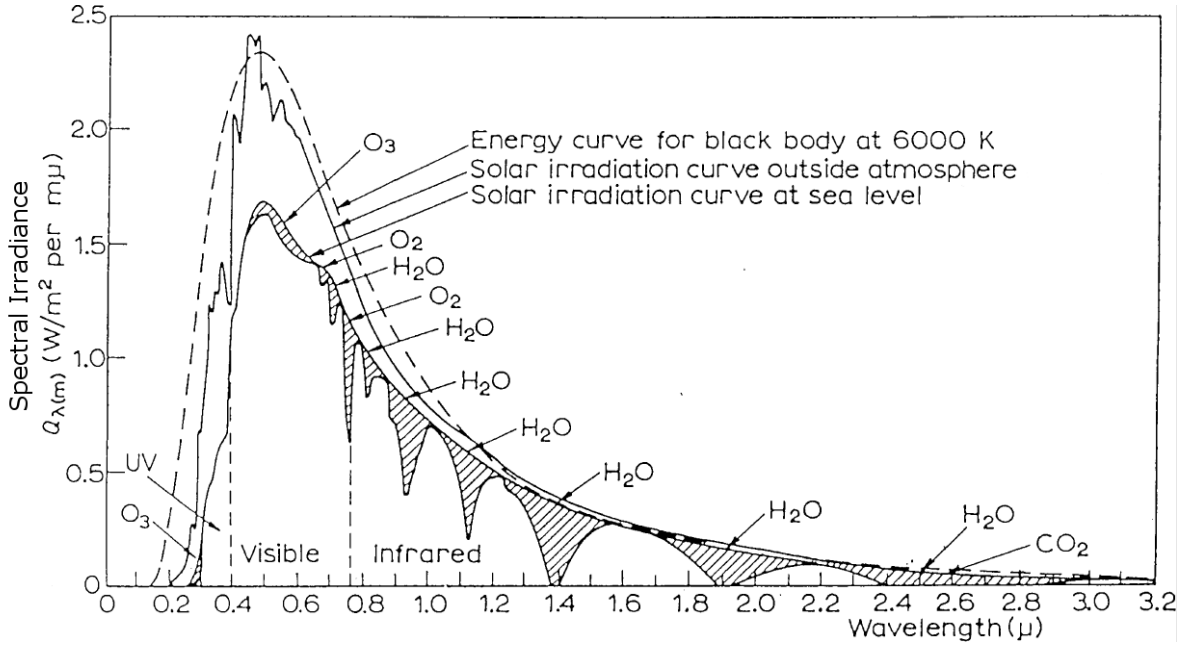

Figure 3.9: Solar irradiation curve inside and outside of the earth's atmosphere compared with the spectrum emitted by a black body at 6000 K. Visible are the strong absorption bands of several atmospheric constituents - among these the water vapour band close to 800 nm (see Fig. 3.6), the wavelength region analysed by the SOLUSAR spectrometer (adapted from Bösch [2002]).

The spectral composition over time of the sun's spectrum is relatively constant. Slight changes to the emitted total irradiance of the sun (cyclical solar variation) and the changes of the earth-sun distance are not influencing the DOAS method. The solar spectrum is not constant across the hole disk though, as the so-called *solar center-to-limb darkening* changes the optical

density of Fraunhofer lines since the radiation originates from different photospheric layers with different temperatures [Bösch, 2002]. This should not affect the SOLUSAR data processing where parts of the spectra with no noticeable impact of Fraunhofer lines are analysed.

3.8.2 Spectral Characteristics of Moonlight

Lunar radiation can be described as combination of sunlight reflected by the lunar surface and the thermal emission spectrum of the moon itself. With surface temperatures in the range of 200 K to 400 K the lunar thermal emission spectrum dominates the spectral region above wavelengths of 4.5 µm in the MIR (mid-infrared) and radio-wave region [Stremme et al., 2009]. In the VIS and NIR spectral region the lunar spectrum resembles the solar spectrum but is further shaped by the reflectance on the lunar disk. The overall reflectance ratio is primarily a function of the lunar phase angle, the angle between the observer (on earth), the reflecting object (moon) and the light source (sun). With phase angles approaching 0° the reflectance and thus the surface brightness increases steadily [Kieffer and Stone, 2007]. This effect is sometimes called *opposition effect* and is attributed to the illumination of the porous features of so-called regolith surfaces and coherent back-scattering effects. Intensity in general is attenuated by the phase angle dependent reflectance, the decrease in brightness is greater for shorter wavelength though. The local lunar reflectance is also strongly dependent on the chemical and morphological composition of the reflecting moon surface [Ohtake et al., 2010].

For DOAS measurements using lunar instead of solar light the main difference lies in the overall low magnitude, which of course is strongly dependent on the size of the illuminated disk. The luminance (a photometric measure of the luminous intensity per unit area) for the sun can reach up to $1.6 \times 10^9\,\mathrm{cd\,m^{-2}}$ at noon, whereas for full moon at clear sky conditions values of around $5000\,\mathrm{cd\,m^{-2}}$ can be registered which is comparable to the luminance of blue sky. This low brightness is further decreased by the opposition effect mentioned above. Furthermore disadvantageous is the decrease of the illuminated surface area with increasing phase angles which can lead to an insufficient entrance slit illumination.

Possible windows for lunar light DOAS measurements hence are situated at night-time some days before and after full moon. Fig. 3.10(a) and 3.10(b) show possible observation windows for a measurement site at Berlin-Adlershof ($\Phi = 52.4272°$, $\Lambda = 13.5344°$) in January and July 2012, respectively. Observation requirements were set as follows: phase angle smaller than 50°, lunar elevation angle greater than 10° and solar elevation below 0°.

The viable measurement time is of course further limited by overcast sky. The emergence of clouds is heavily depending on daytime, season and measurement site. Fig. 3.11 shows the global mean cloud fraction over the time span of a month in January and July of 2012.

3.9 Total Column Concentration Extraction

The basic expression Eq. 3.8 for the determination of gas concentrations using the method of DOAS is not as directly applicable in reality, when seeking total column gas abundances. The narrowband absorption cross section σ_n varies depending on the conditions under which the absorption process is taking place. When travelling from the light source to the measurement site radiation is absorbed in different atmospheric layers with differing temperatures and pressures. As described in Section 3.5.2 these parameters influence the absorption line shape and thus the absorption cross section at a specific wavelength λ. Furthermore it has to be

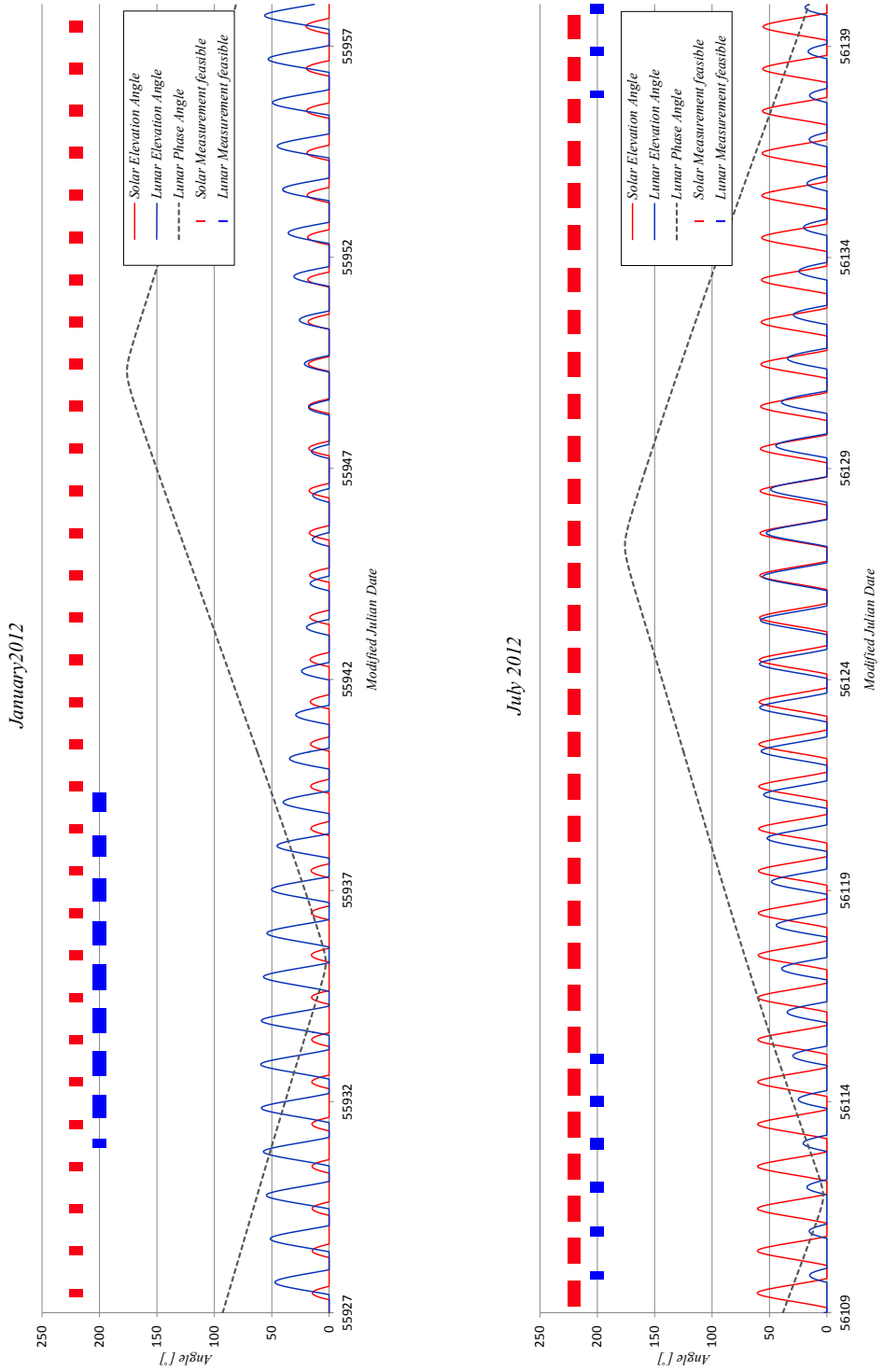

Figure 3.10: Possible observation windows for DOAS measurements using solar or lunar light for the measurement site at Berlin-Adlershof in January and July 2012, respectively. For lunar measurement windows it is assumed that the phase angle is smaller than 50°, the lunar elevation angle is larger than 10° and the sun is below the horizon.

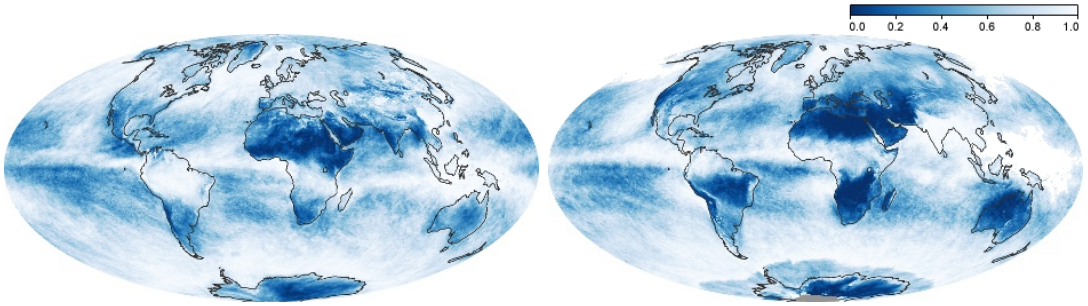

(a) January 2012 (b) July 2012

Figure 3.11: Average cloud fraction of an area over a timespan of a month ranging from no clouds (blue) to totally cloudy (white). Data were collected by the Moderate Resolution Imaging Spectroradiometer (MODIS) on NASA's Terra satellite [NASA Earth Observatory, 2012].

considered that multiple overlapping absorption lines can contribute to the total absorption cross section at a specific λ.

The common strategy for the retrieval of total column water vapour values lies in a comparison of a (preprocessed) measured spectrum with a synthesized reference spectrum, which models line-by-line the absorption process along the ray path based on assumptions on the atmospheric conditions and the water vapour content. The influence of the apparatus (including the detector) on the spectra is modelled as well. Using an iterative least-squares fitting algorithm, the integrated amount of water vapour in the reference spectra synthesis is adjusted until the best agreement between measurement spectrum and the artificial spectrum is found.

Most such algorithms used in this project are adopted from the GEMOSS project. Succeeding sections provide the basic ideas behind the procedures. For the full description of the processing algorithms I refer to Somieski [2005].

3.9.1 Preprocessing of Measured Spectra

Before measurement data can be fed into the above indicated adjustment process, a series of preprocessing steps have to be carried out in order to compute a so-called *transmission spectrum* from the measured data. The so obtained transmission spectrum describes the percentage of radiation per wavelength, which persists after undergoing processes altering the spectral composition on a narrow-band scale, namely by atomic/molecular absorption in the earth's or sun's atmosphere (Fraunhofer lines) and line broadening. As shown in Fig. 3.12 in this preprocessing all broadband effects are eliminated:

1. **Stray Light and Dark Current Correction**
   The raw data (i.e. CCD image of the spectrum) have to be reduced to eliminate the disturbing influence of certain instrumental effects as stray light or detector dark current. Non-consideration of these effects would lead to systematic biases in the spectra analysis. The hereto applied procedures in this project are described in Sections 6.2 and 6.4.

2. **Wavelength Referencing**
   From the stray light corrected data a wavelength-referenced intensity distribution has to be deduced (see Section 6.7)

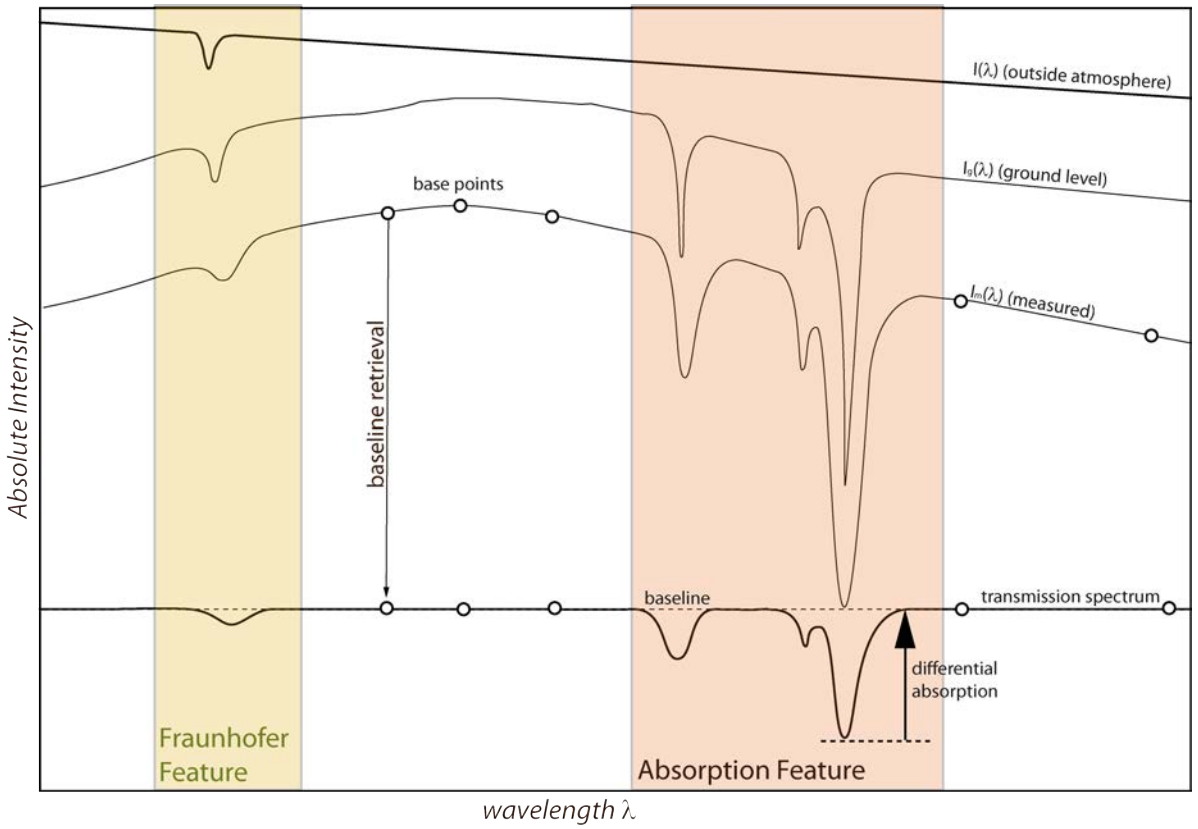

Figure 3.12: The incident sunlight already bears absorption features from the solar atmosphere (Fraunhofer lines). As the light travels through earth's atmosphere the light is generally attenuated by various effects (i.e. scattering). Furthermore narrow absorption structures become visible. The spectral composition is further slightly altered by the measurement instrument itself: absorption lines are broadened. From the measured intensities the transmission spectrum is derived thus getting rid of all broadband intensity variation. This is accomplished through computation of the baseline using base points at frequency where no narrow-band absorption features occur.

3. **Flat-field Correction**
   To eliminate the influence of the instruments wavelength-dependent sensitivity (e.g. due to the characteristics of the optical set-up and the changing local detector pixel sensitivity) the quotient with a flat-field spectrum (continuum spectrum) is computed (see Section 6.6)

4. **Broadband Elimination**
   The applied processes to get rid of the remaining broadband structures largely depend on the observed wavelength range. If specific spectral positions are present in the data, where one can assume that no narrowband absorption is occurring the wavelength-dependent reference intensity (baseline I_0^*) can be computed using said positions as base points (see Fig. 3.12 and description in Section 6.8). If the measured spectrum is closely packed with narrowband absorption features and thus no base points are available, high-pass filtering methods (e.g. Fourier Filter) have to be applied [Platt and Stutz, 2008].

3.9.2 Spectra Simulation

For the computation of a synthetic transmission spectrum, which is comparable with the preprocessed measured transmission spectrum, all major factors influencing the spectral composition of the solar/lunar light have to be considered:

- Absorption features of atmospheric constituents within and adjacent to the measurement range,
- geometry of the ray path through the atmosphere,
- meteorological conditions along the ray path,
- influence of the apparatus,
- influence of the detector.

In the underlying atmospheric model several stacked concentric shell-shaped layers j are defined. To each layer a temperature, pressure and water vapour partial pressure is assigned, as described in Section 3.9.4. Based on these assumptions ray paths can be computed (Section 3.9.3). With the knowledge on the n transitions l occurring within the spectral region of interest based on spectral databases (3.10), the absorption cross section $\sigma_j(\lambda)$ of the layer j can be written as:

$$\sigma_j(\lambda) = \sum_{l=0}^{n} \sigma_{l,j}(\lambda) \tag{3.27}$$

The transmittance t (a number between 0 and 1) is computed by applying Lambert-Beer's Law for all m layers (with water vapour concentrations c_j) through which the light sequentially propagates.

$$t(\lambda) = \exp\left[-\sum_{j=0}^{m} \int_{s_{j,top}}^{s_{j,bottom}} c_j \cdot \sigma_j(\lambda)\, ds_j\right] \tag{3.28}$$

As described in Section 3.6 the influence of the apparatus and detector have to be addressed. The pixel-wise transmittance $t_{pixel}(i)$ becomes:

$$t_{pixel}(i) = \int_{\lambda(i)-\Delta\lambda/2}^{\lambda(i)+\Delta\lambda/2} t(\lambda') * F_A \, d\lambda'. \tag{3.29}$$

3.9.3 Ray Path Modelling

To model the wavelength-dependent atmospheric transmission an accurate description of the ray path is necessary. In this work the same calculation routines are used as in the GEMOSS project [Somieski, 2005]. In the following only the basic underlying principles are explained.

In the model used, the radiation travels from the celestial body through the atmosphere consisting of stacked spherical layers to each of which a temperature T_j, pressure p_j and water vapour partial pressure $p_{H_2O,j}$ is assigned. The determination of these values is described in Section 3.9.4. Using the meteorological data, the local refraction index n_j of the layer j can be computed. Somieski [2005] proposes to use to the formula set provided by Ciddor [1996] and Ciddor and Hill [1999] which is valid in the VIS and NIR.

For situations with relatively high elevation angles of the celestial body, and consequently high angles of incidence onto the boundary layers, the influence of changing refraction coefficients can be neglected. Therefore the simple *geometrical path length* s_n is computed. The length ds_j of the ray path within the layer j from the top boundary (altitude h_{j+1}) to the bottom boundary (altitude h_j) in this model is:

$$ds_j = \sqrt{(R+h_j)^2 + (R+h_{j+1})^2 - 2(R+h_j)(R+h_{j+1}) \cdot cos(\gamma_{j+1} - \gamma_j)} \tag{3.30}$$

with γ_j the angle between the layer entrance point of the ray in layer j and the observation site seen from the centre of the earth. R denotes the earth radius.

$$\gamma_j = \theta - \arcsin\left(\frac{R}{s_j} \cdot \sin(\theta + \pi)\right) \tag{3.31}$$

θ denotes the sun zenith angle. The total geometrical path length s_n from observation point to the assumed tropopause is the sum of the n intra-layer distances:

$$s_n = \sum_{j=0}^{n} ds_j \tag{3.32}$$

For low elevation angles of the radiation source the ray bending is stronger and hence is taken into account. The refraction at the boundary between layer j and $j+1$ according to *Snellius' Law* is:

$$z_{j+1} = \arcsin\left(\frac{n_j}{n_{j+1}} \cdot \sin(\beta_{j+1})\right) \tag{3.33}$$

with z_{j+1} denoting the angle of incidence and β_{j+1} the refraction angle, from which the subsequent angle of incidence z_j can be derived. The bent ray path can be approximated by adjusting the first angle of incidence z_0 and all consequent angles in a iterative process until the bent ray travels in parallel to the geometric path outside the atmosphere. Schödlbauer [2000] proposes a start value for z_0 depending on the meteorological conditions at the observation site.

3.9.4 Atmospheric Modelling

As described in Section 3.5 the shape of the absorption structures is influenced by the meteorological conditions at the site of absorption. Additionally meteorological parameters also influence the refraction index and thus the geometry of the ray path. In order to synthesize a simulated transmission spectrum a suitable meteorological model has to be applied to determine temperature, pressure and water vapour partial pressure for different heights in the atmosphere. The basis of the calculations in this work is the U.S. Standard Atmosphere from 1976 [NOAA, 1976].

The temperature T [K] for an arbitrary height H is described by a series of subsequent linear equations of the form:

$$T(H) = T_b + L_b \cdot (H - H_b) \tag{3.34}$$

with T_b the starting temperature at the bottom of the atmospheric layer (with the height H_b). The subscript b denotes the layer defined in the model of the standard atmosphere, $b = 0$ being the lowest layer near the ground. L_b stands for the temperature gradient assigned to the layer b. The model is slightly adjusted as for the lowest layer the measured temperature at the observation site is used to adjust the temperature gradient L_0.

The total pressure p [Pa] is expressed as:

$$p(H) = p_b \cdot \left[\frac{T_b}{T_b + L_b \cdot (H - H_b)}\right]^{\left[\frac{g \cdot M_0}{R \cdot L_b}\right]} \tag{3.35}$$

p_b is the starting pressure at the layer bottom. As for the temperature, the measured pressure at the observation site is used as starting pressure in the lowest layer. g, M_0 and R are constants (see NOAA [1976]).

The water vapour partial pressure p_{H_2O} is computed using:

$$p_{H_2O}(H) = p_{H_2O,ground} \cdot \exp\Big[\frac{-(H - H_{ground})}{H_v}\Big] \tag{3.36}$$

with $p_{H_2O,ground}$ the measured water vapour partial pressure at the measurement site (height H_0) and $H_v = 1.5\,\text{km}$ the scale height [Somieski, 2005].

3.10 Spectroscopic Databases

For the computation of the line-by-line radiative transfer of the sunlight through the atmosphere, necessary to determine spectrally high-resolved synthetic transmission spectra, line-specific parameters have to be obtained for transitions within the observed wavelength range. Tab. 3.1 lists the line parameters needed to determine the wavelength-dependent absorption cross sections as they are denoted in the current HITRAN database format:

Symbol	Parameter Description	Units	Formula
ν_0	Transition wavenumber	cm^{-1}	3.22
$S_{mn}(T_{ref})$	Line Intensity	$\text{cm}^{-1}/(\text{molecule cm}^{-2})$	3.16
Γ_{air}	Air-broadened width	$\text{cm}^{-1}/\text{atm}$	3.20
Γ_{self}	Self-broadened width	$\text{cm}^{-1}/\text{atm}$	3.20
E_m	Lower-state Energy	cm^{-1}	3.16
n	Temperature dependence of air width	unitless	3.20

Table 3.1: Spectral line parameters as defined in Rothman et al. [1998] needed in the computation of atmospheric solar/lunar transmission spectra with their units and the formula, in which they are used.

Spectroscopic parameters of monomeric transitions for different atoms and molecules, respectively different isotopes and isotopologues, are listed in numerous spectroscopic databases, covering different wavelength and line intensity ranges. In the following the characteristics and differences of three catalogues are shortly described: *HITRAN2008*, *ESA-WVR* and *UCL08*. A more detailed comparison of the catalogues in the wavelength range of SOLUSAR is given in Chapter 7.

3.10.1 HITRAN2008

One of the most widely used spectroscopic databases for the calculation of atmospheric absorption and emission spectra is the *High-Resolution Transmission Molecular Absorption Database (HITRAN)*. It originates from a long running project starting 1960 at the Air Force Cambridge Research Laboratories. Today it is further developed and maintained at the Harvard-Smithsonian Center for Astrophysics (Cambridge MA, USA). The main source of information in the near-infrared for $H_2{}^{16}O$ are Fourier Transform Spectroscopy (FTS) measurements made at the National Solar observatory in Tucson (AZ, USA). They are supported by other measurement methods (e.g. cavity ring-down spectroscopy) and theoretical studies, as ab initio theory [Schermaul et al., 2001].

The database is frequently updated. The latest version HITRAN2008 lists spectral lines of 42 different molecular species and ions, including the six isotopologues of H_2O. Besides individual line parameters ranging from the microwave through the visible range to the ultraviolet for molecules in the gas phase, the database also provides information on the absorption cross section for molecules where lines are not individually resolvable or on refractive indices of aerosols [Rothman et al., 2009].

Somieski [2005] used the version HITRAN2000 and found that line strengths are generally too small. Since then the HITRAN database has seen major updates which also affect the water vapour transition data in the SOLUSAR measurement range: For the HITRAN2004 database 918 new lines belonging to the isotope $H_2{}^{18}O$ have been added between $12\,400\,cm^{-1}$ and $14\,518\,cm^{-1}$[Tanaka et al., 2002]. The data for the most abundant isotope $H_2{}^{16}O$ has been completely updated in the range between $11\,400\,cm^{-1}$ and $12\,895\,cm^{-1}$ based on the work of Mérienne et al. [2003] inter alia. Furthermore the line shape parameters for all non-deuterated isotoplogues have been completely overhauled [Rothman et al., 2005]. In the 2008 update various changes have been applied to the water vapour data. Among these an update of main isotopologue data in the range between $9500\,cm^{-1}$ and $14\,500\,cm^{-1}$ using new fitting techniques [Tolchenov and Tennyson, 2008] for the analysis of Fourier transform absorption spectra recorded by Schermaul et al. [2001]. Again the pressure-broadened half-width parameters have been completely updated for the three main isotopologues. For a comprehensive overview on the update see Rothman et al. [2009].

3.10.2 ESA-WVR

The database ESA-WVR (European Space Agency, Water Vapour Red region) covers monomeric water vapour lines in the frequency range between $8952\,cm^{-1}$ and $15\,000\,cm^{-1}$. It is the result of a study to help in the interpretation of spectral data gathered by different satellite-based atmospheric remote sensing applications. Schermaul et al. [2001] recorded data in near-infrared and visible range obtained in laboratory experiments using the combination of a high-resolution Fourier transform spectrometer and long-path absorption cells (path lengths up to 513 m). The measurements carried out with pure water vapour and with mixtures of water vapour and synthetic air at two different temperatures (252 K, 296 K) showed considerable disagreement to the 1996 version of the HITRAN database. Depending on the absorption band, ESA-WVR line intensity sums are seen to be 16 % to 33 % larger than the HITRAN1996 intensity sums.

Somieski [2005] found that the ESA-WVR line intensities in the GEMOSS measurement range (728 nm to 915 nm) are still too low and conducted a further re-evaluation of certain prominent water vapour absorption lines.

3.10.3 UCL08

The UCL08 line list [CAVIAR consortium, 2010] was built as a part of the "Continuum Absorption at Visible and Infrared Wavelengths and its Atmospheric Relevance" (CAVIAR) consortium project, which involves atmospheric and laboratory measurements and climate modelling calculations [Shillings et al., 2011]. It covers the spectral range between 7500 cm^{-1} and 20 000 cm^{-1} at the HITRAN default temperature (296 K). Compared to the HITRAN database UCL08 has a lower line intensity cut-off: $S_{mn} = 1 \times 10^{-30}\,\mathrm{cm}^{-1}/(\mathrm{molecule\ cm}^{-2})$ for the short list containing around 200 000 lines and $S_{mn} = 1 \times 10^{-36}\,\mathrm{cm}^{-1}/(\mathrm{molecule\ cm}^{-2})$ for the longer list (1.5 million lines). This increased number of weak lines becomes important when conducting long path experiments.

UCL08 was constructed using lines also from new experimental measurements. In certain wavelength areas HITRAN2008 data were taken. For lines known to be present from ab initio calculations, but neither provided by the new experimental data nor the HITRAN2008 database, data from the calculated BT2 line list [Barber et al., 2006] were included. To avoid duplications a line matching based upon the quantum numbers was conducted for the different sources. Where existing, line broadening parameters were taken from HITRAN. Otherwise widths were estimated using a method based on fittings to lines with similar quantum numbers [Shillings et al., 2011].

3.11 Least-squares fit algorithm

In the fitting procedure of the transmission spectrum derived from the measurement and the simulated reference spectrum, the total slant precipitable water vapour PW is iteratively adjusted in the simulation until the two spectra agree best [Somieski, 2005]. The improvements which have to be applied to the pixel-wise transmittance values of the simulated spectrum can be written as:

$$\underbrace{\begin{bmatrix}\delta t_{pixel,sim}(0)\\ \delta t_{pixel,sim}(1)\\ \vdots\\ \delta t_{pixel,sim}(n)\end{bmatrix}}_{\mathbf{v}} = \underbrace{\begin{bmatrix}\partial t_{pixel,sim}(0)/\partial PW\\ \partial t_{pixel,sim}(1)/\partial PW\\ \vdots\\ \partial t_{pixel,sim}(n)/\partial PW\end{bmatrix}}_{\mathbf{A}} \underbrace{\cdot \delta PW}_{\mathbf{x}} - \underbrace{\begin{bmatrix}t_{pixel,meas}(0) - t_{pixel,sim}(0)\\ t_{pixel,meas}(1) - t_{pixel,sim}(1)\\ \vdots\\ t_{pixel,meas}(n) - t_{pixel,sim}(n)\end{bmatrix}}_{l} \tag{3.37}$$

with $\mathbf{v}$ the pixel-wise intensity improvements, $\mathbf{A}$ the design matrix with the partial derivatives with respect to the unknown listed in $\mathbf{x}$. $\mathbf{l}$ stores the differences between measured and simulated pixel intensities (observed minus computed).

An estimation of $\mathbf{x}$ is found by solving

$$\mathbf{x} = \mathbf{N^{-1}A^{T}P\,l} \ \text{ with } \ \mathbf{N} = \mathbf{A^{T}P\,A} \tag{3.38}$$

with $\mathbf{P}$ the weighting matrix of the observations. The terms $\partial t_{pixel,sim}(i)/\partial PW$ in $\mathbf{A}$ describe the influence of a change in PW on the transmittance of the pixel i in the digitized simulated spectrum, which in fact is the mean influence on all wavelengths comprised in one pixel in the digitization process. These again depend on the influence of δPW on the transmittance t on all contributing wavelength λ_i in the convolution process with the apparatus function. $\frac{\partial t(\lambda_i)}{\partial PW}$ describes the influence of δPW on the whole radiative transfer, based on the meteorological model and the wavelength-dependent absorption cross section. For the comprehensive formula please consult Somieski [2005].

4

SOLUSAR - System Design

4.1 System Requirements

In order to reach the project goals described in Chapter 1, which are based on the results and insights obtained in preceding projects carried out by Sierk [2001] and Somieski [2005], a new measurement system named *SOLUSAR (**SO**lar **LU**nar **S**pectrometer for **A**tmospheric **R**esearch)* is designed from scratch with the objective to retrieve atmospheric total column water vapour abundances through the analysis of molecular absorption in sun or moon spectra. Two identical prototype instruments are built, which are designed to meet the following demands:

1. **Improved system sensitivity**
   Enabling the measurement of direct solar radiation and likewise indirect sunlight reflected by the moon surface and thus widening the temporal coverage requires a system design able to deal with radiation intensity dynamics of up to six orders of magnitude. The entire optical design of the light gathering telescope and the spectrometer unit as well as the selection of the used optical elements are optimized for a minimization of the light attenuation in the significant wavelength region. In order to perform under low-light conditions, the detector units and associated electronics must exhibit an adequate level of sensitivity.

2. **Automatic light source tracking telescope**
   For system operation on a moving platform a tracking telescope is implemented able to automatically follow the (virtual) trajectory of the light source and to uninterruptedly guide the gathered radiation onto the spectrometer's entrance slit. A telescope control cycle ensuring movements with sufficient speed is set up to compensate for the platforms tilting action in order to allow continual data acquisition at least for a moderate sea state.

3. **Comparable accuracy to GEMOSS**
   Despite the spectrometer's different optical layout compared to the predecessor instrument GEMOSS (e.g. smaller wavelength range, utilization of lens optics) similar measurement accuracy of the retrieved water vapour concentrations should be achieved with similar temporal resolution of data points.

4. **Autonomous operation with self-calibration**
   The measurement process is autonomously carried out by the measurement system. Calibration routines are periodically performed without need of human supervision. The acquired data is being preprocessed instantaneously thus deriving wavelength-referenced transmission spectra suited for the actual evaluation of water vapour concentrations.

5. **Compact rugged design**
   The new measurement system should allow rapid and easy field deployment. Therefore a smaller, more compact and integrated measurement instrument, sealed in a rugged hull, is designed. The number of additional external components is reduced to a minimum.

This chapter describes the optical, mechanical and electronic design of the measurement system which has been developed to meet the listed requirements 1 to 5. The fulfilment of several of the named goals also requires the application of specific software measures which are elaborated on in Chapter 5 (Control Software) and Chapter 6 (Processing Software).

4.2 General System Design

The most prominent characteristic of SOLUSAR, when compared with the former solar spectrometer designs of GEMOSS and SAMOS, is the assembly of all main instrument parts in a single casing. This integration reflects the direct optical coupling of the telescope unit and the spectrometer unit. Consequently electronic components are for the most part directly attached to the instruments mechanical structure thus contributing to the objective of maximal integration (Fig. 4.1 a).

The enclosed instrument resembles an upright standing pillar with a circular horizontal cross section able to stand on the ground on its own. It has a total height of roughly 1.1 m, a maximum diameter of 0.24 m and weighs around 40 kg (see Fig. 4.1 b). The top part of the instrument consists of a custom-built mirror telescope (described in Section 4.3). Placed right underneath is a group of optical and electromechanical components (including the spectra-recording CCD detector) which henceforward will be called *entrance slit group*. The entrance slit itself defines the beginning of the echelle grating spectrometer situated at the very bottom of the structure.

Initially the concept of an optically decoupled telescope using light-guiding fibres to transport the radiation to the spectrometer has been abandoned due to the more demanding requirements regarding the light guidance factor of the system. Improved light guidance is of great importance as measurements of lunar spectra are aspired while keeping the dimensions of the apparatus at a reasonably compact level. The deployment of optical fibres (even of great quality) leads to considerable transmission losses and more importantly to an enlargement of the aperture thus greatly impairing total light guidance. The re-introduction of an optical fibre interface in a later project phase will be explained and described in detail in Section 4.9.

The spectrometer's simultaneous operating range is rigorously reduced compared to the spectrograph of the predecessor instrument GEMOSS (range of 728 nm to 915 nm). Primarily wavelengths between 789 nm and 801 nm are acquired, which according to Somieski [2005] allows sensing of a sufficiently large number of distinct water vapour absorption lines with different absorption strengths in absence of absorption features of other atmospheric species. With a narrow, simultaneously covered spectral range the readout time of the CCD detector can be significantly reduced. With a detector width of 2048 px, pixel size at 12 µm and a focal length of 400 mm the spectrometer achieves a reciprocal linear dispersion of 7.3 pm/px. This allows a good compromise between a great entrance slit width (for improved radiation throughput) and a sufficient absorption line separation even at high water vapour concentrations. As detection unit a CCD sensor with maximum quantum efficiency is utilised (see Section 4.6).

For the stabilization of the spectrum image on the CCD detector an alignment mechanism using stepper motors is installed which on one hand allows the spectra positioning with sub-

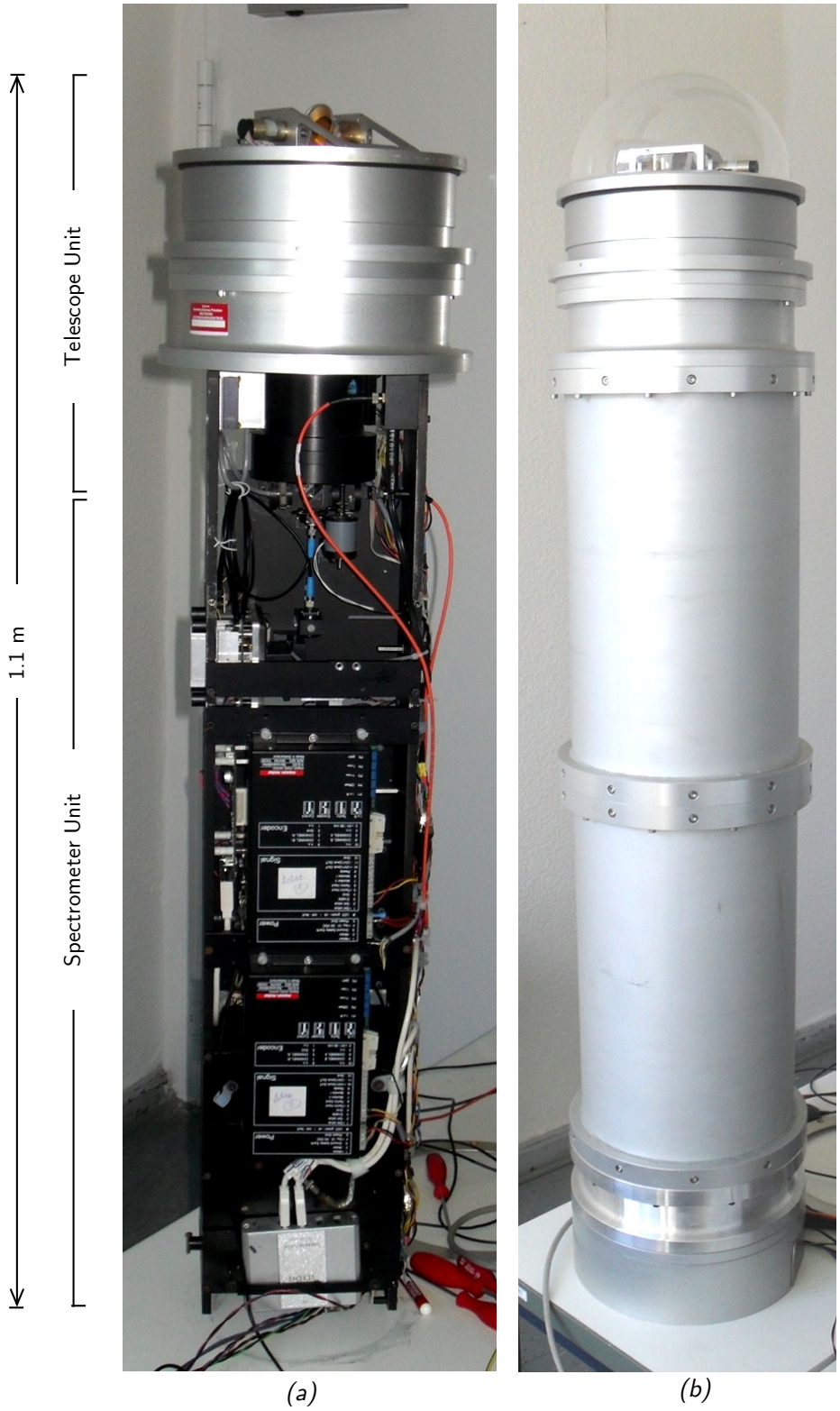

Figure 4.1: SOLUSAR system design: Telescope unit and spectrometer unit are directly coupled (a). For the sake of integration, electronic parts used for system control purposes are directly attached to the internal mechanical structure of the instrument. For weather protection and safe transport the instrument is sealed in the rugged aluminium hull (b).

pixel accuracy and on the other hand permits greater spectrum displacements and thus the observation of adjacent wavelength regions.

The interior instrument structure with its attached optical, mechanical and electronic elements is fully enclosed by a solid rugged aluminium hull. Only the uppermost telescope is sheltered with a transparent acrylic dome providing unhindered all-around view. For reduction of oscillations occurring when deployed at sea, the instrument can be installed in a gimbal mounting to approximately retain the vertical alignment (see Section 4.11).

4.3 Smart Telescope

In this project the common approach of DOAS using non-scattered sun- or moonlight is applied. Therefore the light gathering telescope has to aim directly at the light source and compensate for the earth rotation by adjusting its bearing while the radiation source travels along its trajectory across the sky. If done so the whole solar/lunar disk is constantly imaged onto the spectrometer entrance slit plane from dusk to dawn apart from the influence of sight blocking baffles such as clouds or local features of the landscape or settlements. Beside the requirement of full entrance slit illumination, the telescope has to guide the light onto the spectrometer's main illumination axis, thus reliably feeding the spectrometer with radiation of fairly constant angular radiation distribution and propagation direction.

In practical astronomy the concepts of heliostats (also called siderostats) and coelostats are often applied solutions to guide the light of a moving radiating body onto a fixed spot. Heliostats make use of a single, usually plane mirror which can be turned around two axis to keep it in perpendicular position to the angle bisector of source and target. Coelostats (as often used in tower telescopes) are compensating for the apparent movement of the tracked body by the use of two movable mirrors with the advantage of a non-turning image in the focal plane [Mills, 1985].

The SOLUSAR tracking telescope resembles a heliostat, making use of a three-mirror-system (see Figs. 4.2 and 4.3). The azimuthal target movements can be compensated by turning the rotating platform on which the mirror system is mounted - the surface normals of the mirror planes become aligned with the plane set up by the spectrometer/telescope vertical axis and the sun direction. The changes of the elevation angle of the radiation source are compensated by the primary mirror which is pivotable around a horizontal axis (Fig. 4.2, item b). The light reflected from the primary mirror (elliptic: 22 mm × 30 mm) is folded back by a secondary element (rectangular mirror: 20 mm × 20 mm, item d) and finally brought onto the vertical telescope axis by a third mirror (dimensions like the primary mirror, item f). To minimize intensity losses within the telescope, gold-coated mirrors are used with a reflectivity of at least 97 % beyond wavelengths of 800 nm for steep angles of incidence. In order to precisely achieve beam alignment with the telescope axis, the third mirror is mounted on a three-point bearing which allows orientation adjustment through fine threaded screws. The collimated beam travels from the third mirror along the telescope axis inside a hollow tube down to the focussing lens, imaging the sun spot onto the entrance slit plane.

To produce the image of the sun disk in the entrance slit plane, an achromatic doublet with a focal length f of 150 mm is used (Thorlabs AC254-150-B), designed for the use in the IR region and limiting chromatic and other aberration effects [Thorlabs, 2012]. The dimensions of the telescope are mainly determined by the entrance slit height (1 mm) which has to be fully illuminated. With the apparent sun/moon diameter w' of approximately 0.5°, the lens produces an image with a diameter y' of about 1.3 mm ($y' \approx f \cdot \tan(w')$). Secondly the

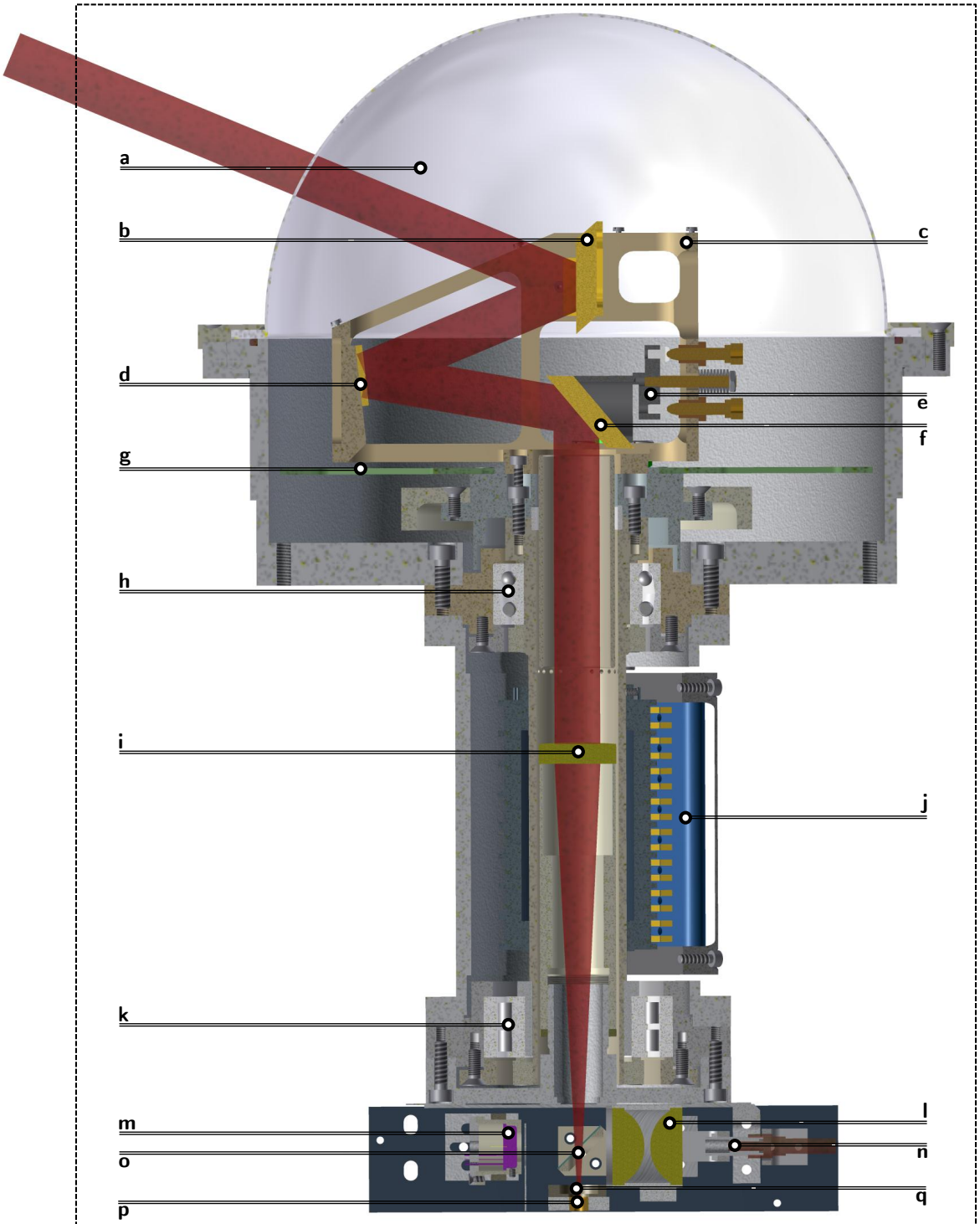

a	*acrylic dome*	**j**	*slip ring (16 contacts)*
b	*elevation mirror (primary mirror)*	**k**	*needle bearing*
c	*mirror system mounting*	**l**	*input optics for argon lamp*
d	*secondary mirror*	**m**	*quadrant diode*
e	*adjustable 3-point mounting*	**n**	*optical fibre conveying argon light*
f	*tertiary mirror*	**o**	*quartz plane plate (beam splitter)*
g	*rotating platform (azimuthal)*	**p**	*homogenizing fibre entrance*
h	*ball bearing*	**q**	*red filter*
i	*focussing achromatic lens*		

Figure 4.2: Vertical section of the SOLUSAR Smart Telescope

telescope dimensions are determined through its aperture which is somewhat larger than the spectrometer aperture ($f/10$).

The revolving platform (diameter: 20 cm) and the structure mounted thereupon holding the mirrors are lightweight and arranged as close to the rotation axis as possible to reduce the moment of inertia, thus helping to speed up the telescope movements when actively compensating for platform tilting (Fig. 4.3). Revolving platform and mirror mounting are both made of aluminium with extensive recesses to reduce weight. To achieve smooth and accurate control over position and acceleration/deceleration, DC-motors are chosen to conduct telescope movements. The azimuth rotation is performed by an eccentrically positioned DC-motor: The motor (Faulhaber 3257 012 CR) has an output power of nearly 80 W and a maximum engine speed of 5000 rpm. For position and velocity control an optical encoder (Faulhaber HEDM 5500 B) plat-
form is ieath
the rev

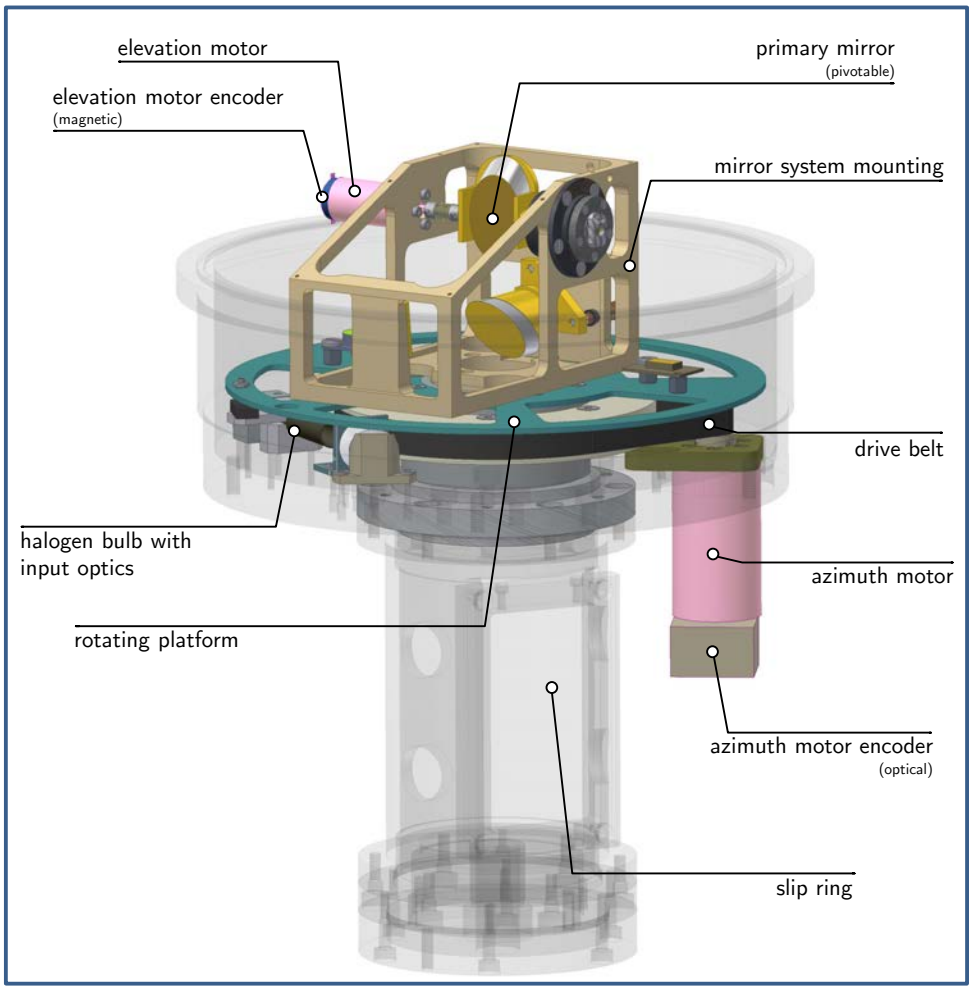

Figure 4.3: Electric and mechanical components involved in the process of telescope movement.

The elevation drive is mounted on-axis. A small DC-motor (Faulhaber 1516 E012 SR) is deployed with an output power of 1.95 W and a maximum engine speed of 12 000 rpm. Preloaded is a low-backlash spur gear with a transmission ration of 76:1 (Faulhaber 15/8-76:1). The near-zero backlash is important as directional changes often occur when the telescope compensates for oscillations of the instrument-bearing platform. For position feedback a magnetic encoder

with a 512 steps/rev resolution is used. With the described encoder/gear set-ups and the micro-stepping capabilities of the motion control card (see Section 4.10.2) pointing accuracies of 32″ for azimuth angles and 17″ for elevation angles can be achieved assuming zero-backlash gears. For smooth rotation of both axes maintenance-free ball and needle bearings are used. The associated steering electronics and the applied algorithms for target tracking are outlined in Sections 4.10.2 and 5.1, respectively.

The telescope includes various additional electronic components: A halogen lamp with the associated collimation optics (see Section 4.8.1), a solid-state temperature sensor, optionally an electronic compass (see Section 5.1.1), a position sensor serving as azimuthal reference point and a line driver. The differential line driver together with the associated line receiver (National Semiconductor DS26C31TM/DS26C32TM) ensures the faultless transmittance of high-frequency signals of the elevation motor encoder even under the influence of strong electromagnetic disturbances.

Several of the aforementioned components are placed on the rotating platform. To allow telescope movements without restrictions from cables, a 16-channel slip ring (LTN Servotechnik SM050-16) is installed underneath the platform wrapping the vertical tube guiding the light to the spectrometer. The slip ring's gold/gold contacts are vertically arranged and allow conducting of maximum 3 A at 48 V. The channels are used to make available:

- Elevation motor PWM signals,
- Elevation motor encoder signals,
- Voltage supply (5 V, 12 V) for the various electronic elements,
- (RS232 connection for compass operation).

The telescope is stored in a massive aluminium encasement and sheltered by a hemispherical acrylic dome for full view of the sky hemisphere. The acrylic dome exhibits transmission ratios of above 90 % for wavelength around 800 nm.

4.4 Spectrometer Unit - Fundamentals

Generally in the field of spectroscopy the wavelength-dependent intensity distribution of polychromatic electro-magnetic radiation is analysed. As the spectral composition can be characteristically altered when light interacts with matter of a specific form, consequent analysis of the spectrum can provide insights into the composition and state of the matter involved in the process. This principle proofs to be a viable solution for countless tasks dealing with the determination of physical and chemical properties or monitoring of physical and chemical processes. As for example the task at hand: the monitoring of atmospheric water vapour mixing ratios which has been explained in Chapter 3.

The primary part of every optical spectroscopic apparatus is at least one diffraction element separating the polychromatic light into its monochromatic components [Palmer and Loewen, 2005]. Various optical elements can be used for the task, e.g. prisms, Fabry-Pérot etalons and most often *diffraction gratings*. Palmer and Loewen [2005] describe the classical diffraction grating as "a collection of reflecting (or transmitting) elements separated by a distance comparable to the wavelength of light under study", whose main characteristic is the spatial modulation of the refractive index. "Upon diffraction, an electromagnetic wave incident on a grating will have its electric field amplitude, or phase, or both, modified in a predictable manner".

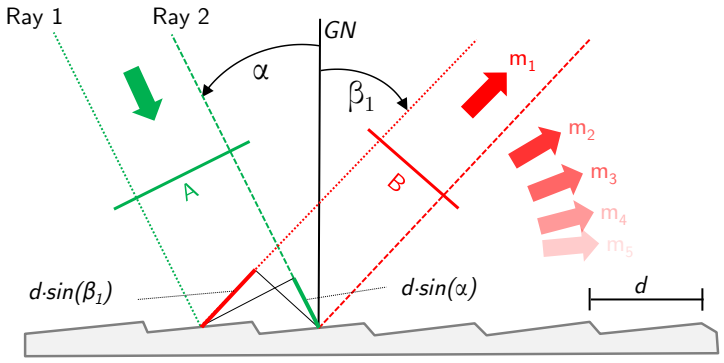

Figure 4.4: Principle of a reflection grating with incident monochromatic light (A) and exiting radiation (B) using planar wavefront representation. Light with incidence angle α (with respect to the grating normal GN) is diffracted at the grooves (perpendicular to the page) and constructively interferes in certain directions β_m thus building different diffraction orders D_m (based on Palmer and Loewen [2005]).

As shown in Fig. 4.4 monochromatic light with an angle of incidence α (with respect to the grating normal) falls onto the grating and is dispersed at each of the small structures on the grating. At certain angles β_m the diffracted light from different facets constructively interferes. For any grating with a groove spacing d, the general *grating equation* describes the relation between the angles α, β_m, the wavelength λ and the diffraction order number, denoted by the letter m:

$$m \cdot \lambda = d \cdot (\sin \alpha + \sin \beta_m). \tag{4.1}$$

4.4.1 Echelle Spectrometer

To satisfy the need for high values of linear dispersion and spectral resolution while keeping the focal length and thus the instrument reasonably small, the application of *echelle diffraction gratings* is often favourable. Echelle gratings, a special class of reflection gratings formed by a sequence of steps, have lower groove densities G (i.e. grooves per millimetre). The groove spacing amounts to a multitude of wavelengths of the analysed radiation. Unlike conventional *echelette gratings* (see Fig. 4.4) the shorter groove facet points in the direction of the incident and reflected light (see Fig. 4.5) and radiation is dispersed in a multitude of diffraction orders which can number in the hundreds. Within a narrow angular range near the so-called *blaze angle* Θ_B high diffraction effectiveness is reached in all diffraction orders. Typical blaze angles lay between 45° (stepping ratio 1:1) and 76° (1:4).

For the operation of an echelle grating in *Littrow-mode*, meaning near auto-collimation ($\alpha \approx \beta \approx \Theta_B$), Eq. 4.1 becomes approximately:

$$m \cdot \lambda \approx 2 \cdot \ d \cdot \sin(\Theta_B). \tag{4.2}$$

The differentiation of Eq. 4.1 for a constant angle of incidence α yields the angular dispersion D, an important measure for the characterization of the dispersive power of an optical

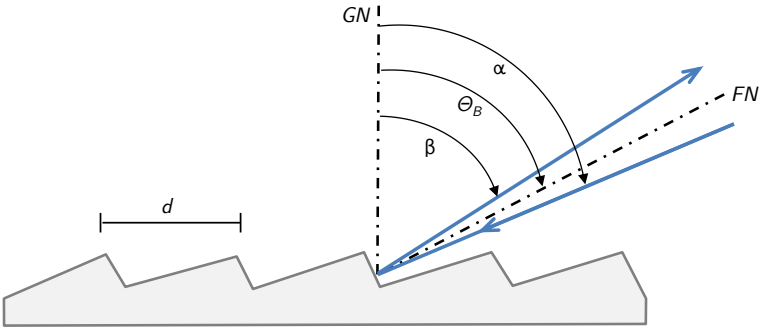

Figure 4.5: Illumination of an echelle grating. The grating is characterized by the groove spacing d and the blaze angle Θ_B (angle between grating normal GN and short facet Normal FN). The short facet of the grating is illuminated with an incidence angle α close to Θ_B. The case where $\alpha \approx \beta$ is called Littrow configuration.

disperser:

$$D = \frac{d\beta}{d\lambda} = \frac{m}{d \cdot \cos\beta} \approx \frac{2 \cdot \tan\Theta_B}{\lambda}. \tag{4.3}$$

To show the superior dispersion power of an echelle grating compared to a conventional grating a look at the relative angular dispersion D_{rel} helps:

$$D_{rel} = \frac{d\beta}{d\lambda_{rel}} = 2\tan\Theta_B \quad \text{with} \quad d\lambda_{rel} = \frac{d\lambda}{\lambda}. \tag{4.4}$$

Through the constantly large diffraction angle, the angular dispersion of echelle gratings is up to one order of magnitude larger than for classical gratings. Fig. 4.6 shows a comparison of the relative angular dispersion of echelle gratings (in auto-collimation) with different blaze angles compared to plane gratings in Czerny-Turner mounting ($\alpha - \beta = 30°$) with different grating constants with respect to the wavelength. D_{rel} for an echelle grating is wavelength-invariant and generally higher than for conventional plane gratings. The difference between the grating classes becomes especially large at lower wavelengths. For echelle gratings with a blaze angle of 78.7° the relative angular dispersion becomes 10!

The previously mentioned linear dispersion L of a spectroscopic instrument is defined as:

$$L = f(\beta) \cdot D \tag{4.5}$$

with $f(\beta)$ being the effective focal length for a specific diffraction angle (again depending on wavelength). The linear dispersion describes the ability of a diffraction element-camera-system to image different wavelengths onto different positions in the image plane.

The diffraction-limited spectral resolving power $\frac{\lambda}{d\lambda}$ of every diffraction grating is the product of the diffraction order m and the number of illuminated grooves N. With the width B of the bundle of rays, the approximate resolving power R can be expressed as:

$$R = \frac{\lambda}{d\lambda} = m \cdot N = \frac{2 \cdot B \cdot \tan\Theta_B}{\lambda} \tag{4.6}$$

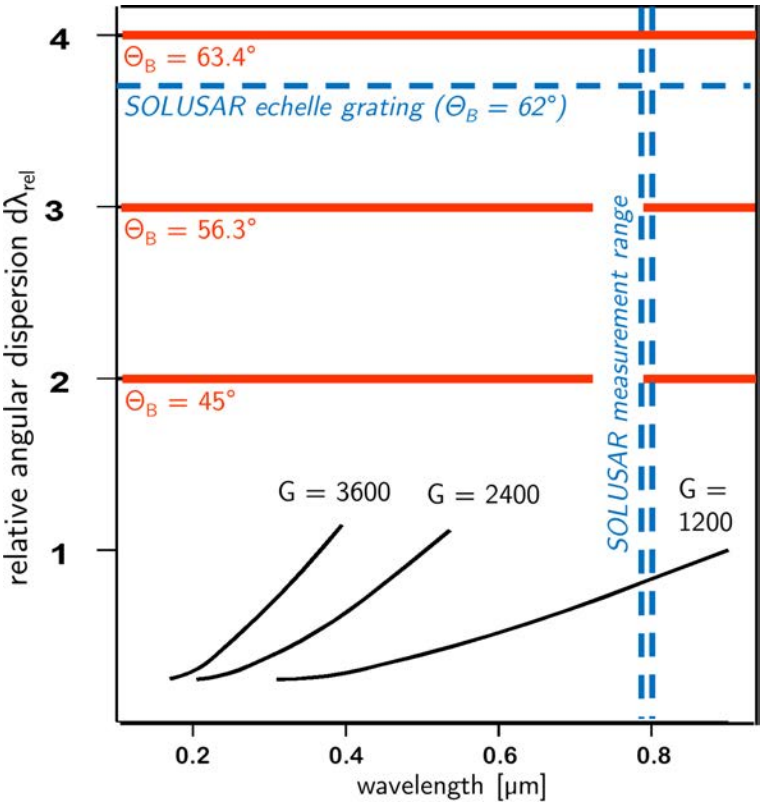

Figure 4.6: The relative angular dispersion for echelle gratings with different blaze angles (Θ_B) is shown in red and for plane gratings (Czerny-Turner mounting) with different grating constants G in black. Also depicted are the primary wavelength region of the SOLUSAR instruments around 800 nm and the relative angular dispersion of the applied echelle grating (adapted from Becker-Roß and Florek [1997]).

Hence both the resolving power and the linear dispersion become larger for higher blaze angles and increase with diminishing wavelengths, which are diffracted into higher diffraction orders.

"The range of wavelengths in a given spectral order for which superposition of light from adjacent orders does not occur is called the free spectral range" [Palmer and Loewen, 2005]. As shown in Fig. 4.7 within the free spectral ranges FSR all wavelengths appear near the blaze-maximum and show highest diffraction effectiveness. FSR increases proportional to λ^2:

$$FSR = \frac{\lambda}{m} = \frac{\lambda^2}{2 \cdot d \cdot \sin \Theta_B}. \tag{4.7}$$

A characteristic feature of every echelle spectrometer is the need for a so-called order-sorter or cross-dispersion element, as the diffraction orders produced by the echelle grating are altogether overlapped and have to be separated optically. Prisms, transmission gratings or echelette gratings with low dispersion can be used as cross-dispersion elements, diffracting transversely to the main diffraction element. The internal separation with the combination of the two elements yields a 2-dimensional multiple order structure (see Figs. 4.7 and 4.8). Thus, using 2-dimensional semiconductor detectors, highly-resolved broadband spectra can be acquired simultaneously with great sensitivity. For echelle monochromators the bandwidth can be limited externally to a single diffraction order, e.g. through spectral filters [Sierk, 2001] or a pre-monochromator [Florek and Becker-Roß, 1995].

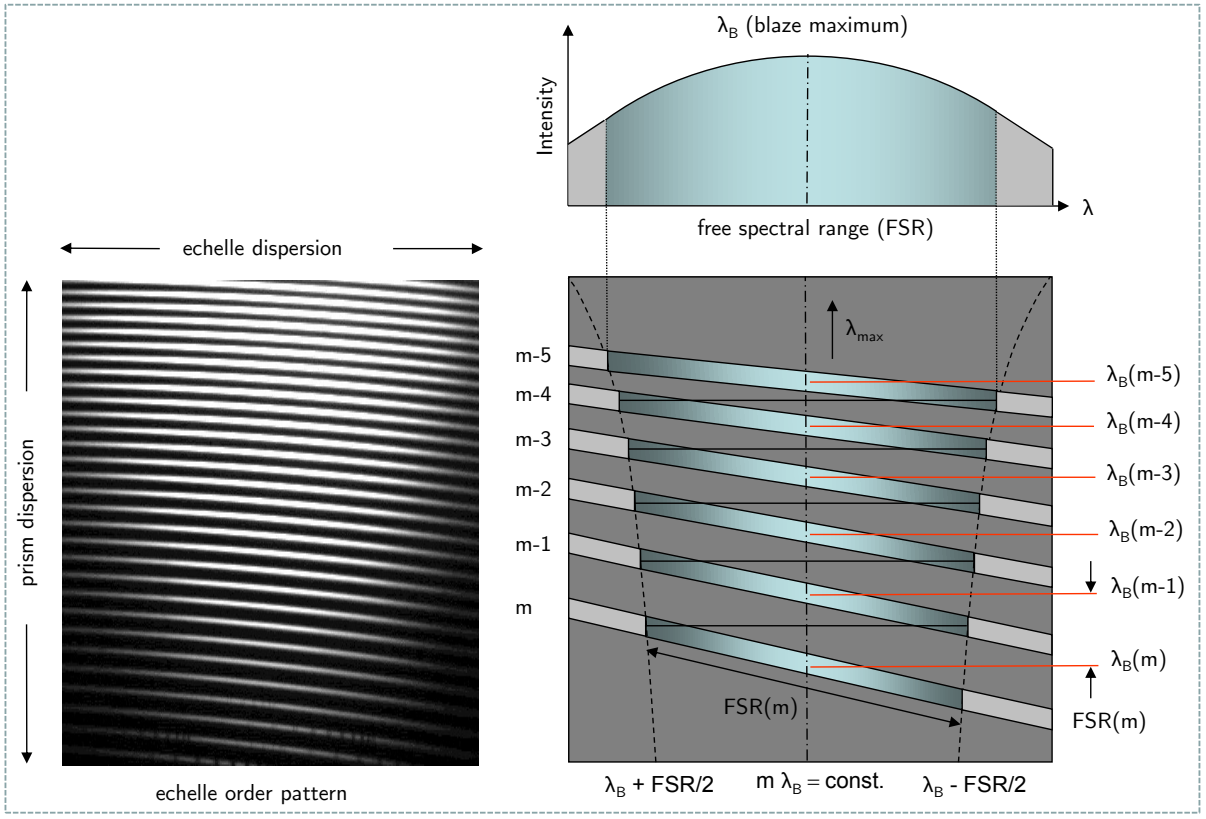

Figure 4.7: The combination of an echelle grating and a prism yields a 2-dimensional pattern of bent diffraction orders (left side, measured spectrum). In each diffraction order m an intensity crest (blaze maximum) occurs at wavelength λ_B with diffraction angles at Θ_B. The free spectral range FSR denotes the order-dependent spectral range where every wavelength appears with the highest diffraction effectiveness (right side, schematic depiction).

The deployment of echelle gratings allows the construction of high-resolution spectrographs with short focal length of the optics and relatively wide entrance slits. Unfavourable are the need for a second disperser element and the greater space requirements of the grating due to the large blaze angles. When choosing an appropriate grating, one defines the angular dispersion with the blaze angle, whereas the grating constant determines the number of diffraction orders and the free spectral range.

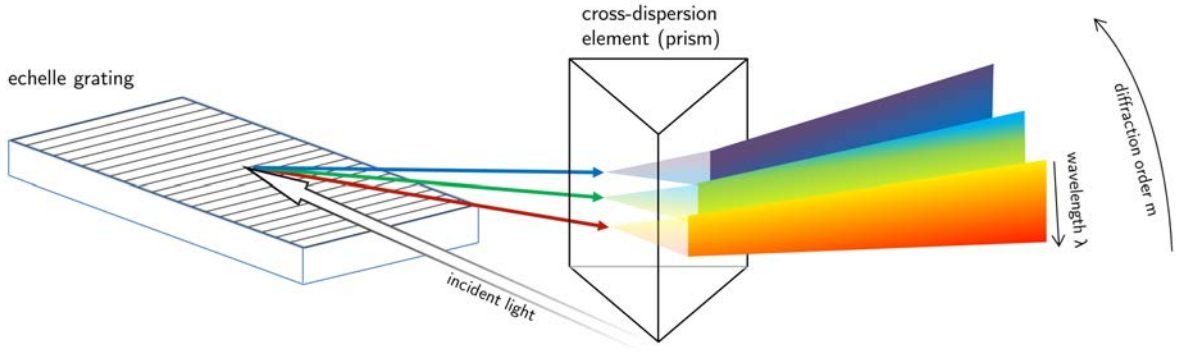

Figure 4.8: Generation of a two-dimensional diffraction order structure using an echelle grating and a prism to separate the overlapped echelle-generated diffraction orders.

4.5 SOLUSAR Spectrometer

4.5.1 Mounting of Plane Gratings

As shown in Fig. 4.5, echelle gratings are illuminated by a parallel ray bundle with a fixed angle of incidence, as every other planar diffraction grating. For each wavelength a parallel ray bundle is leaving the grating after diffraction with a dedicated angle. To produce a monochromatic image of the entrance slit in the spectrometer's focal plane both, collimation optics to generate a parallel bundle as well as camera optics for the subsequent imaging onto the detector are needed. Different spectrometer mountings are distinguished based on the type of optical imaging components and their spatial configuration. In the most noted configuration – called *Czerny-Turner* – spherical concave mirrors are used both for collimation and camera optics. The focal lengths and deflection angles of the two mirrors are individually optimized with the objective of minimal aberration in the spectrometer's focal plane. Resembling plane grating mountings are also applying parabolic mirrors or achromatic lens optics for the ray bundle imaging.

In case of minimal deflection angles between the incident and diffracted ray bundles the same imaging optics can act both as collimator and camera and is therefore travelled through twice by the radiation: On the way from the entrance slit to a planar dispersing element and on the way back in the direction of the detector. Said optical auto-collimation configuration for plane gratings and prism spectrographs was first described by Otto von Littrow and successfully applied for various instruments [Harrison et al., 1948; Sawyer, 1951]. Formerly a substantial drawback of this concept was the false light reflected by the lens optics in the direction of the detector. Nowadays this problem can be effectively tackled either through high-performance anti-reflection coatings on aberration corrected achromatic lenses or through application of paraboloid mirrors with minimal surface coarseness and high reflectivity reaching into the UV.

Today the Littrow configuration is especially suited for the optical design of highly compact spectrographs. Due to its outstanding imaging quality and narrow, elongated architecture it has also been chosen as template for the SOLUSAR spectrometer design. Therefore the entirety of the assembly consisting of telescope, spectrometer and detector together with the adjoined mechanical and electronic modules can be mounted along a unified optical axis and thus conveniently stored inside a cylindrical protective tubing (see Fig. 4.9).

4.5.2 Echelle Grating Dimensioning

The starting point regarding the dimensioning of the SOLUSAR spectrograph was the objective to achieve a pixel-related bandwidth of about 7 pm/per px needed for the sufficient resolution of absorption structures. This task had to be fulfilled on the basis of the optical, mechanical and electronic components available on the market, namely scientific camera systems, diffraction gratings and prism materials.

Based on the decision to apply the CCD detector described in detail in Section 4.6.3, it directly follows that the linear dispersion which has to be produced by the spectrograph is $L = \frac{\mathrm{d}l}{\mathrm{d}\lambda} = 1.64\,\mathrm{mm/nm}$. Eq. 4.3 given above shows that the demanded angular dispersion of a diffraction at moderate focal lengths can only be achieved through application of a grating with a diffraction angle above 60°. Conventional echelette gratings in low diffraction order numbers cannot diffract into such high angles even for radiation with lower wavelengths. Solely echelle gratings are able to achieve diffraction efficiencies around 60 % over a multitude of orders and over extensive spectrum segments.

The leading manufacturer *RGL (Newport)* provides a series of high-end echelle gratings with blaze angles of around 63° which corresponds to a stepping ratio of 2:1. Gratings with a multitude of different grating constants between 23 g/mm to 316 g/mm (g denoting the number of grooves) are available for divided surfaces of up to 200 mm times 400 mm. In case of SOLUSAR the grating *408E* by RGL with a groove density of 79 g/mm and a blaze angle of 62° has been selected. With the equations in Section 4.4.1 this yields the diffraction order $m = 28$ and a free spectral range of about 30 nm for the SOLUSAR measurement range. The primarily addressed 12 nm broad wavelength range around the central wavelength of 795 nm for these gratings lays in the range with the highest diffraction efficiency (blaze maximum). With the high angular dispersion of the grating the demanded linear dispersion can already be achieved with a focal length of 400 mm.

For said focal length *Thorlabs (USA)* offers an achromatic doublet (*AC508-400-B*) with a good surface quality which produces low stray light amounts and disposes of an anti-reflection coating for radiation between 650 nm and 1050 nm. Consisting of two lenses of different materials (N-LAK22/N and N-SF6HT) and radii of curvature this doublet produces minimal aberrations over a relatively widespread image field and can thus be applied as focus lens in a Littrow system. In contrast to the application of mirror optics, a considerably slimmer architecture can be reached with the application of the transmission optics described above.

4.5.3 Internal Cross Dispersion

As described above the diffraction of an echelle grating leads to an overlap of the free spectral ranges of the individual diffraction orders in narrow angular interval. In a Littrow spectrograph using lens optics the diffraction order separation can either be conducted using transmission

gratings or prisms with double radiation passage. Especially for longer wavelengths transmission gratings produce a high dispersion. For this reason special NIR transmission gratings by *Thorlabs* have been tested as order-sorter elements in the SOLUSAR development. Unfortunately said gratings exhibited strong stray light and the diffraction efficiency of maximum 60 % with the double passage lead to a considerable energy loss. Further experiments with new holographically manufactured phase gratings could not be effectuated for lack of time. Therefore a dispersion prism made from heavy flint glass (SF10) with a high refraction index in the NIR and high transmission is applied. The inclusion of a folding plane mirror between prism and echelle grating allows the arrangement of all optical components along one axis despite the strong ray deflection by the prism. The folding mirror can be tilted in two directions thus allowing the spatial stabilization of the spectrum on the detector (see Fig. 4.14).

4.5.4 Ray Tracing

The optical design of SOLUSAR's Littrow spectrograph was optimized with the help of the ray tracing software package *ZEMAX* regarding the different spectroscopic target values namely the spectral resolution, echelle dispersion, pixel-related bandwidth, cross dispersion, aperture, throughput, as well as the various mechanical constraints as overall size, detector dimensions and the assembly and adjustment tolerances. Figs. 4.10 and 4.11 show the resulting configuration of the optical spectrometer components as shaded model and as 2D layout, respectively. For the construction of the mechanical layout the data of the ray paths and optical component dimensions were directly transferred to the CAD software.

The passage of the ray bundles under different angles of incidence with respect to the prism's principle plane on the way from the grating to the detector inevitably leads to a bending of the spectra along the diffraction orders. The detector is sufficiently high to fully collect the spectral data even when applying a 1 mm tall entrance slit. Fig. 4.12 shows the imaging of different wavelengths belonging to the primary SOLUSAR measurement window (either water vapour absorption lines or argon emission lines) and the bending of the diffraction orders. Also wavelengths belonging to the neighbouring orders are depicted. The prism dispersion is dimensioned in a way that these neighbouring orders appear mostly outside the detector area. These orders could be moved into the measurement range by tilting the adjustment mirror if desired. Fig. 4.13 gives account on the theoretical imaging quality of SOLUSAR. The image size of the single spots (belonging to the entrance slit mask) is considerably smaller than the airy disk in the center of the image which describes the theoretical limit of the imaging quality.

4.6 Detector

The development of new spectroscopic instruments is to a large degree driven by the vast improvements achieved in the field of detector technology. Since the introduction of solid-state array detectors, merging the advantages of the previously used photographic plates and photo-multiplier tubes (PMT) [Welz et al., 2005], a large set of different detector technologies has emerged like charge-coupled devices (CCD), photodiode arrays (PDA), CMOS-based image sensors or charge injection devices (CID) to name a few. Despite the considerable differences in technology and detector parameters they unanimously share the extremely high geometrical accuracy and photometric performance.

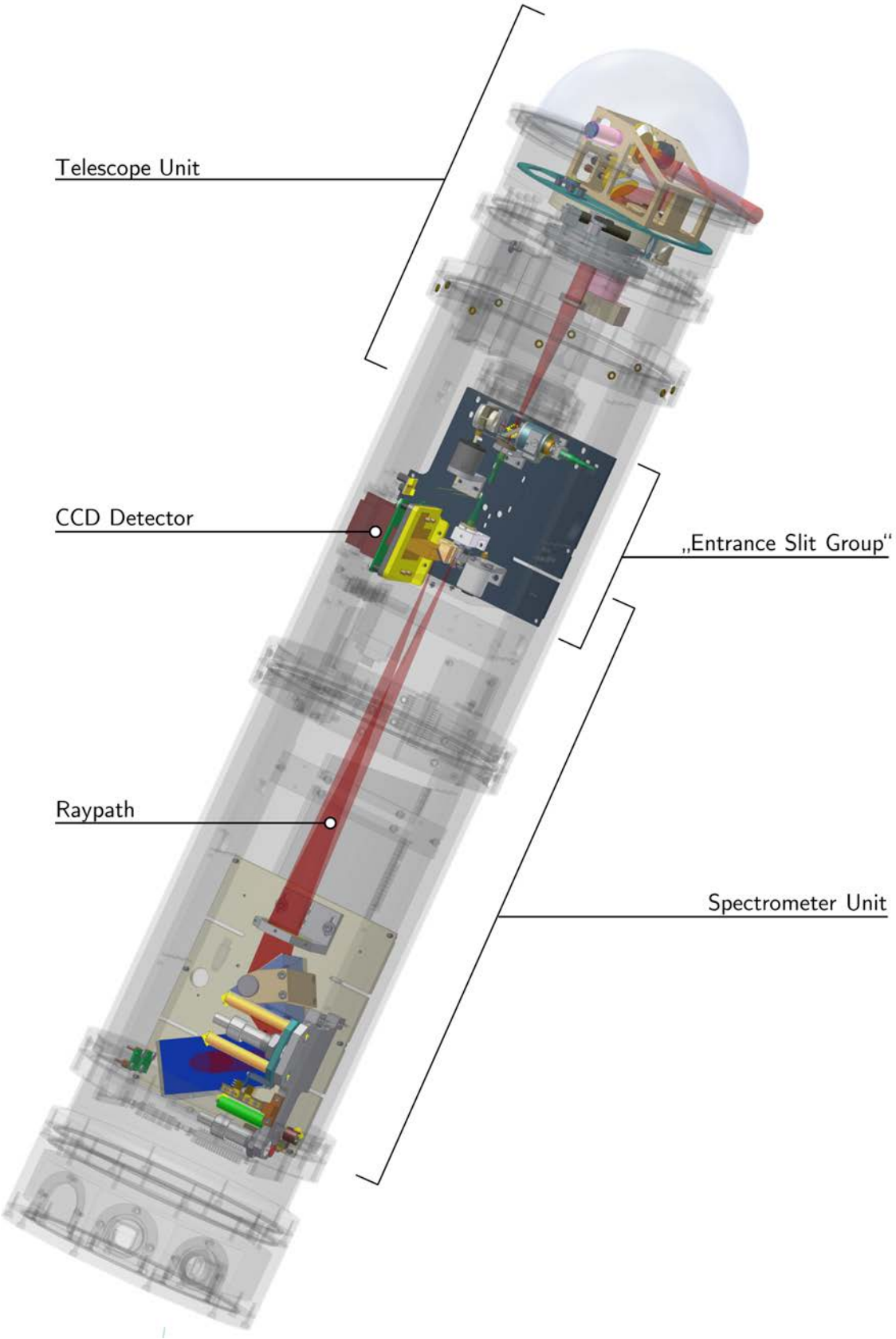

Figure 4.9: Overview on the optical layout of SOLUSAR

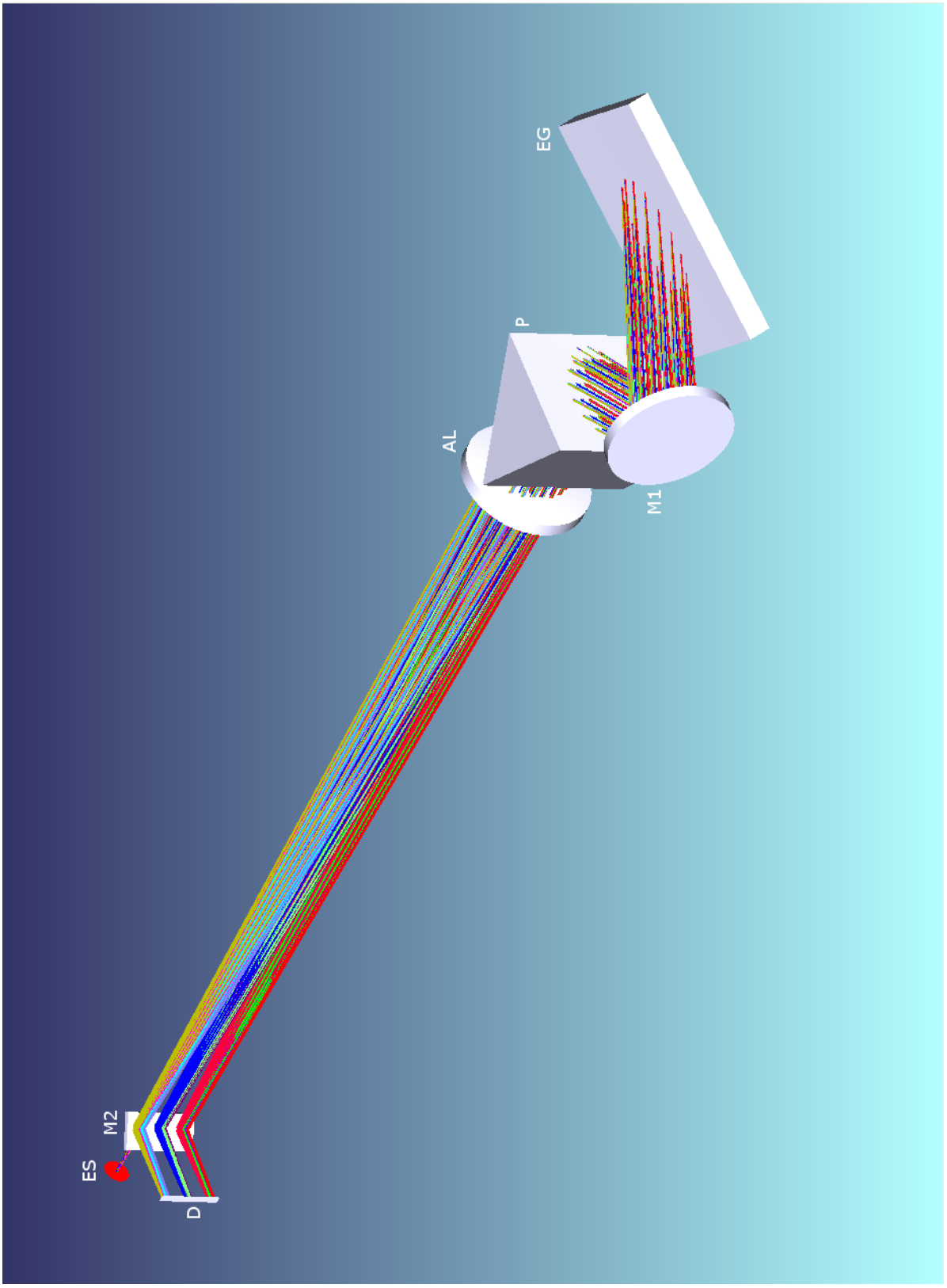

Figure 4.10: Optical setup of the SOLUSAR spectrometer (Littrow configuration): Coming from the entrance slit (ES), the light is collimated by an achromatic lens (AL) and is then sequentially diffracted by a prism (P) and the echelle grating (EG) and on the reverse path again by the prism. Finally the generated spectrum is imaged onto the detector (D). The ray path is folded by the two planar mirrors (M_1 and M_2). Depicted are the ray paths for the same wavelengths of diffraction order 28 as listed in Fig. 4.12.

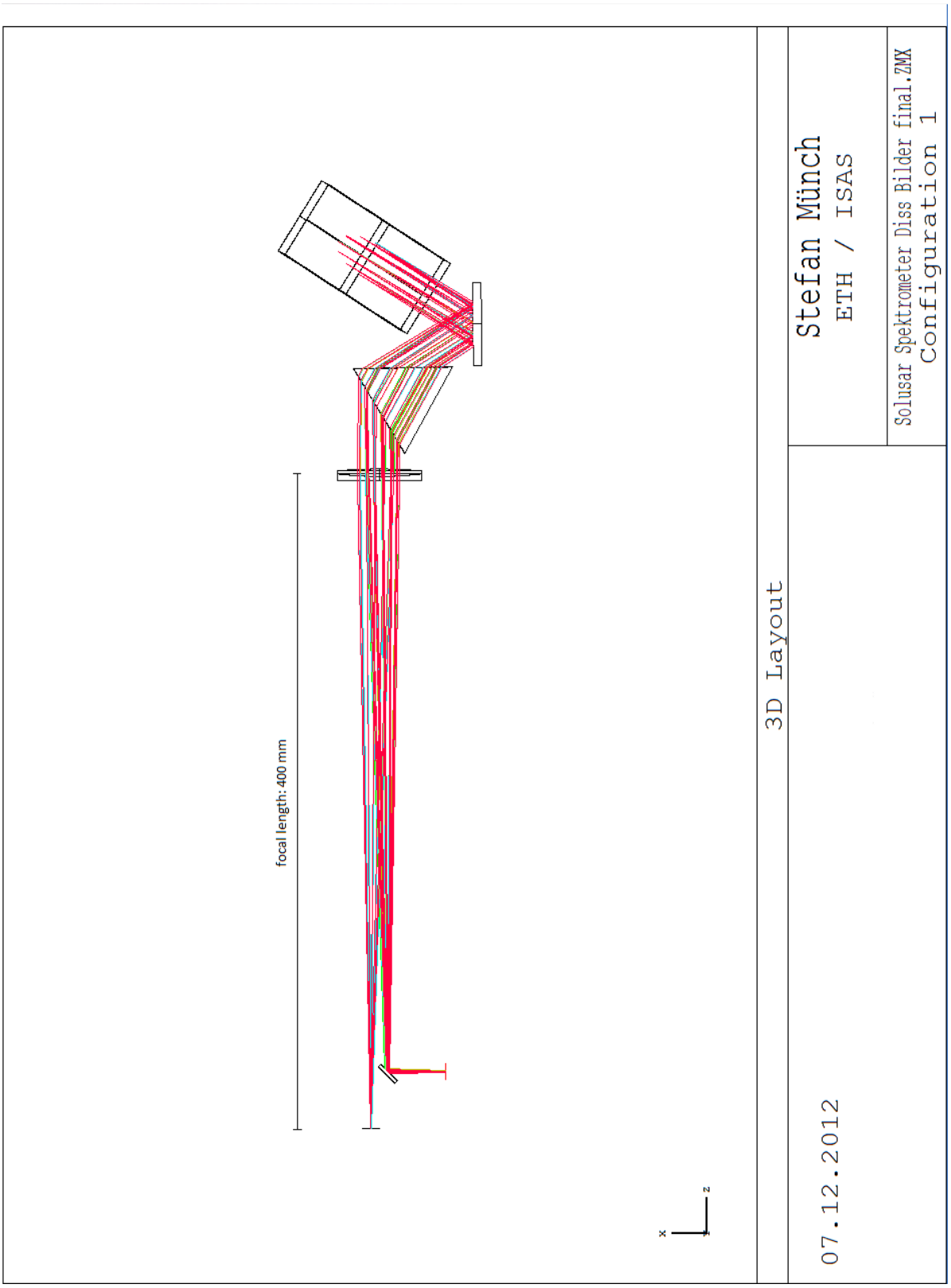

Figure 4.11: True-to-scale image of the SOLUSAR spectrometer setup.

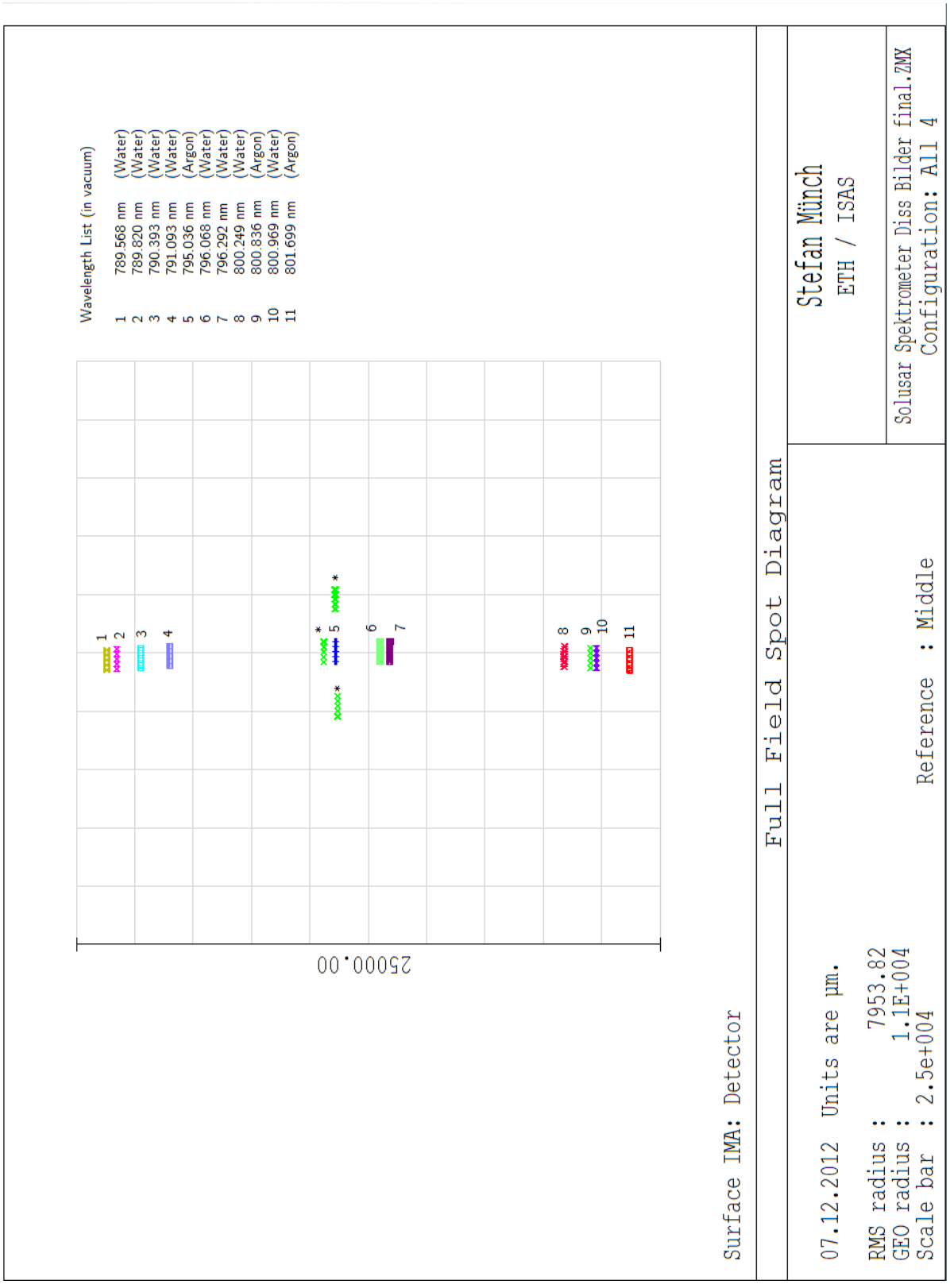

Figure 4.12: Computed spot diagram of eleven wavelengths, within the primary SOLUSAR measurement range, belonging either to strong argon emission or water vapour absorption lines. The entrance slit height is 1 mm. The diffraction order shows the characteristic bending due to the prism influence. The depicted lines denoted with a (∗) are virtual wavelengths to illustrate the gap between neighbouring diffraction orders.

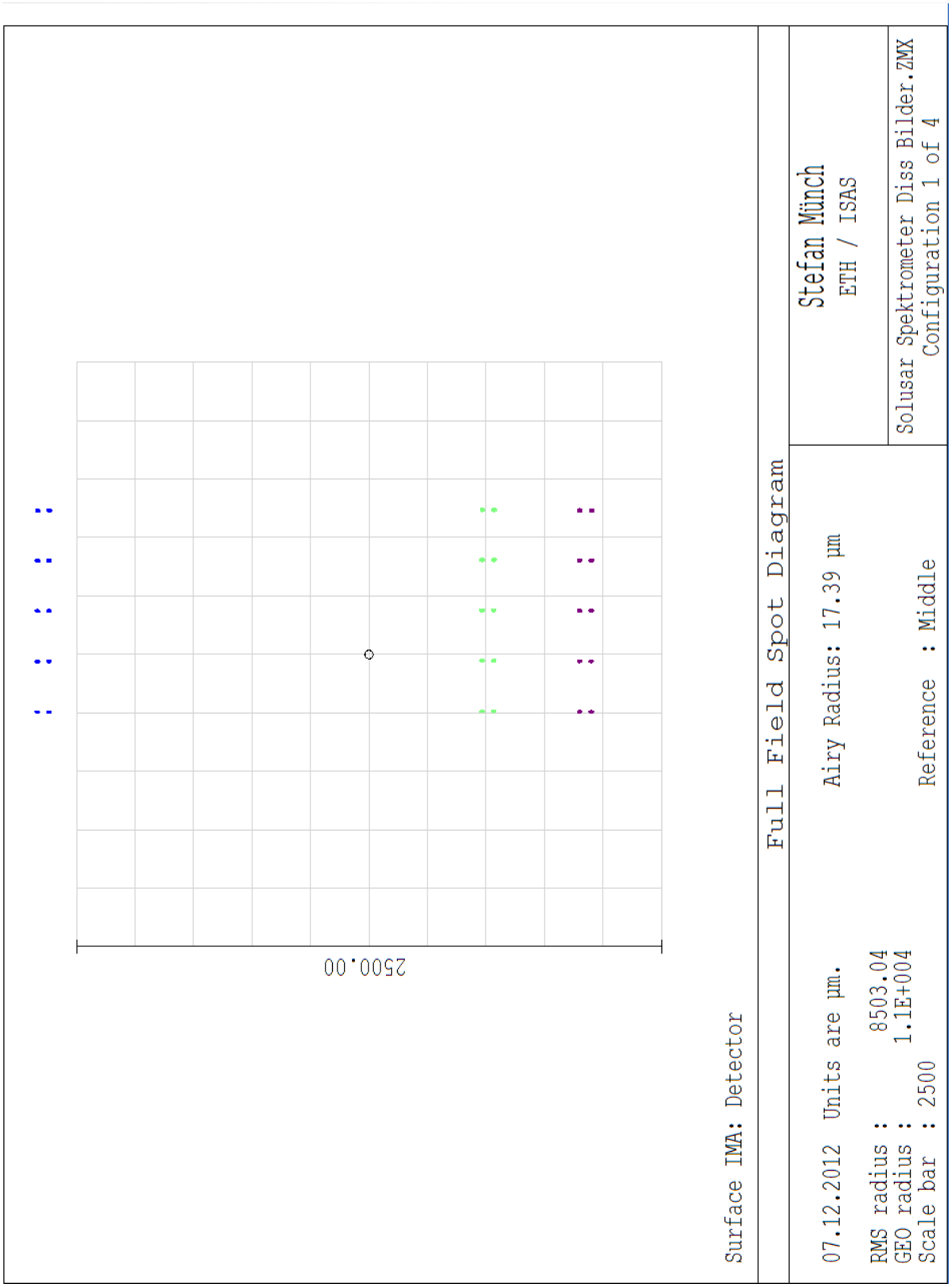

Figure 4.13: Computed image of the entrance slit (height: 1 mm, width: 50 µm) on the CCD sensor at three different wavelengths. The entrance slit is denoted by ten points belonging to the slit mask. Each spot is considerably smaller than the airy disk in the center of the image, describing the diffraction limited resolution of the optical system.

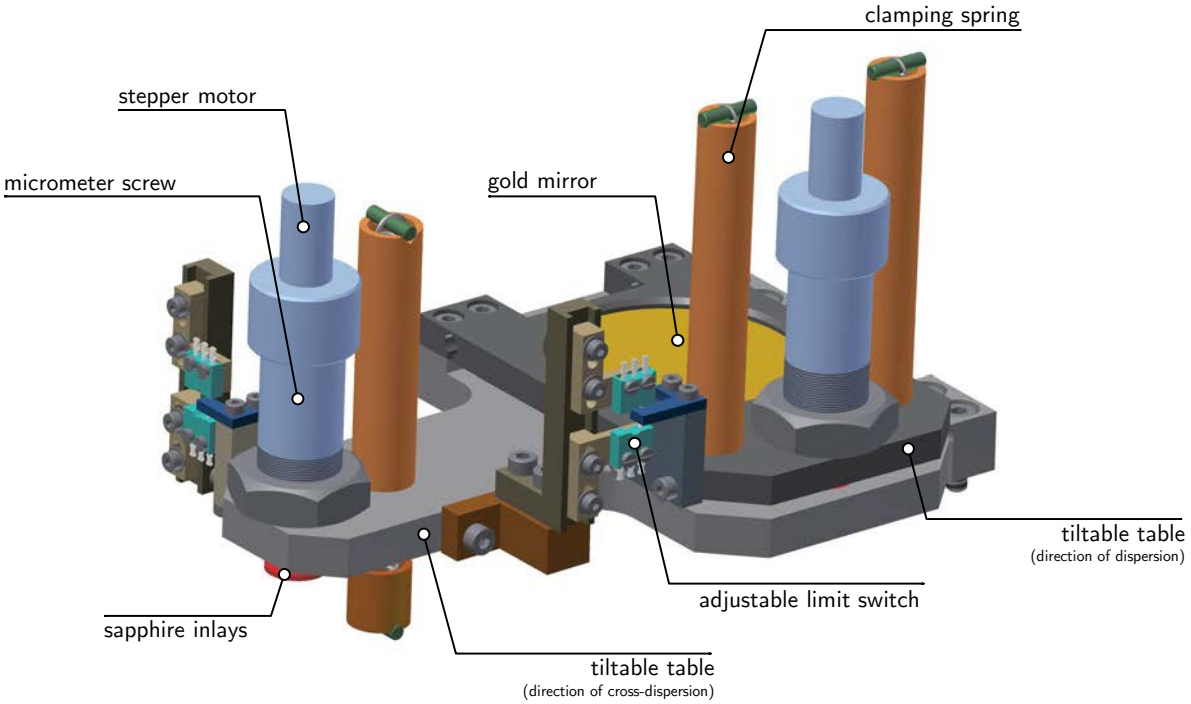

Figure 4.14: The spectrometer's deflection mirror is mounted on two stacked tiltable platforms together allowing 2-dimensional shifts of the spectrum image on the CCD sensor. As the tilting is controlled by two micrometer screws powered by stepper motors, spectrum positioning with an accuracy of below 0.1 pixel is achievable.

4.6.1 SOLUSAR Detector Requirements

During the selection of an appropriate detector for the SOLUSAR measurement system various detector parameters had to be validated. The most demanding requirements are set by the intention to acquire lunar spectra:

- *Sensitivity:* The acquisition of spectra with sufficient signal strength under low-light conditions requires a high detector quantum efficiency (QE).
- *Chip size:* The dimensions of the photo-active detector plane must allow the simultaneous acquisition of that diffraction order section bearing the aimed spectral range with a substantial entrance slit height. Additionally visibility of some free space between orders is desirable for stray light determination purposes.
- *Readout Speed:* High-frequency readout of the detector should allow rapid acquisition of a large number of spectra and thus an improved S/N-ratio.
- *Noise susceptibility:* Low-light measurements should not be too heavily compromised by readout noise and dark current influence.
- *System Integration:* Detector head and controller unit must fit into an instrument where room is sparse. Low heat dissipation, easy interfacing and programmability are desirable as well.
- *Acceptable costs*

Some of the above mentioned objectives are indeed subject to trade-offs, as e.g. detector size and readout speed. The detector best fulfilling the demands at the time of selection was a

back-thinned CCD sensor *Hamamatsu C9260-933-17*, described in detail in Section 4.6.3. In the subsequent section the underlying technological principles are shortly outlined.

4.6.2 Charge Coupled Device (CCD)

CCD detectors are among the most common digital imaging devices nowadays, applied in countless cases ranging from consumer articles (e.g. digital cameras, cellphones) over industrial processes to untold scientific applications. CCDs have proven to be especially suited for numerous analytical applications such as spectroscopy, microscopy, x-ray imaging and many more [Denton et al., 1996]. Advantageous are the broad detectable wavelength range (NIR to soft x-ray), the linearity of the generated signal strength with respect to the incident radiation intensity of a certain wavelength, high quantum efficiency, low charge transfer losses [Becker-Roß and Florek, 1997], low read noise, durability and affordability.

Generally CCDs can be described as arrays of MOSFET-like capacitors which together form a photosensitive plane. As shown in Fig. 4.15(a) the detector consists of various doped semiconductor layers (mostly bromide-doped silicon) coated with an insulating transparent layer (silicon oxide) on which structures of transparent electrodes are located. The arrangement of these so-called gates forming a pixel define the spatial resolution of a CCD detector. The edge length of a pixel usually amounts from about one to several microns.

As a photon reaches the detector it traverses the top layers and enters the silicon bulk. If the photon energy exceeds the so-called band gap of the semiconductor, electrons are lifted from the valence band to the conduction band through generation of electron-hole pairs (inner photoelectric effect). Voltages are applied to the detector to enforce the holes to run off deeper into the substrate whereas the electrons are driven to the surface. As shown in 4.15(a) the electrons gather in potential wells underneath the electrodes. Once the light exposure is finished the charge transfer from one capacitor to its neighbouring capacitor is initiated (through a particular gate voltage regimen) until the charge reaches the so-called shift register, from which the charge portions are guided line-by-line, pixel-per-pixel to a signal amplifier and subsequently A/D converted thus producing a 2-dimensional image of the spatial irradiation intensity distribution incident on the detector during the time of exposure.

According to Sweedler et al. [1994] "the quantum efficiency (QE) of the device depends on the number of photons that are absorbed in the silicon with sufficient energy to produce a photoelectron". For an improved S/N-ratio high QE values are desirable. The quantum efficiency is heavily depending on the photon energy (i.e. wavelength). Silicon shows considerable reflectivity depressing the QE, especially for shorter wavelengths. The effect can be reduced using anti-reflective detector coatings. Furthermore the polysilicon gate structures are photon absorbing, thus reducing QE, especially in the UV, where it drops to zero for wavelength shorter than 400 nm for non-coated sensors [Sweedler et al., 1994].

One approach often applied in the scientific scope to improve QE [Holst, 1998] is the use of backside-illuminated CCDs, where photons are directly incident on the thinned backside of the sensor, where no absorbing gate structures are present (Figs. 4.15(b) and 4.15(c)). The thinning process leaves a silicon membrane with a thickness of only 15 µm to 30 µm. The improvement in QE over a broad spectral range is shown in Fig. 4.15(d). Possible disadvantages of this technique lie in the increased fragility and cost of production, a possible moderate rise of dark current and in the number of defect pixels. Furthermore so-called *etaloning* (parasitic intensity structures) can occur when measuring NIR intensities, an effect which is further outlined in Sections 4.6.4 and 4.9.

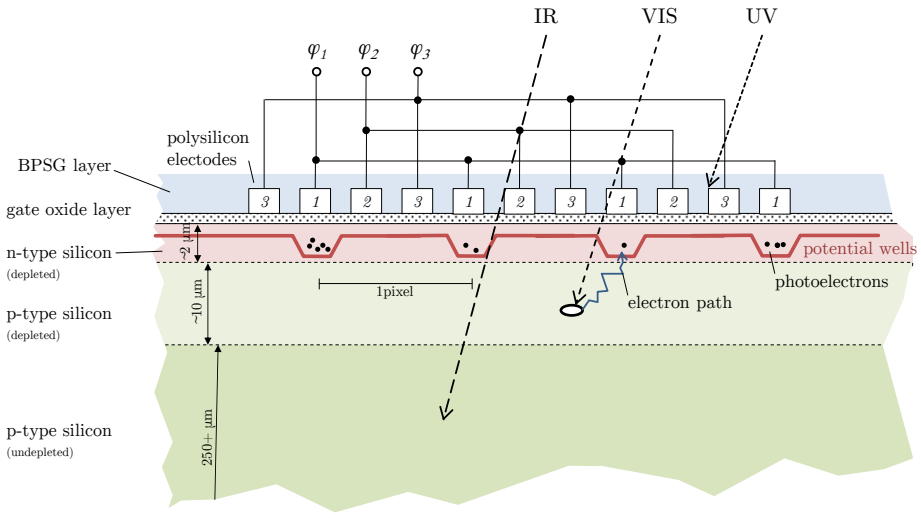

(a) Cross section of a conventional front-illuminated CCD. Incident photons induce electron-hole generation in the silicon substrate, with electrons moving toward the gates, where they gather in potential wells, which are shaped by the applied voltages at the gates (ϕ_1, ϕ_2, ϕ_3). The accumulated charge is a measure for the local signal strength of the incident radiation (adapted from Bradt [2004]).

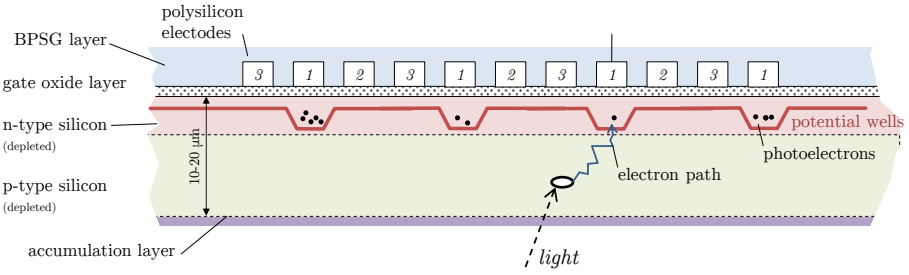

(b) Cross section of a back-thinned CCD: The sensor is illuminated from the rear thus preventing photon absorbtion by gate structures. The silicon bulk is thinned and overlayed by an accumulation layer to supress reflection.

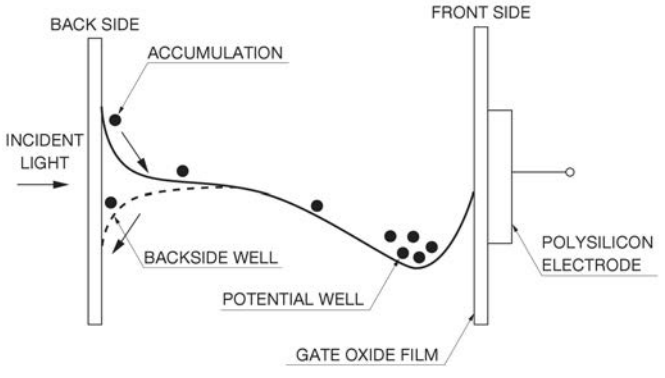

(c) Scheme of the internal potential of a back-thinned CCD [Hamamatsu, 2007].

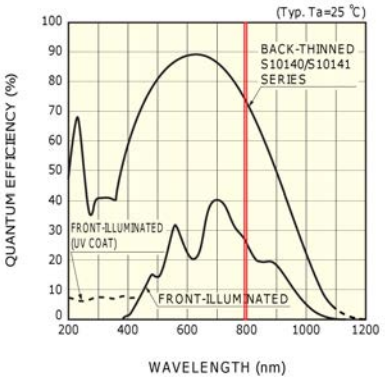

(d) QE-curve of a typical front-illuminated CCD and the back-thinned sensor used with SOLUSAR [Hamamatsu, 2007]. (red: SOLUSAR λ-range)

Figure 4.15: Principle of charged-coupled devices (CCD).

4.6.3 SOLUSAR Detector

The found detector system, best fulfilling the requirements described in Section 4.6.1, is an OEM CCD Board Camera Hamamatsu C9260-933-17 working with a back-thinned Hamamatsu sensor S10141-1108. The exact device specifications are outlined in Tab. 4.1. As shown in Fig. 4.15(d) the back-thinning leads to a quantum efficiency of about 70 % at wavelengths around 800 nm which far exceeds the QE of a front-illuminated CCD (about 25 %).

The detector width allows sensing of the spectral range aimed for with a suitable spectral resolution while keeping the entrance slit width at a reasonable level. With a detector height of 3 mm the use of a 1 mm slit height is viable, considering prism-caused diffraction order bending, while still retaining enough detector area above and below the order for stray light monitoring. The relatively small array size (0.5 Mpx) together with the possibility of on-board *vertical binning* allows readout times for a single spectrum of below 16 ms. Vertical binning, schematically explained in Fig. 4.16, describes the process of vertical transfer of the accumulated charge of every column into one shift-register increment where they are stored until being subsequently integrally read out as a single line, thus limiting the A/D-conversion time span. This procedure can be advantageously exploited in our case as all pixels within a column belong to the same wavelength. Measuring only in the vertical binning mode would allow the spectra acquisition without the need for a mechanical shutter.

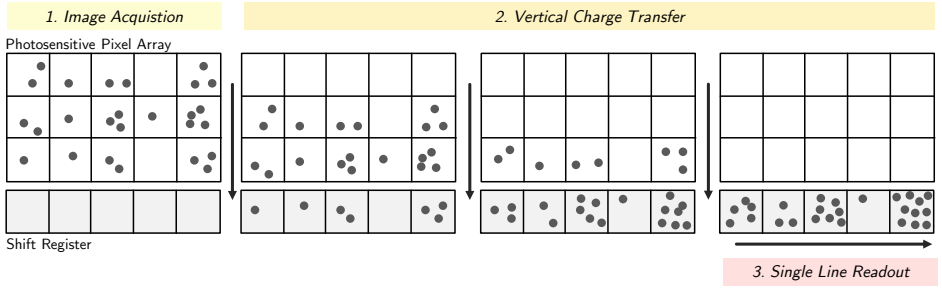

Figure 4.16: Principle of hardware vertical binning

The chosen camera is suited for low-light level detection [Hamamatsu, 2005] which, together with exposure times between 5 ms to 20 000 ms, leads to a high overall dynamic range. It features relatively low noise and low dark signal (compare Tab. 4.1).

As visible in Fig. 4.17, detector head and controller of the camera are separate units connected with a short flat ribbon cable which allows the conform integration into the instrument with confined space conditions. The camera is controlled via a USB 2.0 interface and is programmable using the Hamamatsu software development kit DCAM-SDK.

4.6.4 Etaloning

Etalons are narrow flat optical elements with two partially reflective surfaces facing each other. When illuminated the transmission spectrum exhibited by a perfect etalon with respect to wavelength, is a series of spikes belonging to wavelengths which fit with “an exact integer number of times between the surfaces” [Roper Scientific, 2000]. This resonant behaviour can be used in various optical applications ranging from Fabry-Pérot interferometers over dichroic filters (bandpass filters) to the construction of single-mode lasers.

In imperfect etalons with reflectance well below 100 % “the spectral characteristics soften from a spiky comb to a smooth set of fringes” [Roper Scientific, 2000]. The transmission spectrum

Figure 4.17: OEM CCD camera Hamamatsu C9260-933-17. The detector head (a) is temperature-stabilized by a Peltier element. The sensor head's heat sink(b) is supported by two small fans (c). The camera controller (d) is controlled via USB interface (e). For full galvanic insulation of the camera the USB signal is conducted via optical fibre to the main computing unit. The camera-generated shutter signal is transferred via opto-coupler (f, compare Section 4.10.6). (g) denotes the folding mirror guiding the light from the spectrometer onto the CCD chip. The mounting plate of the camera is blackened as are most mechanical elements inside the spectrometer.

	Parameter	**Value**
Sensor	Name	Hamamatsu S10141-1108
	Type	Back-thinned CCD image sensor
	Sensor Size	24.576 mm × 3 mm
	Effective pixels	2048 (width) × 250 (height)
	Pixel size	12 µm ×12 µm
	Full well capacity	∼ 60000 e^- (high gain mode)
	Amp gain conversion	0.9 e^-/AD count (high gain mode)
	Dark Current (at 20 °C)	max. 50 e^-/px · s
	Readout Noise	20 e^- rms
Camera System	Type	Board Type
	Full frame readout time	2483.2 ms
	Measurement modi	Full frame line-binned
	AD converter	16 bit
	Exposure time	5 ms to 20 000 ms
	Sensor cooling	0 or −10 °C (using peltier element)
	Communication Interface	USB 2.0
	Power supply	12 VDC / 1000 mA
	Ambient operating temperature	0 °C to 40 °C
	Ambient operating humidity	max. 70 % RH

Table 4.1: Specifications Hamamatsu CCD Board Camera C9260-933-17 [Hamamatsu, 2005, 2008]

$T(\lambda)$ depends on multiple parameters: The etalon thickness d, the surface reflectance R, the refractive index η, wavelength λ and angle of incidence Θ and is described by the Airy-Formula [Paul and Fellner, 1999]:

$$T(\lambda) = \frac{1}{1 + \frac{4R}{(1-R)^2} \sin^2(\frac{\delta(\lambda)}{2})} \tag{4.8}$$

with $\delta(\lambda)$ the wavelength-dependent phase shift:

$$\delta(\lambda) = \frac{2\pi}{\lambda} \eta \, d \cos(\Theta) \tag{4.9}$$

When measuring in the NIR region the thinned silicon substrate of the back-illuminated CCD becomes partially transparent. Additionally the back plane, whose anti-reflection coating is often not optimized for the NIR, and the silicon oxide layers near the gate (with a refraction index of about 1.5 with respect to the silicon bulk with 4) form two partially reflective surfaces. This influences the quantum efficiency: the transparency reduces QE, an effect which is partially compensated as some photons re-enter the bulk because of the reflectance (thus increasing the effective path length and the absorption probability in the photosensitive layer).

A more remarkable disruptive side-effect is the building-up of standing wave patterns [Roper Scientific, 2000] of constructive and destructive interference. This leads to a modulation of the actual intensity distribution on the chip which often appears as “marble structures", as shown in Fig. 4.18 . The amplitude of the fringing structure can reach up to several percent of the useful signal. For back-thinned CCDs the structure is mainly caused by two effects: *spatial etaloning* and *spectral etaloning*.

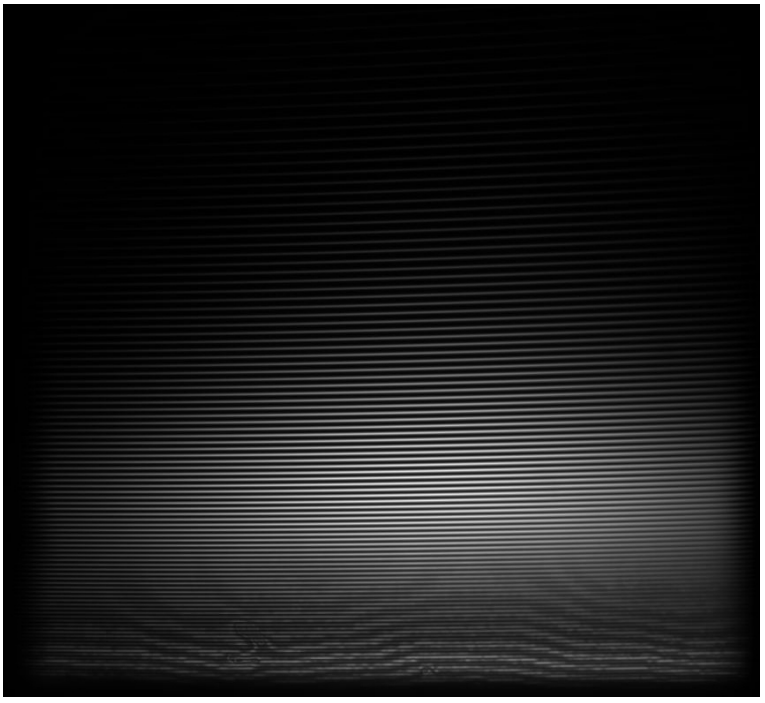

Figure 4.18: Spectrum of a flat-field lamp produced by the spectrometer TwinCompass (echelle spectrograph; focal length: 135 mm; grating: 316 grooves/mm; blaze angle: 63°) covering a wavelength range from 350 nm (top) to around 900 nm (bottom). The spectrum is recorded with a back-thinned CCD-Camera exposing prominently the interference structures caused by etaloning which only occur at longer wavelengths.

Spatial etaloning describes the effect of an imperfect silicon layer thickness. When illuminated with monochromatic light, spatially distributed interference patterns become apparent. With the shift between constructive and destructive interference only at $\frac{\lambda}{2}$ and the refractive index of silicon at 4, the necessary thickness deviation for light of 800 nm is only about 0.05 µm (or $\frac{\lambda}{16}$). In contrast to conventional imaging applications this is of special importance in spectroscopy, where specific locations are in fact illuminated with quasi-monochromatic light, thus preventing an averaging out of the etalon fringes as possible with a broader local spectral distribution.

Spectral etaloning denotes the dependence of the interference structure on the wavelength of the incident radiation. Areas of maximum constructive interference occur with a periodicity of several nm wavelength depending on thickness (here assumed to be constant) and the wavelength region.

When a back-thinned CCD experiences a constant illumination situation with respect to spatial intensity distribution, wavelength composition and illumination direction, it exhibits an interference structure which is highly constant, both location-wise and amplitude-wise. This constant modulation pattern can basically be treated the same way as varying pixel sensitivities of the detector whose effects are eliminated through division of the primary retrieved spectrum with a flat-field spectrum (see Section 6.6). With the illumination and therefore the pattern slightly changing, the effect can be partially extinguished by using tall entrance slits and averaging out by vertical binning. This however only works with marble structures not aligned with CCD columns. The appearance and treatment of etaloning in the case of SOLUSAR is described in Section 4.9.

4.7 Entrance Slit Group

The entrance slit represents the *field stop* of the optical system. Around the entrance slit the ray bundles become the smallest, making a suitable place for the positioning of various additional optical components. As evident in Fig. 4.19 all these elements are mounted on a single aluminium base plate for the sake of correct adjustment preservation.

The converging ray-bundle descending from the telescope first meets a thin quartz plane plate with an angle of incidence of 45°, thus acting as a beam splitter. The two surfaces of the plane are reflecting roughly 8 % of the intensity which is then directed onto the quadrant diode used for the control of the telescope aiming (see Section 4.10.2). Using the same quartz plane, light emitted by a spectral lamp can be coupled into the spectrometer using an optical fibre and transfer optics (see 4.8.2). In case of solar measurements the highly intense radiation can be attenuated by swivelling in two grey filters (Section 4.7.1). The spectral broadness of the remaining light let through is then reduced by a red filter plate to limit the amount of radiation entering the spectrometer unit thus constricting false and stray light. The radiation enters the *homogenizing fibre* (compare Section 4.9) in the telescope focal plane. The optical fibre is mounted using SMA connectors with the fibre exit practically touching the entrance slit diaphragm. The spectrometer illumination is controlled by an electronic shutter (see Section 4.7.1). Close to the entrance slit lies a folding mirror guiding the light coming from the spectrometer onto the CCD detector nearby – a typical setup for spectroscopic instruments in Littrow configuration.

The entrance slit area, with multiple ray paths converging, is the place where most of the optical adjustment measures take place. Through the introduction of a homogenizing fibre the required effort is greatly reduced: A perfect alignment of telescope axis and spectrometer axis is no longer necessary. Furthermore the various SMA connectors are allowing to comfortably feed

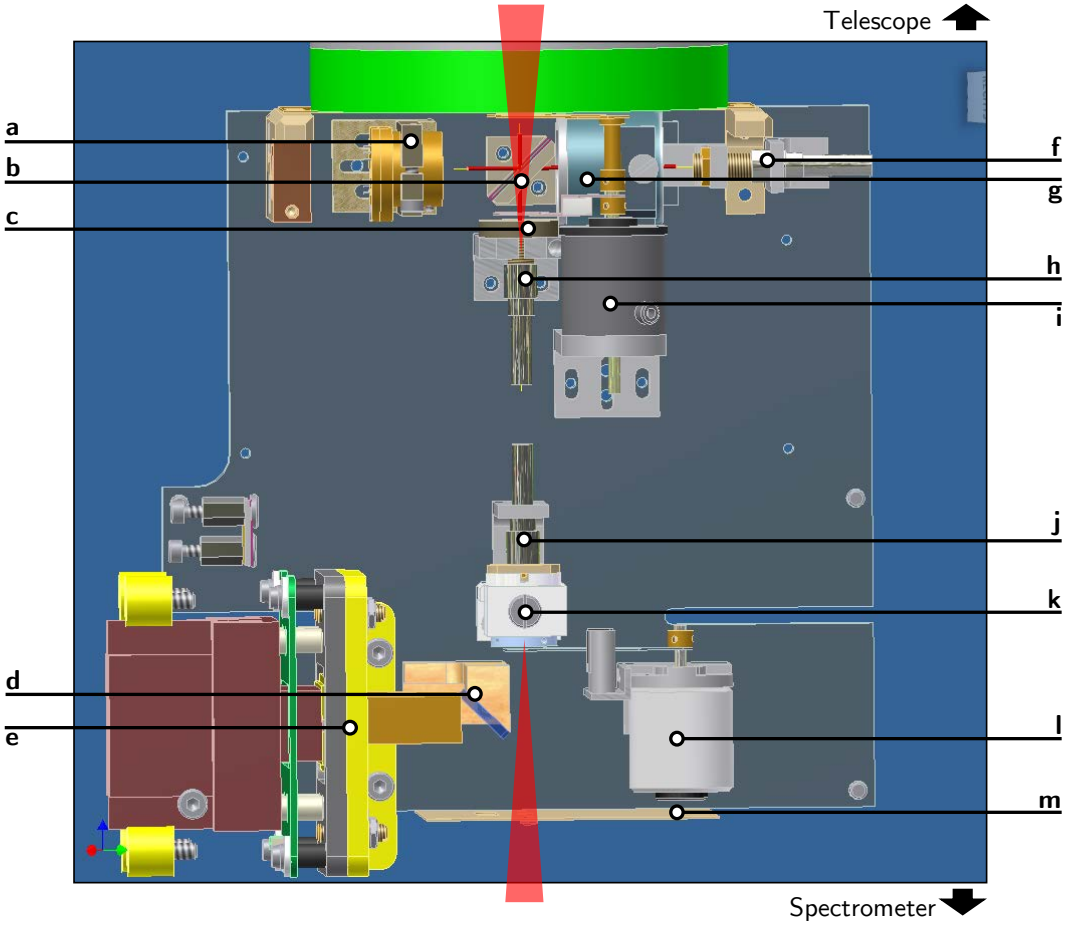

a	*quadrant diode*	**h**	*homogenizing fibre entrance*
b	*beam splitter*	**i**	*rotary solenoid – grey filters*
c	*spectral filter*	**j**	*homogenizing fibre exit*
d	*folding mirror*	**k**	*entrance slit*
e	*back-thinned CCD detector*	**l**	*rotary solenoid - shutter*
f	*optical fibre conducting argon light*	**m**	*diaphragm*
g	*argon light input optics*		

Figure 4.19: "Entrance Slit Group": Optical elements gathered below the telescope around the spectrometer's entrance slit.

in additional external light sources. E.g., the right position of the homogenizing fibre entrance in the focal plane of the telescope's imaging lens was found by a backward illumination of the telescope with an LED and a subsequent analysis of the collinearity of the exiting radiation using another external (calibrated) telescope.

4.7.1 Shutter and Optical Filters

The acquisition of full-frame CCD images (5.2) requires the application of a physical shutter, as the detector ought not to be illuminated during charge transfer to CCD's shift register. The camera provides a trigger signal (TTL signal) which is synchronized with the electronic exposure/readout regime. The chosen optical filter set-up affords minimal exposure times of 10 ms under the brightest conditions when recording sun spectra (summer, noon, clear

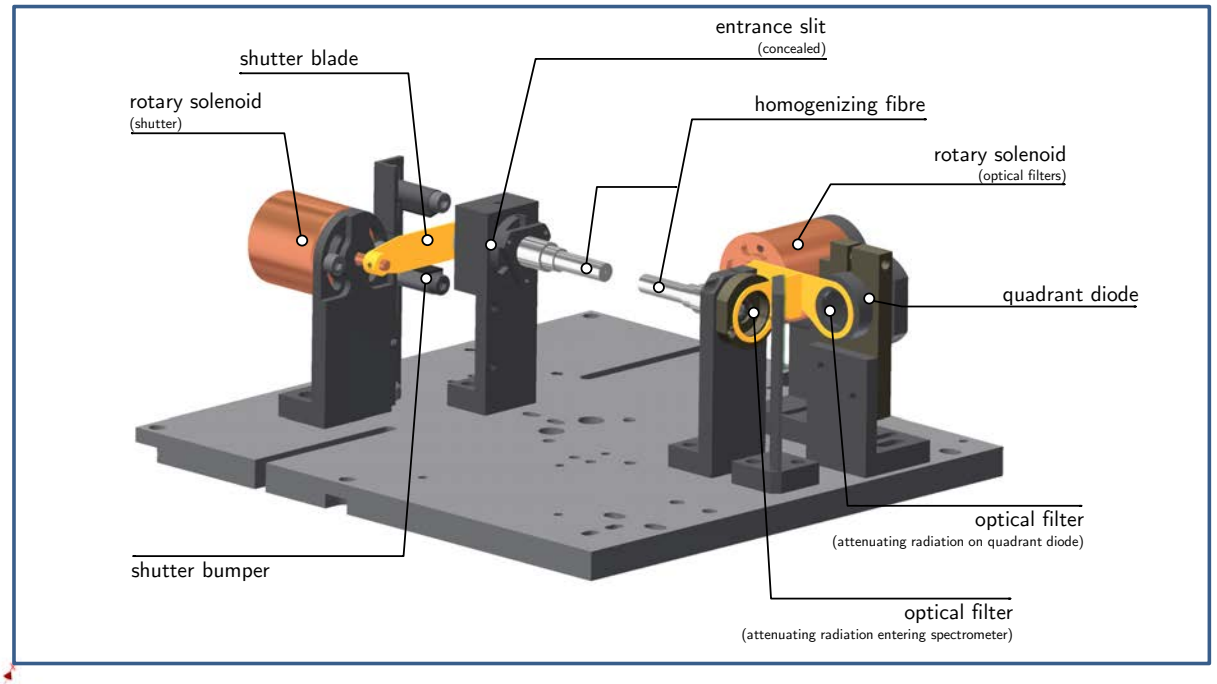

Figure 4.20: Arrangement of the mechanical shutter and the pivotable optical filters.

The shutter, placed right after the entrance slit (see Fig. 4.20), consists of a rotary solenoid and an attached small shutter blade discontinuing the ray path. The rise and fall time of this system amounts to around 1 ms. When measuring in the millisecond range the shutter shows resonance behaviour impairing the linearity between exposure time and intensity arriving at the CCD. As the behaviour is highly reproducible it can be circumvented through a look-up table listing suitable exposure time/intensity pairs.

As for the shutter a rotary solenoid is used to switch in a pair of grey filters in case of solar measurements. A first filter reduces the integral intensity coming from the telescope by a factor 1.5; a second filter reduces the intensity on the quadrant diode by around two orders of magnitude.

4.8 Built-in Light Sources

For various calibration purposes, which are outlined in detail in Chapters 5 and 6, two light sources are integrated into the measurement system which are shortly described in the following subsections.

4.8.1 Flat-field Lamp

A small halogen bulb (Gilway L1040 Clear-End Halogen Lamp) is statically mounted at the bottom of the telescope encasement underneath the revolving platform. The lamp is powered with 4.5 V and emits light with 70 lm at a color temperature of 1350 K. Fed into the spectrometer the lamp provides continuum spectra necessary for the determination and correction of pixel-sensitivity patterns belonging to the CCD. Additionally it is used to derive the diffraction order edges used for spectra stabilization, stray light determination and spectra binning. Further it serves as internal position reference (for further details on all points mentioned here see Chapter 5).

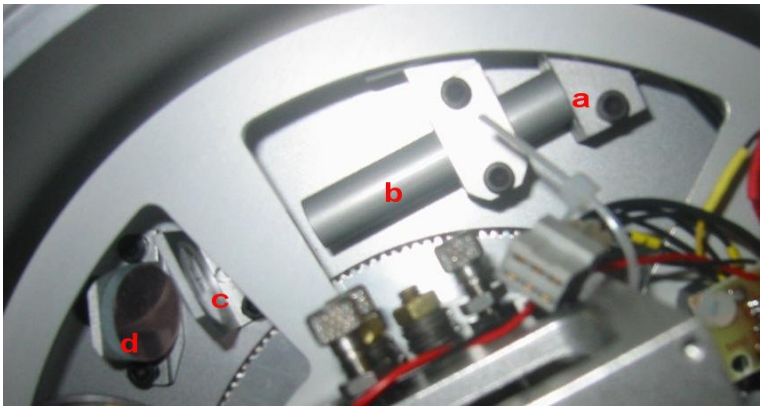

Figure 4.21: Mounting of the halogen bulb (a) inside a baffle tube (b) at the bottom of the telescope encasement underneath the revolving platform with the collimator lens (c) and the deflection mirror (d).

As shown in Fig. 4.21 the bulb is stored in a horizontal tubing (to avoid false light in the telescope) which guides the light to a small collimation lens. The light is then redirected by a planar mirror into the direction of the primary telescope mirror. The generated halogen bundle is slightly narrower than the solar ray bundle which is of relevance regarding spectrometer illumination (compare Section 4.9). Unlike the argon lamp (Section 4.8.2) with its more direct feeding in of the light via the quartz plane plate underneath the telescope, the halogen light feeding in makes use of the high-quality achromatic lens thus limiting chromatic aberration and improving quality of the imaging onto the entrance of the optical fibre.

4.8.2 Spectral lamp

To provide the acquisition of spectra with isolated emission lines a spectral lamp with argon fill is included in the spectrometer. Excited argon exhibits three emission lines in the mainly targeted wavelength range between 789.0 nm and 802.0 nm (see Tab. 6.3) strong enough to be recorded with exposure times of a few seconds. Additional argon lines appear in adjacent

wavelength regions, being of help when obtaining data in the spectral vicinity of the primary window.

The integration of a rare gas lamp, proving distinct single lines, serves numerous purposes, i.e.:

- *Wavelength Stabilization:* The emission lines with their assigned wavelengths form "anchors" in order to keep the spectrum image at a definite position on the sensor. For a description of the spectrum stabilization procedure see Section 5.3.
- *Dispersion Computation:* Using the emission lines' wavelengths and their respective positions on the chip a scale assigning a wavelength to every CCD pixel column can be estimated (see Section 6.7).
- *Apparatus Function Determination:* The monitoring of emission line profiles with respect to the position on the sensor serves as an estimation of the apparatus function width (see Section 5.4).
- *Adjustment Process:* For the optical adjustment during and after the instrument's construction process, the argon spectra were used to find the position of the spectrometer's achromatic lens providing the best image focus (over the whole sensor width) by minimizing the emission line's FWHM (Full Width at Half Maximum). In case of a readjustment this procedure can easily be reapplied. As a narrow but high entrance slit is used, a good vertical alignment with respect to the CCD sensor is indispensable. This setting, also to be optimized for the entire sensor area, is achievable through rectification of the emission lines along the detector columns.

(a) StellarNet SL2 calibration lamp (b) Argon-filled UVP Pen-Ray with power supply

Figure 4.22: Spectral lamps for different calibration purposes.

Initially deployed was a *StellarNet SL2* emission lamp which can be powered using the 5 V available in the measurement system (see Fig. 4.22(a)). With the inclusion of a homogenizing fibre (see Section 4.9) and the accompanying large intensity losses, recording of usable emission spectra required exposure times up to 10 s which heavily obstructs the measurement procedure. Thus a stronger light source paired with a new optical coupling was introduced: The *UVP Pen-Ray 11AC-2* light source, a low-pressure, cold cathode UV lamp with a U-shaped quartz tubing holding the gas fill and the electrodes placed at one side (Fig. 4.22(b)). Exposure times for the acquisition of argon spectra can thus be reduced by roughly a factor of 10. A combination of two aspheric collimation lenses mounted head-to-head, images the light coming from the lamp through an optical fibre onto the entrance slit (visible in Fig. 4.19, letter f). The

lens combination is mounted closely to the fibre exit (quartz fibre, diameter 600 µm) covering the full numeric aperture and producing a slightly magnified image to fully cover the slit. This again increases the intensity by a factor 2.5 to 3.

Inconveniently the Pen-Ray lamp is in need of a high ignition voltage and is operated with AC voltage. In order not to introduce another source of possible electromagnetic disturbance in the instrument, the power supply is located externally. The lamp itself is stored underneath the telescope (Fig. 4.19, letter e).

4.9 Homogenization Unit

According to the description given in Section 4.2 the SOLUSAR measurement system was conceived to consist of directly coupled telescope and spectrometer units, omitting the use of optical fibre harming the system's light throughput. With the apertures of the telescope and the spectrometer well accorded, measurements under low light conditions (moonlight) with reasonable exposure times would have been possible. In the initial coupling set-up, depicted in Fig. 4.23, the light gathered by the telescope unit is directly imaged by an achromatic lens onto the entrance slit.

Test measurements with the described set-up proved the tremendous sensitivity of the chosen instrumental approach. Lunar spectra around full moon are obtainable with exposure times between 8 s to 10 s reaching up to 50 % of the CCD's full well capacity. The application of preprocessing algorithms described in Chapter 6 on solar and lunar spectra, however, does not produce satisfactory transmission spectra. A determination of the baseline intensity I_0 with an accuracy of better than 1 % is regarded as a necessary foundation to derive water vapour concentrations of sufficient quality. As shown in Fig. 4.24(a) to 4.24(c) every single spectrum is heavily affected by the influence of etaloning as described in Section 4.6.4. Vertical binning is by no means sufficient to eliminate the structures, as the overlaying pattern is sometimes (especially at the CCD edges) aligned with the CCD columns.

The flat-field correction (see Section 6.6), which should, in case of an invariant modulation pattern, eliminate these structures is failing to do so, as can be seen in the flat-field spectrum quotients in Fig. 4.24(d).

4.9.1 Causes of Etaloning Distortion in SOLUSAR Transmission Spectra

Though visually not perceivable, there are considerable differences between the etalon fringes exhibited on a solar spectrum and those on a flat-field spectrum from the instruments halogen lamp, which becomes apparent when computing the pixel-wise ratio of the two spectra types which should exhibit only smooth broadband intensity modulations. Given the similar amplitude and sharpness of the modulation features, already slight lateral position deviations between the two patterns cause severe distortions of the computed transmission spectra. Two main reasons are found to contribute to the slightly altered etalon fringe patterns:

- *Different Ray Bundles:* The acquired ray bundles from the different light sources do not have the same morphology: Foremost the bundle diameter of the acquired sun radiation is defined by the mirror system, whereas the halogen bundles are restricted by the associated collimation lens rendering it considerably smaller (roughly two times in diameter). Additionally the ray path of collimated halogen bundles does not follow the

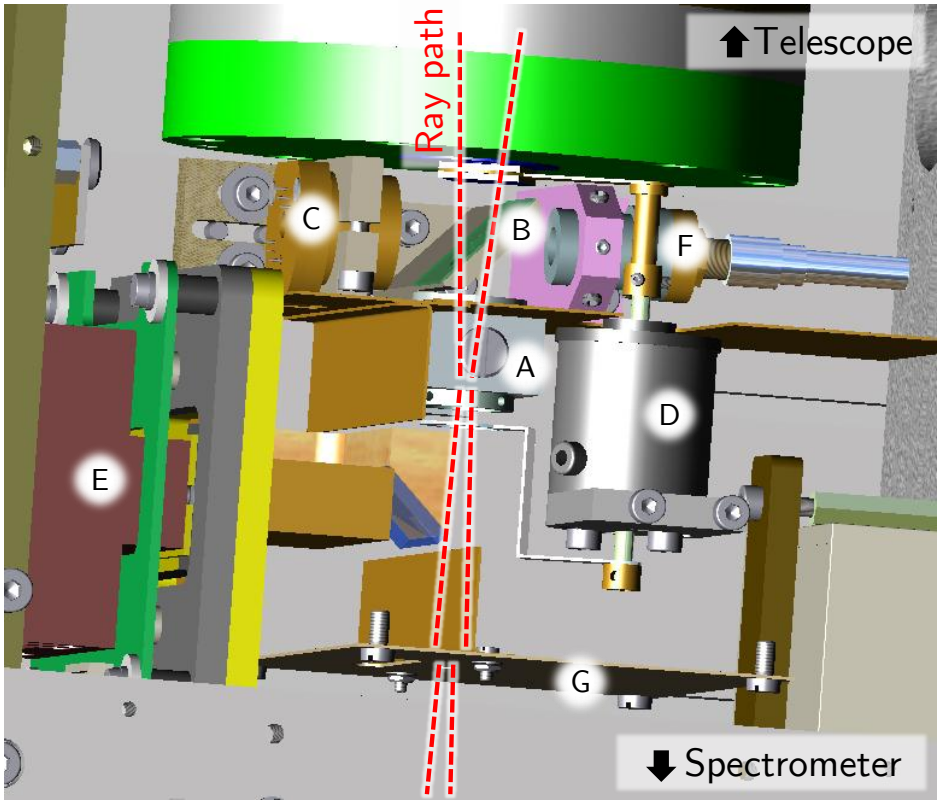

Figure 4.23: Original set-up of the telescope/spectrometer interface: The incoming light from the telescope is directly guided onto the entrance slit (A), passing the partially transparent quartz plane plate (B). This plate is branching off a small intensity portion onto the quadrant diode (C) and is coupling in light coming from the argon lamp via optical fibre (F). By use of a rotary solenoid (D) two optical filters can be switched in, attenuating the light guided in by the telescope and even further decreasing the intensity entering the spectrometer in case of sunlight measurements. To prevent stray light spreading various baffles are used (as, e.g., G), also serving as aperture stop. (E) denotes the back-thinned CCD detector.

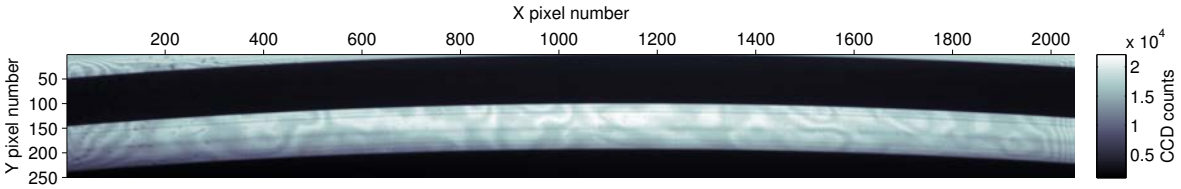

(a) SOLUSAR full frame image of a halogen spectrum (entrance slit height 1 mm) exhibiting marble structure caused by etaloning effects in the backthinned CCD.

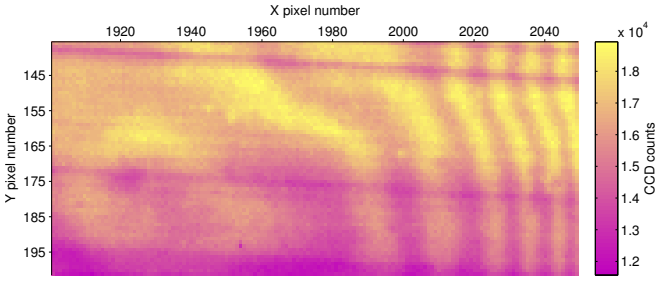

(b) Extract of Fig. 4.24(a) showing the etalon structure on the right side of the detector. The nearly horizontal lines are caused by entrance slit impurities.

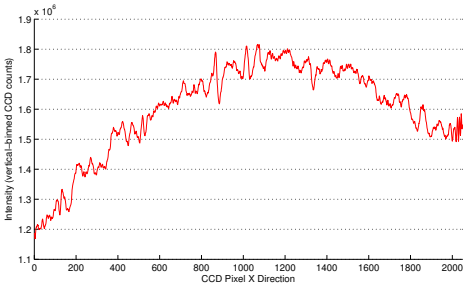

(c) Vertical binning of the halogen spectrum from Fig. 4.24(a). The interferences cannot be averaged out. Intensity differences of up to ± 5 % occur already on a very short distance (e.g. around column 900).

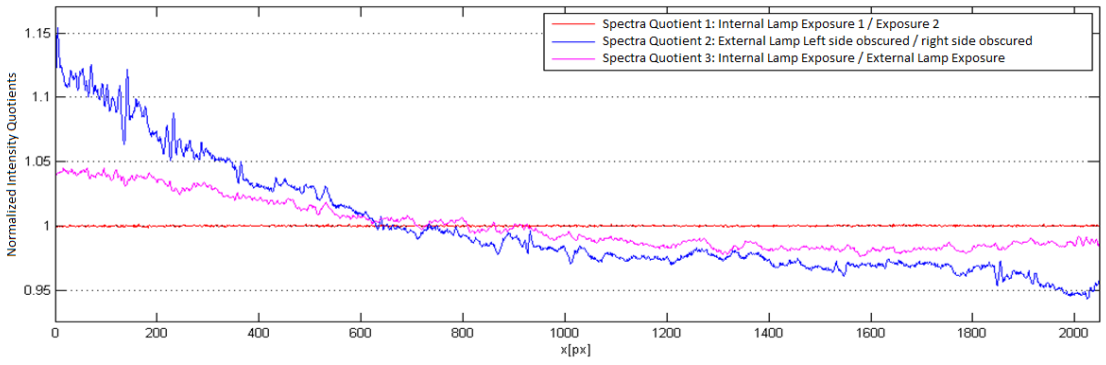

(d) Influence on flat-field spectra quotients: The red line denotes a quotient between subsequently obtained spectra of the internal halogen lamp (exposure time always at 2 s). The blue and pink line show the distorted baseline when computing quotients from spectra with differerent spectrometer illumination. As the interference patterns differ they cannot be eliminated through spectra division.

Figure 4.24: Etaloning structures in SOLUSAR spectra.

vertical telescope axis with absolute precision due to adjustment limitations.
Eq. 4.8 shows the influence of the angle of incidence on a perfect etalon. Also in the case at hand the back-thinned CCD seems to produce slightly different interference patterns depending on the angular radiation distribution.

- *Changing Entrance Slit Illumination:* Between the spectrometer's illumination by the sun or the moon and the flat-field lamp also the field-wise distribution is changing. E.g. the projected sun disk on the entrance slit alone can show a surface brightness which varies spatially over time, due to the influence of clouds et cetera. The intensity distribution over the entrance slit height in any case differs from that evoked by the halogen lamp which is shaped by the imaged glowing coil of the halogen bulb.

4.9.2 Etaloning Countermeasures

In order to gain solar/lunar spectra and corresponding flat-field spectra modulated by an approximately constant etaloning structure, the light entering the spectrometer has to undergo an antecedent homogenization of the radiation distribution: The intensity distribution over the entrance slit height (field homogenization), as well as the angular distribution of intensity in the ray bundles entering the spectrometer (aperture homogenization), should become independent of the light source. A wide range of different optical measures, outlined in the following sections, have been tested regarding their homogenization efficiency and their accompanying loss of overall intensity, whose confinement is of utmost concern.

Homogenizing Rods

One possibility to homogenize light with uneven intensity distribution having lately emerged are so-called *Light Pipe Homogenizing Rods*. These bars manufactured by *Edmund Optics* either of N-BK7 glass or quartz glass (for applications in the UV) dispose of a hexagonal cross section. (Similar products with a square cross section are manufactured by *Newport*). Such devices ought to transform the output of a non-uniform light source to a uniformly bright beam through internal total reflection randomizing the entrance angles. This is claimed to work independently of the spectral features of the light source and while keeping the numeric aperture practically unaffected. Hexagonal light pipes are available with diameters ranging from 2 mm to 20 mm and lengths between 25 mm to 125 mm. For SOLUSAR such a rod has on the one hand to deal with a very small input aperture (around $f/15$), what makes narrow and long rods desirable. On the other hand it should be as short as possible to not excessively compromise the instrument's compactness. A length of 75 mm and a diameter of 2 mm was found to be appropriate. In the case at hand the application of this rod results in intensity losses of up to a factor 3 due to a larger exit facet compared with the telescope produced spot size (diameter 1.2 mm).

Experiments with a test set-up simulating the telescope illumination however showed, that light pipes of the chosen type do not provide a sufficient redistribution of the intensity given the small aperture and the hence limited number of internal reflections. Neither in near-field, which should guarantee a uniform entrance slit illumination nor in the far-field at the collimation lens a intensity distribution sufficiently independent of the light source is achieved.

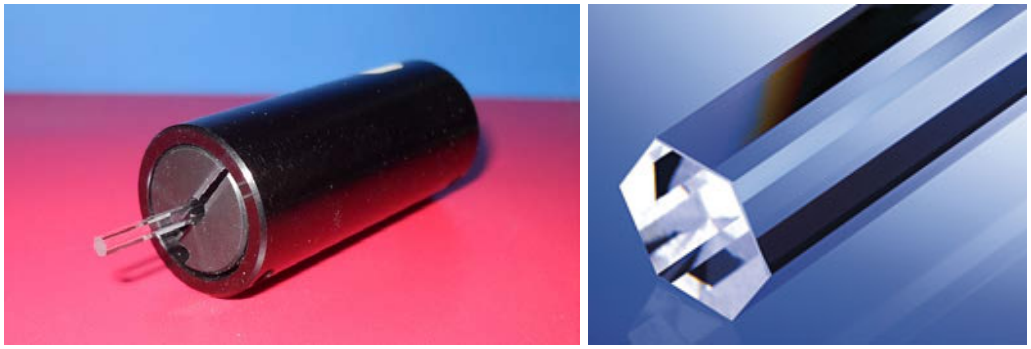

(a) 75 mm homogenizing rod with mounting. (b) End of a homogenizing rod.

Figure 4.25: NBK-7 homogenizing rods by *Edmund Optics* used to scramble structured light sources through total reflection.

Polymeric Optical Fibre

Light guiding cables made from polymers (POF) can be used as homogenizers. Compared to classical optical cables made from glass, POF cables do not provide as excellent mirroring characteristics. This on one hand leads to a better angular redistribution of the intensity, the effect which is sought, on the other hand the aperture of the incoming light cannot not be retained and the intensity output is distributed over the whole numeric aperture (NA) of the fibre. The tested *Toray Raytela PG-series* fibres have a NA of 0.5. Together with certain transmission losses of the fibre, this, in case of SOLUSAR, leads to massive intensity losses of up to a factor 40, as large amounts of the light bundles do not reach the spectrometers achromatic lens. This behaviour is even amplified, when using long fibres (up to 2 m) which are coiled several times, which then again would provide the best homogenization results (see Section 4.9.3).

Quartz Optical Fibres with Hexagonal Cross Section

Lately quartz fibre cables with non-circular but quadratic, rectangular or hexagonal cores have emerged (see Fig. 4.26). They are applicable in various cases ranging from very tightly packed bundles of quadratic fibres used in astronomy to the scrambling of the intensity structures of diode lasers. With hexagonal cross sections and small diameters, such cables can be seen as very long, narrow and flexible homogenizing rods described above. Optical fibres *Optran NCC UV/WR* fabricated by *Ceramoptec* [Ceramoptec, 2011] with a core diameter of 400 µm and different cable lengths (400 mm and 800 mm) have been tested. Given the 1 mm entrance slit the application of thicker cables would be desirable, but is prohibited by cable bending limitations and the sparse space inside the instrument.

Besides its overall homogenizing quality being short of the one provided by longer polymer fibres (see Section 4.9.3), the solution is accompanied by the disadvantages of a reduced diffraction order height: With a 400 µm core and the non-consideration of pixels close to the diffraction order edges, the usable diffraction order height decreases from 77 pixel to 36 pixel thus reducing the S/N-ratio by nearly 40 %. A smaller diffraction order height also slightly increases the proneness to the electric disturbances described in Section 4.10.6.

Figure 4.26: Cross section of optical fibre with a quadratic light-guiding core [Photonics, 2010].

One of the main advantages lays in the far better preservation of the aperture compared to polymer fibre, as long as the light conductor is not excessively bent. The surface brightness when using a 400 µm hexagonal fibre compared to a 1000 µm polymeric fibre is 5 to 6 times higher. Hence the overall loss compared to the initial direct coupling of telescope and spectrometer amounts to roughly a factor 7 to 8.

Generally the integration of any optical fibre massively facilitates the pre-operational adjustment of the instrument, as described in Section 4.7. Also the speed requirements for the telescope control cycle are generally reduced as slightly off-axis images of the sun produced by the telescope do no result in partial non-illumination of the slit.

To further improve the homogenizing efficiency of the fibre the telescope's achromatic lens was replaced by a lens with a shorter focal length (50 mm instead of 150 mm). By making better use of the fibre's acceptance angle an enhanced mixing should have been reached, as the number of reflections increases. However the exhibited effect on the baseline was minimal, whereas the overall intensity decreased again, as the spectrometer aperture was exceeded even more, an effect which is not fully compensated for by the smaller image size of the sun spot (0.4 mm) on the fibre entrance.

Holographic Diffusers

Matt screens are often used to produce diffuse light conditions, but with the setback of a greatly increased illuminated field. Holographic diffusers, grained foils made from polycarbonate, are able to produce diffuse illuminations with a far smaller expansion of the aperture (see Fig. 4.27(b)). Holographic diffusers from *Edmund Optics* have a transmission efficiency of above 85 %, are applicable in the VIS/NIR region and are available with different diffusion angles ranging from 0.5° to 80°. In case of SOLUSAR the efficiency of holographic diffusers with diffusion angles between 0.5° and 10° has been tested in various arrangements.

An introduction in the halogen ray path in the telescope to reduce the imposed structure of the lamp coil remained unsuccessful, as it does not solve the problem of the smaller halogen bundle width.

A more elaborated approach has been tested using the same space as the homogenizing fibre in front of the slit, by introducing an intermediate imaging set-up, as depicted in Fig. 4.27(a). The beam coming from the telescope is collimated, constricted by a round diaphragm (aperture diameter 3 mm) before being redistributed by a holographic diffuser. The diffused light is

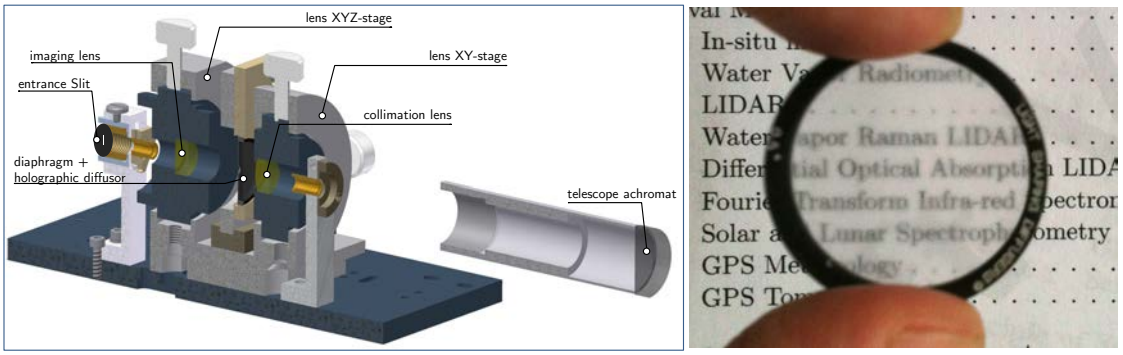

(a) Intermediate imaging setup in front of the entrance slit using a holographic diffuser in a collimated beam.

(b) Effect of a holographic diffuser with diffusion angle of 0.5°

Figure 4.27: Homogenization by means of beam-smoothing holographic diffusers

subsequently imaged by a second lens onto the entrance slit. Both lenses are positioned with translating optics mounts allowing a precise adjustment of the ray path. Surprisingly, these measures did not have a significant effect in terms of baseline smoothing, even when applying a coarse-grained diffuser.

4.9.3 Homogenization quality

The assessment of the homogenization quality of the different approaches described above is carried out phenomenologically by analysing the structure of flat-field spectra quotients. In case of DOAS possible sustaining broad-band intensity structures are not that problematic, but short scale distortions have to be omitted to allow a proper deduction of the concentration of a specific absorbing species. In order to test the effect of the different solutions, the sun illumination has been emulated using a simple optical set-up in the laboratory with a halogen lamp illuminating a circular diaphragm which together with a suitable collimation lens produces a disk image of the correct size in the focal plane of the telescope. To fathom the effect of different illumination situations, various spectra quotients are computed: E.g. quotients of two spectra produced by the “artificial sun” described above, one with the right-hand side of the diaphragm covered, the second with the left-hand side obscured, or – in an experiment resembling more closely the reality – quotients from the internal halogen lamp and the external lamp set-up.

To further confirm the findings above, comparisons of the intensity variation over the diffraction order height are revealing as well. Figs. 4.28(a) and 4.28(b) show as examples the vertical profiles of the diffraction order in the spectra of the internal and external flat-field lamp, in the original set-up and when using a polymer fibre with a diameter of 1000 µm as homogenizer. With the latter solution the strongly differing intensity distribution in the optical field can be unified.

Tab. 4.2 shows results produced by spectra quotients when dividing spectra with the diaphragm partly covered on one or the other side. The used homogenization method, the diaphragm coverage, standard deviation of the normalized intensity quotient on the CCD and further remarks on the remaining structures in the computed baseline are listed. The best results regarding homogenization are reached using the 2 m polymer fibre (compare Fig. 4.28(c)).

#	Method	Illumination	σ_{NIQ}	Comment
1	HEX	○ / ○	1.1 ‰	only regular noise
2	HEX	○ / ○ (different dark image)	1.7 ‰	slight non-noise structures visible
3	HEX	◐ / ◐	1.8 ‰ to 2.5 ‰	overall trend: max. intensity difference: 8 ‰
4	HEX	◐ / ○	3.8 ‰ to 5.9 ‰	similar to # 3
5	HEX	◐ / ◑	10.1 ‰	overall trend: max. intensity difference: 20 ‰
6	HEX	# / ○ (intensity loss: 70 %)	1.5 ‰	similar to # 2
7	POF	○ / ○	0.9 ‰	slightly more rippled than # 1
8	POF	◐ / ○	3.8 ‰	seems slightly smoother than # 4
9	POF	◐ / ◑	5.3 ‰	seems slightly smoother than # 5

Table 4.2: Effect of two optical fibres in various illumination situations on the quality of SOLUSAR spectra. σ_{NIQ} is the standard deviation of normalized intensity quotients of a vertically binned spectrum in a detector window width of 100 px. In case of the hexagonal fibre (HEX) with a 400 µm core, a cable length of 400 mm was taken. The exposure time was set to 2 s. For the polymer fibre (POF), a length of 2000 mm (1000 µm core diameter) has been chosen. The exposure time was set to 12 s to reach similar pixel intensity levels as with the hexagonal fibre. The symbols describing the illumination have the following meaning: ○: diaphragm fully open; ◐: left side of the diaphragm covered; ◑: right side of the diaphragm covered; #: diaphragm covered with partly light permeable mesh.

The hexagonal fibre produces nearly as good results but with a far lower intensity diminution. Therefore it is opted for the latter solution.

To further confirm the findings above, comparisons of the intensity variation over the diffraction order height are insightful as well. Figs. 4.28(a) and 4.28(b) show vertical profiles of the diffraction order in spectra of the internal and external flat-field lamp, for both, in the original set-up and when using a polymer fibre with diameter of 1000 µm as homogenizer. With the latter solution the strongly differing intensity distribution in the optical field can obviously be unified considerably.

4.10 Electronics

In order to build a compact measurement system and to ensure ease of transportation, electric and electronic parts, necessary for powering and control of the included sensors and actuators, are mostly directly attached to the instrument's internal mechanical structure (see Fig. 4.1). Even though a most integrated approach was strived for, certain elements are left out of the instrument: First and foremost the idea to include the central computing unit has been abandoned due to weight and heat dissipation reasons.

Fig. 4.29 shows a schematic depiction of the electronic concept, whereas in Fig. 4.30 the actual physical arrangement of the electronics within the instrument is illustrated. The concept

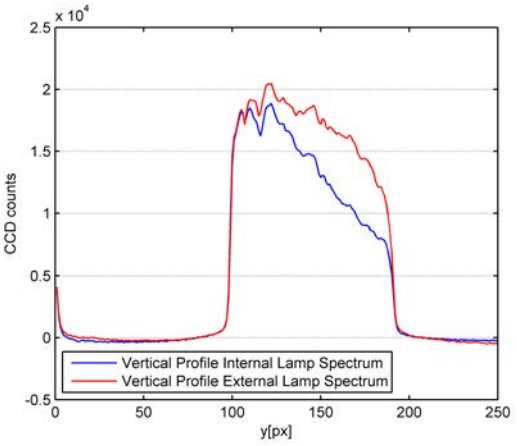

(a) Without homogenization

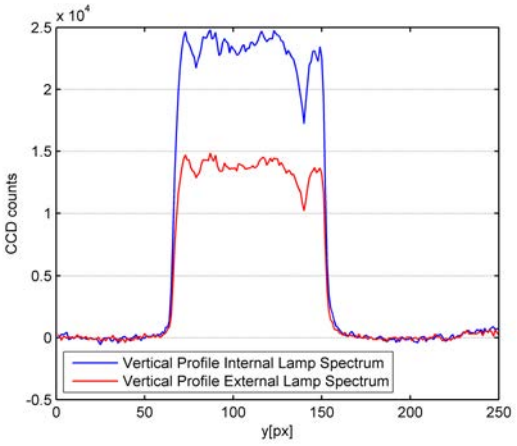

(b) With homogenization using a 2 m polymer fibre (diameter 1000 µm)

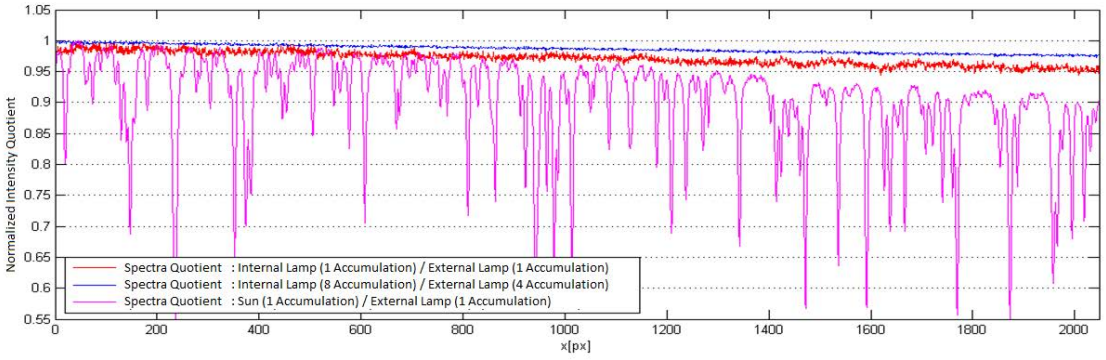

(c) Effect of homogenization with a 2 m polymer fibre. The absence of short-scale changes in the baseline apart from noise can clearly be observed in the quotients computed from the spectra of the two lamps. Broad-band trends are remaining, which mainly occur due to different light source temperatures and spectrometer characteristics.

Figure 4.28: Effect of proper beam homogenization on the vertical intensity distribution over the entrance slit height.

sketch shows the latest implementation including some deviations to the initial concept which had to be applied to handle occurring electromagnetic interferences (see Section 4.10.6) and changes related to the use of the homogenizing fibre. These deviations are adding some further complexity, but do not signify a total concept overhaul.

The entire measurement system (instrument plus external components) is powered with 12 V in order to make measurements possible at remote sites using car batteries. The whole measurement system has a total power consumption of 70 W to 80 W. A potential autarchic measurement set-up could, with the help of electric buffers, be supplied by solar panels with around $2\,m^2$ surface assuming set-up in a sunny region. Many instrumental components are in need of different DC voltages, which are provided through DC/DC-converters inside the instrument (5 V, ± 15 V). The power supply for the spectral lamp which requires higher voltage (especially for lamp ignition) is placed externally to prevent disturbance spreading caused by the voltage step-up. For the power supply of the CCD camera a separate car battery is used (see

4.10.6).

The chosen approach also shows certain disadvantages: The compactness of the instrument leaves only sparse place for the electronic parts. As components and wires cover almost the whole internal mechanical spectrometer structure from the bottom up to the telescope, maintenance and repairing works can be difficult and time-costly, especially during the period of instrument development. Furthermore, a considerable amount of heat dissipation from several components (i.e. camera controller, DC/DC-converter, servo drives) sealed inside the instrument can locally lead to temperatures up to 60 °C in summertime. The vertical structure allows strong temperature gradients (up to 20 °C between camera and spectrometer) adding further to the strain on the opto-mechanical system. This makes frequent recalibration of the system mandatory during the beginning of the measurement process until a certain thermal equilibrium has been reached.

Generally it was tried to separate digital and analogue electronic parts to the greatest extent possible to avoid ground loops. The wiring of the supply lines is designed to cope with higher currents caused by the low supply voltage. Issues of electric security including protective earthing have been thoroughly considered.

4.10.1 Computer Unit

As central computing unit each measurement system uses an industrial computer of the type *Aaeon AEC-9260* (Fig: 4.31(b)). Similar computer systems have been successfully applied in several projects at *GGL* (e.g. [Somieski, 2008]). In order not to introduce another heat source, the plan to place the main CPU inside the instrument as well has been discarded. The used processor (Intel Core 2 Duo running at 1 GHz) has to be powerful enough to handle numerous (partially time-critical) parallel tasks during the measurement process (see 5.5). Round-the-clock system operation is ensured by a so-called *automotive hard-drive*, which disposes of an enlarged temperature range and a rugged shock and vibration resistance (Seagate EE25.1 Series, [Seagate, 2007]). The motion control card (see 4.10.2) uses a PCI-slot, several USB and serial ports are necessary for the operation of various sensors and devices (Camera, GPS-module, meteorological sensor and I/O-module). The computer is cooled over a heat-sink connected to the corrugated computer aluminium encasement. For further specifications of the computer unit see Tab. 4.3.

Parameter	Value
Name	Aaeon AEC-9260
Type	Fanless Embedded Control PC
Processor	Intel Core 2 Duo 1 GHz
Memory	1 GB RAM
Hard Disk Storage	40 GB, 2.5 ” Automotive-HD
Expansion Slot	1 x PCI / PCI-E
Ports	4x USB 2.0 / 3 x RS232
Power Supply	9 VDC to 30 VDC
Size	214 mm x 95 mm x 238 mm
Operating System	Windows XP

Table 4.3: Control Computer Specifications

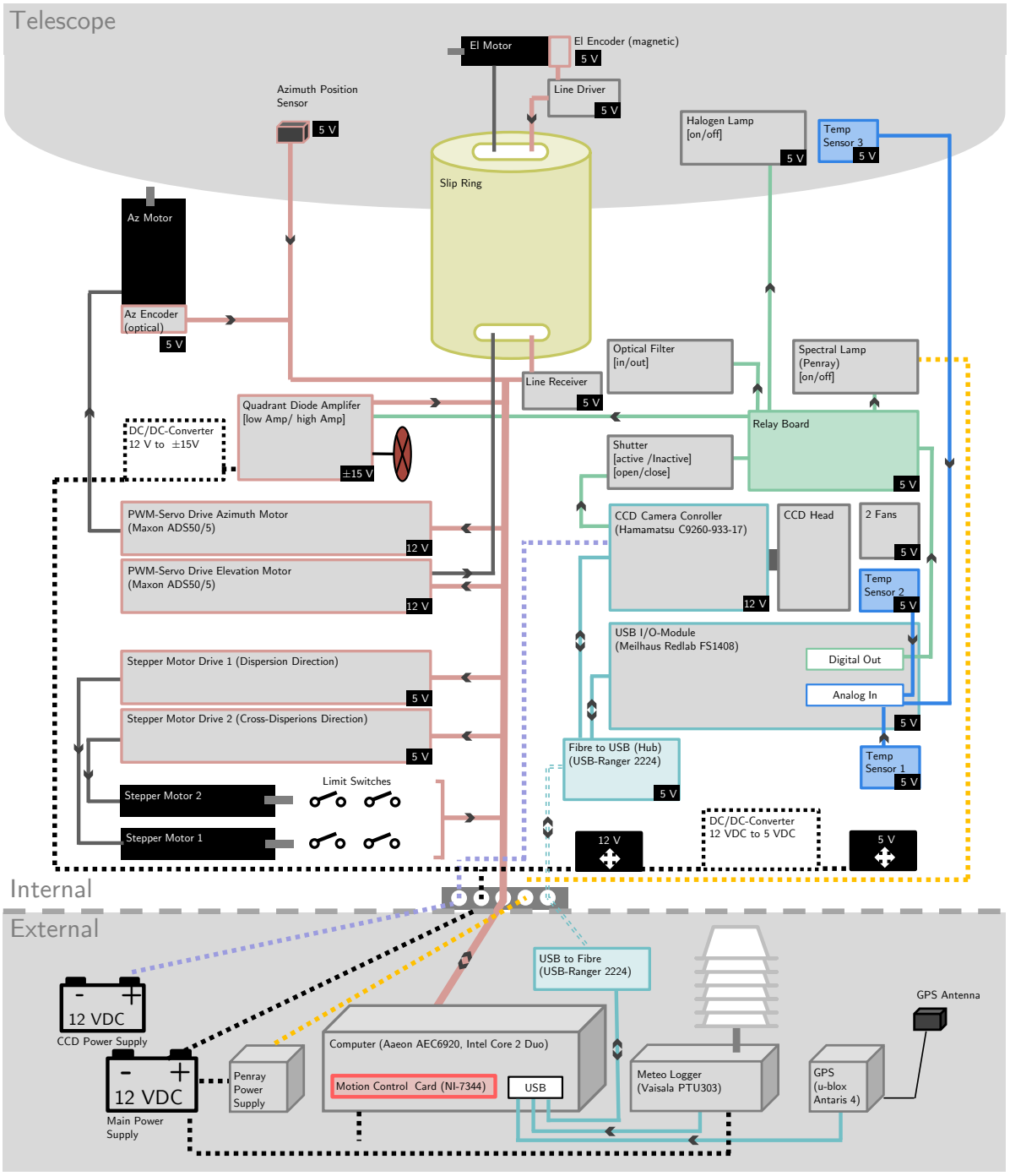

Figure 4.29: Schematic overview of the electric and electronic components belonging to the SOLUSAR measurement system: All components are directly or indirectly supplied by car batteries. Externally located are the central computing unit and the meteorological and GPS sensor. Many components inside the instrument (e.g. CCD camera, I/O-module) are controlled via USB, whereas all components associated with motor control are operated via the motion control PCI-card stored in the industrial computer (left side, red lines).

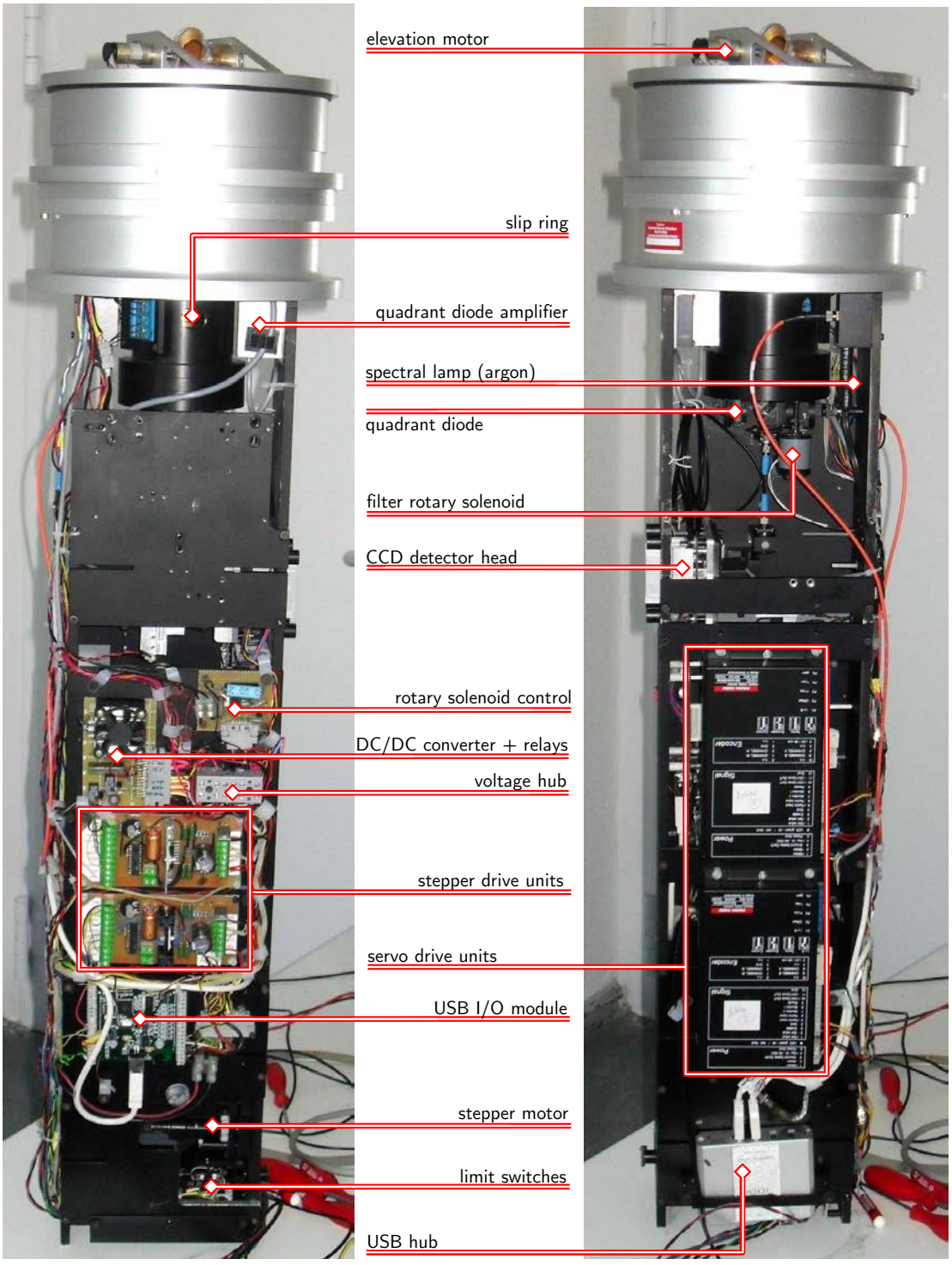

Figure 4.30: Internal arrangement of certain electronic components.

(a) Measurement Systems SOLUSAR I and SOLUSAR II set up at ISAS, Berlin with associated external components, such as computers and power supplies (underneath the table)

(b) Industrial computer Aaeon AEC-9260

Figure 4.31: SOLUSAR Measurement set-up

4.10.2 General Aspects of SOLUSAR Motion Control

The SOLUSAR measurement system disposes of totally four motor axes: Two DC motors in the telescope and two stepper motors to tilt the spectrometer's deflection mirror with high-precision. During the sun tracking procedure the telescope motors have to run simultaneously and the mirror system alignment is updated with high frequency. In order to enable spectrum stabilization via Fraunhofer lines (see Section 5.3) the possibility to concurrently move the folding mirror actuators is desirable. The motion control card *National Instruments NI PCI-7344* stored in the industrial computer allows control of up to four axes, each configurable either as DC motor or stepper motor axis. The axes can either be controlled independently, or simultaneously in coordination or even mapped together following trajectories in an artificial coordinate space [National Instruments, 2003]. Servo axes can be controlled in closed loop procedures using feedback of quadrature encoders (or analogue feedback). Stepper axes can be operated in open and closed loop mode.

The motion control card uses a double core architecture with a 32-bit CPU and a digital signal processor (DSP). Inter alia the CPU tasks include communication handling with the host computer, on-board program execution and multi-axis interpolation [National Instruments, 2003]. The DSP conducts the closed-loop motion control (PID control) and generates the motion trajectories. It is supported by a FPGA-chip which, among other things, acquires feedback signals from encoders and conducts the motion interfacing (driver control).

Axis movements can either be initiated by host computer programs using the sophisticated NI-Motion Application Programming Interface (API), whose functions are available for high-level

languages (e.g. C, C++). Also for LabVIEW a full function set exists. Or motion control is conducted through the above mentioned on-board programs which can be stored on the cards ROM (read-only memory, 128 kB) or RAM (random access memory, 64 kB). Up to 10 on-board programs can be executed in parallel. The command set, compared to the NI-Motion library, is greatly reduced but allows the composition of simple motion control algorithms including basic integer arithmetic. Test implementation of the telescope control cycle with on-board programs have proven though to be considerably slower for the task at hand and more tedious in maintenance than conventional host program execution.

Every axis disposes of input channels for home position (used for the telescope azimuth axis as an approximate null position implemented by means of a capacitive position sensor), reverse and forward limits which can be connected to limit switches (both used for the two stepper axes to define the limit positions using mechanical micro switches).

The card disposes of an 8-channel multiplexed 12-bit A/D-Converter, of which four can be used as analogue feedback channels. The voltage range lies between −10 V and 10 V, and is programmable within the given boundaries. The multiplexer scan rate is 25 µs per enabled channel. In our case they are used for the quasi-simultaneous acquisition of the signals from the four quadrant diode channels.

The D/A-converters for the control of the DC-motors can drive between −10 V and 10 V with a 16 bit resolution. Stepper axes can either operated in step/direction or CW/CCW input mode. The update period for both axis configurations is 62 µs. Generally digital and analogue signals are separated (with a respective ground channel) to prevent noise carry-over. The NI-7344 must be supported by driver units to power the actuators.

Folding Mirror Motorization

To tilt the folding mirror in the spectrometer, motorized micrometre screws are used, as visible in Fig. 4.14. The screws are driven by stepper motors *Faulhaber PRECIstep AM1020A-025*. Combined with gear and screw, a maximum lift of about 8 mm can be achieved with 10^5 steps. Given the base lengths of 122 mm (dispersion) and 75 mm (cross-dispersion), this results in theoretical angular resolution of 0.14″/step and 0.22″/step, respectively. This provides a position accuracy on the CCD detector, at the given spectrometer focal length, well under the required 0.1 px in dispersion direction; in cross-dispersion direction it is slightly above.

The operation of the precision screws driven by stepper-motors, is far less delicate than the telescope control, because the precise positioning is not time-critical (compare Section 5.1). As driver the standard combination of the stepper motor controller L297 and the dual full bridge driver L298 (both STMicroelectronics) is used. The wiring (in connection with NI-7344) is shown in Section A.2.

4.10.3 Telescope Control Hardware

The telescope's task is to uninterruptedly feed the spectrometer with radiation of constant radiation distribution. In the original set-up this is achieved by imaging the light source onto the entrance slit which ought to stay fully illuminated during the whole measurement cycle. With the sun disk's image only slightly greater than the height of the entrance slit (1 mm) already small image displacements result in an incomplete slit illumination. In the worst case telescope misalignments of just below 3′ already lead to signal reductions.

With the introduction of a homogenizing optical fibre (see Section 4.9) the performance requirements of the telescope cycle are considerably lowered. The entrance slit is illuminated by the directly attached optical fibre whose exit surface plane should by conception provide uniformly distributed intensity independent of the illumination situation on the fibre entrance plane. Slightly eccentric spot positions result only in a general attenuation of intensity assuming perfect homogenization quality. Applying a 400 µm core hexagonal fibre, no attenuation occurs for displacements not exceeding 5.5′.

The mechanic and electronic hardware components involved and their interplay is depicted in Fig. 4.32.

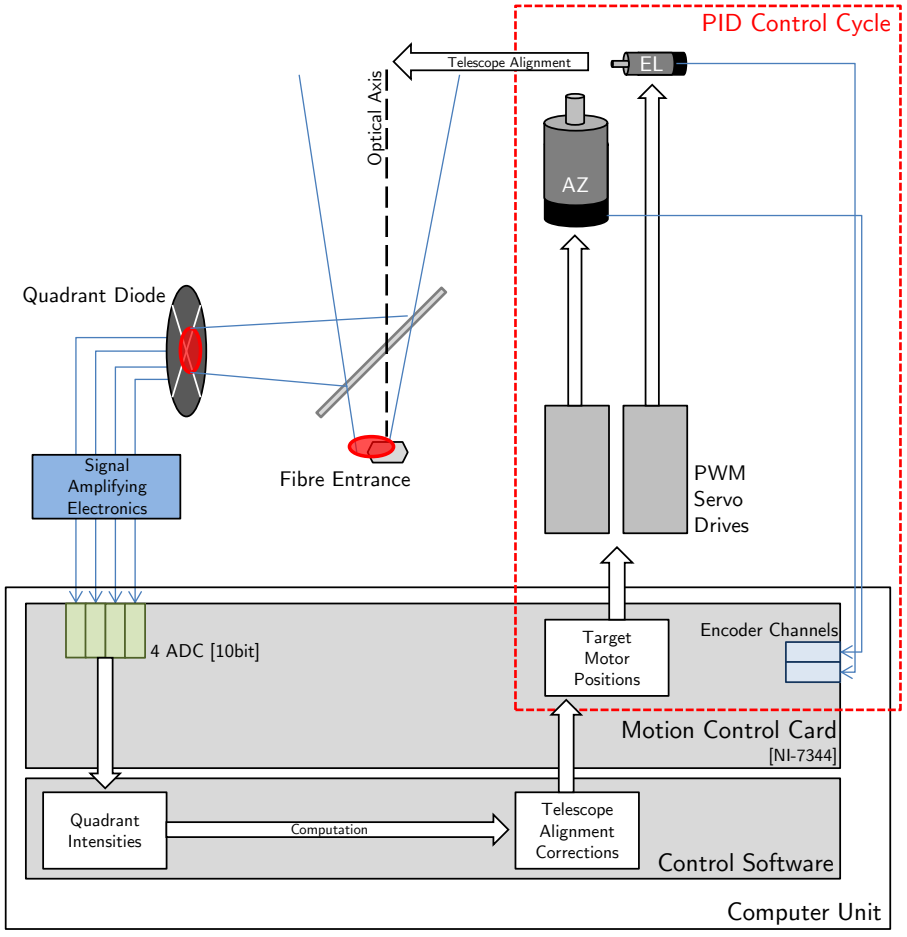

Figure 4.32: Scheme of the active telescope control cycle: The intensities on the quadrant diode are sensed by the motion control card's A/D converters. The registered values are transposed into information on the displacement of the spot from the quadrant diode center and hence from the optical axis. The displacement is then eliminated by adjusting the telescope motor positions.

Quadrant Diode

The sensor implemented to determine the misalignment of the telescope, thus serving as the main feedback sensor in the control cycle, is a circular quadrant diode *JQ 50P* by *Electro Optical Components (EOC)*. The total diameter of the photosensitive area amounts to 7.89 mm and the active area is 12.5 mm^2. The non-photosensitive gap between the quadrants is 50 µm

wide. The spectral range lies between 400 nm and 1100 nm. The portion of the light branched off by the beam-splitting quartz plane plate is not yet spectrally restricted.

The quadrant diode is mounted on a holder, allowing precise three-dimensional adjustment of its location. The position of the diode perpendicularly to the beam has to be adjusted to ensure that a placement of the sun image at the center of the homogenizing fibre entrance corresponds exactly to a central position on the quadrant diode. The adjustment in the third dimension affects the imaging of the light beam and thus the responsiveness of the telescope control cycle. If the spot becomes too small and rarely illuminates all quadrants at a time, the position determination of the intensity center of gravity is rendered almost impossible (see Eq. 5.17) which can lead to unwanted overshooting of the motor system when trying to adjust the telescope alignment. A reasonable spot size has been found at about 20 % to 30 % of the total diameter. The exact procedure to deduce the spot position on the detector from the measured intensities is described in Section 5.1.2.

As for the recording of the actual spectra, the telescope alignment procedure has likewise to deal with a dynamic range of signals reaching up to six orders of magnitude: Contributions to handle said dynamic range come from the A/D-channels of the motion control card acquiring the signals with a 12-bit resolution, from the optical filter regime described in Section 4.7.1 and most importantly from the signal amplifier module developed at ISAS Berlin, whose schematic circuit diagram is depicted in Fig. 4.33.

For each channel the photo current generated by the diode is converted into voltage with an impedance converter based on the operational amplifier (OpAmp) *AD549* by *Analog Devices*, which is suited for applications which provide very low signal current [Analog Devices, 2008]. The voltage is then further amplified, whereby the signal amplification can be raised by another factor of 1000 for lunar measurements. Thermal noise (Johnson-Nyquist noise) can be accounted for being the main disturbance source. The noise voltage U_{JN} after the impedance conversion can be calculated by:

$$U_{JN} = 2 \cdot \sqrt{k_B \cdot T \cdot \Delta f \cdot R} \tag{4.10}$$

with k_B the Boltzmann constant, T the absolute temperature, R the resistance (1 MΩ) and Δf the bandwidth (determined by the time constant τ of the RC circuit: $\Delta f = \frac{1}{2\pi\tau} = \frac{1}{2\pi RC}$). In our case this results in a noise voltage of slightly above 10 µV, which is supported by experimental evidence. With an amplification by a factor of 1000 and an AD-converter measurement range of 0 V to 10 V this helps to cover up three orders of magnitude of the whole dynamic range between solar and lunar measurements.

The 1 MΩ resistors used in the circuit (Vishay CNS 020, [Vishay, 2012]) have very small temperature coefficients of ± 10 ppm/°C (at 70 °C). To minimize the integral drift of every amplifier channel, the different electronic components (especially resistors) have been tested regarding their temperature behaviours and a suitable combination has been selected. When measuring in high-amplification mode the remaining offsets and their drifts are monitored and computationally eliminated.

To prevent the occurrence of parasitic currents which could easily exceed the specified bias current of the OpAmp (10 fA) various measures are adopted: The electronic components are mounted highly isolated onto the circuit board using underlying Teflon sockets with the OpAmp connectors not soldered onto the board. The circuit surface is particularly purged and enclosed in a hermetically sealed aluminium casing which itself is insulated from the instrument's mechanical structure with a plastic foil.

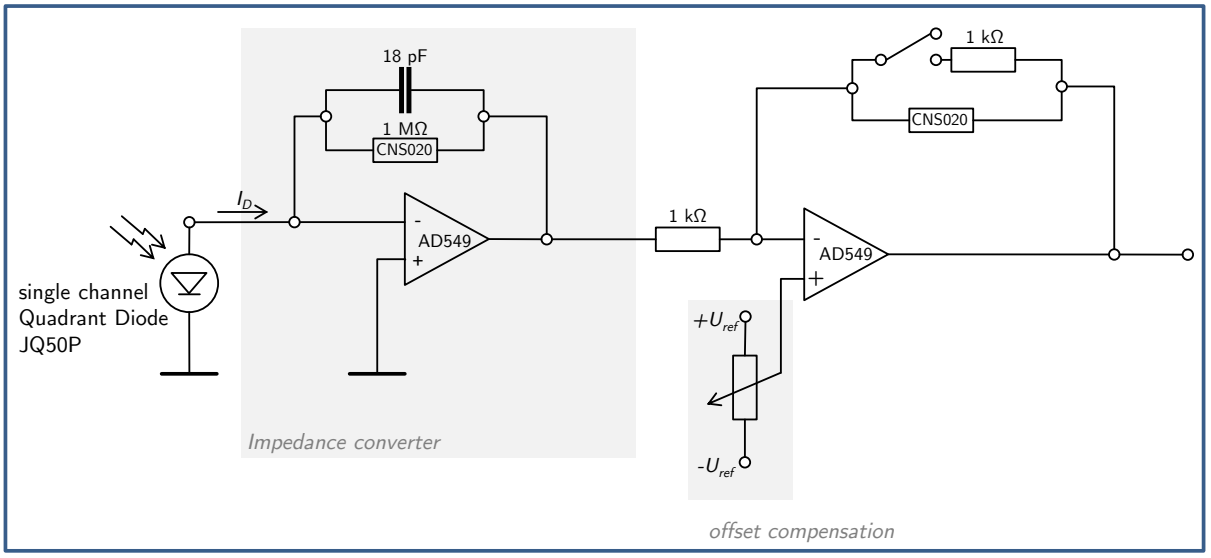

Figure 4.33: Single channel of the amplifying electronics used to register the signals of the quadrant diode. The current produced by the photodiode is converted into voltage with an impedance converter and further amplified. The amplification grade can be increased by a factor 1000 in case of lunar measurements.

With the set-up described above, telescope tracking of the lunar disk has been successfully carried out, even for very low lunar phase angles. Fig. 4.34 shows the integral quadrant diode intensity when scanning the lunar disk with the telescope using a rectangular grid pattern. Under clear sky conditions with the elevation angle at 41° and the lunar phase angle at 102° the S/N ratio ($\frac{A}{\sigma_A}$, with A the signal amplitude) for a single channel was at about 7 to 8.

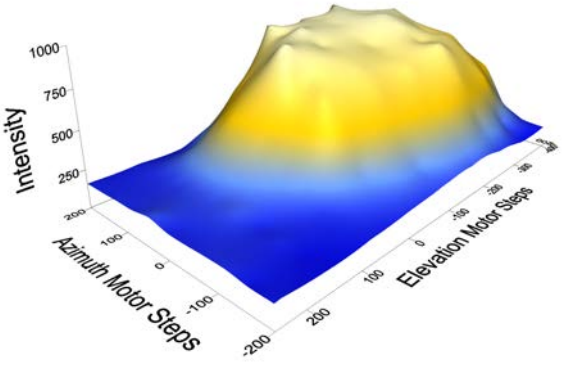

Figure 4.34: Registered integral quadrant diode intensities when scanning the lunar disk with the telescope following a rectangular grid pattern. The maximum signal amplitude reaches up to 600 counts for all channels combined (above the offset socket of approximately 200 counts). The mean standard deviation of intensity for a single telescope position reaches up to 20 counts per channel. The scan was conducted at a moon phase of 102° and an elevation angle of around 41° under clear sky conditions.

DC Motor Drives

In absence of motion control card on-board drivers, the telescope's DC-motors are powered by servo-amplifiers *Maxon ADS 50/5* [Maxon Motor, 2009].

For operation with high efficiency the analogue DC-voltages generated by the motion control card are transformed into pulse width modulation signals (PWM) by this high-performance amplifier which is supplied with 12 VDC to 50 VDC. To ensure quick acceleration and deceleration for both motion directions a 4-quadrant servo amplifier is used. As depicted in Fig. 4.35(a), such an amplifier consists of an H-bridge with two times two transistors in a row, each with a fly-back diode in back-direction. By switching one channel permanently and applying a PWM signal to a second, as shown in Fig. 4.35(b), acceleration and braking in clockwise and counter-clockwise movements can be initiated. The motor speed is determined by the ratio of the pulse-length between upper and lower state.

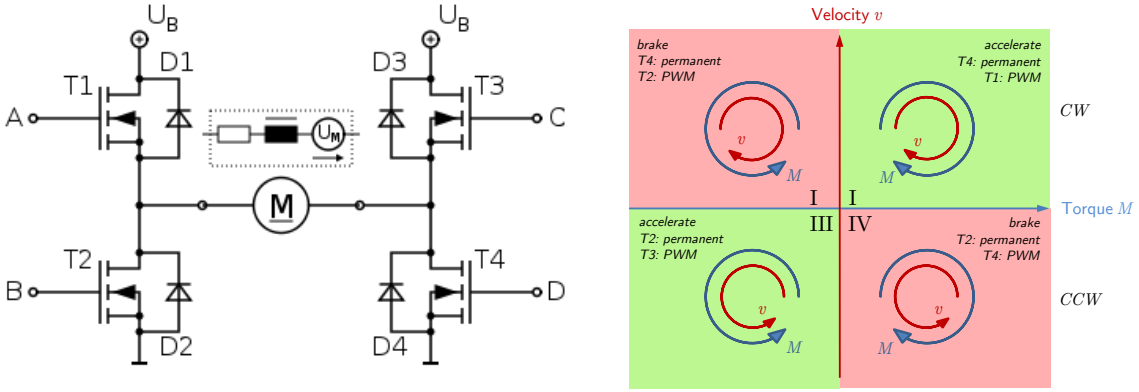

(a) Electronic scheme: H-bridge around DC-motor (with equivalent circuit diagram). 4 channels (A-D) where each disposes of a transistor (T1-T4) and a fly-back diode (D1-D4); (from [Wikipedia, 2013])

(b) Operation modes: Acceleration and deceleration can be effectuated for both travel directions by permanently switching one channel and apply a PWM-signal to a second

Figure 4.35: Principle of a 4-quadrant servo drive.

The PWM frequency is 50 kHz. The unit gives access to several parameters through potentiometers, such as gain, current limit or speed limit. It can be operated in various modes: i.e. current control mode or encoder mode. The electronic connection with the motion control card is depicted in Appendix A.1.

4.10.4 USB I/O-Module

For device control and data acquisition a data interface module *Meilhaus Redlab 1408FS* is installed. This compact device (83 × 80 × 26 mm) is powered and controlled via USB 2.0. It disposes of analogue input channels (8 single-ended or 4 in differential mode) acquiring data with a 14-bit resolution within a configurable measurement range (max. ± 20 V). Three channels are used for continuous monitoring of the temperature inside the measurement instrument. Temperature sensors *Innovative Sensor Technology TSic 303* are located in the telescope, next to the CCD detector head and in the vicinity of the spectrometer components (see also Fig. 4.29). The solid-state sensor has an accuracy of ± 0.3 K and provides an analogue signal proportional to the temperature [Innovate Sensor Technology IST, 2012]. If considerable temperature changes occur during the measurement process the control software can initiate the start of various calibration routines (i.e. dark image acquisition, wavelength stabilization, apparatus function determination). The temperature sensor circuit board is depicted in Appendix A.4.

Figure 4.36: USB I/O module *Meilhaus Redlab 1408FS* used for digital control of various hardware devices and analogue data acquisition.

Beside two analogue output channels the devices disposes of 16 TTL/CMOS digital channels, programmable as inputs or outputs. They are used to control the binary states of following devices, by addressing either mechanical TTL-relays or MOSFET-switches:

- halogen lamp [on/off]
- argon lamp [on/off]
- quadrant diode amplifier [high/low]
- shutter [active/inactive]
- optical filter [in/out]

4.10.5 External Sensors

To guarantee ease of transport and reduction of cabling, only two sensors belonging to the measurement system remain outside the instrument (see Fig. 4.29). The meteorological sensor is installed slightly apart from the instrument to obtain trustworthy ambient meteorological data. Though in principle possible, it was desisted from placing the GPS sensor inside the instrument, not to further complicate the mechanical and electronic design of the telescope.

Time Referencing and Positioning

For the computation of the sun and moon ephemeris, the geographical latitude Φ and longitude Λ of the observation site and the time *UTC* (*Universal Time Coordinated*) have to be known. For measurements aboard a moving platform with changing coordinates, the data have to be frequently updated. The applied sensor is an *ANTARIS 4 SuperSense EvaluationKit AEK-4H* manufactured by *u-blox*, a 16-channel single frequency receiver (L1 frequency, C/A-Code). The accuracy for positioning is about 2.5 m (Circular Error Probable) [u-blox, 2007]. Timing accuracy is 50 ns. Radio signal acquisition is carried out using a standard active GPS patch antenna. A USB interface ensures both, powering of the device and data connection. The device provides information via UBX or NMEA protocol on position, time and satellite constellation (DOP values) with an update rate of 4 Hz.

Meteorological Sensor

As described in Chapter 3 to conduct a fairly precise computation of the ray path for calculation of the radiative transfer an atmospheric model is used which for the lowest layer takes into account the meteorological conditions at the measurement site. For highly precise determination of local temperature, air pressure, and relative humidity the widely used *Vaisala*

(a) GPS-Sensor u-blox Antaris 4

(b) Meteorological Sensor Vaisala PTU300

Figure 4.37: External sensors belonging to SOLUSAR measurement system.

PTU303 device is applied (see 4.37(b)). The key specification of this sensor is given is Tab. 4.4.

4.10.6 Electric Disturbance Suppression

When acquiring fullframe CCD images persistently overlaying stripe patterns can be observed (compare Fig. 4.38(a)). The pattern intensity and characteristics is found to be totally independent from the actual signal that is recorded by the sensor or from the CCD exposure time. It was assumed that the disturbances are electrically impressed onto the signal ahead of the CCD's A/D conversion. Due to the intensity invariance of the interferences, they become increasingly disturbing at low signal intensities.

The aforementioned disturbance pattern can be eliminated entirely by disabling the telescope actuation system. It was strongly indicated that the disturbances arise from an interference of the CCD sensor readout clocked at 50 kHz and the DC motor drivers operating with a pulse-width modulation frequency exactly five times greater (250 kHz). This assumption was supported by a Fourier analysis of single CCD line signals which show a predominant occurrence of signals with repetition lengths of around 2.5 and 5 pixels, respectively, as shown in Fig. 4.38(b).

In order to suppress or at least attenuate the disturbance's influence different measures have been taken, most notably the decoupling of the telescope motor/driver system from the instrument chassis. Therefore the azimuth motor is attached using non-conducting plastic screws with a plastic foil between motor and chassis. Both servo amplifiers are likewise electrically detached from the mechanical structure. Said measures reduce the amplitude of the occurring disturbances by roughly a factor 2.

Furthermore a full galvanic insulation of the CCD camera from the measurement system has been carried out to prevent the spread of disturbances via signal, power or ground conductors. This includes different actions (see also Fig. 4.39):

	Parameter	Value
Pressure	Sensor	Vaisala BAROCAP (Class A)
	Measurement range	500 hPa to 1100 hPa
	Accuracy at 20 °C	±0.1 hPa
	Total accuracy (−40 °C to 60 °C)	±0.15 hPa
	Long-term stability	±0.1 hPa/yr
Temperature	Sensor	Pt100 RTD 1/3 Class B IEC 751
	Measurement range	−40 °C to 60 °C
	Accuracy (at 20 °C)	±0.2 °C
Humidity	Sensor	Vaisala HUMICAP 180
	Measurement range	0 % to 100 % RH
	Accuracy (at 15 °C to 25 °C)	±1 % RH (0 % to 90 % RH) ±1.7 % RH (90 % to 100 % RH)
Various Specs	Communication Interface	RS232C
	Operating Voltage	10 VDC to 35 VDC (24 VAC)
	Ambient operating temperature	−20 °C to 60 °C
	Ambient operating humidity	non condensing
	Data Logger Module	10 s logging period 13.7 million logged points

Table 4.4: Specifications of the meteorological sensor Vaisala PTU303

- The CCD camera is henceforth powered by a separate car battery and thus fully decoupled from the power supply of the measurement instrument and from any influence of the power grid.
- The digital signal line transmitting the camera-driven status signal of the shutter system is galvanically isolated by means of an optical coupler.
- USB 2.0 signals for host communication and data transmission are converted to an optical signal and transferred via an optical fibre.

The USB signal transducer is an *Icron USB Ranger 2224* shown in Fig. 4.40. It allows the non-electronic transmittance of USB 1.1 or USB 2.0 signals over distances up to 500 m with data rates up to 480 Mbps. The system consists of a local unit connected to the host computer and a remote unit communicating with the USB devices through an integrated 4-channel USB-hub. In the local and remote unit the signals are converted from USB to optical signals and vice versa. The optical signal is transmitted via a multimode optical fibre [Icron, 2010a,b].

4.11 Instrument Mechanical Structure, Enclosure and Mounting

Most parts of the instrument's mechanical structure are made of aluminium which guarantees sufficient mechanical stability, good machinability while keeping the weight and costs relatively low. However, the internal vertical main carrier structure of the spectrometer attached to the telescope's encasement is made from invar (alloy of 64 % Fe, 36 % Ni, thermal expansion coefficient: 1.2 ppm/°C) to minimize thermal expansion along the optical axis of the spectrometer which could impair spectra image quality due to defocussing.

The enclosure of the instrument is of great importance, as in the case of SOLUSAR the whole instrument is located outside without shelter and hence can be exposed to all weather conditions including precipitation and markedly changing temperatures. Secure preservation of

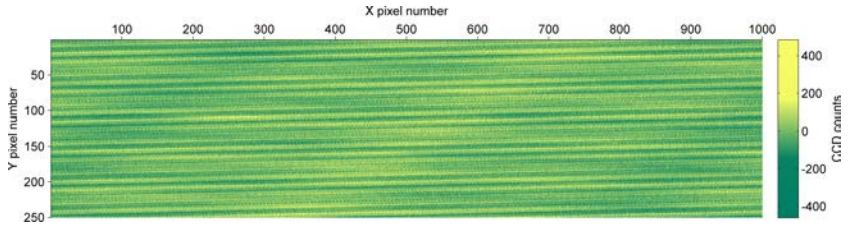

(a) Typical stripe pattern on fullframe CCD image with amplitudes reaching up to 500 counts (maximum count number 65536)

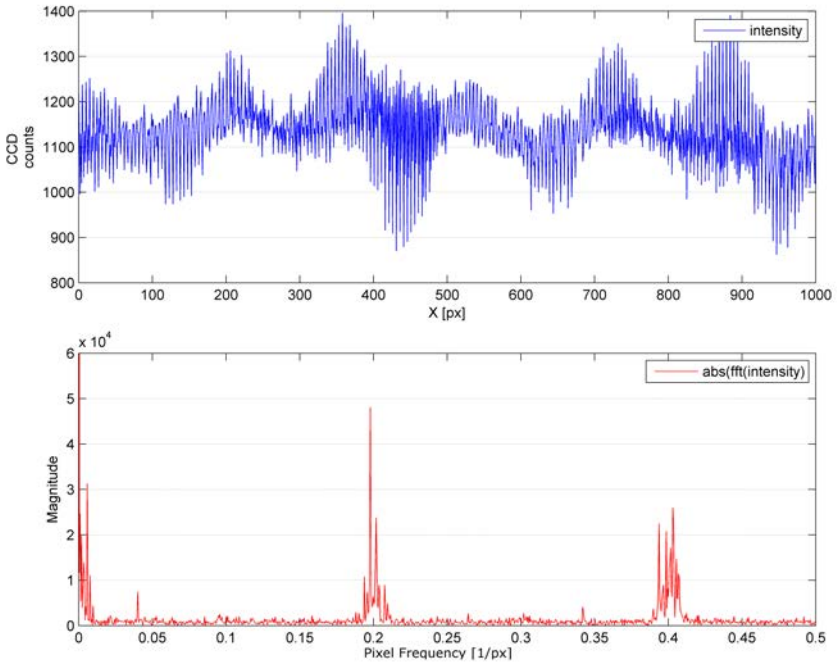

(b) Fourier analysis of a single CCD signal line. The occurring pixel frequencies hint at interference between the 50 kHz CCD pixel clock and the 250 kHz PWM frequency of the DC motor drivers

Figure 4.38: Electronic disturbances overlaying the spectral information on the CCD

the measurement capability has to be safeguarded under these conditions while still allowing relatively easy access to the different internal parts of the instrument, either optical or electronic. Additionally, a steady powering and data connection to the external control unit must be secured in every case of application.

The spectrometer is enclosed in a cylindrical aluminium tubing which is attached to the encasement of the telescope. The hull has a maximum diameter of nearly 25 cm and a thickness of 5.5 mm which provides the ruggedness in case of instrument transport. For maintainability reasons and to facilitate the closing/opening procedures the hull is sectioned into vertical parts, as shown in Fig. 4.41(b). The final version of the hull containing the stretched instrument consists of totally five sections: A top interface part enabling the connection to the telescope, the two main parts covering the spectrometer, a small additional part to compensate the additional instrument length due to the introduction of the homogenizing fibre and and the bottom part with the terminating baseplate.

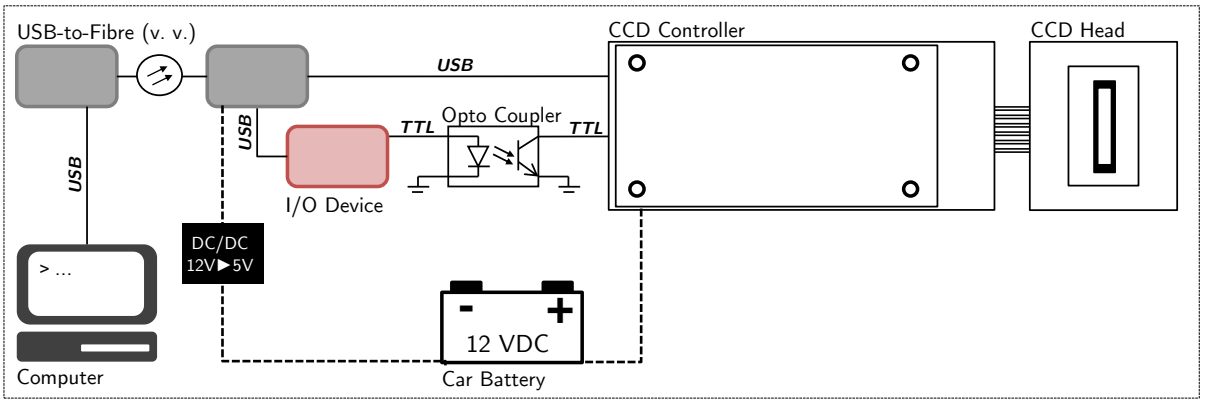

Figure 4.39: To prevent the spreading of electromagnetic disturbances by wire, the camera system is galvanically isolated using a separate power supply and optical decoupling of signal lines.

Figure 4.40: Icron USB-Ranger 2224. Data transfer between the various devices on the instrument side and the host computer is accomplished through conversion to optical signals and transmission via optical fibre. USB lines on the instrument side are bundled in a 4-channel USB-Hub (right device, powered by the car battery supplying the camera) and data conveyed via multi-mode fibre to the host-side device.

To avoid the ingress of water the joints of the different enclosure parts are all sealed with O-rings. In the bottom part a total of three waterproof cable passages are included for the lead-through of power cables, motor steering cable and USB lines. To prevent water condensation inside the instrument desiccant bags are inlaid.

For short-time instrument deployments the system can stand stable on the enclosure's base plate. For fixed installation or the application on a moving platform the instrument is constructed to be mountable on a tripod. The instrument is held by an outlet of the telescope encasement in the mounting opening of the tripod (see Fig. 4.41(b)). For stationary application the instrument is mounted in a four-legged stand which can be bolted to a ground plate (Fig. 4.42(a)). In case of a deployment on a vessel the instrument is held in a gimbal mounting (Fig.4.42(b)) which should reduce the largest amplitudes of the instrument's vertical tumbling. The gimbal joint is borne by a tripod. To limit the influence of sudden occurring up-lifts each leg is mounted on a shock-absorbing damping element.

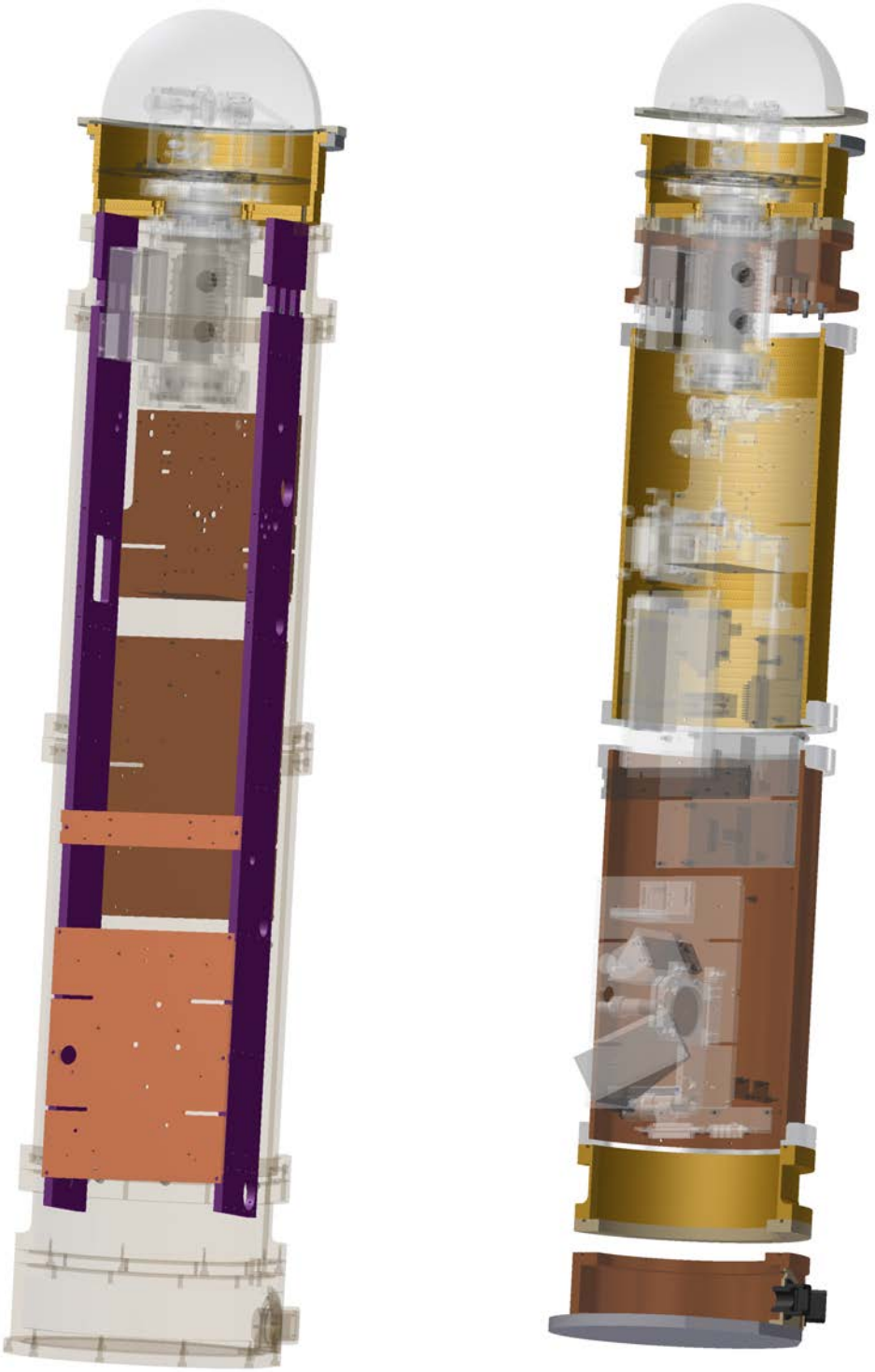

(a) Vertical main carrier structure made from invar (purple colour) attached to the telescope encasement. Copper coloured are the aluminium base-plates carrying the various optical components.

(b) Instrument hull: For maintenance purposes the aluminium hull is sectioned in several parts. The joints are sealed with O-rings to avoid the ingress of water.

Figure 4.41: CAD display of the SOLUSAR instrument mechanics.

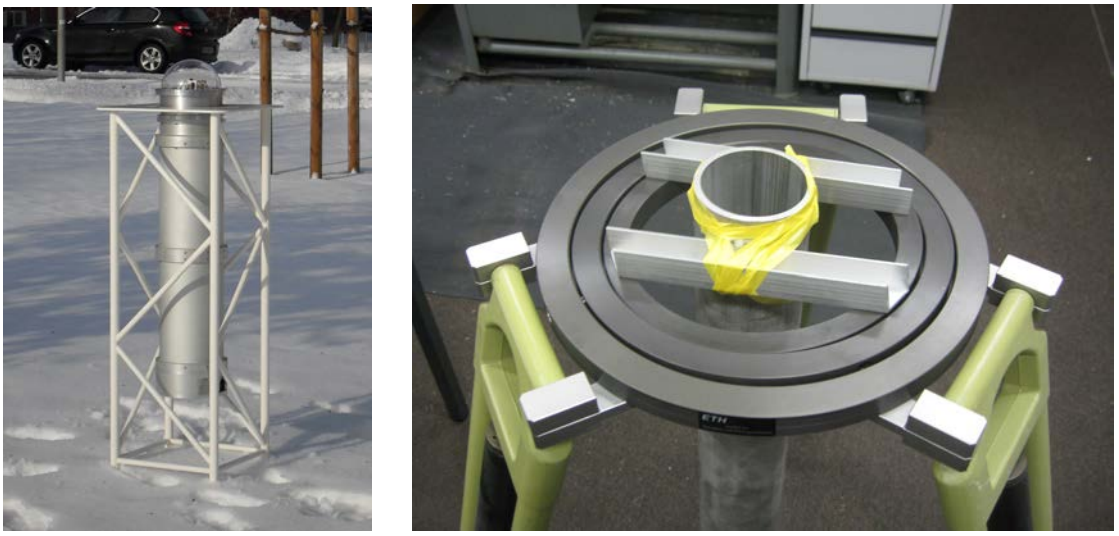

(a) Instrument stand for static measurements

(b) Tripod with gimbal suspension for vertical stabilization of the instrument during deployment on moving platforms. In this picture the instrument is simulated by means of a vertical tube

Figure 4.42: SOLUSAR instrument stands.

5

Measurement Process

This chapter describes the algorithms contained in the software which has been developed for the automatic control of SOLUSAR's measurement process. For the sake of readability the chapter is roughly divided into issues belonging to *telescope control*, *camera control* and *spectrometer control*. In the software itself these aspects are not as clearly separated as the different tasks are deeply entwined and run in parallel.

Furthermore some developed algorithms that are not used in the final control software version are described and discussed. Additionally possible future algorithms are outlined which could be beneficiary and helping to streamline the whole measurement process.

5.1 Telescope Control

As described in Section 4.3, the fundamental task of the telescope unit is the collection of as much light as possible from the radiation sources sun and moon and to guide it precisely onto the entrance slit thus feeding the spectrometer unit. For the predecessor measurement set-ups GEMOSS and SAMOS an astronomical telescope was modified for the specific purpose. As these instruments were designed solely for static application on ground-based measurement sites, tracking of the slowly moving target was accomplished only through pursuit of the computable sun trajectory. This procedure will be called *ephemeris tracking* henceforward .

In order to enable instrument operation on tilting platforms such as vessels, it is mandatory to dispose of a telescope unit which fulfils its primary task even if the instrument's vertical axis is undulating with respect to the gravity vector so that the computed azimuth and elevation angles of the targeted celestial body can only be used as a first approximation of the target direction. The algorithms performed to track the light source – also under unclear alignment of the instrument – and the preliminary procedures for the telescope orientation are outlined in this section.

5.1.1 Telescope Orientation

Before the actual tracking process can be initiated various referencing processes have to be carried out in order to determine conversion parameters between the different coordinate systems:

- *Internal Orientation*: Referencing of the manoeuvrable telescope mirror system with respect to the entire measurement system.

- *External Orientation*: Determination of the instruments orientation in a horizontal topocentric coordinate system, the system in which the celestial body's coordinates are computed.

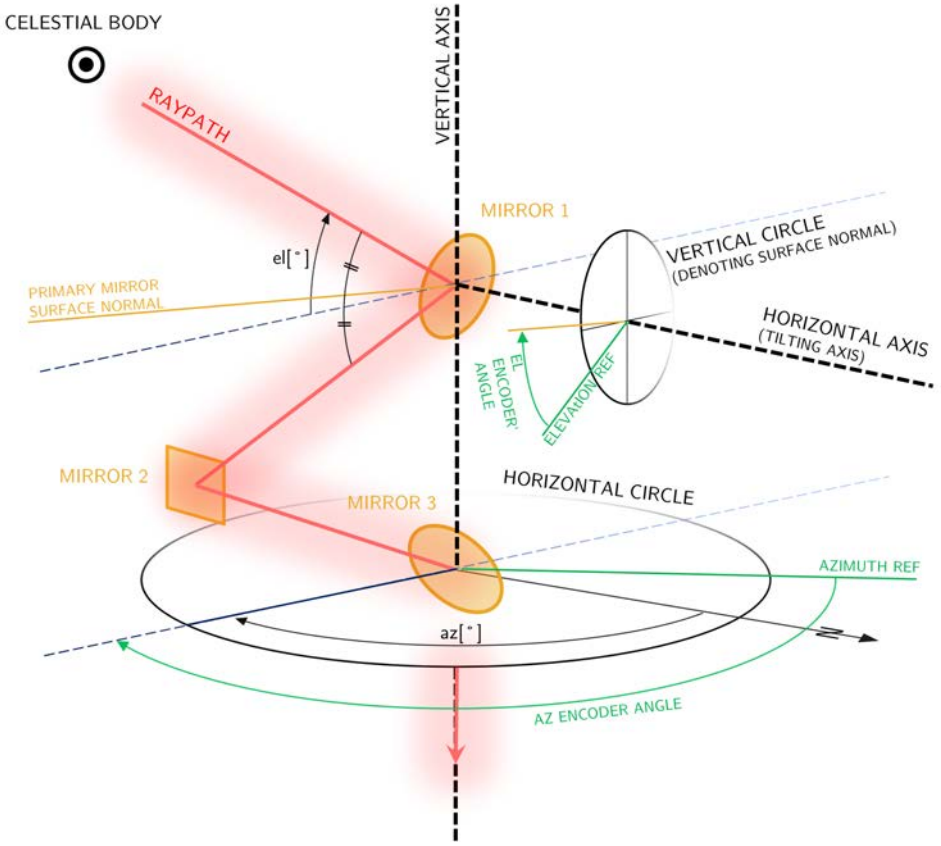

Figure 5.1: Relation between the horizontal topocentric coordinate system in which the celestial body ephemerides (azimuth and elevation) are expressed and the telescope motor coordinate system, when the measurement system is perfectly vertically aligned. The determination of the transformation parameters between the two coordinate systems is described in Section 5.1.1.

The internal orientation of the instrument is conducted only once after the initialization of the instrument. The external orientation however has to be carried out repeatedly when measuring in a *dynamic mode* (on a moving platform). The instrument orientation steadily changes and has to be redetermined after interruption of the measurement cycle, either due to various calibration tasks which are slotted in, or due to bad weather conditions. When measuring in *static measuring mode* the external orientation procedure is also carried out only once.

Internal Orientation

The internal orientation process is conducted to determine the alignment of the mirror system in reference to the whole spectrometer instrument. The position encoders of the telescope motors do not dispose of index channels which could serve as position reference points. Therefore the collimated beam of the halogen lamp (stationary mounted in the telescope encasement underneath the revolving platform) directed onto the telescope's primary mirror, serves as internal aiming reference: The orientation process consists of a search algorithm to find the

mirror system alignment where the halogen light spot (center of gravity of its intensity distribution) is precisely imaged onto the quadrant diode center and thus perfectly illuminates the entrance slit.

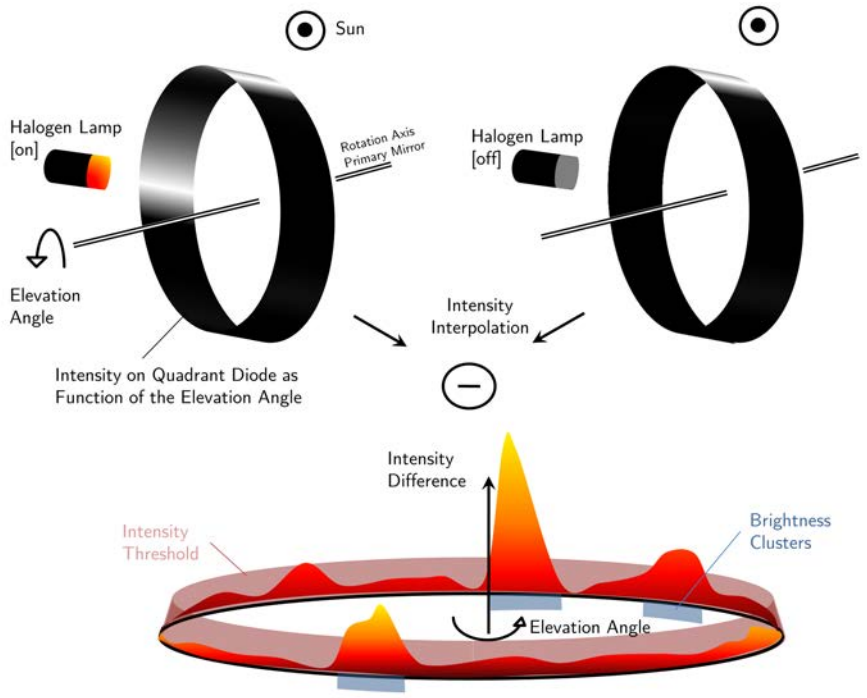

Figure 5.2: Depiction of the internal telescope orientation algorithm: In an approximate azimuth plane the direction of the collimated halogen beam is searched by analysing the quadrant intensity differences during two elevation mirror revolutions, with the bulb switched on and off, respectively. Thus the influence of external light, as from the sun, on the search procedure can be limited.

An approximate vertical plane containing the beam of the halogen bulb and the vertical telescope axis is found with the help of an inductive position sensor (mounted underneath the revolving platform) serving as an initial azimuth reference. The approximate elevation of the halogen bulb beam direction is searched in said plane by analysing the integral brightness recorded on-the-fly by the quadrant detector during a whole revolution of the elevation mirror (mirror 1) conducted with relatively slow velocity. In order to suppress the possible influence of the far brighter sunlight and its reflections within the telescope, the brightness differences during two revolutions - with the halogen lamp switched on and switched off respectively - is used as shown in Fig. 5.2. The brightnesses are recorded together with the corresponding motor positions in each of the two revolutions. For the sake of a rapid process sample points are acquired as fast as the electronic set-up allows as the mirror moves and not at specified way-point halts. To subsequently harmonize both scan samples location-wise, the intensity for specific positions is interpolated using a *piecewise cubic hermite interpolation (PCHIP)* algorithm. This algorithm links subsequently measured supporting points $[el_i, I_i]$ and $[el_{i+1}, I_{i+1}]$ (el being the elevation angle and I the integral quadrant intensity) with a cubic polynomial $s_I(el)$ for el between el_i and el_{i+1} of the form:

$$s_I(el) = a_i(el - el_i)^2(el - el_{i+1}) + b_i(el - el_i)^2 + c_i(el - el_i) + d_i \tag{5.1}$$

The polynomial coefficients are chosen in a way to ensure continuous first derivatives s_i' at the supporting points. PCHIP in contrast to the widely used cubic spline interpolation does not

provide as smooth results since the second derivatives do not have to be continuous. It however copes better with noisy data and allows faster computing. For a more detailed description of the algorithm and how the coefficients are determined, see Boor [2001].

The sample period of the set of raw data points $[el_i, I_i]$ is about 500 elevation motor steps, which corresponds to an elevation angle resolution of roughly 1°. As the integral intensity of the whole quadrant diode is continuously registered, every sample point covers up to ± 300 steps, if the telescope is azimuthally well aligned. Thus no run-through of bright spots should go unnoticed. The interpolation sample period is 200 steps. After the interpolation of both samples intensity differences for each interpolated motor position can be computed. Typically this exhibits one area where greater brightness differences occur - the approximate direction of the halogen light. But not uncommonly additional areas with considerable or even stronger intensity differences can be observed, mostly caused by rapidly changing illumination situations (cloudy weather) between the two mirror revolutions. To quickly identify the sought position in the intensity difference sample, contiguous clusters of positions with brightnesses exceeding a certain intensity threshold are identified. Consequently the telescope mirror is made to aim at the brightest position found within the clusters and it is checked if a power on/off of the halogen bulb results in a sufficient intensity lift on the quadrant diode. With this procedure an approximate reference direction is reached and the automatic tracking algorithm later described in Section 5.1.2 can be initiated to perfectly place the halogen light-spot image on the quadrant diode center and thus find the final reference direction of the telescope motor system. The described process normally lasts between 15 s and 30 s.

To limit the above described influence of incident sun light during the search procedure the telescope is protected from radiation sources outside the current azimuth plane with a light-weight aluminium cover as shown in Fig. 5.3.

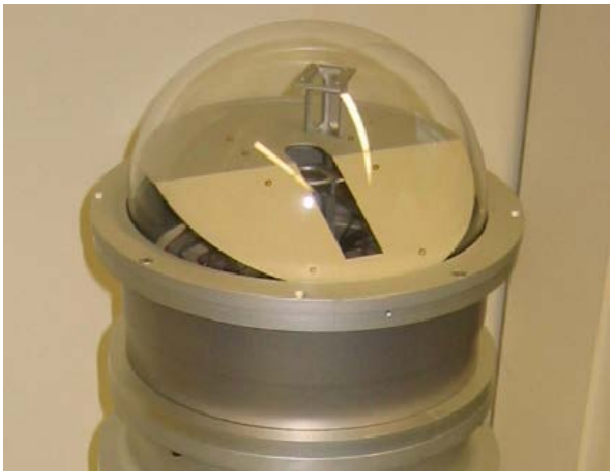

Figure 5.3: Light-weight aluminium cover mounted on the revolving mirror system. It minimizes the occurrence of false light in the telescope while not compromising the speed of azimuthal rotation.

External Orientation using the Sun

For the external orientation in *static deployment* of the instrument only the azimuthal alignment of the instrument has to be determined, if the instrument is properly vertically mounted. For this purpose SOLUSAR makes use of the sun or moon ephemerides, which can be computed given the time and coordinates of the measurement site. With the telescope directly

aiming at the respective celestial body, the azimuthal offset o_{az} of the internal reference direction can be determined. The search is facilitated by the known elevation motor position $c_{elev,cb}[counts]$ at a given time t, which can be computed by:

$$c_{elev,cb}(t) = \frac{S_{elev}}{360 \cdot 2} \cdot el_{cb}(\Phi, \Lambda, t) + \Delta c_{elev} \tag{5.2}$$

with el_{cb} being the apparent elevation of the celestial body at the position with geographical latitude Φ and longitude Λ at the time t (UTC). Ephemerides are computed using the *libnova* celestial mechanics library [libnova]. S_{elev} denotes the motor steps per single revolution. Due to the law of reflection a change of the aimed elevation angle requires only a mirror rotation of half the size, which is considered in the equation by the factor 2. Δc_{elev} is an instrumental constant reflecting the fact that the reference position (halogen bulb) does not correspond to an elevation angle of 0°.

Given the computed position of the elevation motor the telescope conducts a search move for the sun or moon which consists of an upward spiral movement around the vertical axis covering an elevation range of $[el_{cb} \pm 1°]$ with 0.5° between spiral cycles (approximately the apparent diameter of sun and moon). During the movement the intensities on the quadrant diode are again monitored in order to find the brightest spot along the trajectory. Analogue to the internal orientation process, the found approximate direction to the celestial body is then refined again using the quadrant tracking algorithm (Section 5.1.2). The azimuthal offset o_{az} in degrees then is:

$$o_{az} = az_{cb}(\Phi, \Lambda, t) - c_{az,cb} \cdot \frac{360}{S_{az}} \tag{5.3}$$

with az_{cb} the current azimuth of the sun at the given site, $c_{az,cb}$ the position of the azimuthal motor when the telescope aims at the target and S_{az} the steps per revolution in azimuth direction.

In order to be regarded as a valid offset value, the target tracking has to fulfil the demands of the *pointing check algorithm* described in Section 5.1.3 for a time period of 10 s, thus indicating sufficiently clear sky. Still in the case of hazy conditions orientation deviations of the offset value of a few tenth of a degree can occur.

In the case of measurements in the *dynamic mode* on a moving platform the procedure described above has certain flaws: There exists a substantial likelihood, that oscillation patterns occur where the telescope aiming does never coincide with the direction of the sun while conducting a vertical search spiral. An alternative search algorithm is proposed. The algorithm has been implemented and experimentally tested, though not in a real measurement set-up on a moving platform. In a first step, similarly to the described upward spiral, an elevation band with a range $[el_{cb} \pm \delta_{el}]$ is scanned with δ_{el} being considerably larger compared to the static mode, due to the virtually undulating horizon. As shown in Fig. 5.4 the elevation band in this case is rapidly scanned sinus-wise to find an approximate azimuth of the brightest spot. Either the entire band can be covered or the search can be abandoned as soon as the brightness exceeds a certain intensity threshold. The threshold depends on the expected apparent magnitude of the tracked celestial body referring to a given date and time.

From the brightest spot in the elevation band thus found, which serves as provisional aiming at the celestial body, a refinement of the search can be initiated by conducting a spiral move around the primary aiming, with the coordinates $[c_{az,0}, c_{el,0}]$ expressed in the motor reference system. The spiral has the form of an Archimedean spiral:

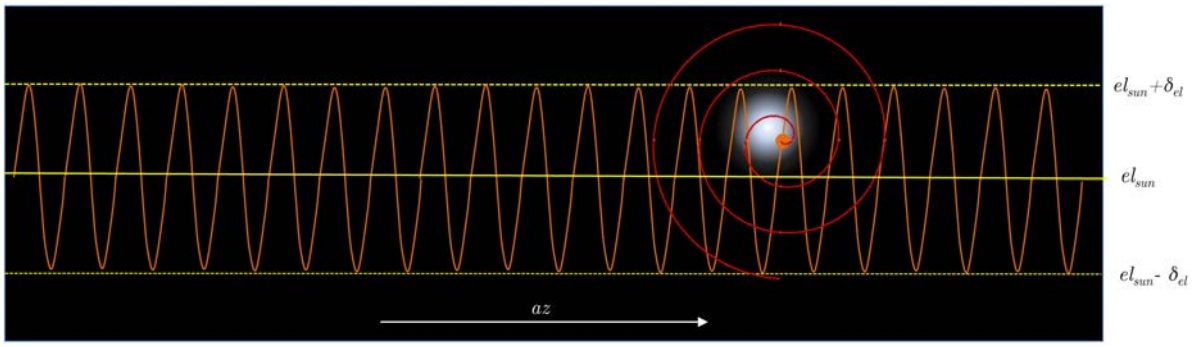

Figure 5.4: Proposed algorithm for external instrument orientation when measuring on a moving platform by means of a search procedure for the aiming at the targeted celestial body. Initially an elevation band is scanned using a sinus-shaped movement pattern while registering the intensities on the quadrant detector. The found approximate telescope alignment is then refined by looking for the brightest spot while the telescope follows an aiming trajectory of an Archimedean spiral.

$$c_{az}(t) = c_{az,0} + a \cdot \phi(t) \cdot \cos(\phi(t)) \tag{5.4}$$
$$c_{el}(t) = c_{el,0} + a \cdot \phi(t) \cdot \sin(\phi(t)) \tag{5.5}$$

with a the factor determining the spiral density and $\phi(t)$ the time-dependent angle.

For both, the Archimedean spiral move and elevation band search move, the so-called *contour mode* of the motion control card is used. This mode allows the approach of various consequent positions in a single move without halting at the specific positions, with both axis, azimuth and elevation, being moved simultaneously in coordination. For the search spiral it is vital, that the base point positions are computed in a way that the covered angular path per time remains constant. If $\phi(t)$ would be increased linearly this would result in a gradually accelerating motor movement. Thus brightness differences at the margin of the search area could vanish due to the shorter residence time of the celestial body's image on the brightness detector (quadrant diode). The arc length b between two consequent points at ϕ_1 and ϕ_2 is computed so it equals the distance between subsequent spiral arms:

$$b = \frac{a}{2}\left[\phi\sqrt{1+\phi^2} + \ln\left(\phi + \sqrt{1+\phi^2}\right)\right]_{\phi_1}^{\phi_2} \tag{5.6}$$

To find ϕ_2, Eq. 5.6 has to be solved numerically.

External Orientation using an Electronic Compass

With the measurement system deployed on a vessel, the telescope occasionally has to again find the correct aiming at the radiation source; either due to intermittent calibration tasks or due to obstructed sight i.e. by clouds. To shorten the non-measurement periods, a fast search algorithm is required, a wish not being entirely fulfilled by the above described scan procedure which can last over 30 s. To speed up and facilitate the search process, a device uninterruptedly providing the current bearing of the telescope would be helpful.

One possibility is the installation of an electronic compass device measuring the components of the local field strength of the earth's magnetic field. From the field strengths (M_x^h, M_y^h) measured by two orthogonally placed magnetometers the heading Ψ_M with respect to magnetic north can be computed:

$$\Psi_M = \tan^{-1}\left(\frac{M_y^h}{M_x^h}\right) \tag{5.7}$$

To derive the direction with respect to true geographical north N_G from the computed magnetic north N_M, the local declination angle δ has to be considered, which depends on the observer's location (latitude Φ and longitude Λ and is changing over time t), either by use of a geomagnetic declination chart or an IGRF (International Geomagnetic Reference Field) model [Kao et al., 2006]:

$$N_G = N_M + \delta(\Phi, \Lambda, t) \tag{5.8}$$

The integration of the declination is a major error source, as the local anomalies can deviate from the model values up to several degrees [Kao et al., 2006].

With the compass mounted on a platform which pitches and rolls, reliable heading can be determined by measuring the field strength in all three dimensions and by an additional determination of the pitch (Θ) and roll (Φ) angles. This allows the transformation of the 3-dimensional field vector $[M_x^b, M_y^b, M_z^b]$ into a local level field vector $[M_x^h, M_y^h]$. For the description of the different axes see Fig. 5.5.

$$\begin{bmatrix} M_x^h \\ M_y^h \end{bmatrix} = \begin{bmatrix} \cos\Theta & \sin\Phi\sin\Theta & -\cos\Phi\sin\Theta \\ 0 & \cos\Phi & \sin\Phi \end{bmatrix} \begin{bmatrix} M_x^b \\ M_y^b \\ M_z^b \end{bmatrix} \tag{5.9}$$

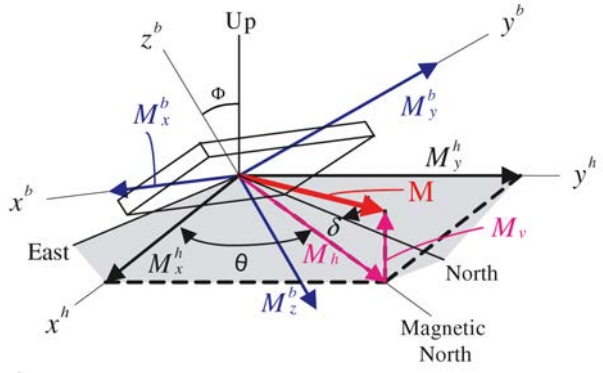

Figure 5.5: Heading determination using a three-axis magnetic compass (adapted from Kao et al. [2006]).

The accuracy of an electronic compass can be compromised by a multitude of error sources, ranging from errors of the magnetometer or of the inclination sensors over misalignment to hard and soft iron field distortions [Mach, 2003]. *Hard iron distortion* is induced by the presence of a magnetized object in constant distance to the sensor which imposes a permanent bias onto

the magnetometer. The corresponding hard iron distortion correction E_H of the heading Ψ_M can be estimated using following function:

$$E_H(\Psi_M) = R_H \cdot \sin(\Psi_M + \epsilon_H) \tag{5.10}$$

with Ψ_M the measured heading, R_H the amplitude and ϵ_H the phase shift of the hard iron influence, respectively. Further non-magnetized ferrous materials in the vicinity of the sensor are magnetized by the earth's magnetic field as a function of their alignment and consequently distort the total magnetic flux density sensed by the magnetometers. This is the so-called *soft iron distortion* influence on the heading Ψ_M that can be modelled using following approach:

$$E_S(\Psi_M) = R_S \cdot \sin(2\Psi_M + \epsilon_S) \tag{5.11}$$

with R_S, ϵ_S being amplitude and phase of the soft iron error signal.

As a model for the entirety of magnetic distortions $E(\Psi_M)$, including the influence of misalignment errors (coefficient a) the following equation can be used:

$$E(\Psi_M) = a + b \cdot \sin(\Psi_M) + c \cdot \cos(\Psi_M) + d \cdot \sin(2\Psi_M) + e \cdot \cos(2\Psi_M) \tag{5.12}$$

In case of SOLUSAR a digital compass *Honeywell HMR3300* with three-axis solid-state magneto-resistive sensors was tried to deploy, which is tilt compensated and can operate in a tilt range of ± 60° using a pair of accelerators (for the electronic scheme please see Appendix A.5). The specified heading accuracy is 1° with the resolution at 0.1° [Honeywell, 2005]. The update rate is 8 Hz. The sensor (dimensions: 37 mm by 25 mm) is mounted on the moving platform of the telescope. This allows the use of routines of the sensor performed by the onboard microcontroller to eliminate modest hard iron distortion. These require one complete slow turn in a level plane to expose the sensor to a set of different headings.

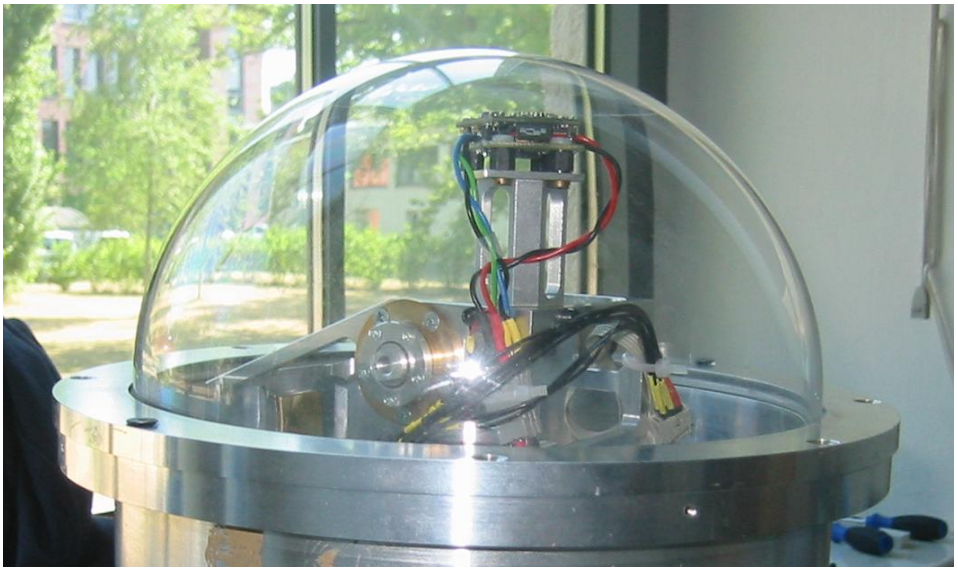

Figure 5.6: Electronic compass *Honeywell HMR3300* mounted on the revolving platform.

Testing showed that given the location of the compass within the telescope (compare Fig. 5.6) the measurement values of the heading are heavily affected by the magnetic fields produced

by the azimuthal DC motor. The on-board calibration routine is not capable to eliminate the effect, the distortion field strength clearly exceeds the earth's magnetic field strength. However, even more important is that the sensor varies its distance and exposure to the motor during the calibration turn, a fact that cannot be handled by the calibration routine. Efforts to shield the motor with sheets consisting of mu-metal (nickel-iron alloy with high magnetic permeability) to attenuate, at least, the impact of the interfering field remained unsuccessful.

As the sensor allows output of raw magnetometer measurement values instead of computed headings and inclinations it was tried to perform heading computation using additional information: Mach [2003] proposes a least square algorithm to find the parameters of Eq. 5.12 with the use of a gyroscope. The gyroscope determines the yaw rate of the movement. In our case this task can be perfectly performed by the azimuth motor encoder providing information on the rotation angle during the calibration revolution around the vertical axis. For n positions (preferably evenly distributed across a whole revolution) measurement data is acquired and headings computed according to Eq. 5.9. For each measurement position k we have:

$$\Psi(k+1) = \Psi(k) + \delta\Phi \tag{5.13}$$

with $\Psi(k), \Psi(k+1)$ the true headings at two consequent measurement points and $\delta\Phi$ the yaw angle increment between the two points. To include the determined headings through measurement Ψ_{meas}, Eq. 5.13 is rewritten to:

$$\Psi_{meas}(k+1) - E(\Psi_{meas}(k+1)) = \Psi_{meas}(k) - E(\Psi_{meas}(k)) + \delta\Phi \tag{5.14}$$

For any future index k Eq. 5.14 becomes:

$$k \cdot \delta\Phi - \Big[\Psi_{meas}(k) - \Psi_{meas}(0)\Big] = \Big[-E(\Psi_{meas}(k)) + E(\Psi_{meas}(0))\Big] \tag{5.15}$$

A stack of these observation equations can be solved using LSQ-algorithms to estimate the parameters b, c, d, e in Eq. 5.12. The full set of formulas for a gyroscope compass calibration is found in Mach [2003]. In the case at hand the raw magnetometer data were previously reduced by subtracting component-wise the field strength of the azimuth motor permanent magnetic field. For this purpose a full telescope revolution with a resolution of 1° was performed. The field strength differences were obtained between the original compass mounting position and a 30 cm uplifted position (with same alignment with respect to the telescope), where the influence of the motor should be limited.

Overall the application of the procedure described above improved the quality of the computed heading values only moderately. However, the accuracy remained very low (uncertainty of the heading clearly above ± 5°). Furthermore tests indicated that rotations and rotational oscillations with moderate velocity are not well mirrored by the sensor, as its response to field strength changes is lagging behind. All these findings render the device, unfortunately, practically inapplicable for the given task and clearly inferior to the scanning procedure.

Another possibility to search a celestial body in absence of orientation data is the deployment of a small zenith-looking image sensor (e.g. web-cam) in combination with a suited fish eye lens with a field-of-view covering the entire visible sky. From the images the alignment of the telescope with respect to the sun could be extracted with high frequency using image processing routines. Such a sensor could also provide information on the current weather situation (e.g. cloud coverage, haziness) and could thus even be used to preliminarily determine an optimal

exposure time for the spectrometers CCD sensor. This approach has not been implemented as yet.

5.1.2 Smart Telescope Control Cycle

The telescope's optical, mechanical and electronic design is conceived to fulfil the target tracking task also when the instrument is deployed on a moving platform, such as a vessel (or any other platform with a comparable moderate oscillation behaviour). The objective of the telescope's target tracking is to uninterruptedly fully illuminate the entrance slit during the measurement process. With the introduction of a light homogenizing fibre the requirements regarding the responsiveness of the telescope control cycle have been considerably reduced, since the exit face of the fibre is also uniformly illuminated if the image of the sun does not precisely hit the center of the entrance face of the optical fibre. However the larger the lateral deviation the lower is the intensity of the recorded spectra, as can be seen in Fig. 5.7.

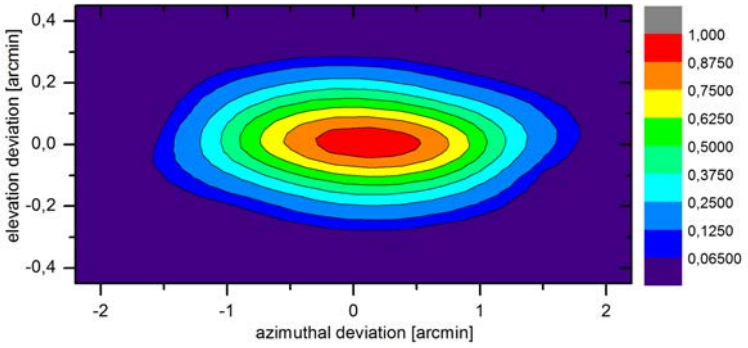

Figure 5.7: Relative spectrum intensity as a function of telescope misalignment, when using a homogenizing fibre (hexagonal 400 µm cross section). Measurements were conducted using spectra of the internal halogen lamp. The different dependence for the two directions (azimuth and elevation) is a result of the prolate shape of the halogen coil. In case of an imaged sun disk it is less pronounced.

The mechanical and electronic components involved in the telescope control cycle have been outlined in Section 4.10.3. This section shortly describes the signal handling in the autonomous telescope alignment process. The different steps are schematically depicted in Fig. 5.8.

Quadrant Diode Signal Treatment

The main feedback sensor providing information on the telescope's misalignment to the regulator (motor system) is the quadrant diode. As shown in Fig. 5.9(a) the imaged spot of the tracked light source partly illuminates four collaterally arranged photodiodes (each with the shape of a circular quadrant). From the intensities on the diode quadrants $I_1, \ldots, I_4$, the current deviation $[X_{CoG}, Y_{CoG}]$ of the spot's intensity center of gravity from the quadrant diode center can be estimated using the formulae:

$$X_{CoG} = \frac{(I_2 + I_4) - (I_1 + I_3)}{\sum_{j=1}^{4} I_j} \tag{5.16}$$

$$Y_{CoG} = \frac{(I_1 + I_2) - (I_3 + I_4)}{\sum_{j=1}^{4} I_j} \tag{5.17}$$

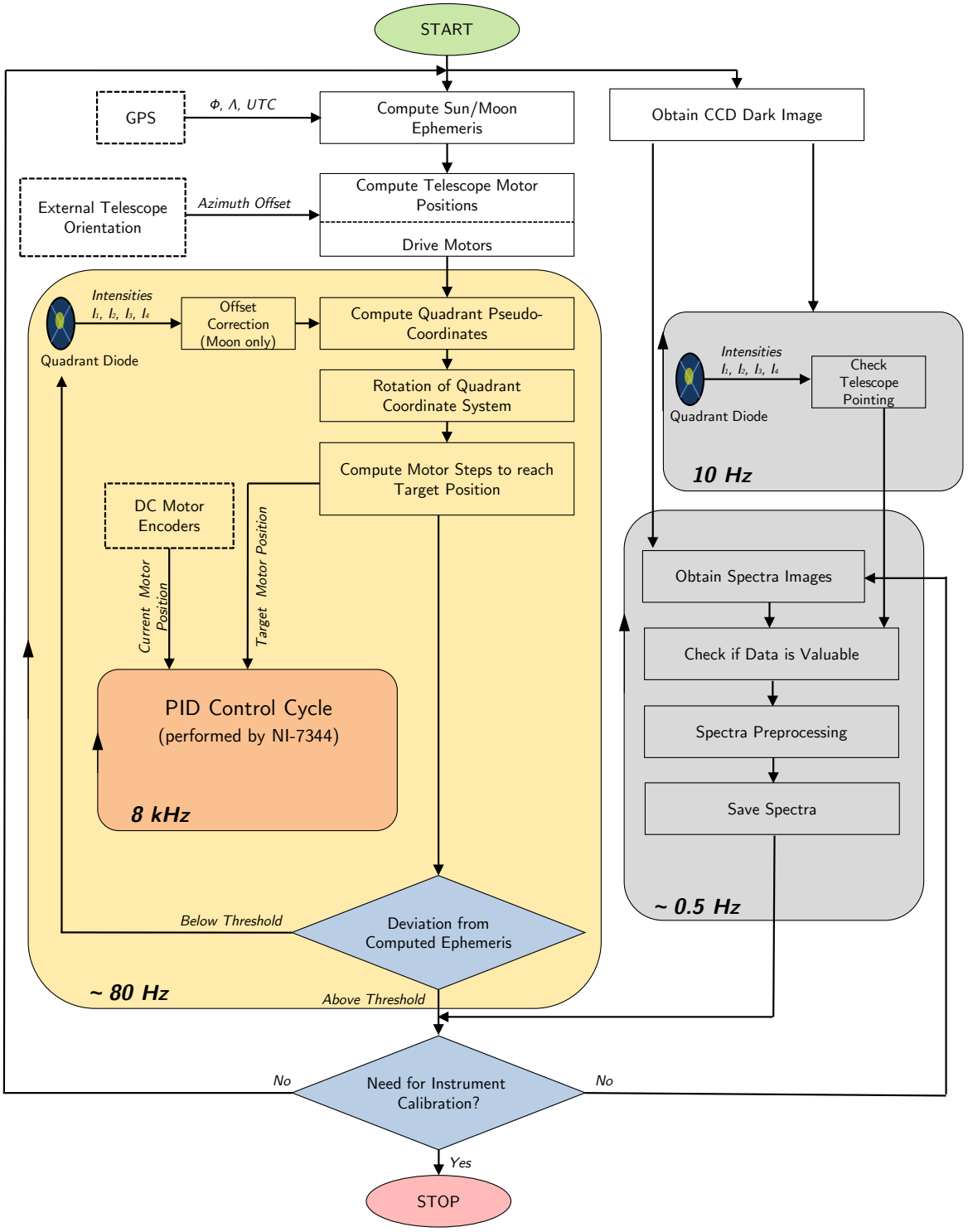

Figure 5.8: Scheme of the process steps involved in the telescope control cycle when tracking the sun or the moon. The initial telescope alignment is computed using location and time data provided by the GPS sensor and the sun/moon ephemerides. From there the automatic control cycle using the quadrant diode as primary feedback sensor takes over (yellow box). The reduction of the computed telescope angle offsets is conducted by the motion control card's PID cycle, which is constantly fed with adjusted target positions (update rate 80 Hz). In parallel, the image acquisition process is taking place. Acquired spectra images undergo a validity check based on the telescope pointing accuracy during the exposure time.

The electric current induced by the photodiodes (which in principle is proportional to the incident radiation intensity) is transformed to voltage using an amplifier unit (see Section 4.10.3) and acquired by the motion control card's A/D converters with a frequency of about 80 Hz. In case of lunar measurements an offset correction for each diode channel has to be applied. These offset values can change over time (and with temperature) and thus have to be redetermined frequently, at least prior to lunar measurement sessions. From the digitized voltages, $[X_{CoG}, Y_{CoG}]$ can be computed and subsequently a target position for the motor system is deduced. As the orientation of the telescope motor axes with respect to the spectrometer and thus to the quadrant diode depends on the current azimuth of the celestial body, a rotation of the coordinate system by a corresponding angle $\epsilon(Az)$ has to be considered when computing the telescope's target motor position set $[S_{Az}, S_{El}]_{target}$:

$$\begin{bmatrix} S_{Az} \\ S_{El} \end{bmatrix}_{target} = \begin{bmatrix} S_{Az} \\ S_{El} \end{bmatrix}_{current} + \begin{bmatrix} C_{Az} & 0 \\ 0 & C_{El} \end{bmatrix} \begin{bmatrix} -\cos\epsilon & -\sin\epsilon \\ \sin\epsilon & -cos\epsilon \end{bmatrix} \begin{bmatrix} X_{CoG} \\ Y_{CoG} \end{bmatrix}_{current} \tag{5.18}$$

$[S_{Az}, S_{El}]_{current}$ is the current motor system position (provided by the DC motor encoders), $[C_{Az}, C_{El}]$ denotes the conversion factors between the motor coordinate system and the rotated quadrant diode "pseudo-coordinates". The conversion factors are found experimentally for each measurement system. Foremost they depend on the image spot size on the quadrant diode. As shown in Figs. 5.9(b) and 5.9(c) the size of the image spot strongly influences the intensity ratios of the different quadrants and thus the deduced coordinates. By a slight defocussing, the area of displacement from which reliable information on the spot position can be derived can be enlarged and telescope movements become smoother. A small spot size on the other hand makes the system very sensitive to small deviations from the normative position. However Fig. 5.9(d) shows that the coordinates provided by the quadrant diode can become quite inaccurate, especially for non-round spot shapes. For spot shapes as produced by the halogen bulb, crescent moon or a sun disk partly concealed by clouds, considerable differences to a precise Cartesian coordinate system are observed, which can lead to tracking detours hampering the tracking responsiveness.

Further the mentioned conversion factors are influenced by the motor system tuning. As shown in Fig. 4.32 the movement from the current position to the target position is monitored and controlled by the motion control card with a PID (proportional-integral-derivative) control cycle using the encoder signals as feedback. Based on the momentary error $e(t)$ (difference between desired set point and the process variable; here the remaining motor steps to target position) the differential equation of the controller output $u(t)$ (in this case the DC motor currents) can be written as [University of Michigan, 2013]:

$$u(t) = \underbrace{K_P \cdot e(t)}_{P} + \underbrace{K_i \int_0^t e(\tau)\, d\tau}_{I} + \underbrace{K_d \frac{d}{dt} e(t)}_{D}. \tag{5.19}$$

The output portion $\boldsymbol{P}$ – proportional to the error e – is steered by the proportional gain K_P. P (because of its time independence) produces an instantaneous reaction. Increasing K_P in our case stiffens the motor axis; too large values can lead to the control cycle instability though. The integral term $\boldsymbol{I}$ compensates for the accumulated control deviation over a passed integration time. The longer a deviation exists the higher becomes I. Its influence is controlled via the integral gain K_i. The I portion of the cycle is comparably slow, but capable to fully eliminate persistent deviations. The derivative portion $\boldsymbol{D}$ has a damping effect, predicting the system's behaviour through analysis of the error slope thus helping to improve the setting time and acting as shock absorber. Its influence is controlled through the derivative gain K_d.

For each controlled telescope axis of the two measurement systems an individual PID parameter set had to be found in an iterative procedure. By analysing the step response of the motor systems, a configuration where settling times ("the time required by the response curve to reach and stay within a range that is approximately the final value" [National Instruments, 2012]; here: deviation smaller 0.1°) and rise time (time to closely approach the final position for the first time) become minimal. With the chosen electronic design the rise time is of special importance as the target position $[S_{Az}, S_{El}]_{target}$ is instantly overridden as soon as new quadrant diode values are available, which is usually clearly before the motor system reaches the former target position. The optimization of the rise time ensures quick approach of the target position, thus allowing the telescope to closely follow the moving target in continuous movement. In Chapter 8 an enhanced, more direct implementation of the control cycle is outlined as an outlook.

5.1.3 Target Tracking

When measuring in static mode the telescope tracks the light source using the described control cycle. The initial telescope alignment though bases on the computed sun or moon ephemerides. Using the tracking algorithm from there, an optimal intensity gain also under cloudy conditions is guaranteed. The deviation from the celestial body's theoretical trajectory however is constantly monitored and if becoming too large the telescope aiming is set back to the alignment given by the current ephemerides. The default maximum deviation is set to 2°. Also slight alignment errors resulting from inaccurate external orientations can be compensated in this way. Fig. 5.10 shows a typical telescope aiming trajectory in case of cloudy conditions.

5.2 CCD Readout

In order to gather as many photoelectrons per time unit and to push the S/N ratio as high as possible not only the CCD characteristics have to be considered, but also the way the camera is operated in the measurement process. In the case at hand mainly the readout mode and exposure time settings are relevant.

5.2.1 Full Frame Readout vs. Hardware Binning

The OEM CCD Camera described in Section 4.6.3 allows a so-called vertical hardware binning readout mode. The imaging of the entrance slit is aligned with the CCD columns. All photoelectrons produced during the exposure and stored in the potential-wells of a specific column belong to the same small wavelength interval. Charges thus can be summed up to find the total intensity per wavelength.

The use of hardware binning theoretically allows higher measurement frequencies because only a single line (the filled shift register containing the charges of all 250 rows) consisting of 2048 pixels has to be A/D converted instead of 250 lines of which one full-frame image consists. The readout of a full frame image lasts about 2.5 s, whereas a full line binning readout takes 15.2 ms.

However, comparing the two readout modes one has to consider also the capacity of the shift register per column. Though not officially specified, tests have shown that one pixel of the shift register of the used CCD detector clearly cannot store the charges of all 250 pixels in the

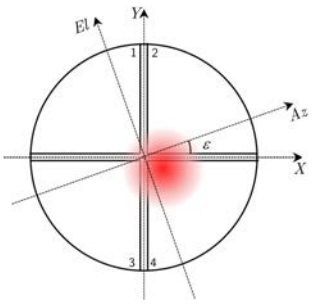

(a) Scheme of a quadrant diode sensor with an imaged intensity spot. For translation of the derived spot coordinates into the telescope system a rotation with an angle ϵ is needed

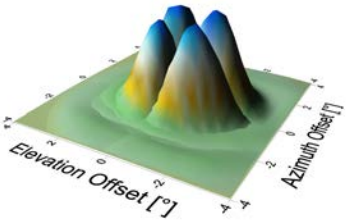

(b) With a defocussed image spot the intensity hills become pointy, as the area where the spot illuminates only one quadrant is minimal

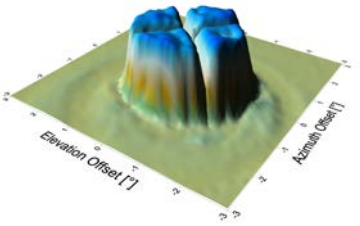

(c) A smaller spot results in flat-top intensity distributions, which allows a computation of reliable spot coordinates only near the diode center

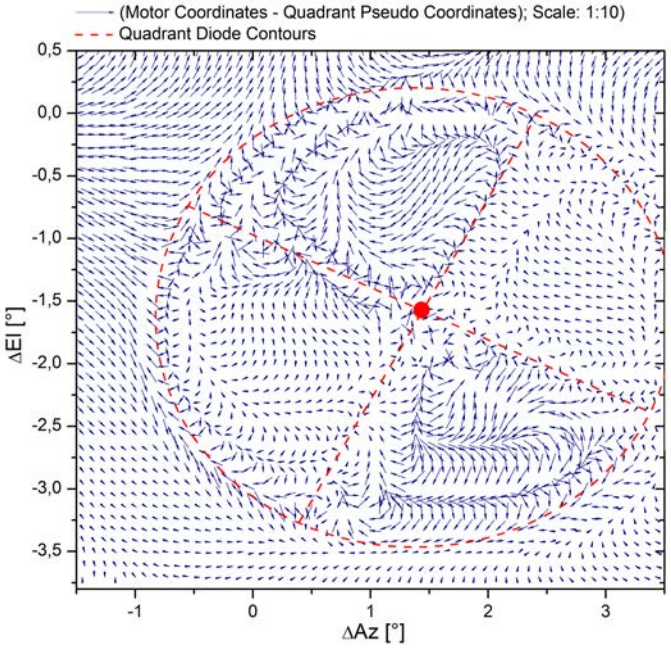

(d) Scaled differences between the computed pseudo coordinates derived from quadrant photodiode intensities and the actual telescope alignment (conversion factors $[C_{Az}, C_{El}]$ (compare Eq. 5.18): 1 pseudo coordinate unit $\equiv$ 15°). This scan has been recorded using the internal halogen lamp with its prolate spot shape. The rounder the spot is the more reliable the derived coordinates. Inaccurate coordinate mapping can lead to slightly prolonged target "catching" times.

Figure 5.9: Retrieval of spot coordinates using a quadrant photodiode sensor.

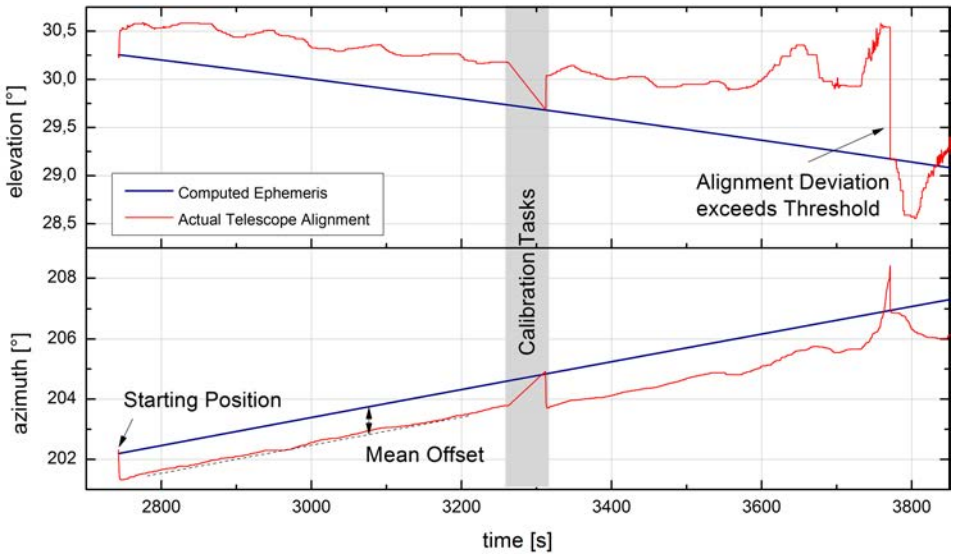

Figure 5.10: After pointing in the direction based on the calculation of the target's ephemerides (considering the instrument's external orientation), the telescope enters the automatic tracking mode, by reducing the imaged spot's distance from the center of the quadrant photodiode, thus feeding the spectrometer with as much radiation as possible. This cycle is interrupted if the deviation from the theoretical ephemerides exceeds a defined threshold (here set at 1°) or if calibration tasks have to be slotted in.

column if the spectrum approaches saturation at the brightest pixel, even though the imaged spectral information does not cover the whole but less than 40 % of the CCD area. Due to the limited shift register capacity (which is believed to be around two times the amount of the single pixel full well capacity) exposure times have to be drastically reduced. In the case of bright sunlight even the shortest exposure time of 5 ms leads to over-saturation of the shift register. Hardware binning measurements are only possible with an additional attenuation of the sunlight using a filter. Hence the theoretical advantage of binning measurements to register considerably more photoelectrons per time unit is greatly degraded. Assuming a pixel saturation of 80 % for full-frame images with the exposure time at 30 ms, one can acquire non-saturated binned images by lowering the exposure time to 5 ms and through filter attenuation by a factor of 10. With this exposure and the given readout times around twice as many photoelectrons can be acquired in binning mode, rendering the S/N-ratio only a factor $\sqrt{2}$ higher.

The readout of full-frame images on the other hand has further advantages as various useful details can be retrieved which would be lost in the process of hardware binning. The position of the main diffraction order on the CCD image is visible, as are parts of neighbouring orders at the top and bottom of the image. Full frame image readout has following advantages:

- *Spectra stabilization*: The diffraction order's edges can be utilized to determine the position of the spectrum on the chip in direction of cross-dispersion. This allows a better stabilization of the spectrum compared with an algorithm using the intensity center-of-gravity of emission lines produced by the spectral lamp.

- *Stray light correction:* Image areas only illuminated by stray light are found in the "intensity valleys" between diffraction orders. These areas are utilized in a stray light correction algorithm which is specifically applied to every single image. This is enormously useful as stray light and false light fractions can vary significantly depending on the illumination situation.

- *Omitting pixels outside diffraction order:* Only illuminated pixels within the borders of the extracted diffraction order edges are used in the process of vertical software binning. Hardware binning only allows the definition of a straight top and bottom border. As the diffraction orders of SOLUSAR are strongly bent a large number of pixel mainly containing stray light and various sorts of noise would be included. Omitting said pixels improves the S/N-Ratio.

- *Reducing the influence of spectra drift:* Due to the before discussed influence of etaloning effects, the computation of transmission spectra with high quality heavily relies on the vertical stability of the spectrum position. Sun and halogen spectra should be computed using the information of the exact same matrix elements whose fraction of the intensity should also be stable over time. This can be accomplished through frequent application of the stabilization procedures which on the other hand is time-costly. When working with full-frame images this issue can be addressed more pragmatically by leaving pixels out of the computation which are close to the diffraction order edges, where in case of drift the greatest intensity variations occur.

- *Visual control of various additional features:* Various effects, such as electromagnetic interference patterns, stains or dust particles on the CCD, strong incident false light or unequal entrance slit illumination can be recognized more easily by the operator.

- *Easier recognition of saturation:* The etaloning creates considerable intensity differences. In binning mode, situations where few pixels reach saturation and the exposure time has to be lowered, are not as easily discernible as in full-frame images.

- *Omitting influence of hot pixels:* Possible hot pixels can be identified and the corresponding defect information omitted from the processing.

- *Reduced Readouts:* With electric interferences imprinted on readout, higher overall signals per readout are favourable.

Given these benefits the acquisition of full-frame images seems advantageous over hardware binned readouts, even with the lower photoelectron yield. Only the apparatus function retrieval process requiring high-speed image acquisition still relies on binning measurements of emission lines.

5.2.2 Exposure Time Determination

In case of lunar measurements the camera exposure time is fixed at 20 s, the longest allowed by the camera system. The exposure time for solar measurements depends on the apparent magnitude of the sun (function of the sun ephemerides) and the weather conditions. Different things have to be borne in mind when determining a suitable exposure time:

1. The main objective is to collect as many photons per time unit as possible to maximize the S/N-Ratio. The brightest pixel should reach charge levels of at least 60 % to 70 % of the well capacity. This is especially mandatory since the number of out-read spectra has to be minimized in order to reduce the influence of electromagnetic interferences imprinted on every readout. Given these interferences, signal intensities of at least 30 % to 50 % have to be reached in order to gain spectra whose main deteriorating factor is shot noise. Hence long exposure times are desirable.

2. In situations where the intensity reaching the detector rises quickly, as at sunrise or more importantly under rapidly changing cloudy conditions, the brightest pixel can become saturated rendering the recorded spectra useless. Longer periods with discarded spectra essentially lead to a diminished mean photoelectron acquisition rate. Also serial redetermination of the exposure time is undesirable due to associated retrieval of dark images. An exposure time leaving a considerable margin to the upside is thus favourable.

As the quadrant photo diode is actively involved to maintain the telescope alignment during the spectra acquisition process, its data can also be used to continuously monitor the changes in the incident brightness with high frequency.

With a 10 Hz frequency the total spot intensity on the quadrant diode, the computed spot displacement and the pointing integrity flag from there deduced (TRUE if total intensity above minimal threshold and $X_{CoG} < 0.25 \wedge Y_{CoG} < 0.25$) are stored in a queue for 100 s. After a full spectrum has been acquired (or after a longer period with no successful spectrum retrieval) the mean (TRUE-flagged) quadrant intensity during the spectrum acquisition time (around 60 s) is obtained from the queued data to re-evaluate the exposure time. The exposure time is inversely proportional to the spot intensity and adjusted based on the latter to reach a 75 % maximum CCD saturation. The conversion factor was found experimentally. If the new exposure time does not leave the interval of $[0.9, 1.1]\times$ the former exposure time, the latter is maintained to not interrupt to measurement cycle. If the maximum spot intensity deviates more than 10 % from the mean value in the period under consideration, it is taken as calculation base for a new exposure time determination in order to avoid CCD saturation.

5.3 Wavelength Stabilization

The position of the diffraction order structure on the CCD chip can slightly vary over time. The variations during the measurement process are caused by the influence of temperature changes on the internal mechanical structure and the optical elements. The temperature is mainly influenced by the ambient temperature, the incident solar radiation on the instrument hull and the thermal dissipation of the various electronic components inside the instrument (primarily camera cooling and DC/DC converters). With a vertical temperature gradient inside the instrument of up to 20 °C gradually establishing itself after start-up, spectra drifts can reach 10 px. As soon as a certain thermal equilibrium is reached, the displacement rate never exceeds 3 px/h but is normally much lower. Larger position deviations only occur in case of instrument transportation. The long-term stability of the spectrum, if the instrument is stored in-house, is very high (displacements of below 20 px after months).

The active stabilization of the spectra position on the CCD sensor using the motorized deflection mirror (see Section 4.5.4) in the spectrometer is conducted for various reasons:

- To precisely maintain the recorded spectral range in which the sought absorption lines are located and to dispose of a proper wavelength reference.
- In order to conduct a flat-field correction using a halogen spectrum the exact same CCD matrix pixels with their specific sensitivities ought to be illuminated. The diffraction order has to be vertically stable and the wavelengths should be always assigned to the same CCD column. This is of particular importance in the case of SOLUSAR due to the appearance of strong etaloning patterns. Already smaller drifts of the spectrum could corrupt a correct computation of the baseline.

- For the correction of stray light influence, sufficiently sized non-illuminated areas above and below the diffraction order sought after must be available in every recorded spectrum image.

The spectrum stabilization procedure (in dispersion and cross-dispersion direction) is normally conducted every 10 min.

5.3.1 Stabilization using Lamp Spectra

The spectrum stabilization in principle can be conducted using the intensity centres of gravity of the argon emission lines only. Since the vertical profiles of the lines are strongly influenced by the etalon fringes depending on their position on the CCD, the determination of the vertical position using these emission spectra had to be abandoned. Instead the cross-dispersion position (coordinate y_{CCD}) of the spectrum is determined by means of the edge detection algorithm described in Section 6.3. This procedure allows a stable determination of the y_{CCD} with an accuracy well below the demanded 1 px.

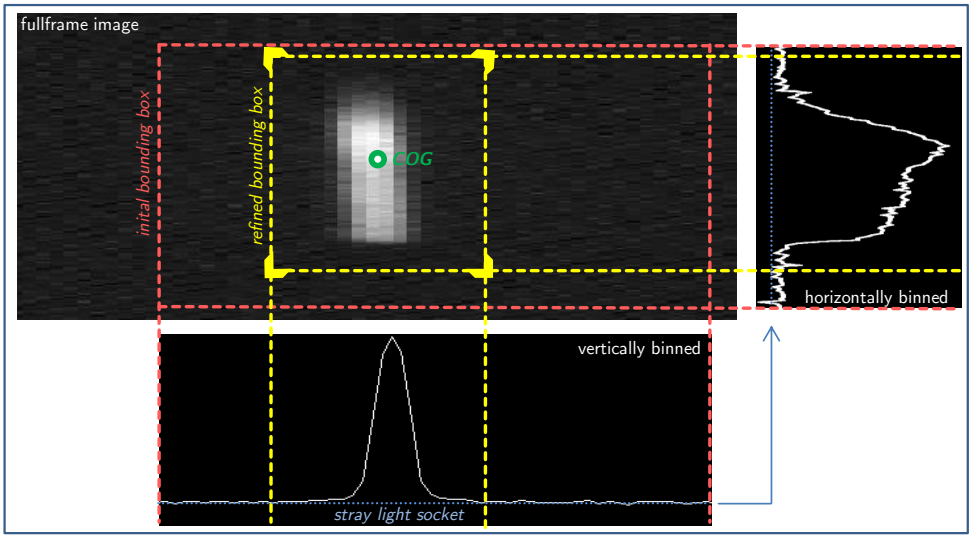

Figure 5.11: To determine the intensity center of gravity of an argon emission line, from an excerpt (initial bounding box) of a full frame image, a vertically and a horizontally binned profile is computed. In the vertically binned data (step 1), the refined box boundaries are set, at the position where the intensity (coming from the intensity maximum) increases again. In the horizontally binned data (step 2) the boundaries are set where the intensity dips below the stray light intensity socket which has been determined in step 1 as well.

From the difference of the scheduled normative and the actual spectrum coordinates the necessary driving distances of the folding mirror's stepper motors is deduced. To manage the hysteresis of the motor/drive system the target position is always approached from the same side. For small spectra displacement the final position is normally reached with one correction

cycle (duration for x_{CCD} and y_{CCD} adjustment around 20 s). For displacements greater than 20 px often two cycles are necessary to meet the required precision.

5.3.2 Stabilization using Solar/Lunar Spectra

In principle the monitoring of the spectrum position and the correction thereof can also be accomplished using solar spectra themselves as they bear all the necessary information. Thus the stabilization process would fit in the spectra recording process much more seamlessly. If the algorithms are fast enough a monitoring of the spectrum position is possible after every acquisition of a full-frame solar spectrum. Whereas the algorithms determining y_{CCD} can cope with a spectrum filled with absorption lines (see Section 6.3), an algorithm retrieving x_{CCD} from dedicated Fraunhofer lines with sufficient accuracy and speed has not yet been found.

In case of lunar spectra also the vertical position determination is tricky, as the S/N-ratio can drop to such low levels, that occurring hot pixels and electric interference patterns heavily affect the robustness of the used algorithm to extract the diffraction order edges.

5.4 Dynamic Apparatus Function Determination

As explained in Chapter 3 the apparatus function describes the spectral impact of the measurement instrument on the measured light composition. The characteristics of this influence are given by the utilized optical elements in the measurement system, particularly the entrance slit width. The apparatus function width can slightly vary over time, which affects the sensed absorption line width and should be taken into account in the spectra processing. The main cause for temporal variations is thermal expansion of the mechanical structure and optical elements, slightly altering the imaging geometry leading, e.g., to defocussing.

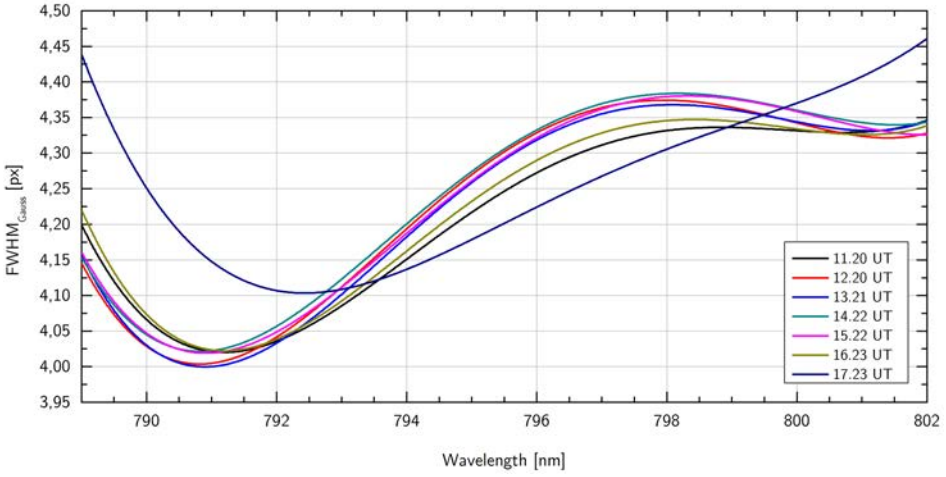

Figure 5.12: Variation of the apparatus function width over a 6 h measurement session on a sunny late summer day (August 15, 2012). Data from SOLUSAR II.

As evident in Fig. 5.12 the temporal variability of the line width of the monitored argon lines, from which the apparatus profile is deduced, is generally very low on a short time scale. However, sudden considerable changes can occur, with alteration of the mean FWHM (full width at half maximum) of the fitted Gauss profiles reaching up to 8 % to 10 % within an

hour. On a long-term scale, the SOLUSAR I mean apparatus function width has broadened from about 3.8 px to 4.9 px over a timespan of 1.5 years.

Not only a temporal dependency is observed, but also a dependency on the position of the line structure on the CCD. Possible explanations for the different apparatus function widths depending on the x_{CCD} coordinate on the CCD could be:

- The focal plane does not exactly concur with the CCD detector plane. The apparatus function width could be affected by a slight obliqueness of the focal plane, or by different aberration effects such as distortion.
- For each wavelength the light bundles passing the spectrometer and reaching the detector slightly vary and thus also the influence of the apparatus on the line width, as visible in Fig. 5.13.
- The prism slightly twists the slit image. The grade of the rotation is wavelength dependent. In a vertically binned spectrum rotated lines lead to increased line widths.

In order to monitor the apparatus influence a calibration routine is performed every 30 min. In this process a series of argon spectra at different positions on the detector are recorded. A relatively uniform distribution of argon lines over the whole detector width is desired in order to compute a trustworthy description of the spatial variability of the apparatus function. To accomplish this the argon spectrum image is shifted over the CCD. To speed up the process which takes around 1 min emission spectra are acquired using the camera's hardware binning mode. Due to the constrained movement radius of the tiltable mirror only 28 images can be obtained (position spacing around 70 px), leaving the right CCD side somewhat scarcely covered with spectral lines (see Fig. 5.13). From the obtained argon line width a polynomial of fourth degree is estimated describing the spatial variability of the apparatus function.

Most often apparatus functions are described using the Voigt profile described in Section 3.5.2. As shown in Figs. 5.14(a), 5.14(b) and 5.14(c), fits of obtained argon lines with a Voigt profile contain only a minimal Lorentz contribution. A fitting of the apparatus function using a Gauss-only distribution function seems to provide an equally (or even more) accurate description of the apparatus influence.

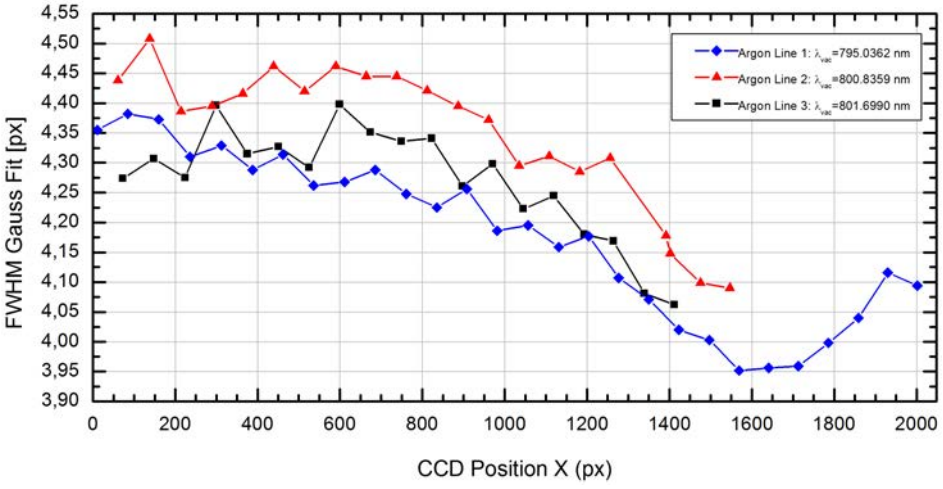

Figure 5.13: Dependence of the apparatus function width on x_{CCD} as determined with three prominent argon lines. Whereas lines 1 and 3 seem to be in very close agreement, line widths estimated using argon line 2 are on average around 0.1 px higher.

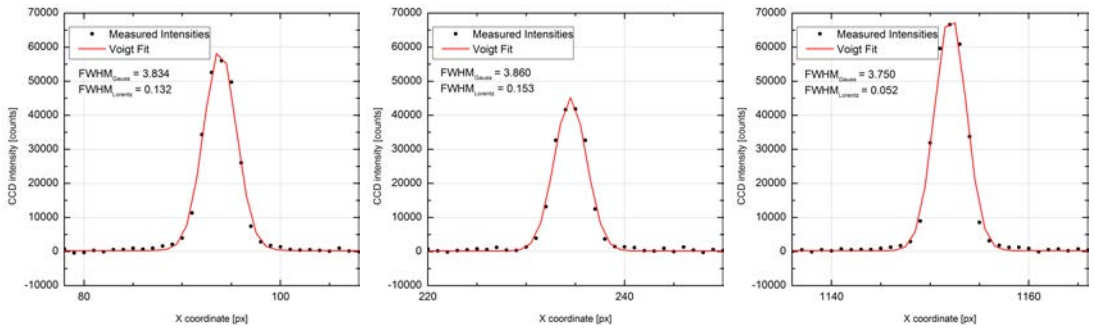

(a) argon line 1 (λ_{vac} =801.6990 nm)

(b) argon line 2 (λ_{vac} =800.8359 nm)

(c) argon line 3 (λ_{vac} =795.0362 nm)

Figure 5.14: Voigt profile fits of the three argon lines within the primary SOLUSAR measurement range. The Lorentzian portion is only minimal. Gauss-only fits often reach better correlation coefficients than Voigt profile fits.

5.5 Control Software

Within the SOLUSAR project two control software packages have been established. First a software platform, mainly used for testing purposes allowing the user to directly take control of every single task of the measurement processes and the way they are conducted, has been developed. Out of this bundle of procedures, the most serving algorithms were then included in the main control software package called *SOLUSAR Auto Control (SAC)* which fully autonomously controls the measurement process of the instrument, giving the user nothing but the possibility to set certain parameters before start-up. Only the latter software package will be described henceforward. Control software has been developed using the LabVIEW™programming language (by *National Instruments*), which is well-suited for steering and control applications.

SOLUSAR Auto Control is written in close accordance with the design pattern *Queued State Machine* proposed by Blume [2007] (see Fig. 5.15(a)). Analogue to first-in, first-out buffers, this software architecture allows to store and execute subsequent processes. New processes can be added either through Graphical User Interface (GUI) manipulation or by any state of the main process itself. For the handling of urgent tasks, processes can also be inserted at the front end of the buffer or at any specific position within the queue. This is especially helpful when dealing with the various calibration routines which occur aperiodically. This architecture also is performance friendly, as in case of an empty queue, the loop goes to sleep allowing parallel background processes to run efficiently [Blume, 2007]. The software is designed to ensure scalability: Addition of new tasks to the main loop and/or integration of parallel loops should be effortless.

The main software design difficulties lay in the establishment of an efficient handling of various (partly time-critical) loops which are running in parallel:

- *Main Loop:* Determines the main measurement regime, organizes the main measurement routines and the various calibration tasks.
- *Quadrant Read Loop:* Reads out and pre-processes the information coming from the quadrant sensor with high frequency. The process can be halted if no specific telescope alignment is needed thus freeing a considerable amount of CPU time.

- *Spectra Preprocessing and Saving Loop:* Acquired spectra data from the main loop are stored in a data queue and preprocessed as described in the subsequent chapter. The wavelength referenced transmission spectra are equipped with the dedicated meta data (meteorological data, ephemerides et cetera) and stored.
- *Meteo Loop:* Registers the values of the system's ground meteorological station
- *Event Handler:* Registers user-generated events at the Graphical User Interface
- *Various:* Various small loops used to make different status information of the measurement instrument available to the user.

Data sharing between the above mentioned loops is mainly implemented through queues and notifiers, which allows high speed and uses only limited memory. Processing the recorded spectra in near real-time has not yet been realized, as these tasks are in need of considerable processing power, which is not available when using the current hardware set-up.

The GUI, as depicted in Fig. 5.15(b), provides the possibility to set certain measurement parameters (foremost to set the time periods between the different calibration routines or to choose the orientation procedure) gives information on the activity of the various sensors (e.g. quadrant diode), monitors the instrument temperatures, and displays the retrieved spectra and the current apparatus function.

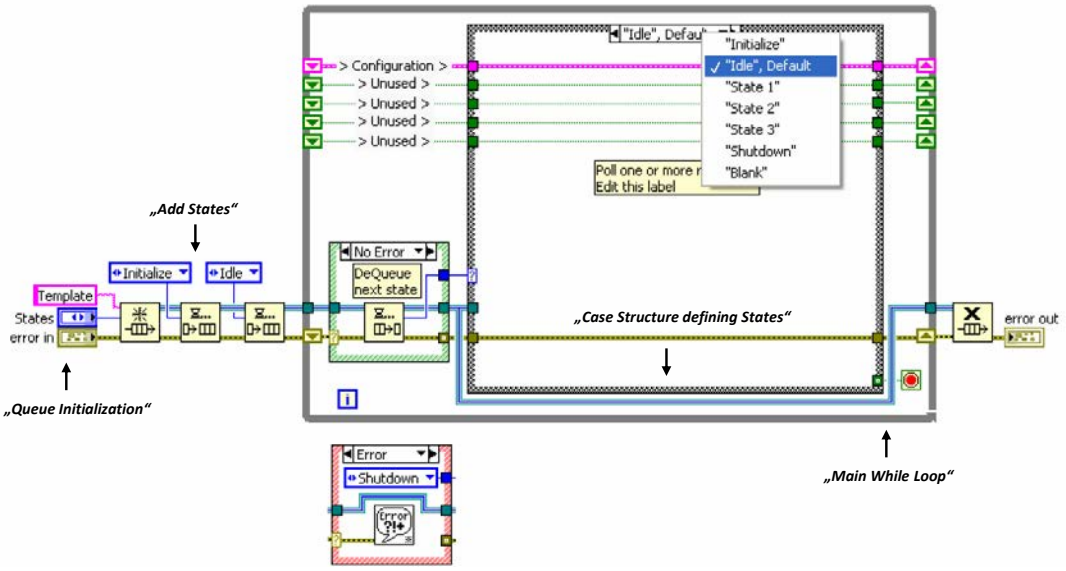

(a) Template for a Queued State Machine design pattern to handle subsequent software states in a LabVIEW™program, as proposed by Blume [2007]

(b) Graphical user interface of the *SOLUSAR Autocontrol* software, which provides information about the current status of the measurement process and instrument parameters

Figure 5.15: Control Software *SOLUSAR Auto Control (SAC)*

6

Data Preprocessing

The data obtained in the SOLUSAR measurement process described have to be processed to ultimately retrieve atmospheric water vapour concentrations. This chapter is focussed on the preprocessing routines applied to compute transmission spectra from the data. These procedures to a great degree have to take into account the specific hardware characteristics. The subsequent analysis of the transmission spectra to get water vapour concentrations is for the most part similar to the processing applied in the GEMOSS project. Certain dissimilarities, e.g., regarding the use of spectral catalogues and absorption line selection, are discussed in the following chapter.

The rough division into two parts – preprocessing and processing – reflects also the implementation from a software point of view. In our case, the term "preprocessing" subsumes all methods applied to the recorded data taking place immediately after the data have been obtained in order to generate and store wavelength-referenced transmission spectra. All preprocessing algorithms are part of the instruments control software *SAC* (*SOLUSAR Auto Control*, mainly written in LabVIEW), which has been described in Chapter 5. On the other hand the algorithms applied to the solar and lunar transmission spectra belong to the process of total column water vapour extraction and are part of the processing software package *SOLUSAR_Proc* written in C++ (based on the GEMOSS processing software). A schematic overview of all the processing steps is given in Fig. 6.1: The blue box contains the preprocessing steps, whereas on the right side the spectra simulation and adjustment process is shown.

6.1 Retrieved Primary Datasets

During the measurement process different datasets are acquired by the SOLUSAR measurement system (or by appendant sensors) which are required to ultimately retrieve atmospheric water vapour values. In Tab. 6.1 all datasets needed for the preprocessing and processing of the solar/lunar absorption spectra are listed together with their designated use and the retrieval time period. Not included in this data overview are measurement data used to ensure the ongoing measurement process such as feedback signals in the telescope control cycle or instrument temperatures.

6.2 Dark Image Correction

In an ideal charged coupled device (CCD) only incident photons should lead to a generation of electron-hole pairs in the detector's silicon substrate. The number of built pairs theoretically is in a fixed proportionality to the incoming photons of a certain wavelength. In reality though

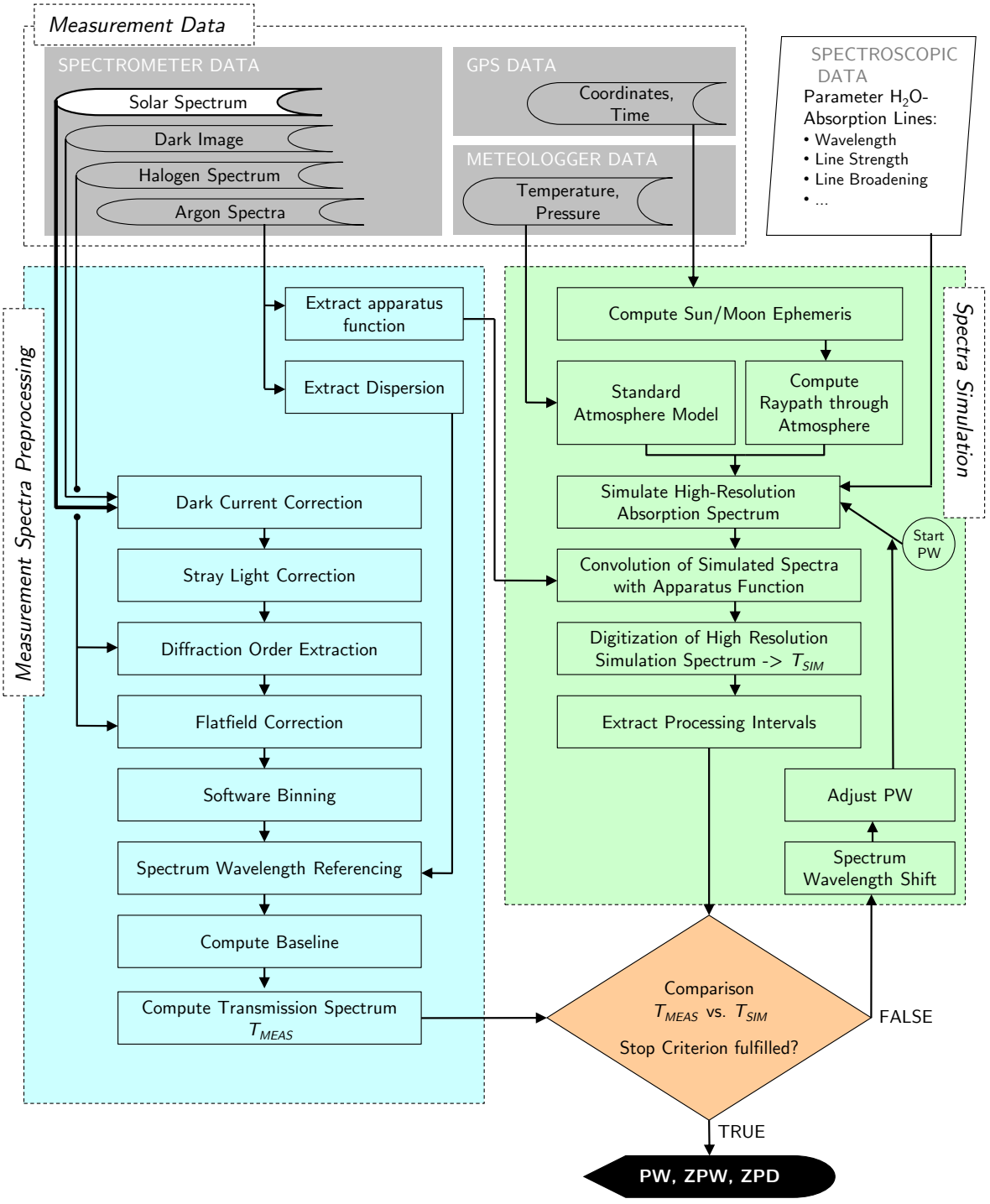

Figure 6.1: Schematic depiction of the SOLUSAR data processing: Measurement data obtained by the SOLUSAR measurement system is preprocessed in order to generate transmission spectra (left side). In order to extract water vapour concentrations the radiative transfer is simulated and the water vapour concentrations in the underlying atmospheric model adjusted until the synthetic spectra match the measurement-derived data (see Chapter 7).

Type / *Recorder*	**Purpose**	**Acquisition Period**
Solar/Lunar Spectra *CCD Sensor*	Primary Raw Data	Sun: $\sim$ 1 min Moon: $\sim$ 10 min
Dark Image *CCD Sensor*	Dark Current Correction Correction of non-spectral stray light	Maximum: 10 min. Sooner if CCD exposure time changes
Halogen Spectra *CCD Sensor*	Flat-field Correction Extraction of diffraction order boundaries	$\sim$ 30 min
Argon Spectra *CCD Sensor*	Wavelength Calibration	$\sim$ 10 min
Apparatus Function *CCD Sensor*	Modelling the influence of the apparatus on retrieved spectra	Maximum: 30 min. Sooner if rapid temperature changes in the instrument are occurring
Meteorological Data *Meteo Sensor*	Atmospheric Modelling (used for ray tracing and radiative transfer computation)	1 min
Geographical Coordinates Universal Time (UTC) *GPS Sensor*	Computation of Target Ephemeris (Raytracing)	Once at the beginning of the measurement process for a static site

Table 6.1: Measurement data retrieved by SOLUSAR and additional sensors used at measurement site

a small electric current occurs even if the sensor is not exposed to light because of random generation of electron-hole pairs as a result of the thermal movement of atoms and molecules. The higher the sensor temperature the bigger the so-called *dark current*. In order to reduce dark current, detectors are often cooled down (e.g. using multi-level Peltier elements, as also in the case at hand).

To further suppress the influence of dark current, images with closed shutter and exposure times similar to the light exposed images are obtained. Dark image intensities are subtracted pixel-wise from the raw spectrum image. Thus the stationary dark current bulk can be eliminated leaving only the influence of dark current shot noise (see Section 7.3.1). The subtraction of dark images also eliminates the offsets of output amplifiers which add exposure time invariant intensity sockets to the data.

Dark images are acquired at least every 10 min, or at every time an adjustment of the exposure time is done and if strong temperature changes (greater 5 °C) in the vicinity of the CCD occur. The number of CCD acquisitions for one dark image equals the number of acquisitions added up for one evaluable solar/lunar spectrum (solar spectrum: around 12 acquisitions per stored spectrum). The CCD sensor is temperature stabilized by the attached Peltier cooler. The sensor allows stabilization at 0 °C or at −10 °C. Though a lower temperature would be beneficial regarding dark current intensity it aggravates the danger of condensed water on the chip. The detector of the SOLUSAR I instrument exhibits a permanent current socket equivalent to around 1450 counts per pixel and a dark current rate of around 120 counts/s. Given the temperature stabilization the influence of the temperature inside the system is small (around +10 counts/°C to 15 counts/°C).

Dark image correction helps also to eliminate false light portions in the instrument which do not pass the entrance slit (compare Section 6.4).

6.3 Extraction of Diffraction Order

As described in Chapter 4, the combination of an echelle grating and a prism yields a two-dimensional structure of multiple curved diffraction orders which are non-equidistant. In case of SOLUSAR a section of one single diffraction order is imaged centrally on the CCD and its position is actively maintained through the wavelength stabilization processes described in Section 5.3. Still, location and shape can slightly vary (which would apply especially between observations of different spectral ranges). Due to following reasons the shape of the diffraction order has to be determined precisely:

- *Spectrum Stabilization*: The diffraction order's edges are utilized to determine the position of the spectrum on the chip in direction of cross-dispersion.
- *Stray Light Correction*: Image areas solely illuminated by stray light are found in the "intensity valleys" between diffraction orders. These areas are used to estimate the stray light distribution over the whole detector area (see Section 6.4).
- *Software Binning*: Include only pixels within the upper and lower diffraction order boundaries in the process of software vertical binning. This improves the signal-to-noise ratio of the retrieved spectra (see Section 6.5).
- *Reduce Influence of Spectra Drift*: Including only pixels in the binning process belonging to the diffraction order core and omitting pixels close to the edges reduces the unwanted influence of fringing structures caused by etaloning in the case of slight vertical spectra shifts.

In order to detect the top diffraction order edge a search window covering the entire CCD width but only 80 of 250 vertical pixels is gradually moved top-down over the intensity matrix until an edge with approximately the sought curvature is found in said window. The search procedure thus is only effective if top edges of neighbouring orders appear below the sought diffraction order on the CCD. Hence a vertical position deviation from the desired position of around $\pm$ 80 px is allowed.

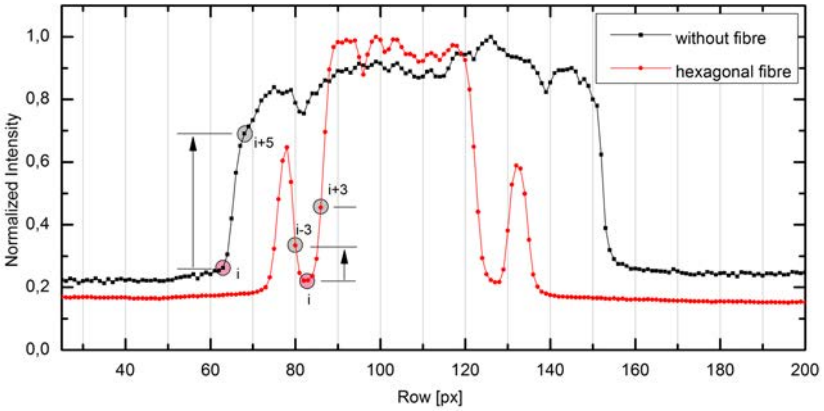

Figure 6.2: Vertical diffraction order profile: In every CCD column the pixel best defining the diffraction order top edge is determined. For measurements with full entrance slit illumination: The pixel at the bottom of the greatest intensity gradient. For measurements with hexagonal fibre: The pixel at the bottom of the upper intensity valley.

Within the search box in every column j one pixel $p_{edge}(i_e, j)$ (i being the CCD row) best describing the edge is determined. This procedure slightly differs for measurement set-ups with and without a homogenizing fibre. As shown in Fig. 6.2 in the case where the hexagonal

fibre is absent the vertical diffraction order section shows single continuous intensity lift with a width reflecting the entrance slit height. The top edge position is defined as the pixel $p(i, j)$ where the intensity difference $p(i+5, j)-p(i, j)$ becomes maximum. More elaborate procedures as, e.g., the application of a Sobel operator for edge detection are slower and do not provide better results.

The illumination with a hexagonal fibre produces an intensity distribution with three connected intensity hills. The central one is attributable to the fibre core, the side intensity lifts to the light-conducting fibre mantle. The edge boundaries are defined as the bottom of the intensity valleys (as the radiation coming from the cladding is not included in the processing), or mathematically where $min[p(i+3, j) - p(i, j), p(i-3, j) - p(i, j)]$ becomes the greatest.

Using the determined top edge pixels $p_e(i_e, j)$ along the CCD a polynomial of second degree is fitted using the method of *iteratively reweighted least squares (IRLS)*, a robust fitting method, particularly apt to deal with outliers. In the case at hand outliers can emerge in spectra with poor signal-to-noise ratio, as with moon spectra. Also in case of spectra with many and possibly broad absorption features, as e.g. caused by oxygen absorption bands, a good estimation of the edge trajectory is more demanding and can also be mastered with IRLS.

In a first iteration the coefficients of the polynomial $P(j)$ are determined by a least square fitting algorithm with equally weighted observations. Based on the residuals r a new weight for every observation is computed using a *bisquare weighting function* w_B:

$$w_B(r) = \begin{cases} \left[1 - (\frac{r}{k})^2\right]^2 & \text{for } \mid r \mid \leq k \\ 0 & \text{for } \mid r \mid > k \end{cases} \tag{6.1}$$

k is the *tuning constant* [Holland and Welsch, 1977]. Mostly, for bisquare weighting, one uses $k = 4.685\,\sigma$ with σ being the standard deviation of errors [MathWorks, 2013]. A common approach to estimate σ is to take $\hat{\sigma} = MAR/0.6745$ with MAR the median absolute residual [Street et al., 1988]. Using the new weights again a least square fit is applied. This procedure is repeated until coefficient differences between iterations fall below a defined threshold.

Experiments using low-noise spectra artificially superimposed with a Gaussian white noise (software wise) show standard deviations of the residual parabola's vertex vertical coordinate y_{vertex} (with respect to the spectrum without artificial noise, called "clean") of below one 1 px for noise with $\sigma_{noise} \leq 1000$ counts and spectra signal up to 7000 counts (see Fig. 6.3). 10 spectra for each noise level were analysed:

σ_{noise} [counts]	Mean$(y_{vertex,noise} - y_{vertex,clean})$[px]	$\sigma(y_{vertex,noise} - y_{vertex,clean})$ [px]
10	0.005	0.081
500	-0.037	0.128
1000	-0.611	0.520

Table 6.2: Accuracy of edge detection algorithm when analyzing noisy spectra.

For noise with σ_{noise} approaching $\frac{1}{6}$ of the signal amplitude the accuracy of the results is rapidly deteriorating as the algorithm is becoming unstable. However, in reality seldom spectra with such weak S/N-ratios are acquired.

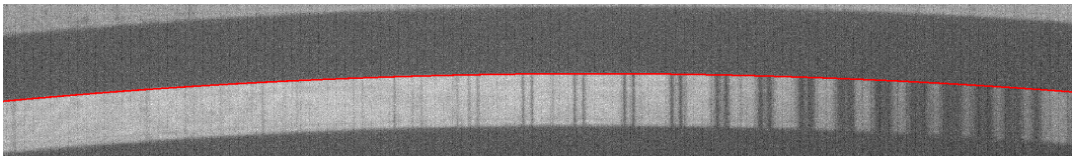

(a) Fullframe image of a solar spectrum section exhibiting broad absorption structures belonging to an oxygen band (right side). To simulate an image with a low S/N-ratio the image is artificially superimposed with Gaussian white noise (σ_{noise} = 1000 counts, spectrum maximum signal 6900 counts). The red line denotes the derived diffraction order top edge.

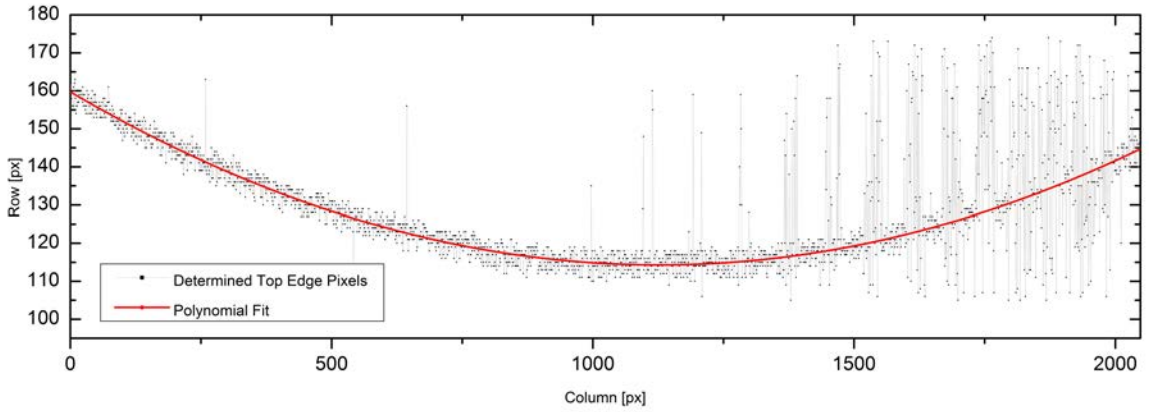

(b) Estimation of a polynomial of second degree from derived "edge pixels" using a robust fitting method.

Figure 6.3: Extraction of the diffraction order boundary in a noisy spectrum with multiple large absorption features.

6.4 Stray light Correction

For the correct determination of transmittance values it is indispensable to thoroughly eliminate the influence of parasitic radiation reaching the detector which does not belong to the actual spectral image of the respective light source. Such interfering radiation can be roughly divided into:

- *False Light:* Radiation illuminating the CCD detector coming from parasitic reflections of the telescope-gathered light at optical and mechanical components inside the instrument (both spectrometer and other parts). Through custom hardware measures (baffles) the influence of false light can be extenuated to a large extent, though a small but significant portion remains (up to several percent of the overall intensity in case of bright sunlight at high elevation angles). Certain false light sources cannot be fully suppressed, such as reflection at the spectrometer's collimation lens.

- *Stray Light:* Light having at least partially passed the diffractive optical elements of the spectrometer. Originating from the optically non-ideal behaviour of the spectrometer elements (mainly the echelle grating), the possibilities to eliminate these intensities using hardware measures are limited.

Whereas the ratio between the useful signal and the stray light intensity is fairly constant, false light intensities do not necessarily correlate with the spectra signal strength, as it can

be shed onto the detector during periods with the shutter being in closed state. Remaining portions of false light are mainly extinguishable via dark image correction (see Section 6.2).

Only in case of high water vapour abundances and at the same time low elevation angles absorption lines are becoming fully saturated in the wavelength region between 789 nm to 801 nm which would allow retrieval of stray light information from within the diffraction order, as it has been applied in the GEMOSS project.

Given the vertical diffraction order spacing and the entrance slit at 1 mm, significant void areas on the chip remain which are in this case used as false/stray light "gauges" (henceforward called *stray light areas*). With every spectrum available as full frame image, to every picture an individual stray light correction can be applied by analysing said stray light areas. Only pixels with a distance greater than 25 px from the diffraction edges are considered (in case of measurements with a hexagonal fibre).

The analysis of spectra images obtained under manifold conditions (with respect to spectrum intensity, light source, wavelength range and applied instrument) shows that the remaining compound disturbing intensity additives are in most cases more or less evenly distributed over the whole detector area. However, as shown in Fig. 6.4(a) considerable stray light gradients can occur which are predominantly vertically aligned with respect to the CCD. The stray light intensity differences can exceed 500 counts.

A column-wise modelling of the stray light bulk assuming a linear intensity distribution yields good correction results. Local stray light portions depending on the intensity of absorption features at this particular position in the diffraction order are found to be in fact negligible. But if such phenomena were existing they would also be eliminated using the subsequently described correction model. As shown in Fig. 6.5, for the correction of the stray light socket of the CCD column j, the pixel intensities of the stray light areas above and below the diffraction order are analysed to compute the corresponding stray light slope along the column. To improve the statistics and also reduce the susceptibility to dust particles and stains on the the chip, pixels belonging to the neighbouring n columns $j - n$ to $j + n$ are included in the computation as well.

Fig. 6.4 shows the reduction of the stray light portion of a halogen spectrum recorded in the original measurement set-up (without homogenizing fibre). Recorded after a longer period without instrument maintenance the image exhibits multiple stains and dust particles, locally depressing the stray light level up to 10 %. Fig. 6.4(b) shows a computation of the stray light distribution over the whole detector area. Depicted in Figs. 6.4(c) to 6.4(e) are the intensity residuals after applying different stray light correction models. In an optimal case the pixel intensities should become zero in the "valleys" between the diffraction orders. In all cases a linear description for the in-line stray light slopes is used. As evident in Fig. 6.4(c)(left side) the correction using $n = 0$ renders the correction strongly susceptible to dust particles leading to local underestimation of the stray light influence. The susceptibility can be reduced either by strongly increasing n (see Fig. 6.4(d); $n = 100$), or by moderately increasing n (see Fig. 6.4(e); $n = 20$) but using a robust slope estimation method (bisquare, analogue to Section 6.3). The latter approach copes slightly better with locally increased stray light portions, but tremendously raises the computation time by around a factor of 10 to generally above 1 min which is considered too high given the acquisition period of solar spectra at 1 min. Alternative models (such as polynomials) provide far poorer results. Therefore a LSQ linear estimation with $n = 100$ is adopted.

The linear models seem to generally slightly overestimate the stray light portion. However using hexagonal fibres the evaluable stray light areas become larger and thus the estimation

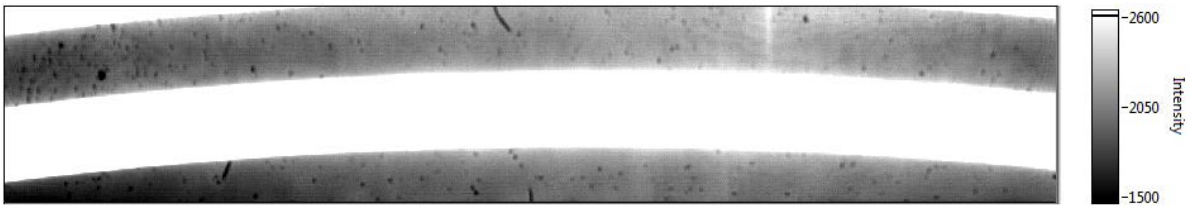

(a) Stray light background exhibiting dust particles (dark stains) and local stray light features

(b) Determined stray light bulk (column-wise LSQ-fit, $n = 20$)

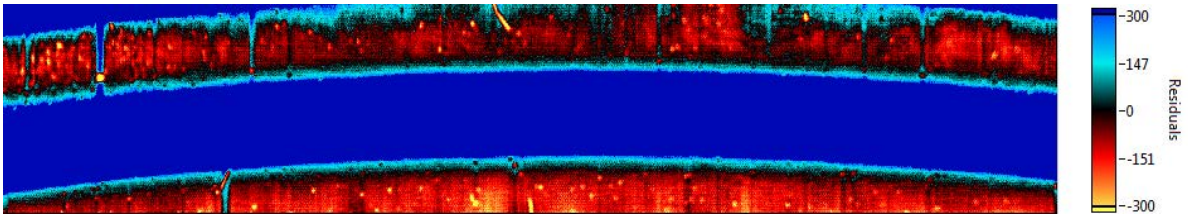

(c) Intensity residuals after linear correction with LSQ estimation; $n = 0$

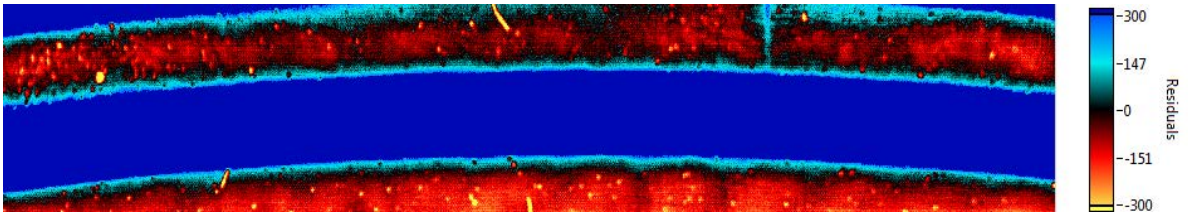

(d) Intensity residuals after linear correction with LSQ estimation; $n = 100$ (ultimately adopted method)

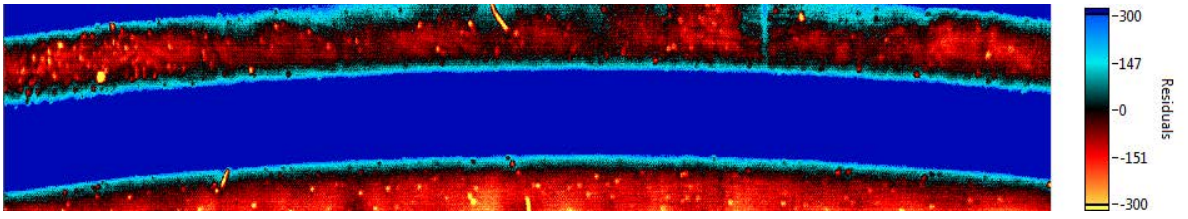

(e) Intensity residuals after linear correction with robust bisquare estimation; $n = 20$

Figure 6.4: Column-wise correction of the stray light influence using different linear approaches by means of a halogen spectrum

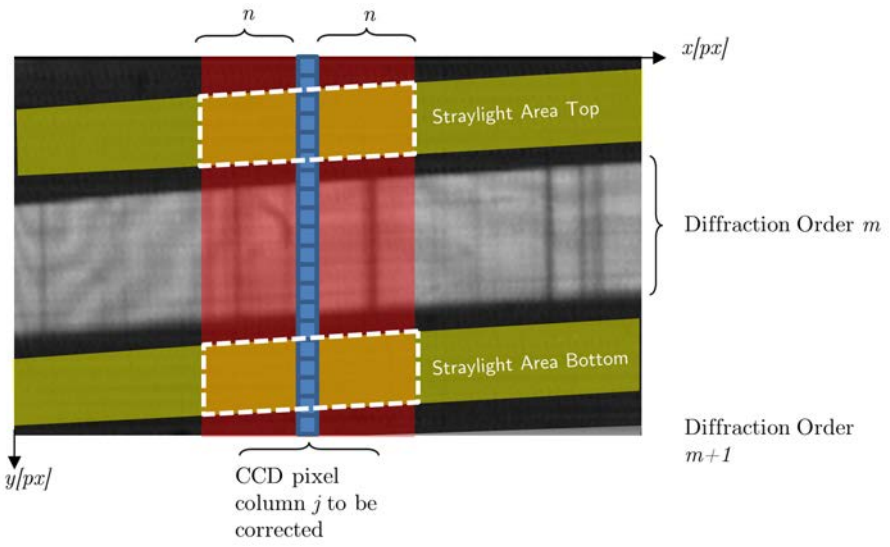

Figure 6.5: On every recorded spectrum a column-wise correction of the stray light influence is applied. The stray light information for column j is retrieved from pixels belonging to defined stray light areas above and below the diffraction order as well as from the columns $j - n$ to $j + n$. To model the stray light socket a linear model is used.

more accurate and reliable. The remaining residuals per column are then generally below 0.4 % with respect to the maximum intensity of the measured spectrum.

6.5 Vertical Binning

One major difference between SOLUSAR and its predecessor GEMOSS is the very narrow simultaneously obtained wavelength range of only 12 nm (GEMOSS: 187 nm). Consequently only a part of a single diffraction order has to fit vertically onto the CCD chip, yielding the possibility to use a taller entrance slit (and thus improving the S/N ratio) while using a small height detector.

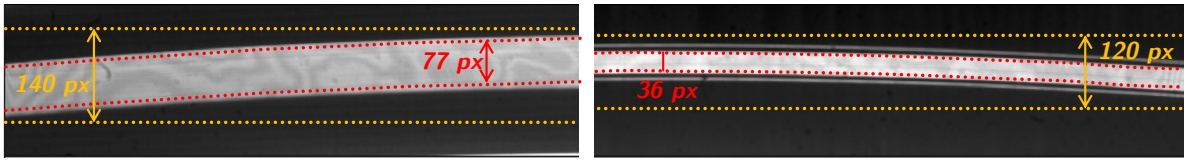

Figure 6.6: Vertical binning boundaries for measurements with (right side) and without a homogenizing fibre (left side). The orange lines denote the binning boundaries for hardware vertical binning, the red lines stand for the binning edges in the software binning procedure.

As described in Section 5.2.1, the hardware-side totalling of the pixel intensities belonging to the same column (and thus wavelength interval) is abstained from, and thus has to be conducted software-wise. Incorporated in the computation are only pixels within the diffraction order boundaries, determined using the algorithm described in Section 6.3. Furthermore to reduce the influence of spectra drift, 5 pixels at both diffraction order edges, where the intensity gradient becomes largest, are not included as well. With the introduction of the homogenizing fibre the usable diffraction order height shrinks from 77 px to 36 px. Given the curvature of

Argon Emission Line	λ_{air}	λ_{vac}	A_{ki}
I	794.8176 nm	795.0362 nm	1.86×10^7
II	800.6157 nm	800.8359 nm	4.9×10^6
III	801.4786 nm	801.6990 nm	9.28×10^6

Table 6.3: Bright argon emission lines within the SOLUSAR measurement range with their wavelength in vacuum and air respectively and transition probability A_{ki} according to *NIST Atomic Spectra Database Lines Data, 2012*.

the diffraction orders, using hardware binning a rectangle with a height of up to 140 px must have been recorded with many pixels carrying but noise (see Fig. 6.6).

6.6 Flat-field Correction

Ideally every pixel of the CCD matrix should respond equally to a defined incident light portion. Consequently a signal with uniform intensity distribution over the whole detector should result in an equally uniform image output (flat-field). This is essential for applications where the exact brightness of each pixel is measured (e.g. spectrometry or astrometry).

In reality there are different effects leading to artefacts in the spectral images:

- Individual gain of each pixel of the CCD detector,
- Etaloning (interference structures),
- Characteristics of the optics (e.g. intensity variance within a diffraction order produced by an echelle grating).

All these effects can altogether be treated as variant pixel sensitivities. For the elimination the quotient between the solar/lunar spectra and a halogen spectrum is computed pixel-wise (both stray light corrected and vertically binned), yielding the baseline-referenced transmission spectrum (see Section 3.9.1).

6.7 Wavelength Referencing

In order to be comparable with simulated data sets, measured spectra have to be wavelength referenced as well. Due to the stabilization of the spectrum on the CCD array during the measurement process the relation between pixel and wavelength is kept fairly steady. Smaller deviations of the spectrum position can be corrected with minimal shifts of the wavelength scale during the adjustment process. Already well referenced data though considerably speed up the adjustment process. The wavelength assignment in the primary wavelength range for every pixel is conducted using the three prominent argon lines in the wavelength range, listed in Tab. 6.3 and shown in Fig. 6.7.

With the spectra stabilization process repeated every 10 min, the wavelength scale is computed anew using the acquired argon spectra. Thus potential changes in spectra dispersion can be taken into account. With the extracted three horizontal intensity centres of gravity the wavelength scale is estimated as a polynomial of degree 2. Given the uneven line distribution over the whole CCD width the wavelength scale though becomes increasingly inaccurate as the wavelength gets shorter. The deviation can reach up to 0.15 nm in the worst case.

Figure 6.7: SOLUSAR full frame image of argon emission spectrum in range of 789 nm to 801 nm with the three prominent lines listed in Tab. 6.3

6.8 Baseline Retrieval

Measured spectra where the above described flat-field correction has been applied can still contain broadband structures due to different reasons:

- Apart from the absorption features, the wavelength-dependent sunlight intensity distribution closely resembles the emission spectrum of a blackbody at nearly 6000 K (see Section 3.8.1), whereas the halogen lamp has a temperature of only around 3000 K (exact temperature depends on the applied voltage). Division of the two spectra yields a general intensity trend which is nearly linear in the short SOLUSAR wavelength range (slope of around $-4\,\%$ towards the longer wavelengths).

- The slightly different ray paths of sun light and halogen light inside the instrument can lead to somewhat different intensity distributions.

- Atmospheric effects (e.g. different scattering effects, compare Section 3.2) can imprint broadband structures onto the measured solar/lunar spectra.

In order to process the measurement data according to the algorithms described in Section 3.9 one has to eliminate effects which are not modelled in the synthesis of the artificial transmission spectrum to make the two datasets comparable. The spectrum synthesis only considers narrow-band absorption processes and the broadening of the thus arisen features along the atmospheric ray path and by the apparatus. To transform the measurement data into a narrow-band transmission spectrum, a thorough determination of the baseline intensity is therefore necessary.

For the processing of GEMOSS data the transmission values have been computed separately for each processed absorption line. Therefore so-called baseline intervals in the spectral vicinity of each processed line were required to determine the local baseline I_0. For SOLUSAR, with its small spectral measurement window of 12 nm only, this procedure would imply a considerable reduction of the number of processable lines, since the density of significant transitions and additional Fraunhofer lines is high, the number of transitions with close-by intervals exhibiting negligible absorption is limited. Additionally, the fact that SOLUSAR uses a broader entrance slit leads to increased measured absorption structure widths and leaves scant useful baseline intervals within the measuring range.

Fig. 6.8(a) shows a SOLUSAR measured spectrum over the entire primary wavelength range with possible processable absorption lines and the spectral areas used as baseline intervals in the GEMOSS process. It seems evident that certain areas are showing quite strong deviations from a reasonable integral baseline (see Fig. 6.8(b)) and thus do not actually qualify as suitable reference intensities.

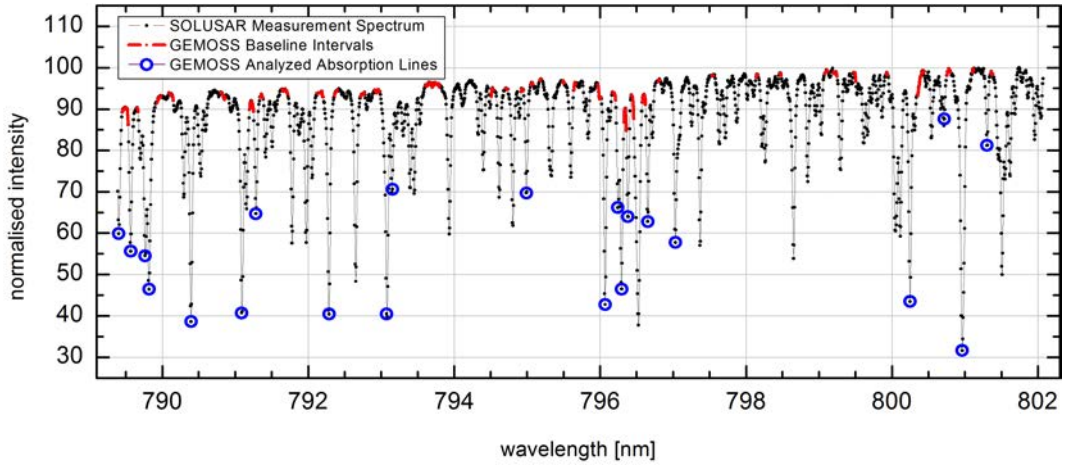

(a) Whole primary SOLUSAR measurement range

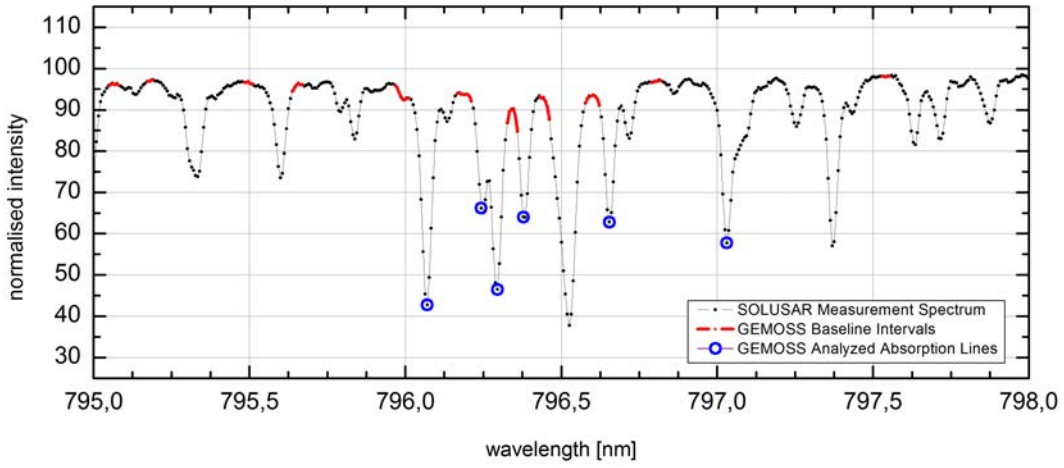

(b) Magnified excerpt of the SOLUSAR wavelength range

Figure 6.8: Example of a flat-field corrected SOLUSAR generated solar spectrum. Identified are water vapour absorption lines used in the GEMOSS project (blue circles) and corresponding base line intervals (red).

Consequently for the SOLUSAR spectra preprocessing a different approach is used to compute I_0: As of now a holistic baseline determination for the entire measurement range is applied, a solution which shows various advantages:

- Consistent baseline for all processable absorption lines (smaller variability of retrieved PW values depending on processed line.)
- Increased number of processable water vapour lines as no baseline intervals in the immediate spectral vicinity are needed.
- Theoretical possibility to extend the evaluation to conglomerate absorption structures.

To evaluate the suitable baseline intervals used for the computation of the integral baseline, solar spectra with differing absorption degrees are evaluated. Baseline intervals should be in theory utterly invariant to absorption changes. Tab. 6.4 lists the intervals which have been found to fulfil that requirement best:

Baseline Interval	Wavelength Range λ_{air}
BI_I	789.80 nm to 789.92 nm
BI_{II}	790.48 nm to 790.56 nm
BI_{III}	793.96 nm to 794.05 nm
BI_{IV}	798.88 nm to 799.02 nm
BI_V	800.90 nm to 800.98 nm

Table 6.4: Spectal intervals used for the determination of the SOLUSAR baseline $I_0(\lambda)$

Fig. 6.9 graphically shows the generation of a transmission spectrum from a representative solar spectrum obtained with SOLUSAR I, by computing a polynomial fit of degree 2 to the baseline intervals listed in Tab 6.4. The advantages, drawbacks and the accuracy of this chosen approach will be further discussed in Section 7.3.2. Preprocessing steps which have to be applied in the case of lunar spectra are described in Section 7.6.

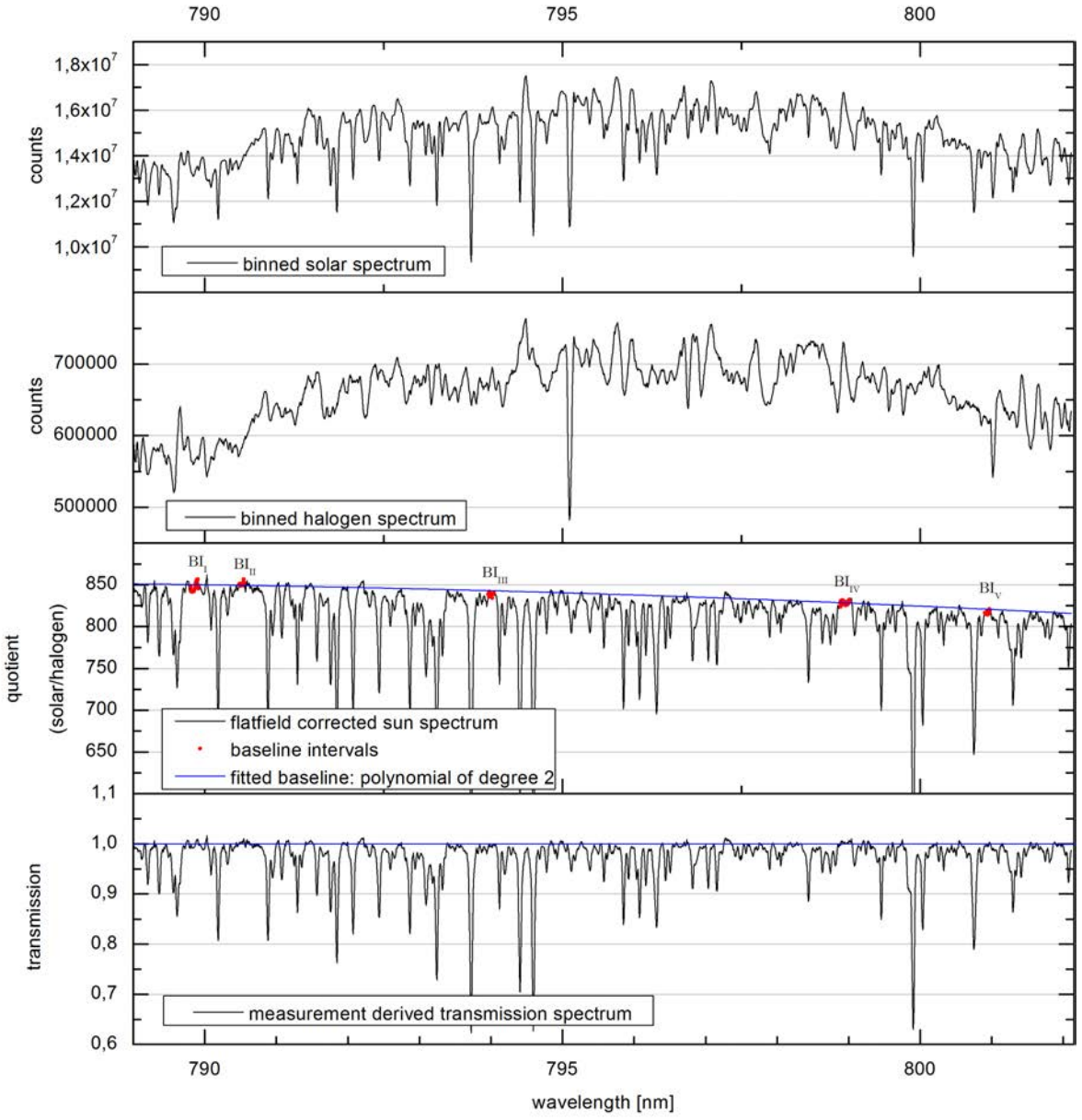

Figure 6.9: Generation of a narrow-band solar transmission spectrum. To eliminate pixel-patterns the binned solar spectrum (after having been corrected for the influence of stray light) is pixel-wise divided by a flat-field spectrum provided by the halogen lamp. The remaining broadband structures in the intensity quotient are eliminated by estimating a baseline intensity from selected baseline intervals, with which finally a processable normalized transmission spectrum can be computed.

7

Data Processing and Measurement Results

7.1 Aspects of Spectra Simulation

The transmission spectra processing follows closely the procedures comprehensively described by Somieski [2005]. Some dissimilarities and further reflections regarding the selection of the underlying spectral database, the selection of suitable absorption lines, and the parametrisation of the adjustment process are outlined in this section.

7.1.1 Comparison of Spectral Databases

When assessing the "narrow-band" absorption cross section at a specific wavelength, the accuracy of the parameters describing the shape of the emerging absorption lines in the spectral vicinity is essential. Deviations, especially of the line strength parameter, lead to systematically divergent results. This of course applies in particular if the whole set of transitions taken into consideration is biased in a similar way.

Somieski [2005] pointed out the great differences in the listed line strengths for major transitions between the HITRAN2000 database and the ESA-WVR database (for a short description of the different datasets see Section 3.10). After comparing solar spectrometry data with WVR and GPS meteorology measurements, it was concluded that both databases on average significantly underestimate the absorption strengths of these major lines. Tab. 7.1 and Fig. 7.1 show a comparison of the line characteristics of 22 absorption lines analysed by Somieski [2005], also belonging to the primary SOLUSAR wavelength range, as found in the different catalogues. The line strengths found in the GEMOSS project mostly also exceed those listed in the recent HITRAN2008 database. Note that the data for said strong lines listed in the UCL08 are identical to the values of HITRAN2008.

Wavelength [nm]	Line Strength $\left[\frac{\mathrm{cm}^{-1}}{\mathrm{molecule}\cdot\mathrm{cm}^{-2}}\right]$			
	HITRAN2000	*HITRAN2008/ UCL08*	*ESA-WVR*	*GEMOSS*
801.3104	5.31×10^{-25}	5.85×10^{-25}	6.39×10^{-25}	5.69×10^{-25}
800.9694	2.26×10^{-24}	2.28×10^{-24}	3.07×10^{-24}	3.24×10^{-24}
800.7175	3.44×10^{-25}	3.78×10^{-25}	3.83×10^{-25}	4.00×10^{-25}
800.2494	2.54×10^{-24}	2.80×10^{-24}	2.88×10^{-24}	3.23×10^{-24}
797.0305	9.83×10^{-25}	1.06×10^{-24}	1.59×10^{-24}	1.59×10^{-24}
796.6537	1.27×10^{-24}	1.31×10^{-24}	1.45×10^{-24}	1.35×10^{-24}
796.3804	8.09×10^{-25}	1.07×10^{-24}	1.24×10^{-24}	1.39×10^{-24}
796.2923	2.11×10^{-24}	2.28×10^{-24}	2.35×10^{-24}	2.47×10^{-24}
796.2457	9.31×10^{-25}	1.00×10^{-24}	1.06×10^{-24}	9.85×10^{-25}
796.0675	2.76×10^{-24}	3.00×10^{-24}	3.07×10^{-24}	3.03×10^{-24}
794.9922	8.58×10^{-25}	9.52×10^{-25}	9.95×10^{-25}	1.04×10^{-24}
793.1534	6.07×10^{-25}	6.49×10^{-25}	9.05×10^{-25}	8.26×10^{-25}
793.0797	2.89×10^{-24}	3.19×10^{-24}	3.35×10^{-24}	3.38×10^{-24}
792.2839	3.10×10^{-24}	3.39×10^{-24}	3.46×10^{-24}	3.49×10^{-24}
791.2860	1.10×10^{-24}	1.15×10^{-24}	1.19×10^{-24}	1.31×10^{-24}
791.0930	3.15×10^{-24}	3.35×10^{-24}	3.35×10^{-24}	4.01×10^{-24}
790.3932	2.84×10^{-24}	3.05×10^{-24}	3.2×10^{-24}	3.62×10^{-24}
789.8202	2.42×10^{-24}	2.75×10^{-24}	2.78×10^{-24}	2.92×10^{-24}
789.7678	1.76×10^{-24}	1.93×10^{-24}	1.91×10^{-24}	1.96×10^{-24}
789.5676	2.02×10^{-24}	2.25×10^{-24}	2.19×10^{-24}	2.22×10^{-24}
789.4061	1.63×10^{-24}	1.77×10^{-24}	1.75×10^{-24}	1.77×10^{-24}
789.1500	8.70×10^{-25}	9.47×10^{-25}	1.01×10^{-24}	1.10×10^{-24}

Table 7.1: Absorption line strengths of specific transitions analysed by Somieski [2005], covered by the main SOLUSAR measurement range. Listed are the values from different spectroscopic databases: HITRAN2000, HITRAN2008, ESA-WVR and the adjusted values by Somieski [2005] (GEMOSS). The line strength parameters for the above listed lines in HITRAN2008 can identically be found in the UCL08 database.

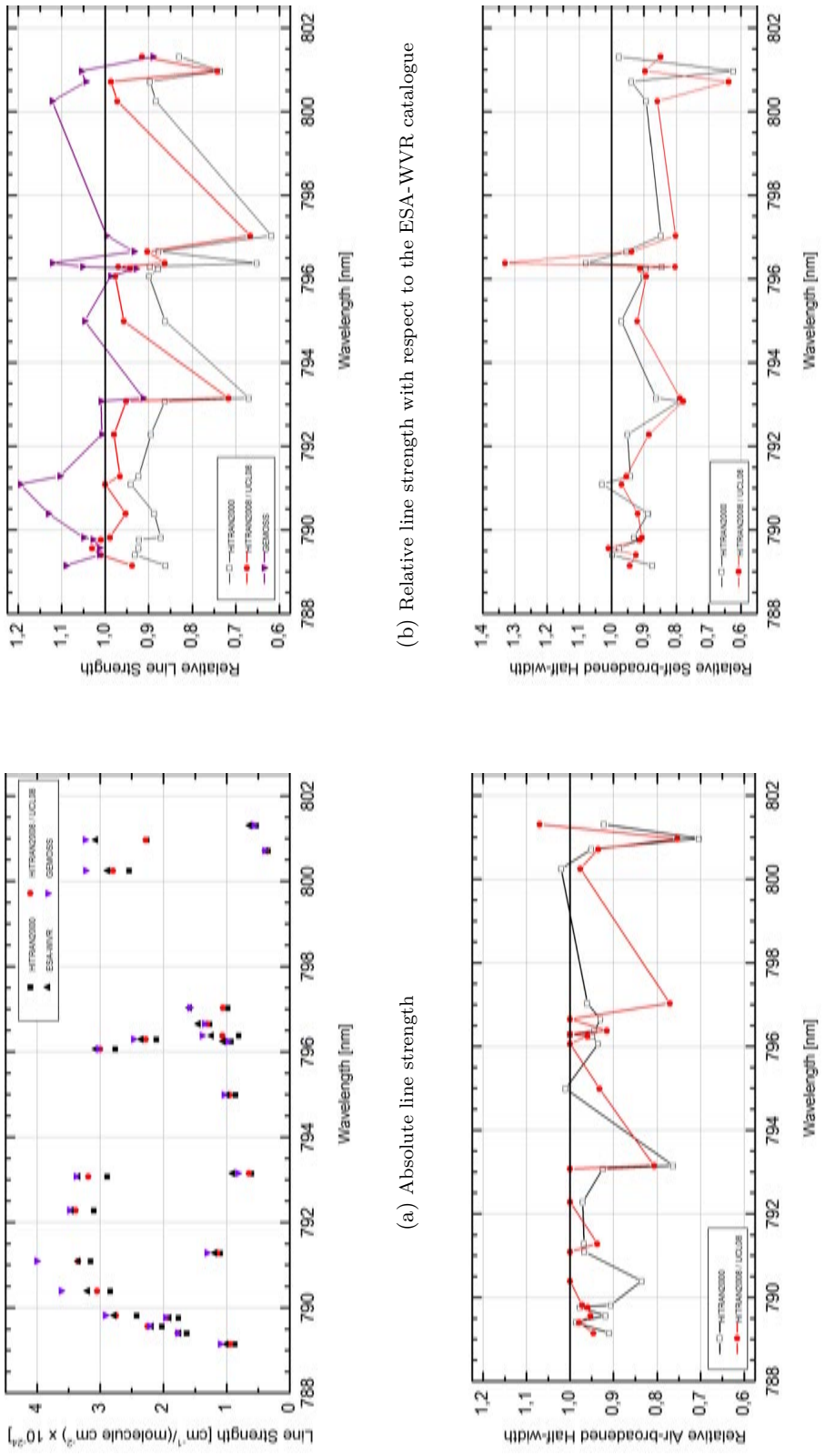

(a) Absolute line strength

(b) Relative line strength with respect to the ESA-WVR catalogue

(c) Relative air-broadened half-width with respect to the ESA-WVR catalogue

(d) Relative self-broadened half-width with respect to the ESA-WVR catalogue

Figure 7.1: Different spectroscopic parameters of a set of 22 strong absorption lines in the main SOLUSAR measurement range, as listed in different spectral databases or from calculations conducted by Somieski [2005]

For the computation of spectra obtained with the SOLUSAR measurement systems, the GEMOSS line strength parameters have not been used for different reasons: Foremost the line strength parameters are only available for major lines, but not for the vast amount of small lines contributing significantly to the overall absorption. Further the procedure to re-evaluate the line strength, as it is applied in the GEMOSS project heavily relies on the correct determination of the baseline, which is represented by distinct baseline intervals in the spectral vicinity of the addressed absorption lines. The invariance of some of the chosen baseline intervals to greater water vapour concentrations though seems questionable (compare Section 6.8).

Fig. 7.2 shows a comparison of the line strength parameter for matched lines in the ESA-WVR and the HITRAN2008 databases. Because the declaration of the set of quantum numbers assigned to the transitions in the ESA-WVR dataset is partially unclear, the matching was conducted using criteria regarding the similarities with respect to wavelength (maximum deviation: 1 pm) and line strength (maximum deviation: factor 3). Fig. 7.2(a) hints at the slightly stronger line strength values in the ESA-WVR database: The sum of the strengths of all 170 matched lines is 5.0 % higher than for the values listed in the newest HITRAN database. Fig. 7.2(b) indicates that the differences for the major transitions seem quite small. As the HITRAN project is an ongoing long-term project based and verified by the work of numerous scientific groups, it is favoured for the processing of SOLUSAR spectra.

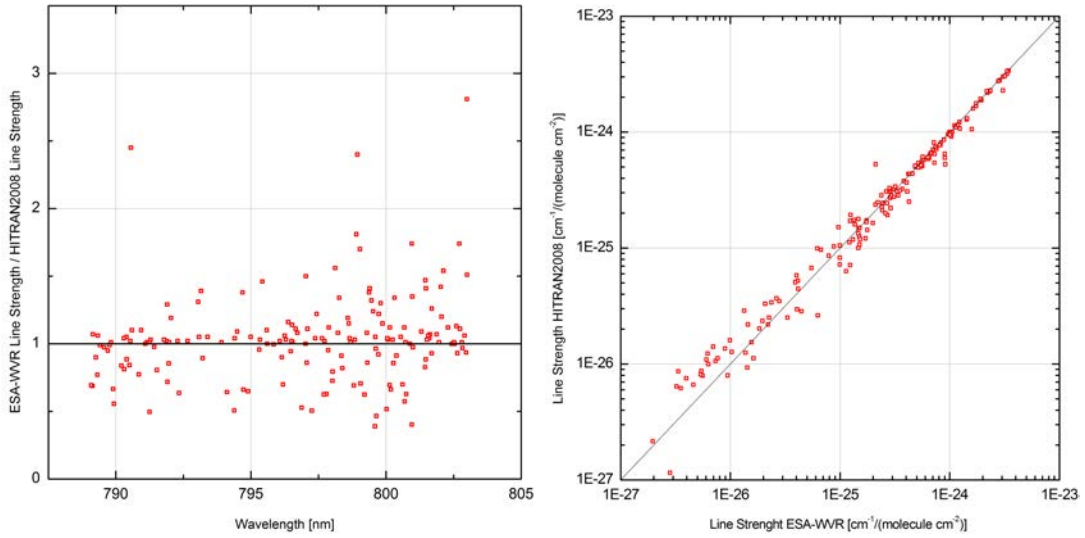

(a) Relative line strength

(b) Scatterplot of the absolute line strength

Figure 7.2: Comparison of the line strength of 170 matched absorption lines in the SOLUSAR measurement range for the ESA-WVR and the HITRAN2008 database.

The difference between the most recently updated databases HITRAN2008 and UCL08 lays in the number of listed lines. Fig. 7.3 shows water vapour lines in both databases with their respective line strengths. HITRAN2008 lists only 737, UCL08 1799 lines in the SOLUSAR range.

Use of the extended UCL08 databases significantly prolongs the spectra simulation time and thus the overall processing time. An analysis of the impact of an extended database on the overall absorption at interesting spectral positions in the SOLUSAR wavelength range is conducted by means of a comparison of synthetic absorption spectra computed on the basis of the different spectral catalogues. The simulations have been conducted assuming

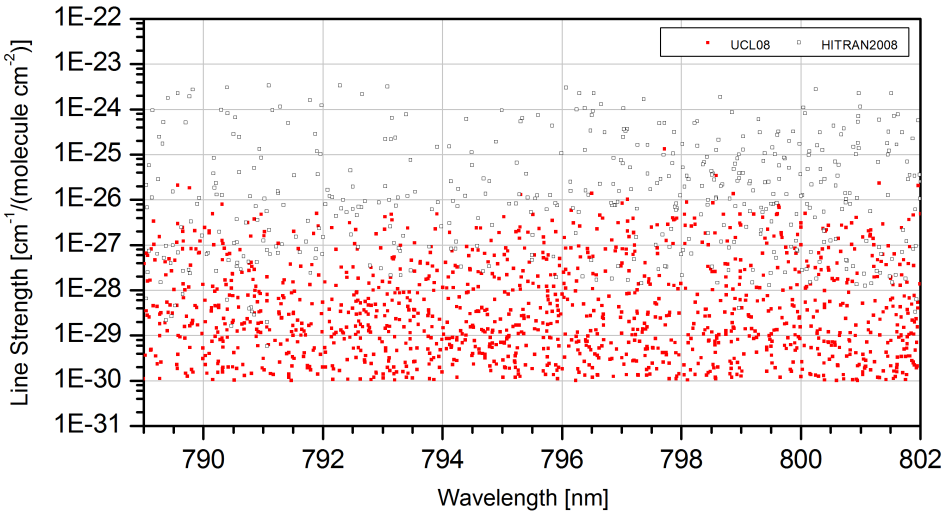

Figure 7.3: Graph of all water vapour lines with their respective line strengths in the spectral range between 789 nm and 802 nm as listed in the HITRAN2008 database and the more extensive UCL08 (short version). All lines present in the HITRAN database are also listed in the UCL08 with identical spectral parameters. The number of HITRAN lines amounts to 737, whereas UCL08 lists 1799 lines in this spectral range.

following measurement conditions: Elevation angle: 25°, ZPW: 10 kg/m^2, apparatus function $FWHM_{Gauss}$: 4 px, spectral resolution: 3 pm, station height: 0 m, station temperature 0 °C, station pressure: 1 atm. The result is shown in Fig. 7.4.

For the major transitions the difference in absorption strength between HITRAN2008 and UCL08 is very small, and mostly clearly below 1 %. In contrast the HITRAN2008 and ESA-WVR results differ very significantly, especially in the "wing" areas of the major transitions. It is concluded that favouring the most recent HITRAN dataset over UCL08 does not significantly compromise the accuracy of the derived water vapour concentrations, but helps keeping the computational effort relatively low.

7.2 Adjustment Process

7.2.1 Selection of Absorption Lines

Regarding the selection of suitable spectral lines respectively surrounding spectral intervals for the analysis of the transmission and deduction of water vapour concentrations, several criteria have to be taken into account:

- Stronger absorption lines yield a better S/N ratio.
- However absorption lines reaching transmission values of below 0.4 ought to be omitted from the processing, as non-linear effects (mainly caused by stray light influence) can considerably worsen the quality of the results.
- Chosen absorption lines ought not have Fraunhofer lines in the immediate spectral vicinity.
- Due to the broad range of different water vapour concentrations and the changing elevation angles, spectra with starkly different transmission values are recorded. In order to

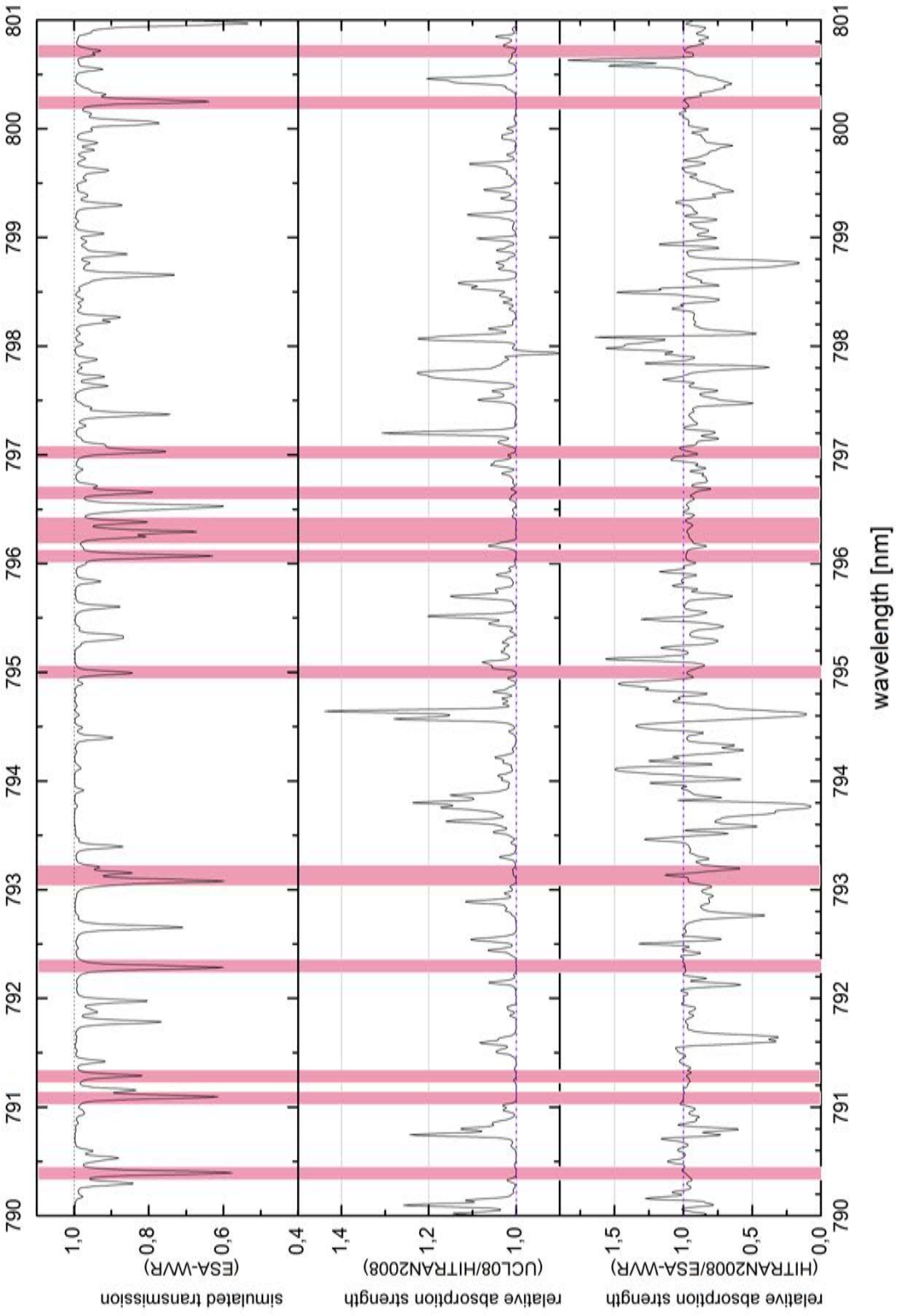

Figure 7.4: Comparison of synthetic spectra, computed on the basis of different spectral databases: ESA-WVR, HITRAN2008 and UCL08. Whereas the relative absorption strength for the latter two is mostly very close to 1 at least for major transitions (marked red), the differences between ESA-WVR and HITRAN2008 can easily exceed 10 % also for major absorption lines. (Please note the different scales of the ordinates between the UCL08/HITRAN2008 and the HITRAN2008/ESA-WVR comparisons.)

retrieve reliable data for the manifold different situations a set of absorption lines with correspondingly different absorption cross sections has to be selected.

- The evaluable range around the point of strongest absorption should be kept relatively small as the analysis of the line's "wings" is generally more prone to errors, as the influence of close-by lines increases.

To test the consistency of the results deduced from different absorption features in the spectral range of SOLUSAR, a variety of spectra obtained under different circumstances regarding water vapour concentrations, season of year and daytime are analysed. Tab. 7.2 gives an overview on the characteristics of six datasets, which all consist of totally 5 spectra each. The spectral features included in this computation are depicted in Fig. 7.5, showing the comparison of a measured transmission spectrum and a fitted simulation spectrum. Most of the chosen major lines were also considered in the GEMOSS project, some further spectral intervals have been added though, some others were totally omitted due to obvious Fraunhofer line influence.

Dataset	Date	UTC Slot	Interval [min]	Mean ZPW [kg/m^2]	Mean Elevation [°]
I	15 August 2012	12.00 - 13.00	20	20.8	49
II	15 August 2012	17.00 - 18.00	10	19.2	10
III	25 May 2012	15.00 - 16.00	5	15.4	33
IV	1 February 2012	13.00 - 14.00	2	3.1	13
V	6 March 2013	14.00 - 15.00	5	7.9	18
VI	15 April 2013	12.00 - 13.00	5	24.9	44

Table 7.2: Used datasets from SOLUSAR I to assess the usefulness of spectral intervals for the retrieval of atmospheric water vapour concentrations.

In this experiment not the absolute deviation of the PW results produced by a single line with respect to the mean water vapour concentration derived from the whole spectrum is assessed, but rather the scatter range of the ratio of single line concentrations (ZPW_{line}) and mean spectrum concentration ($ZPW_{spectrum}$) for a representative set of different exposure situations. If the scattering of said ratio is becoming large for a specific spectral feature, this indicates that the evaluation of said line is yielding unreliable results, possibly caused by underlying Fraunhofer features. Also close-by water vapour absorption lines can inhibit accurate concentration retrieval if inaccuracies with respect to line broadening are present (both atmospheric line broadening and apparatus influence).

Overall biases of retrieved concentrations of single lines with respect to the mean concentrations deduced from all features in the spectrum are mainly caused by inaccuracies of the line strengths listed in the database (and possibly systematic local baseline anomalies). Somieski [2005] adjusted said line strengths through extensive experiments where the "true" water vapor concentrations have been posited as being known – provided by comparison measurements using co-located radiosondes and WVR instruments. In this project such comparisons were not made, which is why a final judgement of line strength validity is not possible. For an estimation of the PW uncertainty caused by line strength uncertainties please see Section 7.3.2.

The results of the experiment described above are shown in Figs 7.6 and 7.7. The mean values of the ratio $ZPW_{line}/ZPW_{spectrum}$ is ranging from 0.86 (line 1) to 1.15 (line 16). Looking at the standard deviations of said ratio, values are ranging between 0.012 (line 17) and 0.123

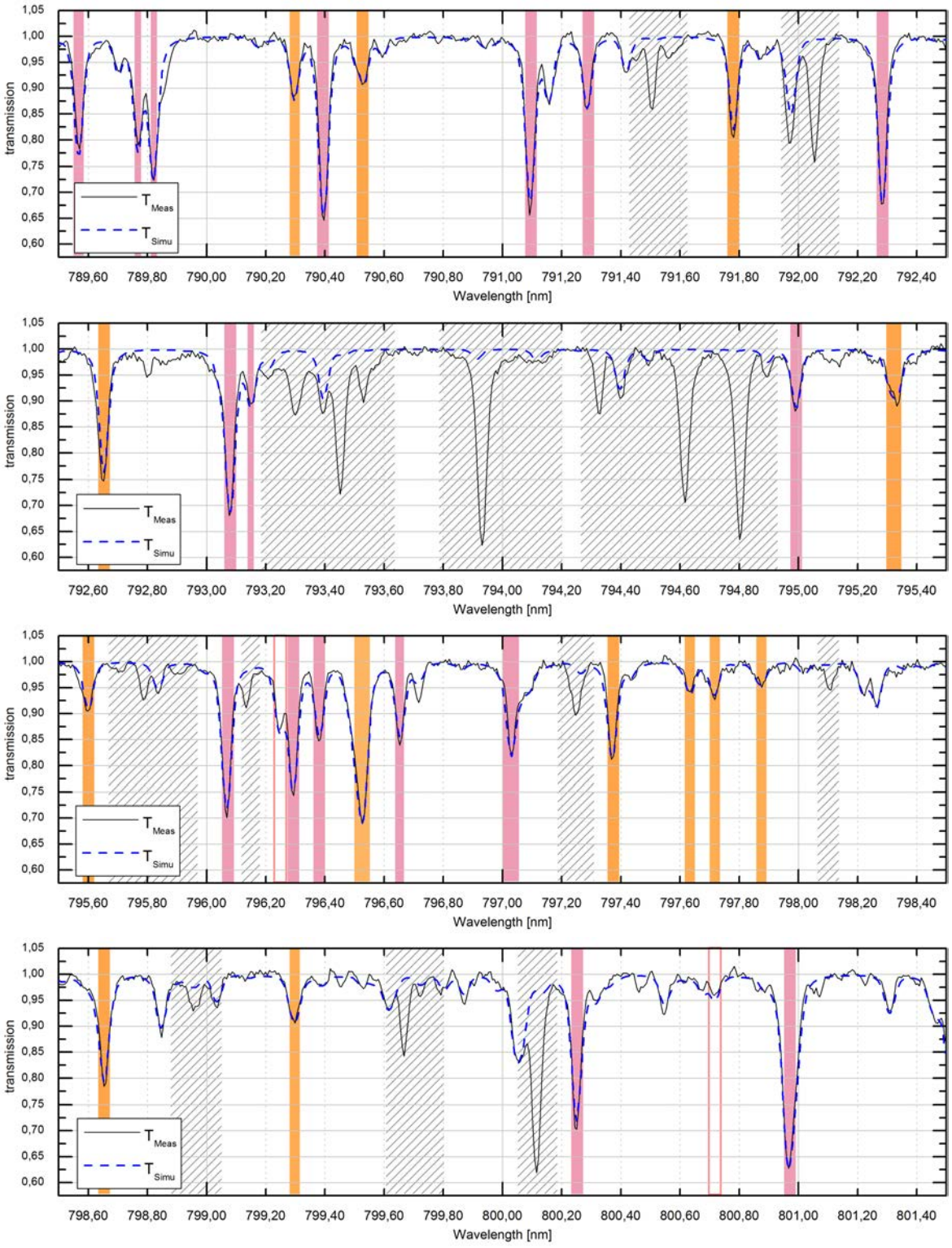

Figure 7.5: SOLUSAR measurement range between 789.5 nm and 801.5 nm. Depicted is an absorption spectrum obtained by SOLUSAR I in late August in the early afternoon hours with an intermediate ZPW. The dashed line shows a simulated transmission spectrum fitted to the measurement spectrum. Identified are the so-called processing intervals whose usefulness is analysed: Denoted with red bars are intervals which have been utilized in the GEMOSS project as well. Orange bars denote newly considered absorption lines. Red-framed blank bars stand for GEMOSS processing intervals not utilized any more. Hatched areas indicate spectral regions with strong Fraunhofer line influence.

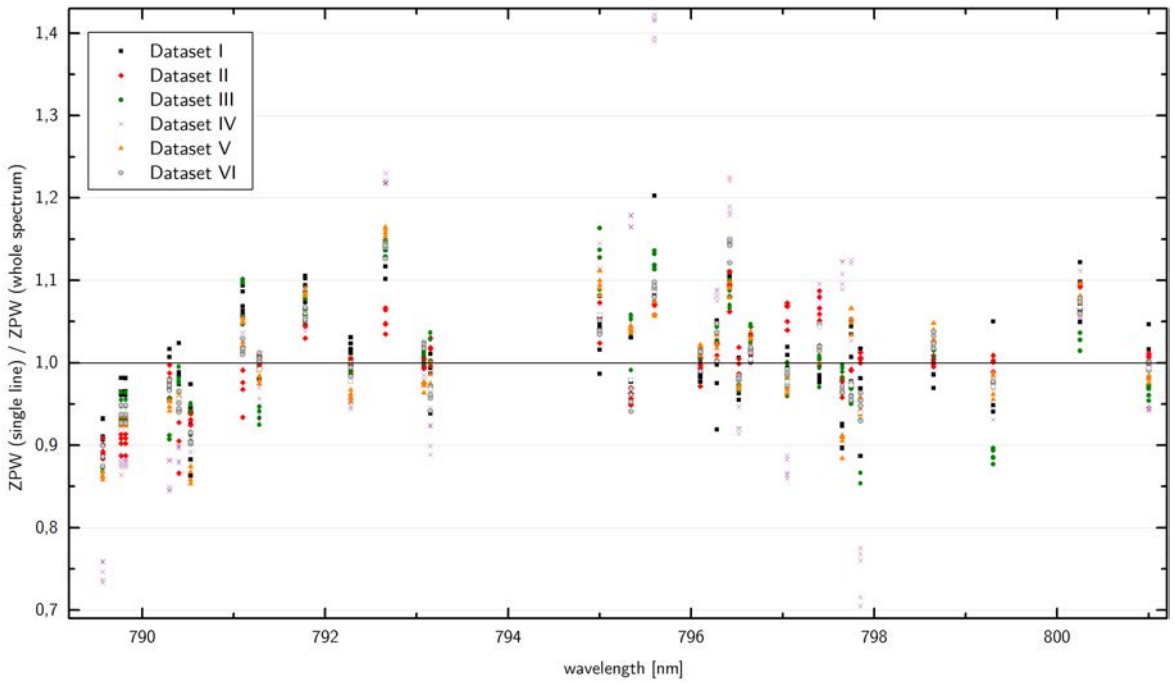

(a) Ratio of ZPW_{line} to $ZPW_{spectrum}$ for all 30 lines in 30 spectra. The belonging to the specific datasets is color-coded.

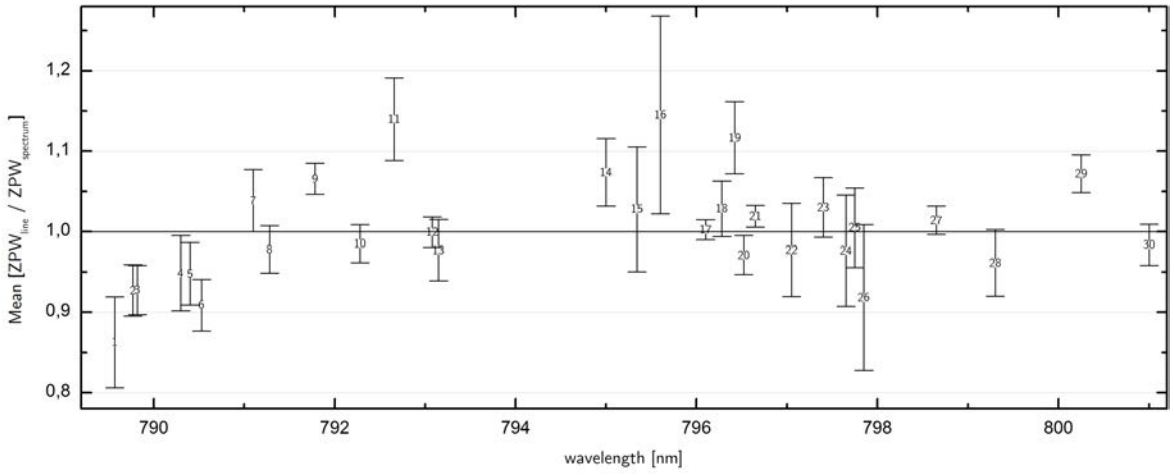

(b) Mean values and standard deviations of the ratio $ZPW_{line}/ZPW_{spectrum}$

Figure 7.6: Analysis of the ratio between the ZPW values extracted by analysis of a single absorption feature (ZPW_{line}) and the values gained from the processing of the whole spectrum ($ZPW_{spectrum}$). Analysed are the 30 absorption features depicted in Fig. 7.5 for measurements belonging to the six datasets listed in Tab. 7.2, each consisting of 5 spectra.

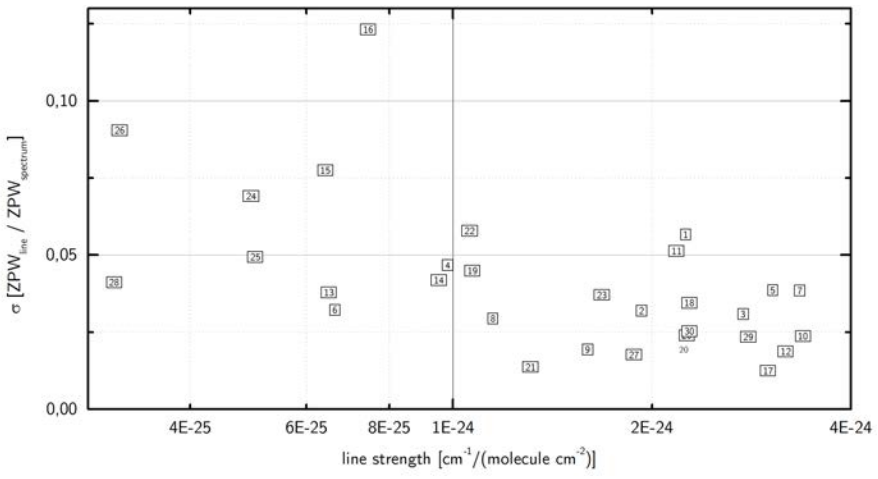

Figure 7.7: Standard deviation of the ratio $ZPW_{line}/ZPW_{spectrum}$ with respect to the line strength.

(line 16). The mean standard deviation is 0.024. Based on these calculations following lines are not considered: Lines 1 and 11 as their reliability with respect to their relatively big line strength is small (see Fig. 7.7). Line 1 might be influenced by some sort of edge effect. Line 16 is a weaker line but it seems strongly influenced by Fraunhofer structures as is also visible in Fig. 7.5 (around 795.6 nm). Albeit strong scattering, lines 15 and 26 are retained as these are weaker transitions necessary for processing of measurements with small transmission values.

Tab. 7.3 gives the full set of absorption lines which are used in for computation of SOLUSAR spectra as presented in this work together with the respective analysis intervals.

Comparing the resulting PW values of distinct lines within the same dataset could give an indication on the precision of the retrieved water vapour concentrations (not the overall accuracy). Modelling errors such as the deviation of the atmospheric model from the true atmospheric state, inaccuracy of the baseline model and apparatus function (and of course line strength) all should influence the spectra belonging to the same set in quite a similar way because of the temporal proximity.

To make the PW values of different spectra comparable, changes in total water vapour concentrations over the dataset time window have to be taken into account, as well as slightly different absorption path lengths. Thus the measured PW_i^m of the spectrum i ($i = 1$ to 5) and the transition m values were converted in "normalized" $PW_i^{m\prime}$ values using following formula:

$$PW_i^{m\prime} = ZPW_i^m \cdot \frac{\overline{ZPW_3^S}}{\overline{ZPW_i^S}} \cdot \frac{PW_3^m}{ZPW_3^m} \tag{7.1}$$

with ZPW_i^m the detected zenithal concentrations derived from spectrum i and line m and $\overline{ZPW_i^S}$ the mean zenith integrated amount derived from all transitions. As reference point in time the spectrum $i = 3$ in the middle of the dataset is taken.

The result of the comparison of the PW of the different spectra belonging to one dataset is shown in Fig. 7.8 and in Tab. 7.4. Comparing the results with the estimation of the compound noise carried out in the later Section 7.3.1 which reveals a rather small dependency of the uncertainty on the PW concentration, indicates that the precision must be influenced

Number	Wavelength [nm]	Analysis Interval [nm]	Line Strength HITRAN2008 $\left[\frac{\mathrm{cm}^{-1}}{\mathrm{molecule}\cdot\mathrm{cm}^{-2}}\right]$
2	789.7678	789.76–789.78	1.93×10^{-24}
3	789.8202	789.81–789.83	2.75×10^{-24}
4	790.2968	790.28–790.31	9.82×10^{-25}
5	790.3932	790.38–790.41	3.05×10^{-24}
6	790.5324	790.51–790.55	6.63×10^{-25}
7	791.0930	791.08–791.11	3.35×10^{-24}
8	791.2860	791.27–791.30	1.15×10^{-24}
9	791.7808	791.77–791.79	1.6×10^{-24}
10	792.2839	792.27–792.29	3.39×10^{-24}
12	793.0797	793.07–793.09	3.19×10^{-24}
13	793.1534	793.14–793.16	6.49×10^{-25}
14	794.9922	794.98–795.01	9.52×10^{-25}
15[a]	795.3361	795.30–795.34	6.41×10^{-25}
17	796.0675	796.05–796.09	3.00×10^{-24}
18	796.2923	796.28–796.31	2.28×10^{-24}
19	796.3804	796.37–796.39	1.07×10^{-24}
20	796.5316	796.51–796.54	2.26×10^{-24}
21	796.6537	796.64–796.67	1.31×10^{-24}
22	797.0305	797.02–797.04	1.06×10^{-24}
23	797.3711	797.36–797.39	1.68×10^{-24}
24	797.6330	797.62–797.65	4.95×10^{-25}
25	797.7184	797.70–797.73	5.02×10^{-25}
26	797.8793	797.86–797.89	3.13×10^{-25}
27	798.6533	798.64–798.67	1.88×10^{-24}
28	799.3092	799.29–799.31	3.07×10^{-25}
29	800.2494	800.24–800.26	2.80×10^{-24}
30	800.9694	800.95–800.99	2.28×10^{-24}

[a] Processing interval actually consists of a doublet of two similarly strong transitions: The line listed above plus another line at 795.3081 nm with line strength 5.41×10^{-25} $\frac{\mathrm{cm}^{-1}}{\mathrm{molecule}\cdot\mathrm{cm}^{-2}}$

Table 7.3: The chosen absorption lines for the evaluation of the solar and lunar spectra obtained by SOLUSAR.

not only by noise but also by additional portions, some of which are also showing a dependency on the absorption strength (e.g. noise influence on baseline retrieval).

Dataset	Mean $\sigma_{PW,line}$ [%]	Min $\sigma_{PW,line}$ [%]	Max $\sigma_{PW,line}$ [%]
I	1.90	0.69	5.74
II	1.41	0.44	3.88
III	1.90	0.28	4.77
IV	1.75	0.27	6.45
V	0.93	0.20	2.44
VI	0.89	0.21	2.09

Table 7.4: Relative standard deviations of the normalized PW values from single lines in spectra belonging to the same datasets. Listed are mean, minimum and maximum relative standard deviation of all lines (only lines from Tab. 7.3 included) for datasets I to VI (see Tab. 7.2).

7.2.2 Adjustment Process Parameters

In contrast to the GEMOSS project where a set of lines with "harmonized" absorption cross section has been generated and used, the HITRAN2008 line set shows large differences in the line strength as described in the section above. To make the matching for the single absorption features better and to speed up the whole adjustment process, all lines have been evaluated separately, apart from lunar measurements as outlined in Section 7.6. Tab. 7.5 gives an overview on the most important parameters used in the adjustment process of solar/lunar spectra.

Parameter	Value
Spectral database	HITRAN2008
Simulation spectrum resolution	3 pm
Expansion of simulated spectrum around analyzed feature	$\pm$ 0.4 nm
Adjustment Break Condition 1	$\Delta_{PW} \leq 0.05\,\mathrm{kg/m^2}$
Adjustment Break Condition 2	$\Delta_{\lambda} \leq 0.2$ pm
Maximum Adjustment Cycles per Line	50
Consideration of ray bending	Elevation angle $< 40°$

Table 7.5: Adjustment Process Parameters

7.3 Assessment of Accuracy

For an ultimate assessment of the accuracy of the built measurement systems the availability of additional information on the true atmospheric water vapour concentrations along the line of sight would be necessary. Apart from the comparison measurements with GPS meteorology presented in Section 7.5, giving an indication on the occurring water vapour concentrations, no alternative measurements, able to serve as real reference are available in this project. Nonetheless it is to some degree possible to estimate the extent of certain uncertainty error sources and how they influence the final PW results. There are many different effects contributing

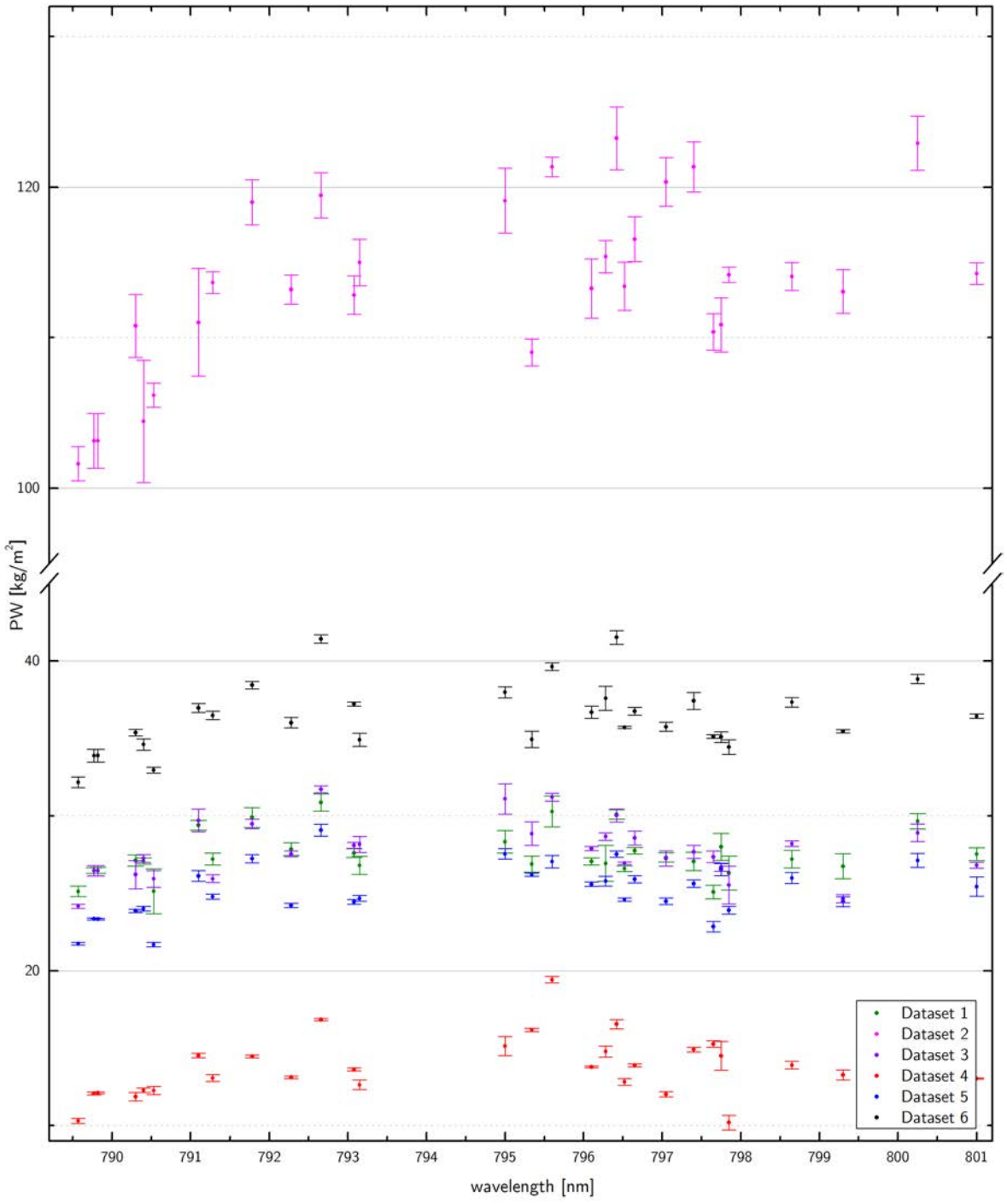

Figure 7.8: Comparison of the normalized *PW* (see Eq. 7.1) of single lines from spectra belonging to the same dataset.

to the overall reduction of precision of DOAS measurements. They can be roughly divided into stochastic errors imprinting noise onto the signal and multiple uncertainty sources which potentially can build up systematic biases.

7.3.1 Stochastic Uncertainty Sources

The signal-to-noise ratio is a crucial measure to qualify the sensitivity of a measurement system. In our case the signal produced by the CCD sensor is a function of the photon flux incident on the detector, the latter's quantum efficiency and the exposure time. On the other hand a multitude of different noise sources contribute to the denominator of the S/N-ratio:

Shot Noise

Inherent to radiation flux is a statistical fluctuation of the arrival interval of photons, which can be described by a Poisson distribution. Accordingly the generation and detection of photoelectrons inside the detector follows the same pattern. This so-called shot noise (or photon noise) of a photodiode detector represents a physical noise barrier which cannot be overcome. The standard deviation σ_{shot} of the signal caused by shot noise expressed in detector counts is:

$$\sigma_{shot}\,[\text{counts}] = \sqrt{\frac{e^-}{\Omega}} \tag{7.2}$$

with e^- the number of accumulated electrons and Ω the detector specific conversion factor (electrons per counts). Ω in this case amounts to $0.9\,\text{e}^-/\text{counts}$ (see Section 4.6.3). For solar spectra, pixel saturation degrees between 60 % to 80 % are tried to be achieved, yielding 45 000 counts per pixel on average. The vertical binning over 36 px (using the hexagonal fibre), which all show similar intensities, and the accumulation of normally 12 exposures for one saved spectrum leads to a mean shot noise for solar spectra $\sigma_{shot,solar}$ of practically negligible 0.02 %. In case of measurements of lunar spectra with only a few hundred recorded counts per pixel though the shot noise influence is of course considerably higher. Assuming intensities of around 200 counts/px and the accumulation of 30 spectra in 10 min this yields a shot noise $\sigma_{shot,lun}$ of around 0.3 %. Also the halogen flat-field spectra are affected: $\sigma_{shot,hlg}$ amounts to around 0.05 %.

Dark Noise

Equivalently to shot noise there is a variability in the number of electrons which are thermally generated in the sensor. The level of this dark noise is mainly a function of the chip temperature and the exposure time. Though not down-cooled as much as e.g. in astronomical applications, the temperature stabilization around 0 °C allows a noise level which in case of the short exposure times of solar measurements and for the recording of halogen spectra is considered negligible. With the applied cooling, the number of thermally generated photoelectrons amounts to around $120\,\text{s}^{-1}$. Thus in case of lunar spectra with exposure times at 20 s the mean standard deviation of a single pixel dark signal is exceeding 50 counts (the actual signal being around 200 counts). Given the averaging through binning and exposure accumulation this yields a $\sigma_{dark,lun}$ of 0.8 % to 0.9 % – considerably higher than the shot noise of the actual signal.

Read Noise / Interferences

Readout noise does not vary depending on the illumination situation and according to the detector specifications amounts to 20 electrons. A more substantial portion of disturbance in our case, however, is emerging from the electromagnetic interferences due to unwanted interactions with the actuator system, as described in Section 4.10.6. Even though partially suppressed by hardware measures a significant portion is remaining. One must concede that said disturbances do not actually qualify as purely random noise, but for reasons of simplicity are treated here that way. As the stripe patterns are slowly rotating, the influence on the vertically binned spectrum is subject to significant change over time. In the best case the uncertainty influence on the binned column can fall to 100 counts for one exposure. In the worst case it can reach values of over 1200 counts though. As a representative mean value 800 counts are assumed. Unfortunately these structures are neither efficiently tackled by summation of various subsequent spectra (pattern rotations is too slow), nor are the broader structures eliminated in the baseline retrieval process – at least not using the chosen polynomial baseline approach.

Given the independence of the two effects, the integral readout σ_{read} uncertainty coming from actual read noise ($\sigma_{CCD,read}$) and the uncertainty due to the electromagnetic interference σ_{EI} can be written as:

$$\sigma_{read} = \sqrt{\sigma_{CCD,read}^2 + \sigma_{EI}^2} \tag{7.3}$$

Solar spectra (taken under following premisses: pixel intensity: 45 000 counts; vertical binning over 36 px and accumulation of 12 exposure per spectrum), have an integral read uncertainty of the transmission $\sigma_{read,sun}$ of 0.05 %. For lunar spectra (pixel intensity: 200 counts; 30 exposure accumulations) $\sigma_{read,lun}$ is found experimentally to lie between 0.7 % to 3.5 % – as a mean value 2 % are assumed. Halogen spectra are affected as well: $\sigma_{read,hlg} \approx 0.2\,\%$.

Stray Light

To assess the performance of the applied stray light correction model which is described in Section 6.4 strong oxygen absorption bands (such as depicted in Fig. 6.3) can be analysed. After applying the procedure the integral intensity over the entrance slit height should become zero for columns in the centre of the saturated absorption lines. As described in Section 6.4 the remaining column intensity residuals have been experienced not to exceed 0.4 %. The mean deviation σ_{stray} is estimated at 0.18 % with respect to the maximum column intensity. For lunar spectra a stray light correction has not been adopted at all, as stray light levels are generally very low and the general S/N-ratio so small that a reliable estimation of the stray light portion seems virtually impossible.

Etaloning

The imprinted etaloning structures qualify as what is sometimes called “spatial noise”, which in contrary to, e.g., normal read or shot noise cannot be averaged out through accumulation of multiple exposures. The fringes undulating between constructive and destructive interference can be seen as a modulation overlaid on the actual signal. Hence also the remaining structures after the division of the solar/lunar spectra and a flat-field spectrum, can be regarded as the result of a multiplication of the actual signal with a wavelength-dependent etaloning factor.

The distribution of the etaloning structures does follow quite closely a Gauss curve. In case of full moon the manifestation of etaloning structures are considered similar to solar measurements. For increasing lunar phase angles the remaining structures become more dominant. Based on the results of experiments described in Section 4.9.3 for the added uncertainty for solar transmission spectra $\sigma_{eta,sun}$ a conservative value of 0.2 % is assumed; for lunar spectra with phase angles between 0° and 50° $\sigma_{eta,lun}$ should range between 0.2 % and 0.6 %.

Compound Stochastic Influence

According to the law of error propagation the compound influence $\sigma_{spectrum}$ of the different uncertainty sources on a spectrum of a specific illumination source (sun, moon, halogen) can be written as follows:

$$\sigma_{spectrum} = \sqrt{\sigma_{shot}^2 + \sigma_{read}^2 + \sigma_{dark}^2 + \sigma_{stray}^2} \tag{7.4}$$

Assumed are Gaussian distributions for all uncertainty portions. With the values listed above for the different noise portions this yields $\sigma_{sun} = 0.19\,\%$, $\sigma_{lun} = 2.2\,\%$ and $\sigma_{hlg} = 0.27\,\%$. Not included in these values is the effect of etaloning which makes itself felt in the computation of the transmission spectra which can be described as the pixel-wise ratio of the solar/lunar spectrum and the halogen spectrum. In this description the influence of etaloning can be seen, as already mentioned, as a signal modulation:

$$t(\lambda_i) = e(\lambda_i) \cdot \frac{SL(\lambda_i)}{H(\lambda_i)} \tag{7.5}$$

with $t(\lambda_i)$ the transmission value at the pixel i (with center wavelength λ_i) and with $e(\lambda_i)$ the wavelength-dependent etaloning modulation of the spectrum. $e(\lambda_i)$ is a number close to 1 and has an uncertainty σ_{eta}. $SL(\lambda_i)$ and $H(\lambda_i)$ are the number of counts of the solar/lunar and the halogen spectra with their respective uncertainties $\sigma_{sun/lun}$ and σ_{hlg} according to Eq. 7.4. The uncertainty of the transmission spectra can be calculated with following expression:

$$\sigma_t(\lambda_i) = \sqrt{\left(\frac{SL(\lambda_i)}{H(\lambda_i)}\right)^2 \cdot \sigma_{eta}^2 + \left(\frac{e(\lambda_i)}{H(\lambda_i)}\right)^2 \cdot \sigma_{spectrum}^2 + \left(\frac{e(\lambda_i) \cdot SL(\lambda_i)}{H(\lambda_i)^2}\right)^2 \cdot \sigma_{hlg}^2} \tag{7.6}$$

This yields following values for the total uncertainty of transmission spectra: $\sigma_{t,sun} = 0.4\,\%$ in case of solar measurements and $\sigma_{t,lun} = 2.2\,\%$ for lunar transmission spectra, signifying that the latter is dominated by the noise of the lunar spectrum itself. For solar spectra the transmission uncertainty could be reduced by around 0.05 % if there was no etaloning influence present.

To derive the influence of transmission uncertainties on the ultimately computed PW values, following expression is used:

$$\sigma_{PW} = \sigma_{ap} \cdot \sqrt{N^{-1}} \tag{7.7}$$

with N the – in our case – single element of the matrix of normal equations $\mathbf{N}$ as expressed in Eq. 3.37. According to Carosio [2001] generally an "a posteriori" standard deviation σ_{ap}

can be computed from the sum of weighted squared improvements (v_i^2) in the measurement process:

$$\sigma_{ap} = \sqrt{\frac{\sum_{i=0}^{n} p_i \cdot v_i^2}{n}} \tag{7.8}$$

For all n observations (number of pixels) in the processing interval the weight p_i is:

$$p_i = \frac{1}{\sigma_t^2(\lambda_i)}. \tag{7.9}$$

In our case said σ_{ap} is a measure for the matching quality between simulated and measured spectra. This matching quality is influenced by stochastic noise but likewise by various systematic effects, such as the accuracy of the apparatus function description. To solely quantify the noise influence on PW values, measured solar spectra were regularly processed. After the last iteration of the matching procedure the remaining improvements v_i from every pixel belonging to the processing intervals were replaced by the above estimated $\sigma_{t,sun}$ and $\sigma_{t,lun}$, respectively, to ultimately determine the noise-induced $\sigma_{PW,noise}$:

$$\sigma_{PW,noise} = \sqrt{\frac{\sum_{i=0}^{n} p_i \cdot \sigma_t^2}{n}} \cdot \sqrt{N^{-1}} \tag{7.10}$$

Spectra were taken from datasets II, III and IV (see Tab. 7.2) thus covering the whole range from very weak to very strong absorption.

	solar spectra			lunar spectra		
Dataset	$\sigma^m_{PW,min}$	$\sigma^m_{PW,max}$	$\overline{\sigma^m_{PW}}$	$\sigma_{PW,min}$	$\sigma_{PW,max}$	$\overline{\sigma^m_{PW}}$
II $\overline{PW}$ =113.6 kg/m^2	0.11 (0.09 %)	1.40 (1.24 %)	0.40 (0.36 %)	0.58 (0.51 %)	7.73 (6.82 %)	2.22 (1.95 %)
III $\overline{PW}$ =27.6 kg/m^2	0.11 (0.39 %)	1.42 (5.12 %)	0.41 (1.47 %)	0.59 (2.20 %)	7.79 (29.5 %)	2.24 (8.19 %)
IV $\overline{PW}$ =13.2 kg/m^2	0.11 (0.82 %)	0.91 (6.66 %)	0.37 (2.76 %)	0.61 (4.48 %)	5.02 (36.6 %)	2.08 (15.2 %)

Table 7.6: Assessment of the influence of stochastic noise in solar and lunar transmission spectra on the retrieved PW values. The experiment was carried out using regularly measured solar spectra from datasets II, III and IV. The normal processing procedures were applied. After the last fitting iteration the actual improvements were replaced by the estimated $\sigma_{t,sun}$ and $\sigma_{t,lun}$, respectively, to ultimately quantify the noise influence on PW values using Eq. 7.10. The mean, minimal and maximal σ^m_{PW} for the m lines in the spectrum are given in [kg/m^2] and as percentage with respect to PW.

The results as showed in Tab. 7.6 indicate that the absolute accuracy of the PW results show very little dependence on the magnitude of the actual PW values, due to the fact that the partial derivatives $\frac{\partial t(\lambda_i)}{\partial PW}$ are changing very slowly with PW. For solar measurements the compound noise influence produces PW uncertainties below 0.5 kg/m^2. In case of lunar measurements the PW uncertainty is estimated slightly above 2 kg/m^2.

7.3.2 Modelling Errors and Systematic Influences

When dealing with measurements obtained under conditions with bright sunlight, the impact of the above discussed errors caused by the imperfection of the hardware, are comparably low with respect to the subsequently discussed modelling errors. However the two categories cannot be seen as being completely independent, as e.g. the imprinted noise in the spectrum heavily affects the accuracy of the deduced baseline intensity by means of the corresponding base retrieval model.

The focus of this section lays on the accuracy of the baseline determination and the apparatus function modelling, and their respective influence on the integrity of the derived water vapour concentrations, both areas where the SOLUSAR measurement system shows distinct differences compared to the earlier apparatuses. The influence of the trueness of the parameters describing the individual transitions, as well as an appraisal of the atmospheric model's influence on the final concentration values are shortly discussed in the following. Further the influence of the instruments optical adjustment on the observed radiation path length is shortly outlined.

Baseline Accuracy

A good appraisal of the baseline intensity is crucial in differential absorption spectrometry. As outlined in Section 6.8 SOLUSAR makes use of a new approach by estimating a unified baseline trajectory for the whole flat-field corrected spectrum. When assessing the validity of the chosen determination algorithm for said wavelength-dependent reference intensity, carried out for each spectrum anew, different questions arise:

1. Is the chosen functional approach able to properly model the remaining broadband structures in computed spectra quotients of a solar/lunar spectrum and a halogen spectrum as they are recorded by this specific apparatus?
2. How well do the chosen "baseline intervals", from which the baseline is derived, fulfil the need for having absorption values very close to zero?
3. How does regular noise (as estimated in Section 7.3.1) affect the accuracy of the baseline?
4. How does a unified baseline approach affect the accuracy of PW values resulting from the evaluation of specific single lines?

The first question is probably the most difficult to answer as various broadband effects can be included in a spectra quotient as listed in Section 6.8. The choice of a polynomial of degree 2 seems a very conservative approach. A certain indication can be obtained by looking at the fitting quality measures, where polynomials of degree 2 most times yield matchings which are not essentially inferior to polynomials of higher orders. The latter, however, often drift-off at the borders of the spectral window. Comparing the baseline accuracy of the two measurement instruments it though seems that for SOLUSAR II measurements polynomials of degree 3 often would have been a slightly better choice. A sample is provided in Fig. 7.9.

As attempts to analytically answer the questions 2 to 4 seem out of range, an experimental approach using solely synthetic absorption spectra is carried out on the base of a Monte-Carlo simulation. For a specific measurement situation with defined ground meteorological values, apparatus function and elevation angle (70°), three simulated spectra (with the resolution of a typical SOLUSAR measurement spectrum of around 7 pm/px) are computed corresponding to different water vapour concentrations ($PW_1 \approx 55\,\mathrm{kg/m^2}$, $PW_2 \approx 20\,\mathrm{kg/m^2}$ and

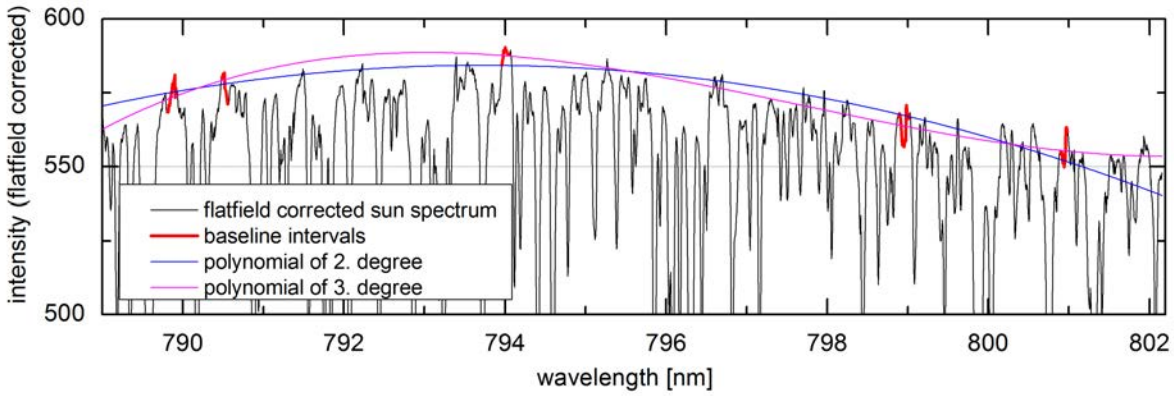

Figure 7.9: Baseline fitting of flat-field corrected solar spectrum as recorded by SOLUSAR II using approaches with a polynomial of degree 2 and 3, respectively.

$PW_3 \approx 7\,\mathrm{kg/m^2}$). From said simulated spectra five different datasets consisting of 20 spectra each (see Tab. 7.7) are derived. For every spectrum on all baseline intervals (see Tab. 6.4) a random Gaussian noise either of the strength as observed in solar spectra ($\sigma_{t,sun}$ =0.4 %) or lunar spectra ($\sigma_{t,sun}$ =2.2 %) is overlaid. From the artificially noisy baseline intervals a baseline polynomial is computed. As in the normal procedure the quotient of spectrum and baseline is calculated. The resulting transmission spectra then undergo the common processing, to compute the concentrations $PW^m_{new\ baseline}$ for all m absorption features, which are then compared to the originally underlying values $PW_{1,2,3}$. A summary of the 5 datasets is given in Tab. 7.7.

Dataset	Underlying PW	Transmission Noise Level	Polynomial Order
B1	$7\,\mathrm{kg/m^2}$	$\sigma_{t,sun} = 0.4\,\%$	2
B2	$21\,\mathrm{kg/m^2}$	$\sigma_{t,sun} = 0.4\,\%$	2
B3	$21\,\mathrm{kg/m^2}$	$\sigma_{t,lun} = 2.2\,\%$	2
B4	$21\,\mathrm{kg/m^2}$	$\sigma_{t,sun} = 0.4\,\%$	3
B5	$55\,\mathrm{kg/m^2}$	$\sigma_{t,sun} = 0.4\,\%$	2

Table 7.7: Datasets for the estimation of the influence of the absorption strength, stochastic noise and polynomial approach on the baseline accuracy using a Monte-Carlo simulation.

Fig. 7.10 shows the results of the Monte-Carlo simulation. Sub-figures 7.10(b), 7.10(c) and 7.10(g), show that with an increasing absorption degree, the systematic deviations of the results due to baseline-induced errors are becoming larger and for single line evaluation lead to an underestimation of up to 6 %. Weaker lines unsurprisingly are much more effected by baseline inaccuracies (see Fig. 7.10(d)). The differences in the biases between dataset B2 and B5 are very small though, indicating that at a certain point the baseline interval sagging is compensated by the stronger absorption level. Lunar noise (dataset B3, Fig. 7.10(e)) considerably increases the standard deviation, but also the systematic errors surprisingly seem higher than in case of the transmission noise in solar spectra. The biases emerging from the estimation with a polynomial of degree 3 compared to degree 2 are higher for lines far off the baseline intervals and mostly lower for absorption structures in the vicinity of the baseline intervals.

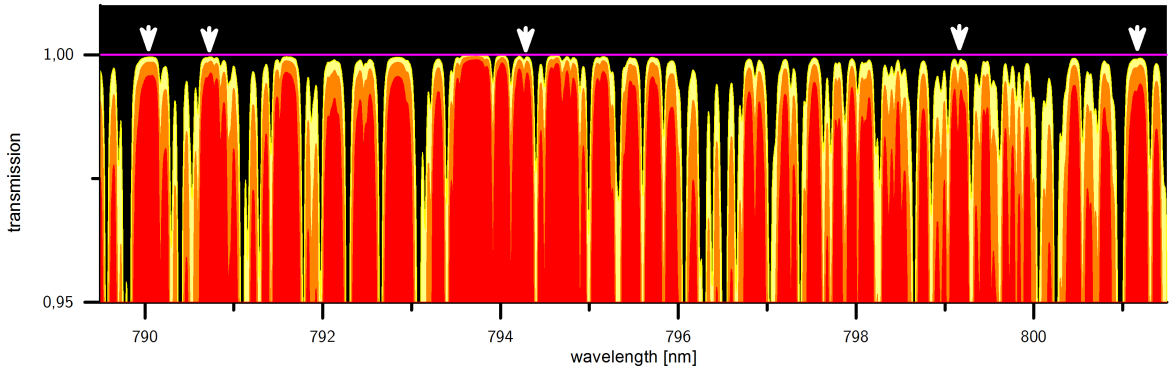

(a) Underlying simulated spectra corresponding to different PW values: Yellow - $PW_1 = 7\,\mathrm{kg/m^2}$; Orange - $PW_2 = 21\,\mathrm{kg/m^2}$; Red - $PW_3 = 55\,\mathrm{kg/m^2}$. White arrows are indicating the baseline intervals.

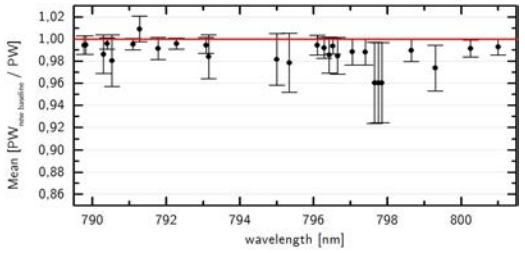

(b) Line-by-line PW comparison for dataset B1

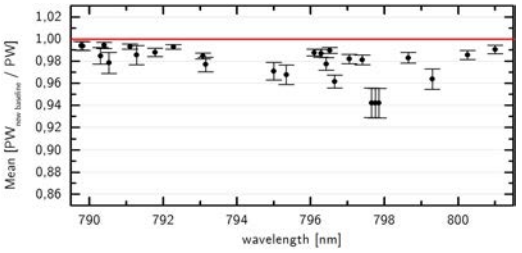

(c) Line-by-line PW comparison for dataset B2

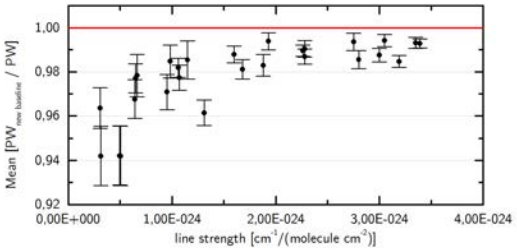

(d) Line strength dependence of the baseline-induced PW uncertainty (dataset B2)

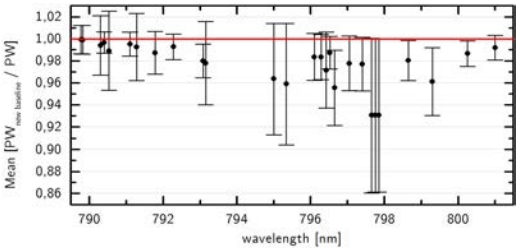

(e) Line-by-line PW comparison for dataset B3

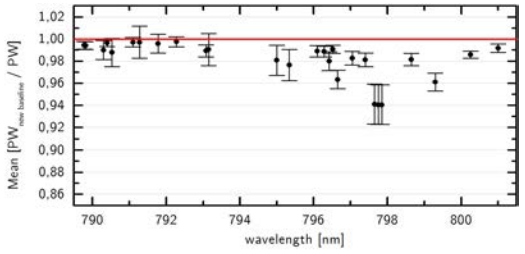

(f) Line-by-line PW comparison for dataset B4

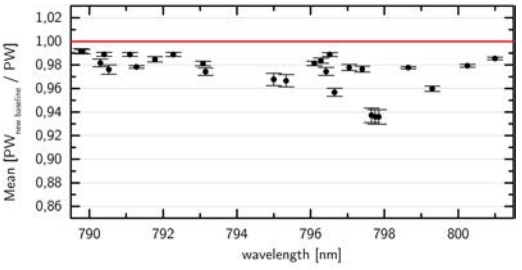

(g) Line-by-line PW comparison for dataset B5

Figure 7.10: Influence of the baseline inaccuracies on the PW retrieval. Simulated spectra corresponding to a certain water vapour concentration undergo the baseline correction process described in Section 6.8. Ahead of the procedure the baseline intervals which are slightly sagging (see Fig. 7.10(a)) are additionally overlaid with transmission noise. For different simulated spectra, noise levels and polynomial baseline assumptions, a Monte-Carlo simulation is carried out to evaluate the influence on the different absorption lines.

Absorption Line Strength Accuracy

Section 7.1.1 showed that the spectroscopic parameters describing the transitions as listed in the different databases yield considerably different PW results. Of all the parameters the accuracy of the listed absorption cross sections, however, is considered to have the greatest influence. It even remains the main uncertainty factor in most DOAS applications [Platt and Stutz, 2008], even though the experimental base of the available datasets is gradually improving.

Regarding the uncertainty of the spectroscopic parameters in the widely recognized HITRAN database we rely on the very rough uncertainty description given by Rothman et al. [2009, 2005]. For all the major transitions used in the computation of PW in this work an uncertainty range of 5 % to 10 % is given with respect to line strength.

Figs. 7.11(a) to 7.11(e) show the response of the PW values to a percentage change in the line strength for all the transitions used. For most lines the expected linear behaviour can be observed where an increase of the line strength by a certain percentage number results in a concentration decrease by around the same percentage. The response of certain lines is not as direct, however, which has to do with additional underlying lines contributing to the overall absorptions. Given the above mentioned uncertainty ranges and averaging the results of up to 27 lines the PW uncertainty caused by the uncertainty of the given line strengths is expected to be somewhere between 1 % to 2 % of the measured PW values.

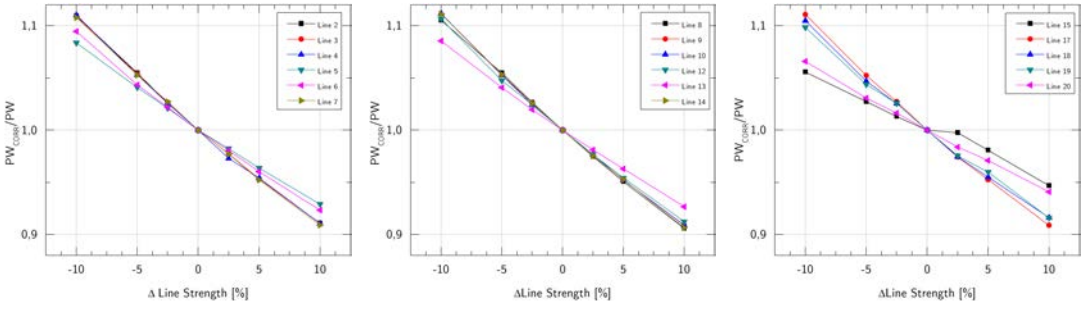

(a) Response of absorption lines 2 to 7

(b) Response of absorption lines 8 to 10 and 12 to 14

(c) Response of absorption lines 15 and 17 to 20

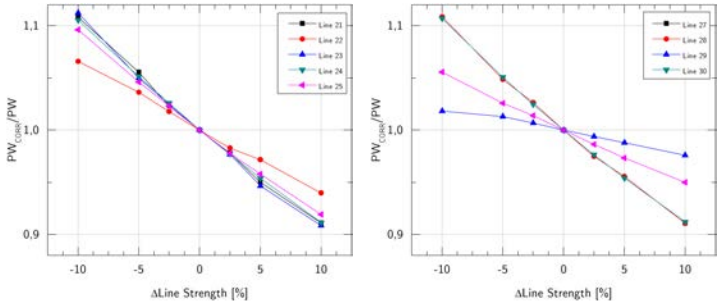

(d) Response of absorption lines 21 to 25

(e) Response of absorption lines 26 to 30

Figure 7.11: Response of the retrieved water vapour values for the used absorption features when altering the line strength parameters.

A better consistency of the line strength parameters would be helpful for various reasons. Foremost a better absolute accuracy could be reached. On the other hand it would also be beneficial for the adjustment process, where as of now every single line has to be matched individually, due to absorption cross sections which seem not to be in line. Such separate processing is, unfortunately, very time consuming and yields processing times with a state-of-the-art PC between 4 min and 8 min.

Apparatus Function Modelling Errors

The assessment of the apparatus function uncertainty influence has to be carried out experimentally. The evaluation of this influencing factor is important as one can observe that measured absorption features are by tendency narrower than structures in the artificially computed spectra which rely on the correct description of the slit function (see Section 3.6). The reason for this overestimation has not become fully clear yet. The hypothesis that the argon emission lines as emitted by the applied Pen-Ray spectral lamp could be in fact broader than specified (FWHM below 1 pm according to LOT Oriel Group [2013]) and therefore do not provide a good model for the apparatus function, has been examined. The emission line shape has been measured using an ultra-high resolution spectrometer *ELIAS* by *Lasertechnik Berlin (LTB)* which is normally used for the spectral characterisation of narrow-band lasers [Lasertechnik Berlin LTB, 2009]. Fig. 7.12(a) shows the profile of the middle line belonging to the argon emission line triplet (see Tab. 6.3) as measured by SOLUSAR with a FWHM at 22.6 pm. The same line measured with ELIAS still shows a considerable profile width of 4.7 pm (Fig. 7.12(b)). The apparatus influence in the ELIAS measurement is characterized through the spectrum of a tunable diode laser (*New Focus Velocity 6312-LN*) in the spectral vicinity (around 774.3 nm) with the FWHM at 0.46 pm which can be treated as negligible (see Fig. 7.12(c)).

Assuming Gaussian intensity distributions of both, the line profiles measured by SOLUSAR (with standard deviation $FWHM_{argon,S}$) and ELIAS (standard deviation $FWHM_{argon,E}$), the standard deviation of the "actual" SOLUSAR apparatus function $FWHM_{SOLUSAR}$ can be calculated:

$$FWHM_{SOLUSAR} = \sqrt{FWHM^2_{argon,S} - FWHM^2_{argon,E}}. \tag{7.11}$$

Based on the corrected emission line widths the polynomial describing the apparatus function can be redetermined which in the presented case yields wavelength-dependent apparatus function widths which are 0.1 $\mathrm{px_{SOLUSAR}}$ to 0.4 $\mathrm{px_{SOLUSAR}}$ lower than before the correction (see Fig. 7.12(d)).

The actual influence of the apparatus function width uncertainty on the derived PW values can be tested by deliberately altering the apparatus function width, an experiment which has been carried out with spectra belonging to datasets 2,3 and 4 as listed in Tab. 7.4. As visible in Fig. 7.13(a) change rates for different datasets lie between 9 % to 11.3 % PW per change of one pixel in apparatus function width ($\Delta FWHM$). Interestingly the experiment shows that the computed mean standard deviation $\overline{\sigma_{PW}}$ (evaluated according to Eq. 7.7) which is a measure for the matching accuracy between measured and simulated spectra, at least for datasets 2 and 3 reaches minimal values for $\Delta FWHM$ around -0.6 px as shown in Fig. 7.13(b). This supports the phenomenological observations mentioned above. For $\Delta FWHM = -0.6$ px the computed PW values are up to 7.5 % lower!

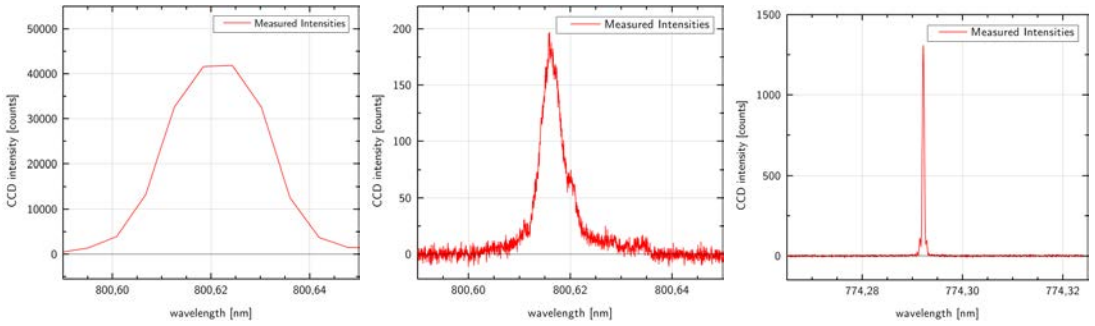

(a) Intensity profile of the argon emission line at $\lambda_{vac} = 800.8359\,\text{nm}$ as recorded by SOLUSAR. FWHM = $3.86\,\text{px}_{\text{SOLUSAR}}$ = 22.6 pm.

(b) Intensity profile of the argon emission line at $\lambda_{vac} = 800.8359\,\text{nm}$ as recorded by ELIAS. FWHM = $121\,\text{px}_{\text{ELIAS}}$ = 4.7 pm.

(c) Intensity profile of a diode laser around 774.3 nm as recorded by ELIAS. FWHM = $14.9\,\text{px}_{\text{ELIAS}}$ = 0.46 pm.

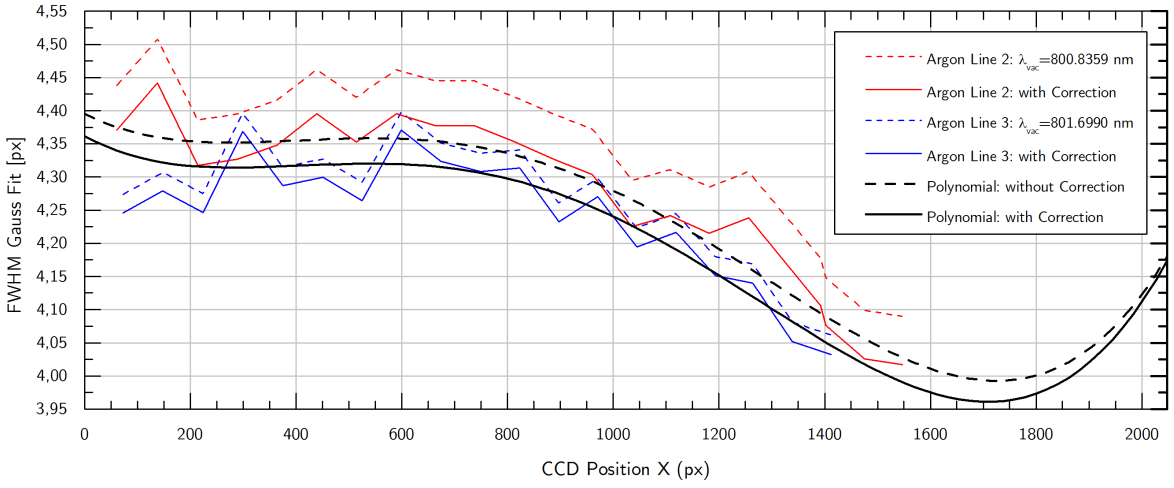

(d) Correction of the retrieved detector position dependent apparatus function by taking into account the line width of argon emission lines as exhibited by a Pen-Ray spectral lamp. Using ELIAS measurement $\text{FWHM}_{\text{line 2}}$ was determined at $0.77\,\text{px}_{\text{SOLUSAR}}$ and $\text{FWHM}_{\text{line 1}}$ at $0.49\,\text{px}_{\text{SOLUSAR}}$. The spectral region of the third line was not accessible with ELIAS. $\text{FWHM}_{\text{line 3}}$ is estimated at $0.4\,\text{px}_{\text{SOLUSAR}}$. Using the corrected data a new polynomial for the apparatus function is determined.

Figure 7.12: Determination of the argon emission line profile widths as exhibited by a Pen-ray spectral lamp which can be applied to correct the SOLUSAR apparatus function overestimation.

Looking at the matching accuracy for the single absorption features (extracted from dataset 3) the picture becomes fairly heterogeneous (see Figs 7.13(c) to 7.13(g)). Most lines have the best matching quality at apparatus function widths which are lower than originally estimated, but in some cases also a broader slit function yields better results. As visible in Fig. 7.13(h) a clear correlation of this behaviour to the line strength cannot be found, though the scattering of the minimal σ_{PW} becomes greater for weak lines.

The reason for these fitting inaccuracies remains unknown to a large degree. Different factors come into mind as possible causes, e.g., the modelling of the radiative transfer through the atmosphere whose influence on the line broadening relies on a correct assignment of the water vapour concentrations to the different atmospheric layers (see Section 7.3.2) or general uncertainties in line broadening parameters as listed by the HITRAN database. Also the fact that the matching accuracies are generally slightly lower (meaning higher σ_{PW}) than evaluated in the assessment of the influence of stochastic noise, points into the direction of some general modelling errors. It therefore also remains a matter of debate whether an expansion of the adjustment process with a precise local estimation of the apparatus function width would improve the absolute accuracy of the retrieved water vapour values or if it would just pretend lower uncertainty.

Atmospheric Modelling Errors

The state of the atmosphere influences the measurement quality on many different levels. The optical transmittance of the atmosphere (together with the elevation angle at the time of exposure) affects the S/N-ratio of the recorded spectra. Furthermore, if atmospheric mistiness is strong, the formula set described in Section 3.9.4 cannot yield accurate results for the ray tracing, as the greater effective path length of the portion of radiation which underwent scattering has not been taken into account.

But also under conditions which qualify as “clear sky”, deviations from the applied atmospheric model can occur, thus distorting the calculation of the radiative transfer: Not only the computed path length and hence the absorption strength (mainly important for measurement with low elevation angles) are affected. Also the shape of the atmospheric features is afflicted, as the vertical distribution of water vapour and the height-dependency of the local pressure and especially temperature affect the line broadening as described in Section 3.5.

By comparing PW values computed with the model based on the standard atmosphere and integral water vapour concentrations computed with data on atmospheric conditions stemming from measurements of co-located balloon radiosondes, Somieski [2005] however showed that the influence of deviations in the atmospheric conditions relative to the standard atmosphere yield errors which are fairly small. For single lines the mean difference for ZPW is about $0.3\,\mathrm{kg/m^2}$. Through averaging over 31 lines the mean difference could be lowered to $0.1\,\mathrm{kg/m^2}$. The investigation had been carried out over a timespan of two month (May/June) with spectra recorded around noon. For further clarification of this matter, additional comparisons of the currently applied model and atmospheric data obtained in situ by radiosondes or through another auxiliary method are certainly desirable to assess the influence of atmospheric models also for other seasons and daytimes. Also comparisons with more regional atmospheric models would be insightful.

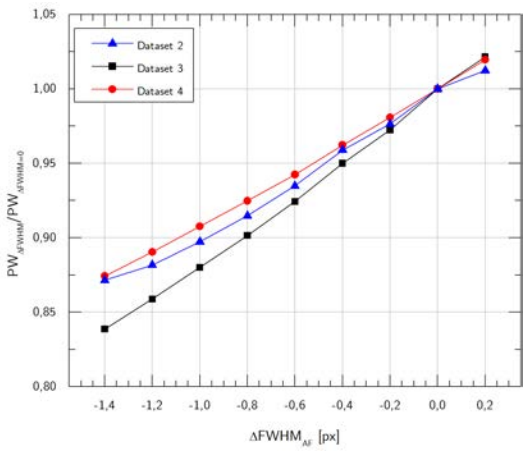

(a) Evaluation of the relative influence of a change in apparatus function width on final PW values on the basis of three different datasets.

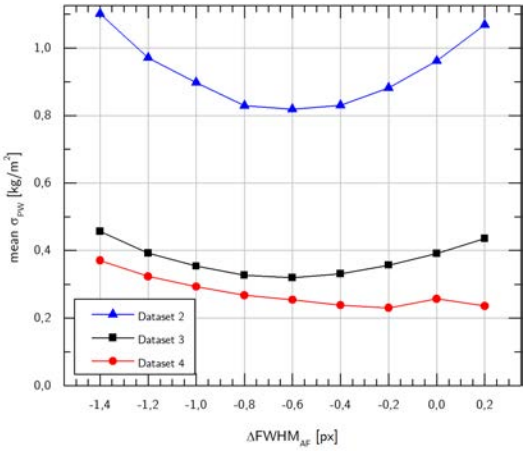

(b) Evaluation of the mean matching accuracy (represented by the mean σ_{PW}) depending on the change in apparatus function width for dataset 2 to 4.

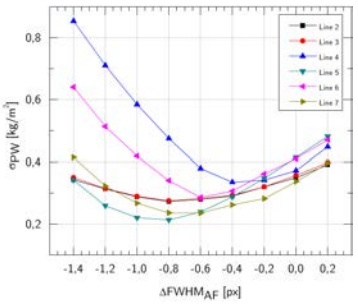

(c) Matching accuracy for lines 2 to 7 (only dataset 3)

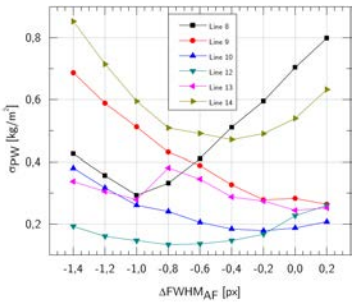

(d) Matching accuracy for lines 8 to 10 and 12 to 14 (only dataset 3)

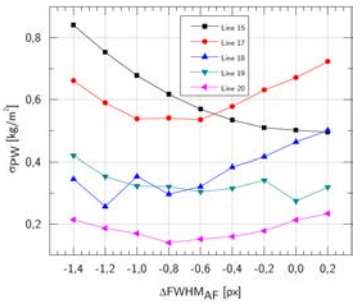

(e) Matching accuracy for lines 15 and 17 to 20 (only dataset 3)

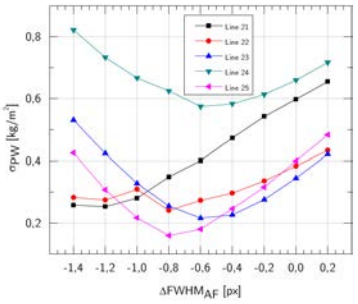

(f) Matching accuracy for lines 21 to 25 (only dataset 3)

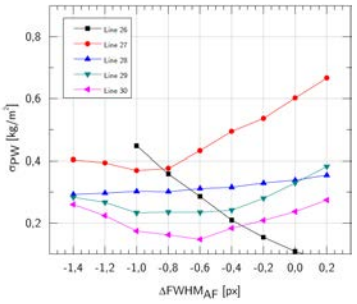

(g) Matching accuracy for lines 26 to 30 (only dataset 3)

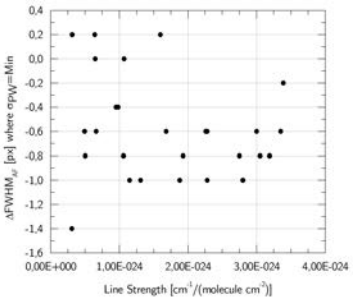

(h) Dependence of point of best matching with respect to absorption line strength.

Figure 7.13: Influence of artificial changes in the apparatus function width on PW values and on matching accuracy between measured and simulated transmission spectra.

Telescope Aiming Errors

One of the most important aspects of the optical adjustment of the instrument lays in the precise relative arrangement of the quadrant diode, which ultimately determines the telescope aiming, and the entrance slit (old set-up) or homogenizing fibre entrance (final set-up), respectively. Not only to ensure that the entrance slit is – directly or indirectly – fully illuminated at any time, but also because it influences, of which extract of the solar or lunar disk the radiation entering the spectrometer is coming from. A small offset in elevation direction can have a considerable influence on the length of the ray path of the observed light in the atmosphere from the light source to the measurement instrument and hence influences the degree of absorption in the retrieved spectra. With the applied fibre (core diameter 400 µm) radiation stemming from an angular section of $\pm$ 4.5′ is collected and mixed in any case.

The quadrant diode and fibre mountings do not dispose of a high-precision positioning possibility (micrometre screws or the like). Therefore it is assumed that the positioning accuracy of the slit with respect to the diode center is around 0.1 mm. Fig. 7.14 shows the impact of a displacement Δx of the slit on the observed radiation path length with respect to the elevation angle. For an elevation angle of 5° and a displacement of the slit with respect to the quadrant diode center at 0.1 mm a maximum deviation of 0.76 % can occur. Depending on how the telescope is oriented with respect to the spectrometer a displacement does not, or only by little, alter the observed elevation though, due to the rotation of the disk image with respect to the fibre entrance (see Section 4.3).

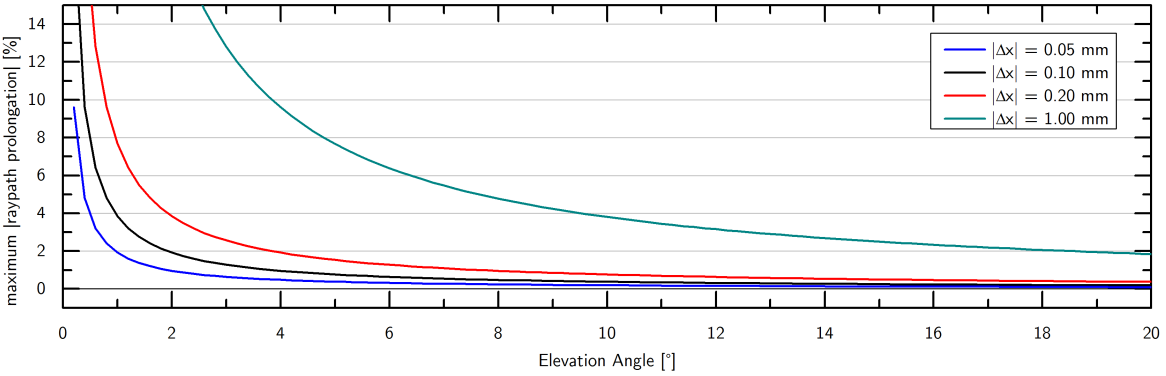

Figure 7.14: Influence of the uncertainty in the positioning of the fibre entrance center with respect to the quadrant diode center on the observed radiation path length (and hence absorption) as a function of the elevation angle e. Applied is the simplest air mass factor model $AMF = \frac{1}{\cos z}$ with $z = 90° - e$ (compare Section 3.8.1).

Fig. 7.14 also shows how big the deviation theoretically can become during cloudy conditions, where, depending on cloud coverage, the telescope aiming undulates between the upper and lower rim of the solar disk ($\Delta x \approx 1$ mm). For elevation angles below 10° the difference in path length between two subsequent observations can theoretically clearly exceed 4 %.

Another slight systematic effect is occurring when measuring at very low elevation angles: With the radiation coming from the lower areas of the solar disk passing through larger air masses and thus being more strongly attenuated by Rayleigh scattering, this generally leads to a lift of the intensity center of gravity of the solar disk (which is imaged onto the center of the homogenizing fibre entrance in the telescope control cycle) with respect to its geometric centre [Bösch et al., 2003]. The extent of this effect has not yet been investigated.

7.4 SOLUSAR I versus SOLUSAR II

As described in Section 7.3.2, alike many other instrumental water vapour retrieval methods, DOAS measurements are not free from influences which can impose systematic errors on the determined final concentration values. Some of the mentioned systematics, as the atmospheric modelling uncertainties or the uncertainty in the published spectroscopic parameters are not varying for the data obtained by different measurement systems with identical design. This however does not apply for the modelling of the apparatus function, which is carried out for each system individually, and for the optical adjustment accuracy. The systematic errors in the baseline determination (caused by baseline interval sagging) affects measurements for both systems in a similar way. But as shown in Section 7.3.2, the process of baseline retrieval gives rise to stochastic uncertainties which together with the regular transmission noise (compare Section 7.3.1) can also lead to deviations between measurements of identically built instruments.

The two measurement systems SOLUSAR I and SOLUSAR II dispose of a fully identical mechanical and optical design. The sole difference lies in the slightly different electronic set-up, which for SOLUSAR I had to be adapted more extensively in order to bring the electromagnetic interferences described in Section 4.10.6 down to reasonable levels (at least for solar measurements). With the two measurement systems parallel measurements have been recently conducted at ISAS. The set-up with the co-located instruments is depicted in Fig. 4.31(a). Fig. 7.15 shows a comparison of the results of the two measurement systems over a time period of around 4 hours with clear sky conditions. Though concentration trends (ZPW) are similarly mirrored there is a considerable offset ranging from $0.8\,\mathrm{kg/m^2}$ to $1.5\,\mathrm{kg/m^2}$ in ZPW. This deviation which increases for higher PW values is also visible in the corresponding scatter plot depicted in Fig. 7.16(a). (To harmonize the time scale of the two datasets in order to calculate the scatter plot data points a linear interpolation has been carried out). Comparing the results of distinct absorption features as shown in Figs 7.16(b) (line 12) and 7.16(c) (line 29) shows an inconsistent behaviour. Fig. 7.17 shows a comparison of the PW values retrieved from the single 27 absorption features (normalized with respect to the PW values evaluated from line 12) for three different concentrations for both measurement systems. Generally SOLUSAR I estimates higher concentrations, but the offset between the two systems becomes larger for longer wavelengths and in tendency for higher concentrations.

The uncertainty of the optical adjustment, of the individual modelling of apparatus function, as well as of the baseline estimation (which, using a polynomial of degree 2, sometimes did not seem fully satisfying in case of SOLUSAR II) can all contribute to this offset, but do not suffice as a complete explanation for these offsets. Revealing is further the look at Fraunhofer lines in the spectra whose transmission values should be invariant to changes in the water vapour concentrations (provided there are no vapour absorption features spectrally near-by). Analysis of distinct Fraunhofer lines show considerable differences between the two systems: SOLUSAR II Fraunhofer lines show minimal transmission values which are 1.1 % to 2.5 % higher than in case of SOLUSAR I. This behaviour can neither be explained through the baseline determination process nor through the different apparatus function widths (which are very similar). It is assumed that some sort of stray or false light on the detector, which is not properly enough treated by the stated stray light suppression algorithms, plays a considerable role in this issue. This requires a closer analysis of full frame images and possibly a better stray light suppression through baffles inside the instruments.

The offset of the PW between the two systems has a strong systematic component which can be quite well modelled by a polynomial of degree 2. The thus corrected residuals ΔPW^* are

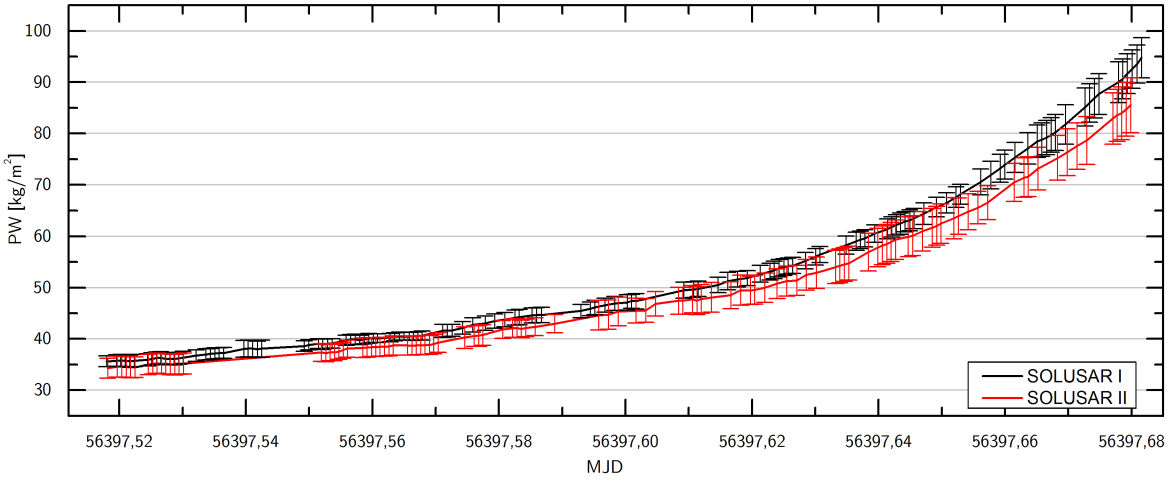

(a) Comparison of the PW values

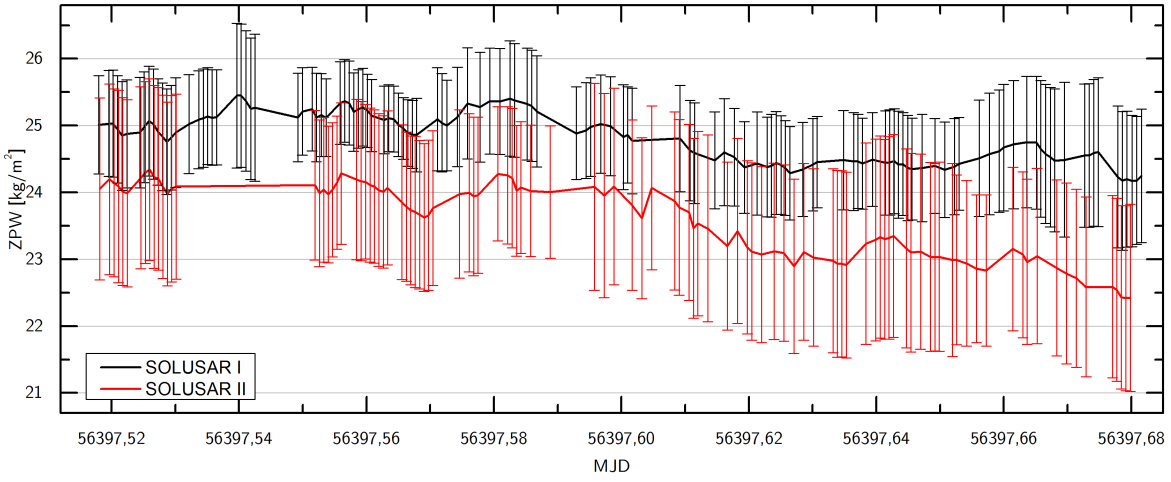

(b) Comparison of the ZPW values

Figure 7.15: Comparison of the water vapour concentrations as retrieved by the co-located measurement systems SOLUSAR I and SOLUSAR II on 15 April 2013 over a period of 4 hours.

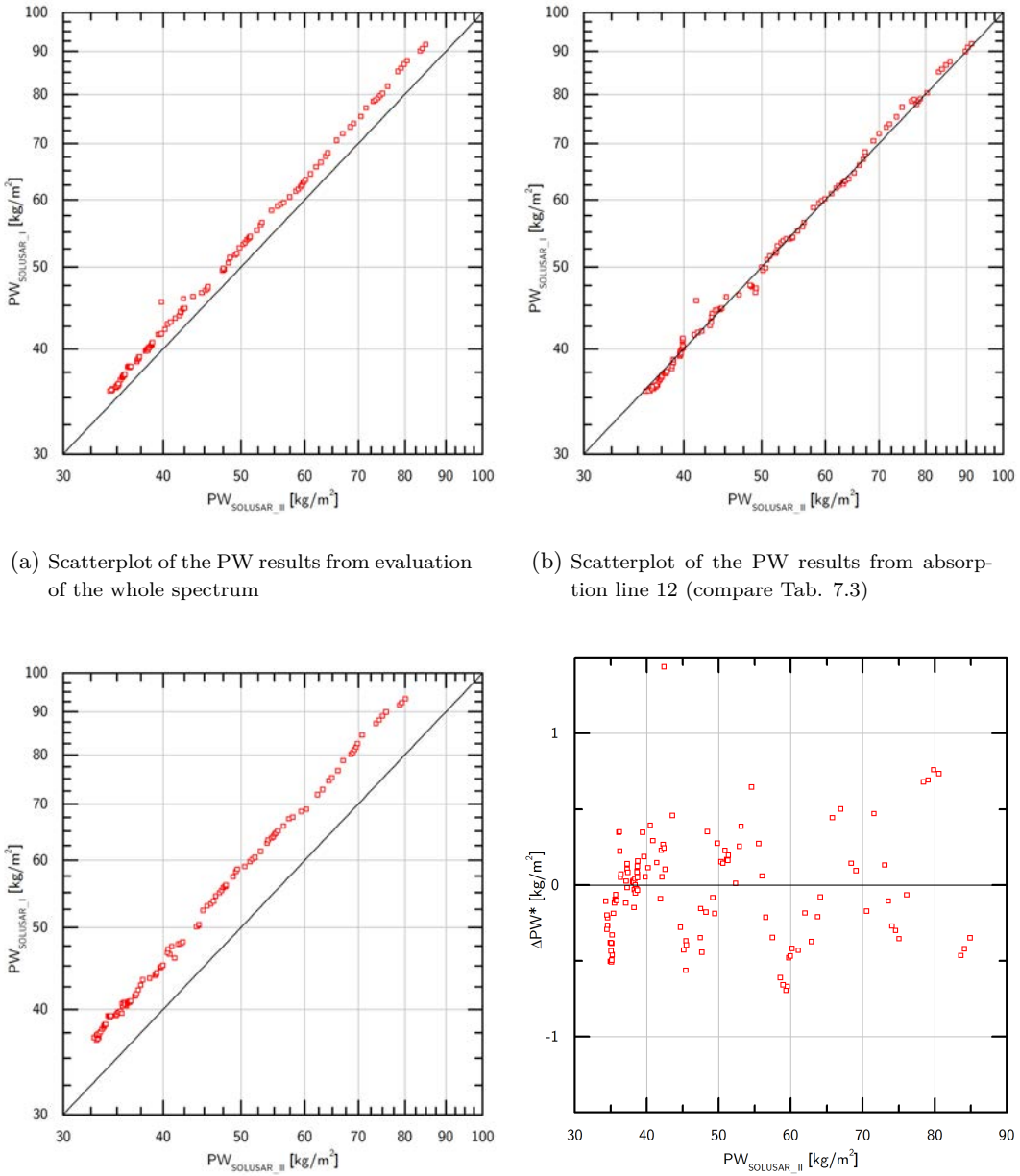

(a) Scatterplot of the PW results from evaluation of the whole spectrum

(b) Scatterplot of the PW results from absorption line 12 (compare Tab. 7.3)

(c) Scatterplot of the PW results from absorption line 29 (compare Tab. 7.3)

(d) Residuals ΔPW^* between the SOLUSAR I and SOLUSAR II measurements after subtraction of the estimated systematic effects ΔPW_{model} which were modelled by a polynomial of 2. degree ($\Delta PW_{model} = 0.00106 \cdot PW_{S_{II}}^2 - 0.01524 \cdot PW_{S_{II}} + 0.7409$)

Figure 7.16: Further comparison of the PW results stemming from SOLUSAR I and SOLUSAR II measurements conducted on 15 April 2013.

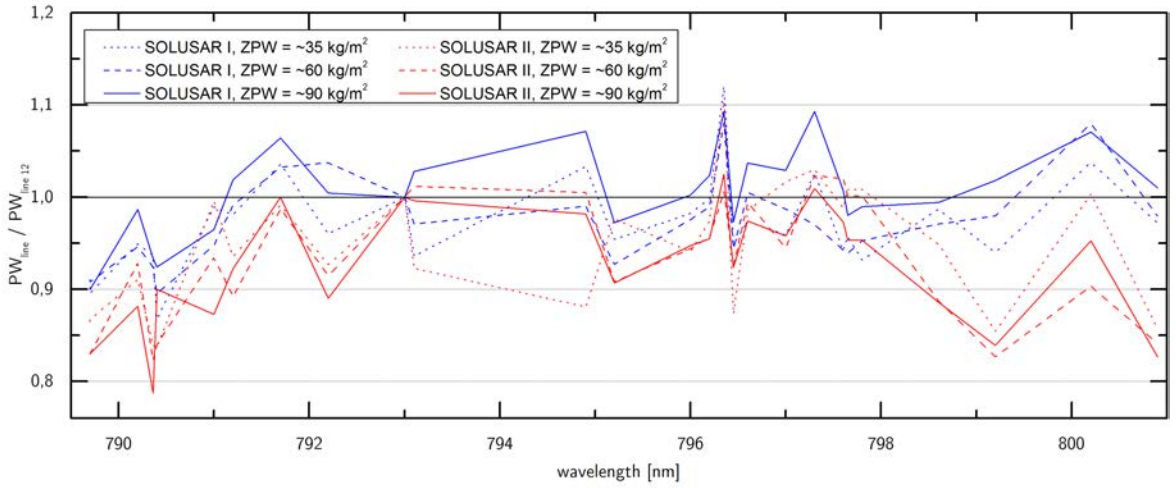

Figure 7.17: Single line PW values (normalized with respect to PW of line 12) for SOLUSAR I and SOLUSAR II measurements retrieved from spectra with three different concentrations.

shown in Fig. 7.16(d). The mean residual value amounts to 0.48 kg/m^2 or with respect to the PW concentration to 1.1 %.

7.5 Solar Spectrometry versus GPS meteorology

As the measurements obtained by the SOLUSAR measurement system are subject to certain systematic errors as outlined in Section 7.3.2, which could have a considerable influence on the final absolute PW values, a comparison with a fully independent measurement approach may give an indication on the size and behaviour of said anomalies. Therefore a GPS receiver has been permanently installed by the GFZ Potsdam at ISAS-Berlin, where the SOLUSAR measurements were conducted as well, in order to carry out GPS meteorology measurement as shortly outlined in Section 2.4.6. The data have been collected and sent to GFZ Potsdam to be ultimately included in the combined processing of the whole receiver network. A system to retrieve PW values in near real time has been established in the "GPS Atmosphere Sounding" Project (GASP), a joint venture of four institutes belonging to the Helmholtz Association starting in the year 2000, for applications in the numerical weather prediction, climate research and space weather monitoring [Dick et al., 2001]. A description of the network set-up (over 200 stations in Germany and neighbouring countries) and the processing strategies involved can be found at Gendt et al. [2004]. To further densify the measurement network increasingly lower-cost single-frequency receivers are applied [Deng et al., 2011]. Also in our case a single-frequency receiver *Novatel Smart Antenna* has been installed.

Figs. 7.18 to 7.20 show the results of the comparison of the ZPW values retrieved from SOLUSAR I and GPS meteorology, respectively, in three time series with very different atmospheric water vapour concentrations. GPS meteorology solutions are regularly provided every 15 min. The SOLUSAR measurement interval was set to 1 min, however gaps can occur in the time-series due to the periodic instrument calibration or due to the appearance of clouds. The results in all three cases reveal considerable permanent offsets with solar spectrometry estimating higher concentrations. Analysis of the offset (compare Fig. 7.21) show a clear concentration dependence, which can be well described by a linear function. For all three datasets combined a scaling factor of 1.087 is computed. If one computes a linear function with no

y-axis offset, as shown in Fig. 7.22, the scaling factor increases to 1.11. As stated in Section 7.3.2 different systematic error sources in aggregation can lead to this overall concentration proportional effect, mainly due to deviations in the line strength parameters and systematic errors in the line broadening assessment (either caused by uncertainties in the published broadening parameters or insufficiently precise determination of the apparatus function). The errors in the baseline determination that also contribute to the error budget, are pointing in another direction (leading to an underestimation of the ZPW).

General concentration trends seem to be recognizable in the data of both measurement methods, though considerable deviations occur. It is important to emphasize, however, that the solar spectrometry ZPW results are based on single slant concentration detection, whereas GPS meteorology deduces its results from slant delays in many different directions. The mean scatter range of the residuals between the two measurement systems ranges from 0.28 kg/m^2 (Fig. 7.19) to 1.09 kg/m^2 (Fig. 7.18).

Regarding the general accuracy of GPS meteorology: Comparison of the PW values derived from GPS meteorology with results from radiosondes and WVR measurements show an agreement in the range of ±1-2 kg/m^2. A main difficulty in the acquisition of near real time concentrations from GPS lies in the rapid satellite orbit prediction [Gendt et al., 2004]. For the analysis of single-frequency receiver data, the main challenge is the accurate modelling of the ionosphere influence. However, Deng et al. [2011] states that the standard deviation of the total delays between double-frequency and single-frequency receivers is below 3 mm (corresponding to about 0.5 kg/m^2 in PW), whereas the bias is nearly negligible.

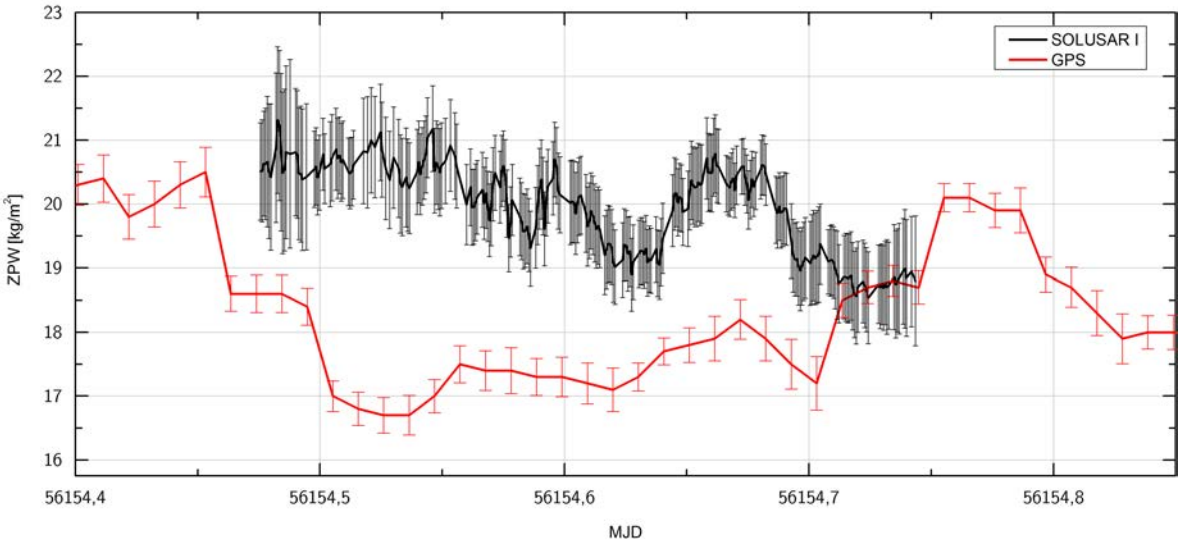

Figure 7.18: Comparison of Solar Spectrometry (by means of SOLUSAR I) and GPS Meteorology on 15 August 2012 in Berlin-Adlershof during ca. 7 h.

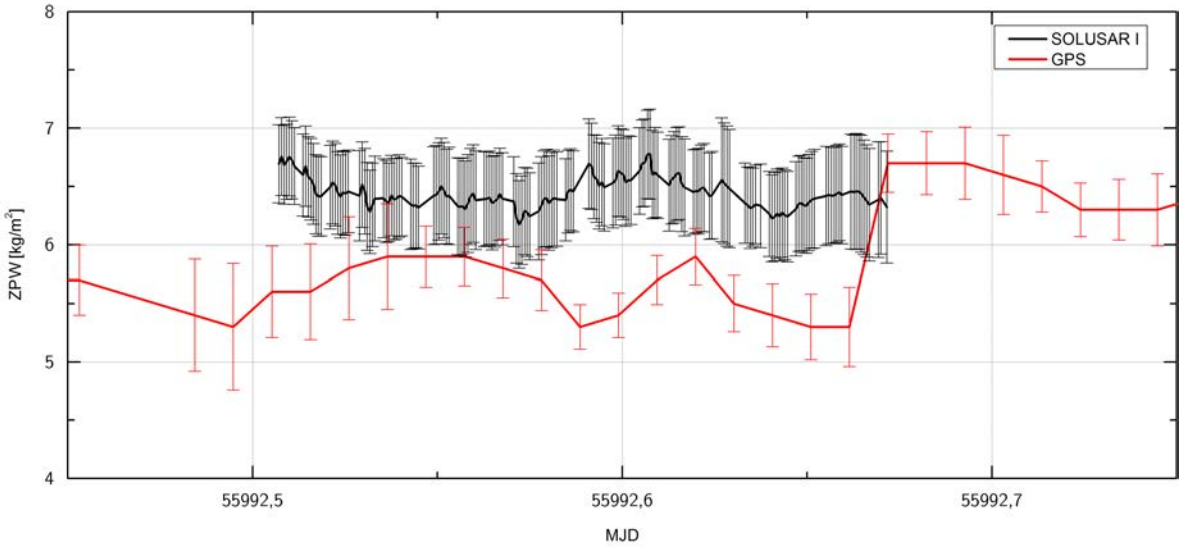

Figure 7.19: Comparison of Solar Spectrometry (by means of SOLUSAR I) and GPS Meteorology on 6 March 2012 in Berlin-Adlershof ca. 4 h.

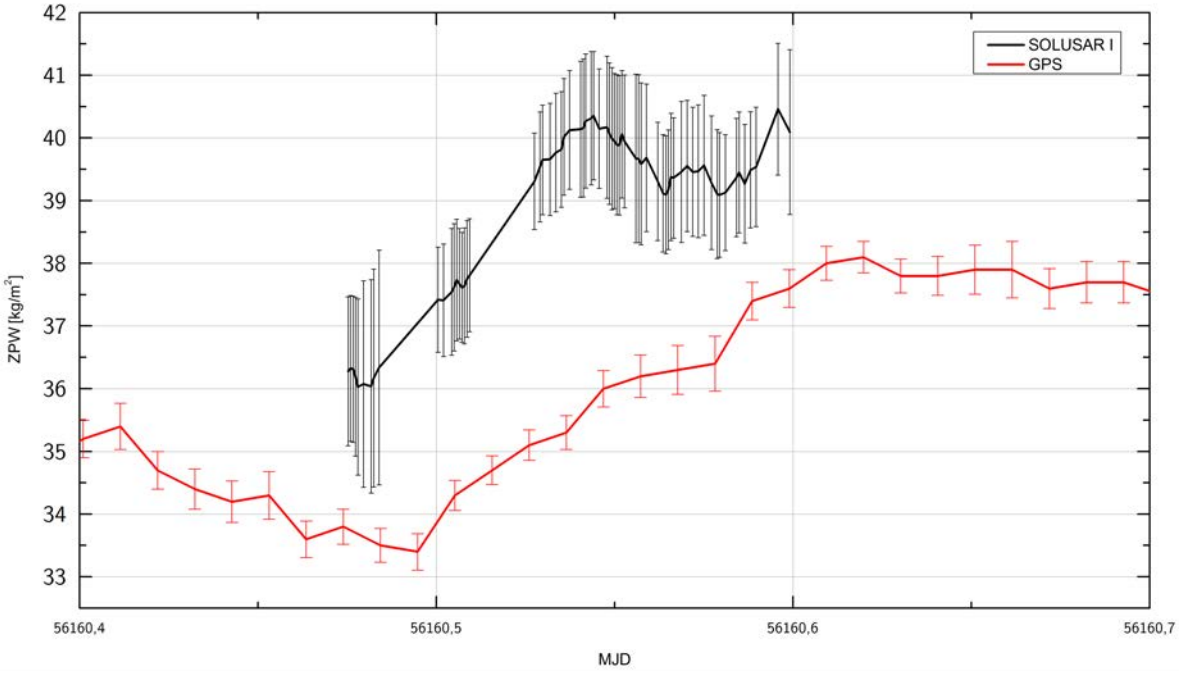

Figure 7.20: Comparison of Solar Spectrometry (by means of SOLUSAR I) and GPS Meteorology on 21 August 2012 in Berlin-Adlershof ca. 3 h.

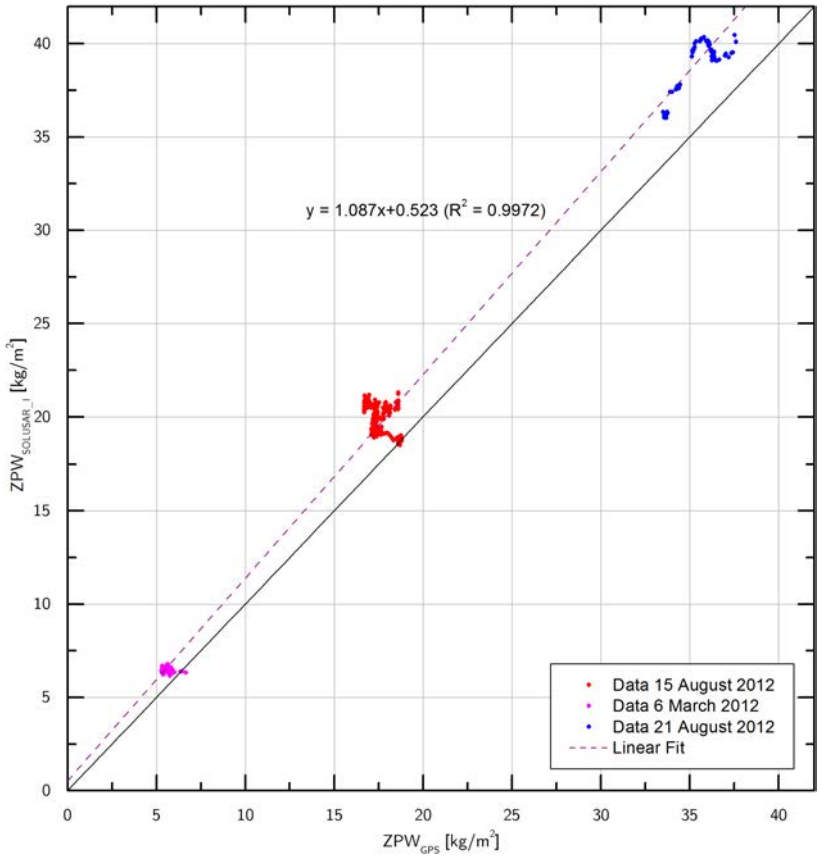

Figure 7.21: Scatter plot of the comparison between GPS meteorology ZPW results and the (interpolated) SOLUSAR ZPW results belonging to three time-series. The comparison shows residuals with a strong concentration dependency which can well be described by a linear function.

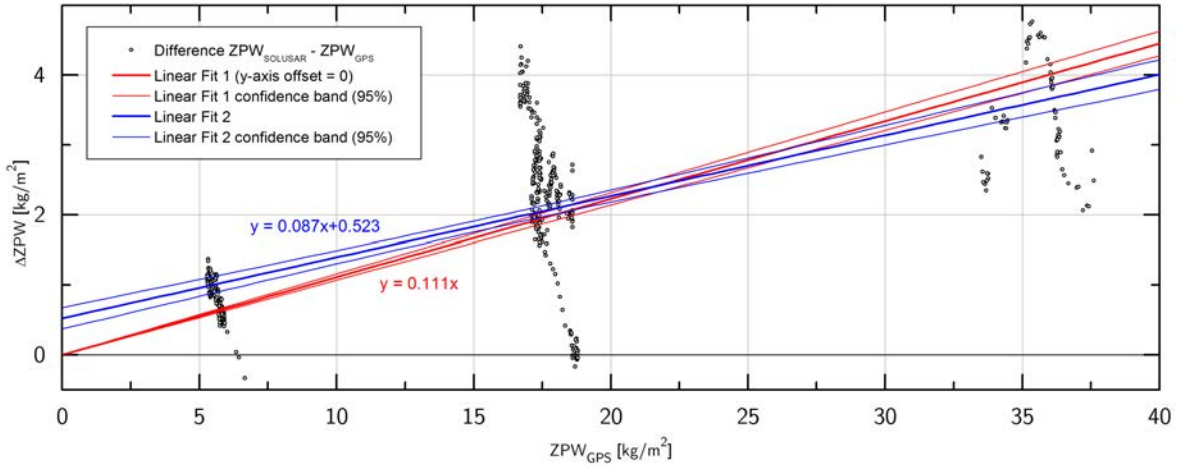

Figure 7.22: Modelling of the differences between ZPW values obtained from SOLUSAR and GPS meteorology measurements, respectively, using a linear approach. The graph shows two estimates, with and without a y-axis offset, with their respective 95 %-confidence intervals.

7.6 Lunar Measurements

As outlined in Chapter 4 the SOLUSAR instruments have initially been conceived to permit measurements at far lower intensities of the background illumination source than possible with the predecessor instruments. Hence the temporal coverage of the measurement method could be extended by allowing night-time measurements using the sunlight reflected by the moon as light source. As described in Section 4.9 the originally planned set-up had to be abandoned in order to eliminate etaloning structures produced by the back-thinned CCD through interposition of a homogenizing optical fibre between telescope and spectrometer. This measure enables proper determination of the baseline in solar spectra in the first place, but unfortunately much complicates the acquisition of processable lunar spectra due to the energy loss of nearly one order of magnitude .

Fig. 7.23(a) shows a typical full-frame image of a lunar spectrum obtained by SOLUSAR I (14 image acquisitions; exposure time: 20 s; lunar phase angle close to 0°; elevation angle $\approx 40°$). In the dark image areas beside the diffraction order, the stripe patterns caused by the remaining electromagnetic interferences described in Section 4.10.6 become visible. Fig. 7.23(b) shows the changing distorting influence on the binned lunar spectra illustrated by the example of three consecutively obtained lunar spectra with similar intensity. The varying overlaying beat is prohibiting the direct application of the baseline retrieval process described in Section 6.8.

To determine and eliminate the overlaying patterns, different solutions have been tested, ranging from various frequency filters, to polynomial and moving average approaches. The solution found to ultimately yield the most adequate and consistent results for different spectra, was a variation of the *Savitzky-Golay filter* algorithm [Savitzky and Golay, 1964]. Savitzky-Golay filters are very often used in analytical chemistry, e.g., for noise cancellation because of their different beneficial attributes such as the preservation of Gaussian profiles of spectral features [Schafer, 2011]. In a Savitzky-Golay algorithm for every sample i of a data series (in our case for every pixel) a new sample value is determined through LSQ estimation of a polynomial of order n. The estimation is carried out on the base of the sample set $[i - M, i + M]$ with an adequately chosen parameter M.

Fig. 7.24 shows the processing of a lunar spectrum (same as in Fig. 7.23(a)) with the described algorithm. Subfigure 7.24(b) depicts the overlaying disturbing beat structures extracted using the Savitzky-Golay approach with the parameters $n = 2$ and $M = 100$. A major issue when applying LSQ estimation of the polynomials, is the strong influence of those samples with strong absorption and the resulting local drag down of the polynomials which becomes visible in ripples in the extracted structure. In the case at hand the problem again can be better tackled through a switch to a more robust estimator, such as the binomial estimation described in Section 6.3. Applying the latter (while using the same Savitzky-Golay parameters) eliminates fairly well these minor defects. To ultimately eliminate the beat structure, the lunar spectrum is divided by the determined broadband signal (Fig. 7.24(c)). Even using this approach some slight sagging behaviour can be observed at spectral wavelengths where broad connected absorption structures (water vapour or Fraunhofer) are occurring, as e.g. around 794 nm to 795 nm. Computing the quotient of two lunar spectra (with assumed similar PW concentrations) after applying the robust Savitzky-Golay filter to both, yields a signal which is clearly dominated simply by noise as hoped for (see Fig. 7.24(d)).

Further investigations though have to be undertaken to optimally tune the filter regarding frequency response, polynomial degree, moving window width and also the characteristics of the robust fitting, in order to find a solution where an optimal deletion of the disturbing signal is given while not removing actual spectral intensity information.

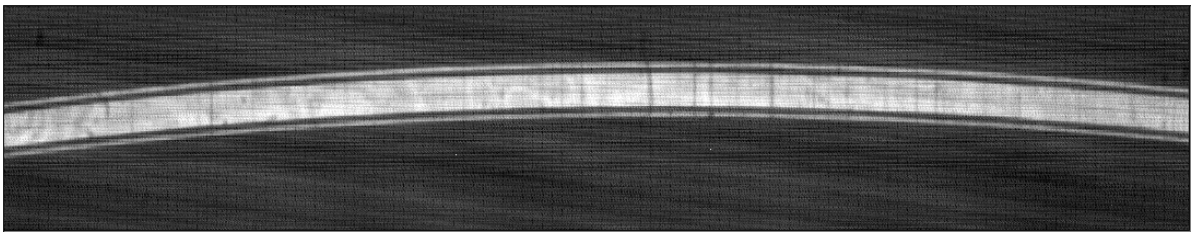

(a) Fullframe image of a lunar spectrum recorded by SOLUSAR on 6 March 2012 (near full moon) at an elevation angle of around 40° and PW value of around 10 kg/m^2 (according to the GPS meteorolgy measurements)

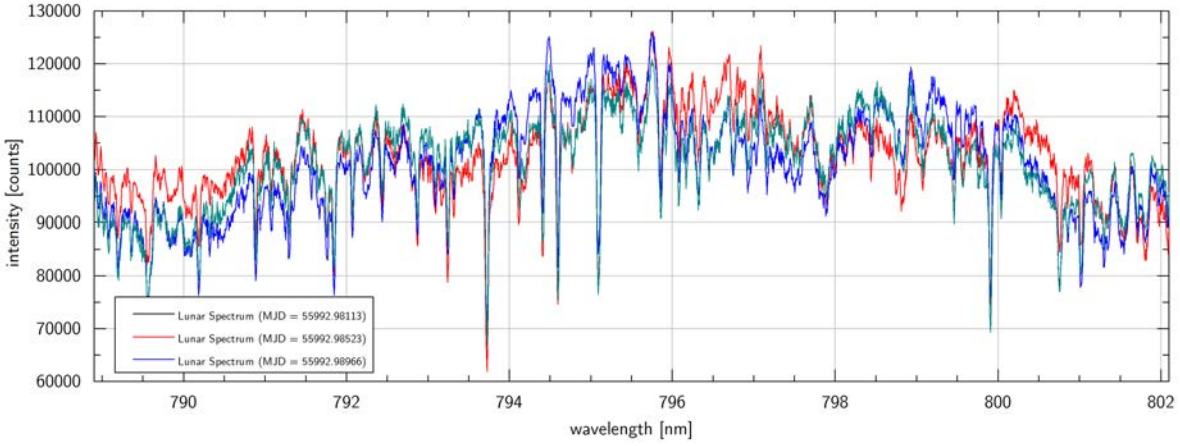

(b) Three consequently obtained lunar spectra with an overlaid moving beat structure stemming from the electromagnetic interferences. The "wavelength" of these broadband structures is also subject to changes between acquisitions.

Figure 7.23: Influence of remaining electromagnetic interferences (after applying the hardware measures described in Section 4.10.6) on lunar spectra acquired by SOLUSAR.

To the Savitzky-Golay filtered lunar spectra the common baseline retrieval is applied. One major issue regarding the processing of lunar spectra using the single line evaluation as described in Section 7.2.2 lies in the bad signal to noise ratio. In case of evaluation of weaker lines or in case of a low PW chances are high that the adjustment does not properly converge and gets trapped in some intensity artefact. For that reason following line groups have been formed for the evaluation of lunar spectra: G1 (lines 2 and 3), G2 (lines 4, 5 and 6), G3 (lines 7 and 8), G4 (lines 9 and 10), G5 (lines 12 and 13), G6 (lines 14 and 15), G7 (lines 17 to 21), G8 (lines 23 to 26), G9 (lines 27 and 28) and G10 (lines 29 and 30).

Fig. 7.25 shows the evaluation of lunar measurements over a period of three hours and the comparison with results of co-located GPS meteorology, according to which fairly stable zenith integral concentrations can be observed. These results are fairly well reproduced by the SOLUSAR instrument through averaging of the results of all ten absorption line groups listed above. The results gathered from the distinct groups range roughly from 70 % to 125 % of the mean value. Samples of the matching between simulated and measured transmission spectra for the different spectral groups are given in Fig. 7.26, exhibiting the low S/N-ratio. The matching quality σ_{PW} according to Eq. 7.7 for the given time series ranges between 0.19 kg/m^2 and 2.02 kg/m^2 with a mean value of just 0.55 kg/m^2 which is even better than expected in the estimation of noise influence presented in Section 7.3.1, most likely due to

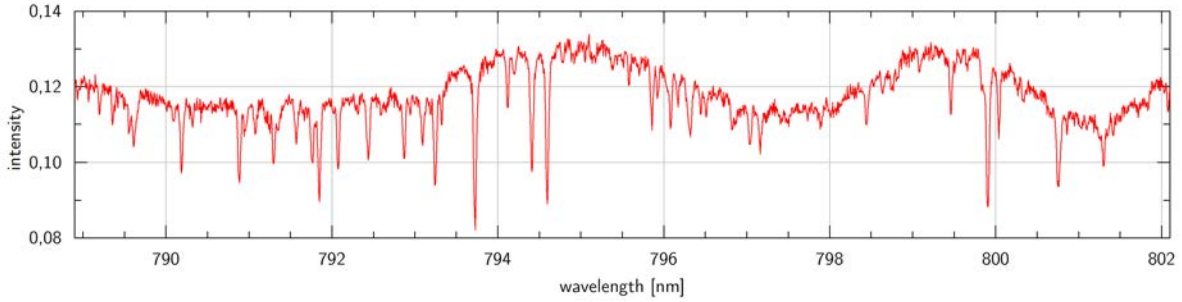

(a) Flat-field corrected lunar spectrum

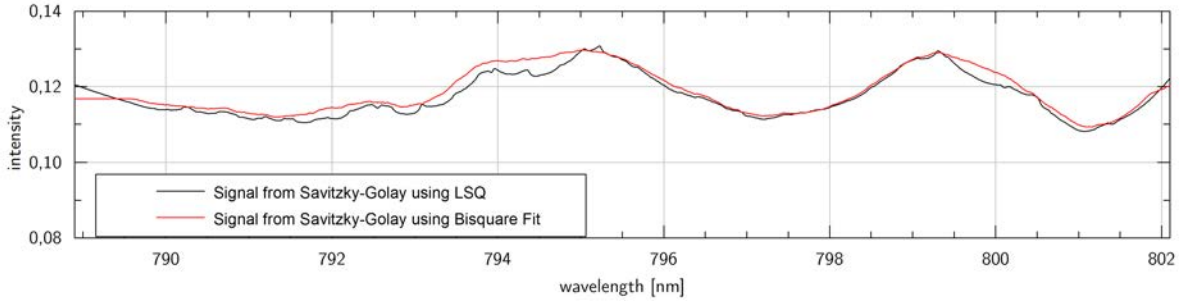

(b) Extracted broadband structures using a Savitzky-Golay approach using least square polynomial fitting and bisquare polynomial fitting respectively. The Savitzky-Golay parameters were set at: $M = 100$; $n = 2$.

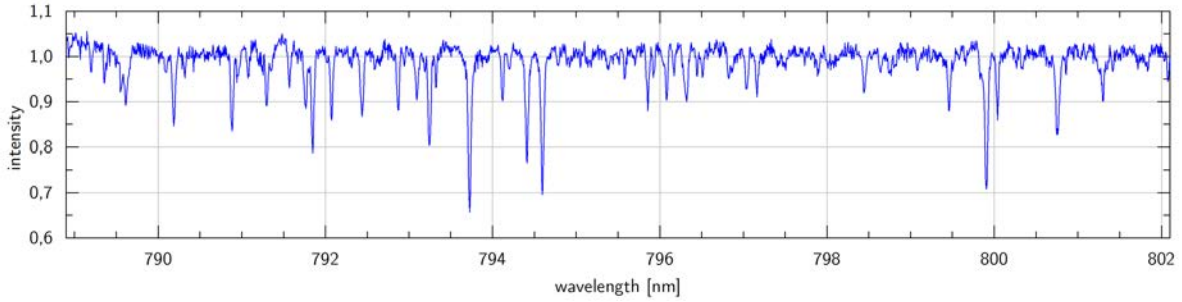

(c) Lunar spectrum after correction with the robust Savitzky-Golay filter.

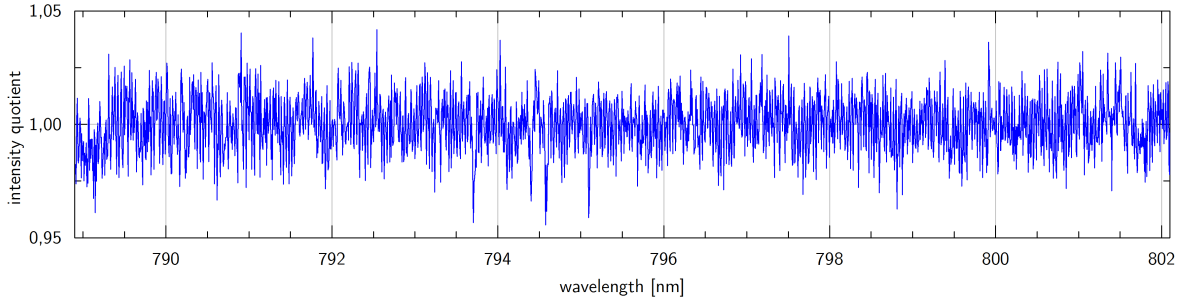

(d) Quotient of two subsequently obtained lunar spectra after undergoing Savitzky-Golay filtering (measurement interval 10 min).

Figure 7.24: Elimination of electromagnetic disturbance induced broadband spectral structures in lunar spectra using a Savitzky-Golay Filter with robust polynomial estimation.

the fact that the electromagnetic interference contribution σ_{EI} to the read noise can change considerably (compare Section 7.3.1).

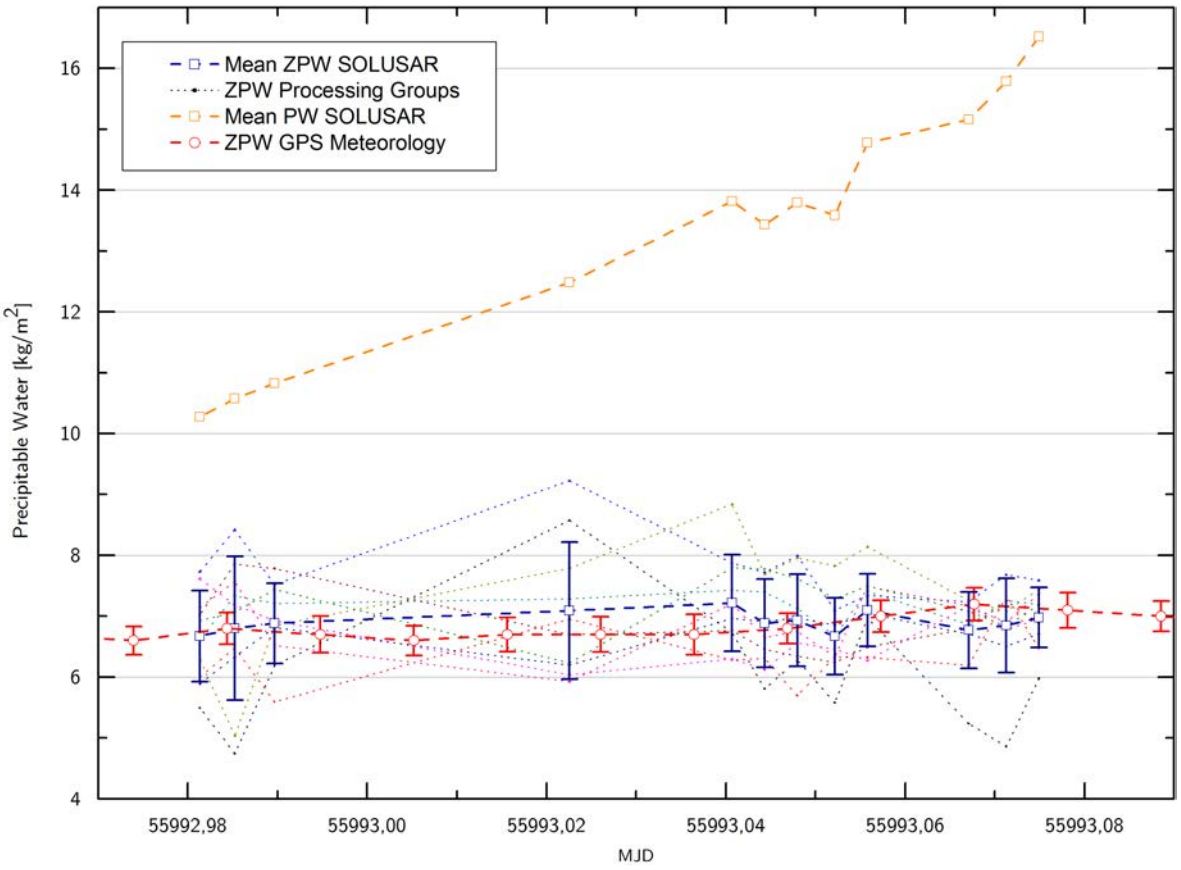

Figure 7.25: Result of a three hour time series evaluation of lunar spectra. According to the GNSS meteorology results the zenith integrated water vapour content is fairly stable. The results are pretty well reproduced by SOLUSAR measurements. Depicted are the mean values gathered through averaging of the results of 10 spectral groups. During the measurement window the moon was descending resulting in an increase of the measured slant integrated water vapour of more than 60 %.

Obtaining and processing lunar spectra using SOLUSAR is possible, even at quite low concentrations. Because of the reasons mentioned above the full potential of the instrument could unfortunately not be exploited. Looking at the potential accuracy of a set-up where no homogenizing fibre is present and instead the original direct telescope-spectrometer coupling is in place (description see Section 4.9), when using a virtual detector with the same characteristics whose performance however is neither hampered by etaloning structures nor by electromagnetic disturbances and where a similar measurement regimen is used (interval between measurement spectra: 10 min):

1. The CCD gathered intensity increases by roughly a factor of 8 (compare Section 4.9.2).

2. Consequently the relative shot noise $\sigma_{shot,lun}$ would be reduced to around 0.1 %. Read noise $\sigma_{read,lun}$ (in absence of interferences) would amount to roughly 0.3 %. Dark noise remains unchanged.

3. The overall noise level of the halogen spectra would also be slightly decreased. It is now estimated at 0.2 %.

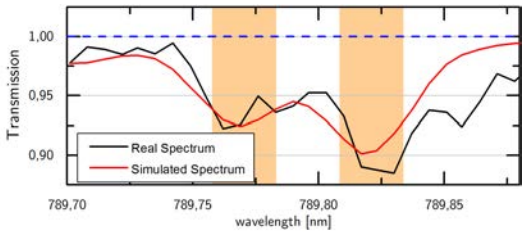

(a) Spectral line group G1

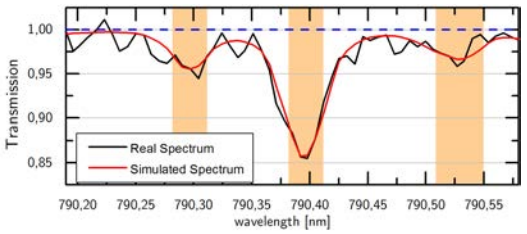

(b) Spectral line group G2

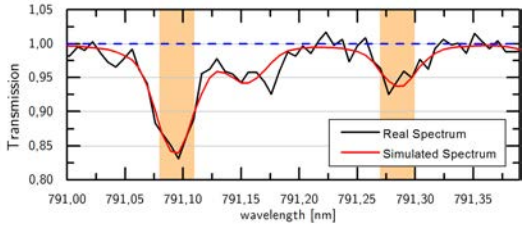

(c) Spectral line group G3

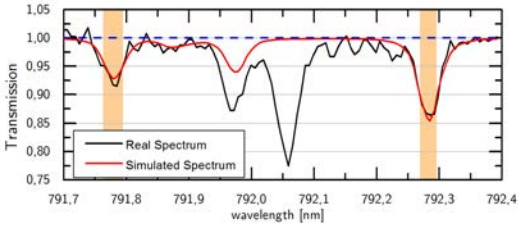

(d) Spectral line group G4

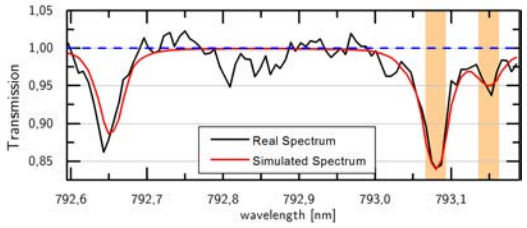

(e) Spectral line group G5

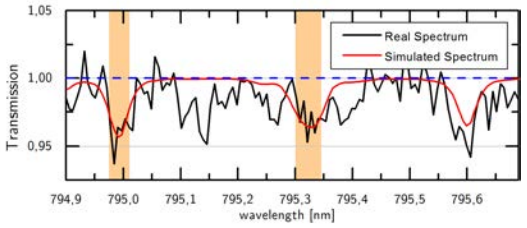

(f) Spectral line group G6

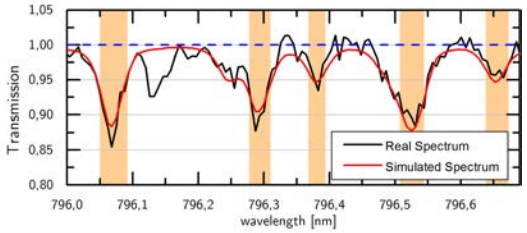

(g) Spectral line group G7

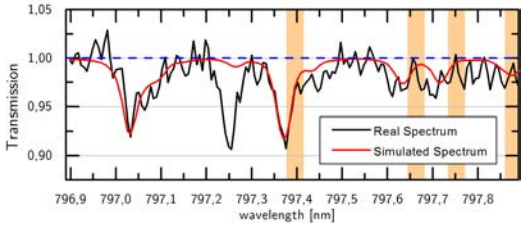

(h) Spectral line group G8

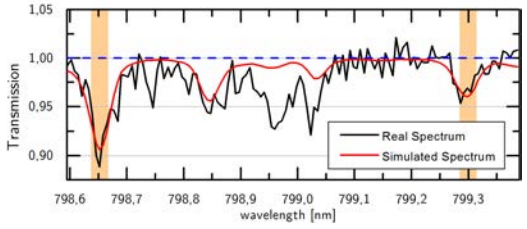

(i) Spectral line group G9

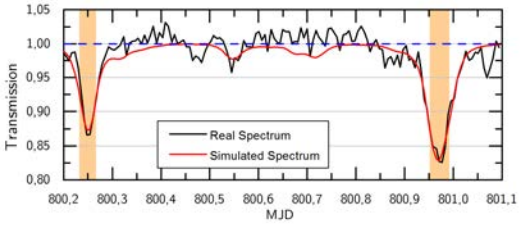

(j) Spectral line group G10

Figure 7.26: Matching between measurement-derived and simulated transmission spectra for a lunar measurement (nearly full moon, elevation angle: 40°, PW $\approx 10\,\mathrm{kg/m^2}$ for the different spectral line groups. The orange vertical bars denote the processed wavelength intervals.

4. According to Eqs 7.6 and 7.4 this would yield an adjusted $\sigma_{t,lun}$ of around 1 % (before 2.2 %).
5. $\sigma_{t,lun}$ would propagate, according to Eq. 7.10, to an PW uncertainty $\sigma^{lun}_{PW,noise}$ of slightly below 1 kg/m^2 for each evaluated line.

Regarding the different systematic biases discussed in Section 7.3.2, only the baseline retrieval would be afflicted by the reduced noise levels.

8

Conclusions and Outlook

8.1 Project Overview and Conclusions

The significance of satellite-based measurement systems in geodesy and earth observation in general is steadily increasing. Many measurement systems belonging to said realm are relying on travel time observations of radio signals through atmospheric layers. With the ever rising demands for improved accuracy of these methods, the precise description of atmospheric refractivity fields is gaining attention as well. In this respect the determination of the spatial distribution of water in its gaseous phase remains a major focus of such research activities. Accurate modelling of local water vapour concentrations succumbs to rapid atmospheric fluctuations with respect to space and time. In response a wide range of different instrumental measurement approaches have emerged over the past decades with vastly different characteristics regarding, e.g., time resolution, spatial resolution (horizontally and vertically), measurement platform, precision (absolute and relative) and cost.

Starting in the mid 1990s the *Geodesy and Geodynamics Lab (GGL)* of the *ETH Zürich* and the working group *Optical Spectroscopy* at the *Leibniz-Institut für Analytische Wissenschaften (ISAS), Berlin* have jointly developed two dedicated measurement systems (SAMOS and GEMOSS) applying the principle of *Differential Optical Absorption Spectroscopy (DOAS)* thus establishing another method supporting to satisfy the demand for the determination of local total column water vapour abundances with high precision and high temporal resolution. Within these projects the DOAS methodology, with its proven utility for the examination of atmospheric trace gas concentrations, has also been successfully applied to this specific aspect of moisture determination. Until then this task (which e.g. is of importance for the correction of data gathered by radio telescopes [Elgered et al., 1991] or the validation of other ground-based water vapour retrieval methods) has mainly been addressed by *Water Vapour Radiometers (WVR)* deducing concentrations through remote sensing of radiation emitted by water vapour.

From the above quoted instrument development projects it resulted that the analysis of spectrally high resolved rotational-vibrational water vapour absorption lines in the VIS/NIR spectral region indeed can provide water vapour concentrations with comparably good precision. As remarkable traits the low susceptibility to drift and jump behaviour [Somieski, 2005], the long-term stability independent of the local meteorological conditions and the comparably low recurring calibration effort needed stood out. Difficulties regarding the reliability of spectroscopic parameters of the evaluated specific single absorption lines, were addressed through a re-determination of line strength parameters and through averaging of the results from a set of distinct lines which are observed simultaneously.

Based on the insights gained from the SAMOS and foremost the GEMOSS project, in a joint project of ETH Zürich, ISAS-Berlin and the Helmholtz-Zentrum Potsdam - Deutsches

GeoForschungsZentrum (GFZ) a new prototype instrument *SOlar LUnar Spectrometer for Atmospheric Research (SOLUSAR)* has been designed and built in two copies, in order to carry forward the research in this field and to explore and treat the following issues related to the application of DOAS to the problem of atmospheric moisture detection:

To address the aspect of confined temporal coverage, the new measurement system has been conceived not only to allow measurements with direct sunlight, but also with solar radiation reflected by the moon surface at night. The entire instrument from the telescope over the spectrometer to the detector is designed to ensure greatest possible sensitivity. By selecting a smaller specific wavelength range (which exhibits a large number of processable water vapour absorption features) which is obtained simultaneously it was feasible to give the measurement system a very compact optical design in comparison with the predecessor instruments, which improves transportability and applicability in the field while not compromising on the spectral resolving power. For the purpose of possible validation measurements of space borne WVR instruments from satellite ground tracks on a vessel at sea, the viability of the attainment of solar transmission spectra on a moving platform was to be examined through implementation of a fast tracking telescope with an automatic control cycle in order to uninterruptedly follow the background radiation source. All these efforts were to conclude with a measurement system producing comparably accurate measurement results as its predecessor (GEMOSS) while operating fully autonomously and calibrating itself without the need for human supervision.

To suffice the demand for highly compact instruments the SOLUSAR measurement systems dispose of an almost fully integrated design. Apart from some external sensors, the power supply and the main control computer unit, all mechanical, optical and electronic components are stored inside a rugged aluminium encasement with a height of 1.1 m, a diameter of 30 cm and a weight around 45 kg. The thorough integration is for another part directly caused by the need for improved system sensitivity which demands a direct optical coupling of the telescope positioned at the top of the instrument and the spectrometer unit directly underneath. As light collecting unit a custom-built heliostat-type telescope is used to guide the sun or moon light into the instrument's unified optical axis to image it onto the spectrometer's entrance slit. The autonomous tracking of the light source is achieved through a control cycle using a quadrant photodiode to provide information on the telescope's misalignment. From this information control quantities for the telescope's motor system are computed and applied. The control cycle operates with a frequency of about 80 Hz. The telescope's opto-electronic components used in this process are likewise specifically conceived for operation both under high intensity and low-light conditions.

To achieve a spectrometer set-up which is compact and at the same time spectrally highly resolving and efficient, advantage is taken of the concept of an echelle grating spectrograph. The spectrometer has a focal length of 400 mm. The diffraction is carried out by means of the echelle grating (blaze angle: 62°) as primary diffraction element and an optical prism to optically separate the superimposed diffraction orders. The optical elements are arranged in the Littrow configuration. Because of the narrow simultaneously captured wavelength range achromatic lenses can be used for beam collimation and concentration instead of mirrors. With an interposed motorized folding mirror between grating and prism the spectrum position on the detector can be stabilized and also the possibility to observe adjacent wavelength regions is provided. The described optical arrangement allows a very slim architecture along the vertical optical axis of the instrument. As detector a back-thinned CCD detector (size: 1 in × 1/4 in; pixel size: 12 µm) is made use of. Given said optical set-up a snippet of a single diffraction order containing a wavelength range of slightly more than 12 nm is imaged on the detector using an entrance slit height of 1 mm (magnification 1:1). A reciprocal linear dispersion of 7.3 pm/px is reached. Together with a 50 µm entrance slit width this allows a good compromise between

sufficient absorption line separation and overall brightness. The obtained narrow wavelength band can be read out quite rapidly given the moderate chip size.

In order to make the measurement instrument run fully autonomously – controlling the various sensors and coordinating the different measurement tasks – a software package has been developed, which is for the most part written in the visual programming environment LabVIEW™ (by National Instruments). The tasks to be performed include among others proper tracking of the moving background radiation sources sun or moon to continuously guide the light onto the entrance slit, over control of the detector exposure regimen to a variety of different calibration tasks, such as telescope orientation, position stabilization of the spectrum on the detector, acquisition of spectra of the internal calibration lamps (halogen flat-field lamp and argon spectral lamp) or repeated determination of the apparatus function. The acquisition period for solar spectra is set at 1 min. In case of lunar spectra, the interval amounts from 10 min to 20 min.

With the vastly different instrument design compared to the predecessor systems, lots of new insights regarding the design of possible future devices have been won: The direct optical coupling of the telescope and spectrometer unit serves exceptionally well to maximize the system radiation throughput and to build a compact system. However in retrospect one has to state that such an approach brings also about a multitude of difficulties: The direct entrance slit lighting is changing the spectrometer's illumination depending on the light source the telescope aims at (sun, moon, halogen lamp) as well as on the meteorological conditions. Not per se a problem, in case of the application of a highly sensitive back-illuminated CCD this has evidently unbearable consequences in form of changing interference patterns (etaloning) which are modulating the actual spectral signal and prohibiting a proper evaluation of the characteristic DOAS baseline intensity. Within the pre-existing overall concept and regarding the already advanced project state, a replacement of the OEM detector unit has turned out to be impossible, as no suitable substitute could be found given the limited space available and very specific detector requirements. Hence an optical solution had to be found which guarantees a stable illumination of the entrance slit over its whole height and a constant angular radiation distribution within the light bundles entering the spectrometer. Unfortunately most of the tested homogenization approaches go hand in hand with a huge loss in energy. The approach found to balance best the need for radiation redistribution and conservation of aperture is a short quartz optical fibre with hexagonal cross section whose entrance is illuminated by the telescope and which conveys the radiation to the entrance slit. The inclusion of a homogenizing fibre limits the sensitivity on one hand on the other greatly reduces the initial calibration efforts. Further it considerably eases the task of target tracking, as the danger of uneven entrance slit illumination in case of telescope misalignment practically vanishes.

The above described solution unfortunately runs contrary to the purpose of directly coupled telescope and spectrometer units, but allows the acquisition of spectra with etaloning influence reduced to bearable levels. The surface brightness on the detector decreased by a factor of 8 which does not afflict the solar measurement, in case of the already weak lunar spectra it is a major liability though. Nevertheless in case of lunar phase angles in the range 0° to 30° the acquisition of lunar spectra with S/N ratios allowing a retrieval of integral slant concentrations could be successfully conducted. Also the telescope's control cycle with the quadrant diode feedback sensor, whose signals are treated by an especially conceived amplifier module developed at ISAS, does operate flawlessly under these difficult low light conditions.

After their acquisition the solar/lunar spectra are directly pre-processed using a set of specifically developed correction and referencing algorithms, namely: dark correction, extraction of the position of the bent main diffraction order, vertical software binning, flat-field correction, wavelength referencing. This ultimately produces processable transmission spectra

which exhibit only the atmospheric absorption features and Fraunhofer lines and are only further shaped through broadening processes along the ray path and by the apparatus. In case of lunar spectra a special filtering algorithm is additionally applied (based on the Savitzky-Golay filter) which helps to eliminate broadband structures stemming from electromagnetic influence on the CCD module by the telescope's actuator system.

For the actual processing of the measurement derived transmission spectra, mostly the same set of algorithms as used in the GEMOSS project is applied. The procedure relies on the matching of the measured transmission spectra with synthetically computed transmission spectra for whose generation the absorption process along the line of sight, including broadening of the absorption features in the atmosphere and by the apparatus, is modelled. The water vapour concentration in the model is adjusted until the best fit with the measurement is found. One major weak point in the application of DOAS is the dependence on the availability of accurate spectroscopic parameters for the rotational-vibrational transitions occurring in the observed wavelength range. Such parameters are provided by numerous spectral databases; in case of SOLUSAR the relatively recent HITRAN2008 database has been selected. More extensive databases (e.g. UCL08) listing also minor transitions are found to not bring a substantial advantage, at least not for the wavelength intervals studied in this work, but are only severely prolonging the processing time. Comparison of SOLUSAR datasets obtained under different conditions on one hand help to reveal which major lines are providing reliable PW values, on the other hand they emphasize inconsistencies in the spectral database regarding line strength, an issue which could not be overcome within this project.

Examinations of the different error sources contributing to the overall uncertainty of the PW values have been carried out. In case of solar measurement the noise-induced PW uncertainty for a single line evaluation is estimated at $0.4\,\mathrm{kg/m^2}$ (slightly higher than in the GEMOSS project). Through averaging of the result this accuracy can of course be improved (maximum by a factor 5 in case of SOLUSAR). The sources contributing mostly are the errors stemming from stray light residuals and remaining etaloning disturbances. For lunar measurements the noise-induced uncertainty is around five times higher ($2.2\,\mathrm{kg/m^2}$). Main contributors in this case are the read noise (respectively the electromagnetic interferences included therein affecting every spectra acquisition on readout) and the dark noise (due to the long exposure time per single image). Further some of the different systematic error sources were assessed more closely: Especially noticeable is the influence of an insufficiently precise apparatus function. Analysis of the matching quality between simulated and measured spectra indicate that the apparatus function width is generally overestimated, with the possible consequence of an assignation of PW values which are up to 7 % too high. The behaviour of different absorptions lines is inconsistent though, giving rise to the question whether the reason for these deviations lies in the uncertainty of the reported spectroscopic broadening parameters.

Furthermore an assessment of the baseline accuracy reveals that the chosen holistic approach – where the remaining broadband modulations in the flat-field corrected spectra are eliminated through a polynomial fit estimated from few distinct baseline intervals – is not only affected by the stochastic noise in said intervals, but in case of strong concentrations and low elevation angles by the considerable drag down of the baseline transmission values. This behaviour is especially harmful in case of weaker absorption features. For high concentrations a mean bias of up to $-2\,\%$ can result.

Comparison with results from GPS meteorology by means of a co-located sensor show considerable biases: Solar spectrometry estimates the ZPW on average 8.7 % higher, which can possibly be regarded as evidence of the various systematic, concentration proportional effects mentioned above and partially of systematic differences between the applied two methods. General trends in the ZPW values though are quite similarly mirrored by the two systems,

albeit with a very different time resolution. Direct comparison of the results of the two (identically built) SOLUSAR measurement systems unfortunately shows certain systematic biases as well, which can reach up to 1.5 kg/m^2. These biases vary strongly between the different absorption features and seem also to be concentration dependent. As the main cause of the described differences a problem with occurring stray or false light in one of the systems is suspected. The mean stochastic deviations (after elimination of the estimated systematic influences) amount to ca. 1.1 % of the slant integral concentration.

Besides the above mentioned etaloning issues, the high system integration produces various challenges regarding the prevention or suppression of electromagnetic disturbances inside the measurement system, occurring through the presence of the manifold electronic components with great power demand (e.g. motor systems, lamps) in the vicinity of very sensitive detector units. Further the asset of a transportable and weatherproof design, unfortunately brings about a greater time expenditure for instrument maintenance as the various components are not as directly accessible. Especially for people who are mere users and have not been involved in the development process, dealing with hardware issues can become quite cumbersome. Fortunately both systems have shown very good long-term consistency of the results and needed little maintenance.

8.2 Outlook

To bring atmospheric water vapour sensing using the DOAS method further ahead, a variety of different issues will have to be addressed. This section provides an overview of the different short-term tasks as well as an outlook on possible future instrument development projects.

8.2.1 Immediate Measures

Concerning the spectra processing of the DOAS measurements different issues remain. For instance to retrieve water vapour values in near real time a considerable speeding up of the data processing would be mandatory. Hitherto processing of a single spectrum takes between 4 min to 8 min. To decrease the evaluation time to about 1 min the programming routines have to be adapted to make use of multi-core processing in particular to quicken the spectra simulation in the adjustment. A solution to provide a more accurate wavelength scale would reduce the number of adjustment iterations and thus considerably speed up the process.

A major task in order to improve the absolute accuracy of the determined water vapour concentrations, is a deepened examination and treatment of the various systematic error sources. In this respect I recommend the implementation of a more sophisticated baseline retrieval algorithm which is better coping with spectra exhibiting strong absorption, where in the current algorithm the transmission values of the baseline intervals used for the polynomial fit are dragged down. Also lower uncertainties of the baseline at the edges of the spectral window are desirable. To achieve said goals, analysis of the measurement spectra alone might not be sufficient. Presumably a dedicated pre-fitting process of a transmission spectrum computed with the current baseline algorithm and a simulated absorption spectrum covering the whole measurement range could be very beneficial. In this pre-fitting process the extent of the baseline interval sagging could be determined and the baseline ultimately be refined in an iterative procedure, while the wavelength scale could also be adjusted simultaneously. To cope with the influence of Fraunhofer features, which are only present in the measurement derived dataset, a robust fitting procedure would have to be applied. Such a pre-fitting step besides a better

baseline would also provide a much improved wavelength scale and initial PW values for the sequential actual adjustment process, to speed up the latter.

To learn more about the inaccuracies in the spectral parameters provided by the spectral databases and about the factors leading to differences in line shapes between measurement and simulation, extensive comparison measurement with other independent retrieval methods are necessary, preferentially those providing concentration profile information, such as, e.g., LIDAR or radiosondes.

To improve the reliability of the results of the two currently existing SOLUSAR measurement systems foremost a closer examination of the occurring false light and its suppression by means of baffles has to be carried out. Possibly also the application of translating optical mounts to render a more precise positioning of the entrance slit with respect to the quadrant diode could be beneficial to the accordance of the two systems.

8.2.2 Recommendations for Future Direct Light Measurement Systems

With the development of the SOLUSAR measurement systems various different aspects of this methodology were to be examined, with partly contradictory design demands which had to be reconciled. The enabling of lunar measurements on one side demands for a large radiation acceptance and efficiency which normally requires more space while on the other side a very compact system should be conceived. The therefore chosen highly integrative design architecture is especially ambitious from the electronic point of view when dealing with extremely sensitive detection units. Moreover for lunar measurements a direct illumination of the spectrometer by the telescope is preferred, which again is a challenge considering the conditions occurring when measuring on a moving platform. For this reason looking at future apparatuses an disentangling of the project objectives should perhaps be aspired.

Generally one can conclude that the direct coupling of telescope and spectrometer unit rather complicates matters more than it helps. Maybe from a transportation/handling and maintenance point of view a separation of the two units would be very convenient as it reduces the bulkiness and the weight of the different units. For solar measurement a direct coupling is not necessary anyway as there is no shortage of intensity. In case of lunar spectra a decoupling by means of a suitable optical fibre would help to get rid of illumination dependent etaloning structures produced by the detector, while a telescope with a higher light collecting efficiency (short focal length, high aperture lens optics) could be installed compensating for the lower throughput. In any case the possibility to easily effectuate a change of the light collection unit depending on the task at hand is appealing (the same applies for the detector unit). Such a unit separation could also benefit from the implementation of individual main control devices for both entities, which could also help to streamline the software. Especially regarding the telescope's only task to follow the light source without need of data storage, the employment of a single-board computer or a dedicated micro-controller with a machine-level implementation of the control cycle could be an appropriate choice. A separation would also massively reduce the complexity from an electronics point of view and help to bring down the susceptibility to electromagnetic perturbations.

A compact spectrometer system with good transportability, easy applicability in the field and low maintenance requirements remains desirable. In that respect the question of the suitable (simultaneously obtainable) wavelength range of the spectrometer has to be raised again. In case of direct radiation solar measurements the NIR radiation portion between 789 nm to 802 nm has proven itself as a viable spectral extract with a high number of useful

absorption lines. Still a slightly bigger range could be helpful to further increase the reliability of the overall retrieved mean concentrations. One possibility to further reduce the size of the spectrometer set-up would be the application of transmission gratings as the diffraction order sorter element instead of the prism. Such gratings have been tested within the SOLUSAR project but were exhibiting stray light clearly exceeding acceptable levels. Recently however transmission gratings produced by photolithography have become available which are specified to produce considerably less stray light [Ibsen Photonics, 2013].

In case of solar measurements a conventional CCD can be used, as the higher quantum efficiency of a back-thinned detector is not needed. In case of a telescope/spectrometer separation as described above the etaloning influence when measuring NIR can be considered as rather small, as the then indispensable connecting fibre acts as a radiation homogenizer – a future application of back-thinned CCDs is still not recommended though, also not for the low-light lunar measurements. A detector unit with a faster readout could possibly help to achieve better S/N ratios but only if the read noise does not increase all too much. To study more deeply the implications regarding the insufficient modelling of the line broadening a slightly higher reciprocal linear dispersion of the spectrometer-detector system would be helpful, which would again require the application of an echelle spectrograph. If lunar measurements with corresponding low-light conditions are desired one should opt for a detector providing the possibility of longer exposure times and lower chip temperatures to reduce dark noise. It could already be shown that lunar measurements are feasible with an noise-induced error which is theoretically only about a factor of 2.5 higher than for solar measurements with the current set-up. The meaningfulness of lunar measurements regarding the much higher instrumental efforts in relation to the additional observations windows gained is disputable though.

Regarding a possible future sea borne application of a telescope-spectrometer combination different aspects should be considered. In the initial set-up with a direct optical coupling, the entrance slit height of 1 mm and the projected sun disk image diameter at around 1.3 mm leave only a scanty reserve for misalignment of the telescope, which seems insufficient for conditions with less moderate state of sea especially with occasional occurrence of jerks. The indirect coupling with interface fibre optics is less prone, as stronger intermittent telescope misalignments do not hamper the entrance slit illumination but simply attenuates the overall intensity. In any case the speed of the telescope control cycle would have to be improved. Especially a more direct feedback loop between the quadrant diode and the motors is necessary. Until now the sensor signals are A/D-converted and processed by the computer unit determining the number of necessary motor steps. The motion control card performs a PID-control cycle to reach the desired position as rapidly as possible. In order to speed up the process this two-step procedure has to be stripped down to a direct control loop, where the applied voltages for the motors are directly computed by a specifically deployed single purpose hardware item. Further a gear would have to be installed for azimuthal movements which acts more directly than a drive belt.

For the telescopes external orientation when operating on a vessel, the digital magnetometers do not seem to be a good choice, as they are not responsive enough to sudden changes of bearing and too inaccurate given the surroundings with partly ferromagnetic materials. The orientation procedures described in this work using the quadrant photo diode as intensity sensor is a feasible solution but shows its flaws concerning speed and reliability. The introduction of a small zenith-looking digital camera in conjunction with a fish eye lens covering the sky hemisphere would offer a variety of new possibilities: Through fast image processing, the current apparent position of the celestial radiation source is readily discernible. Apart from this, it would be possible to derive information on the light source's apparent brightness and thus to make an educated guess on an adequate exposure time. Further under bad weather

conditions the system could be automatically brought to sleep mode and the load temporarily remove from the mechanical system.

8.2.3 Expansion of Methodology

Concerning alternative operation modes differing from the currently applied direct light DOAS, the SOLUSAR measurement system or any similar instrumental set-up with comparable sensitivity, dynamic range and a similarly versatile telescope does indeed offer the possibility to receive and analyse scattered light. Scattered light DOAS has been successfully applied for many decades and for a great number of different atmospheric species. For a comprehensive overview please consult Platt and Stutz [2008]. An application of this method to measure vapour concentrations in the atmosphere would be interesting. In the realm of scattered light DOAS different viewing geometries are distinguished, e.g. Zenith Scattered Light DOAS (ZSL-DOAS) which is often applied for stratospheric studies or Multi-Axis DOAS (MAX-DOAS) where radiation with different elevation angles is gathered. While the former would massively reduce the instrumental requirements for the telescope the latter could help to retrieve information on the spatial distribution of water vapour. A combination of several such instruments would permit the possibility to apply tomographic principles. Scattered light DOAS would also allow a further expansion of the possible measurement time as no direct sunlight is needed at daytime. The major challenge with scattered light DOAS lays in the far more complex modelling of the absorption process as an infinite number of ray paths have in principle to be taken into consideration. Fine modelling of the incident scattering light is difficult, since the corresponding models heavily rely on fairly precise information on the vertical distribution of trace gases and aerosols (and their optical properties) [Platt and Stutz, 2008]. Therefore uncertainties of these data can lead to systematic errors and consequently to a degradation of the overall accuracy. By all means scattering approaches would require an extended wavelength range comparable to the GEMOSS spectral range (728 nm to 915 nm) as for the validation of the ray tracing model, absorption lines of other atmospheric species (such as oxygen or oxygen-dimers) are needed whose vertical concentration profiles are well known.

Curriculum Vitae

Personal Details

Name:	Münch, Stefan Walter
Date of Birth:	5 July, 1981
Citizen:	Zürich (Canton of Zürich)
Nationality:	Swiss

Education and Professional Positions

2008 to 2013:	Research stay at Leibniz-Institut für Analytische Wissenschaften e.V., Berlin (Germany)
2007 to 2013:	PhD student, ETH Zürich
2006 to 2012:	Research Assistant at Geodesy and Geodynamics Lab (GGL), ETH Zürich
2001 to 2006:	Studies of Geomatics Engineering, ETH Zürich Degree as Dipl. Geomatik-Ing. ETH
1996 to 2001:	Mathematisch-Naturwissenschaftliches Gymnasium Rämibühl, Zürich Graduation with Matura Type C

Awards

2006:	ETH-Medal for diploma thesis

Bibliography

Allard, N. and Kielkopf, J. (1982). The effect of neutral nonresonant collisions on atomic spectral lines. *Reviews of modern physics*, 54(4):1103–1182.

American Geophysical Union (AGU) (1995). Water Vapor in the Climate System. `http://www.eso.org/gen-fac/pubs/astclim/espas/pwv/mockler.html`.

Analog Devices (2008). Datasheet AD549: Ultralow Input-Bias Current Operational Amplifier. `http://www.analog.com/static/imported-files/data_sheets/AD549.pdf`.

Ansmann, A., Riebesell, M., Wandinger, U., Weitkamp, C., Voss, E., Lahmann, W., and Michaelis, W. (1992). Combined Raman elastic-backscatter lidar for vertical profiling of moisture, aerosol extinction, backscatter, and lidar ratio. *Applied Physics B: Lasers and Optics*, 55(1):18–28.

Barber, R., Tennyson, J., Harris, G., and Tolchenov, R. (2006). A high-accuracy computed water line list. *Monthly Notices of the Royal Astronomical Society*, 368(3):1087–1094.

Becker-Roß, H. and Florek, S. (1997). Echelle spectrometers and charge-coupled devices. *Spectrochimica Acta Part B: Atomic Spectroscopy*, 52(9):1367–1375.

Bender, M., Dick, G., Wickert, J., Ramatschi, M., Ge, M., Gendt, G., Rothacher, M., Raabe, A., and Tetzlaff, G. (2009). Estimates of the information provided by GPS slant data observed in Germany regarding tomographic applications. *Journal of Geophysical Research*, 114(D6):D06303.

Bevis, M., Businger, S., Herring, T. A., Rocken, C., Anthes, R. A., and Ware, R. H. (1992). GPS Meteorology: Remote Sensing of Atmospheric Water Vapor Using the Global Positioning System. *Journal of Geophysical Research*, 97(D14):15787–15801.

BKG (Bundesamt für Kartographie und Geodäsie) (2006). Workshop on Measurement of Atmospheric Water Vapour: Theory, Techniques, Astronomical and Geodetic Applications (Wettzell / Hoellenstein (Germany), October 9-11, 2006). `http://www.fs.wettzell.de/veranstaltungen/wvr/workshop2006/presentations.html`.

Blume, P. A. (2007). *The LabVIEW Style Book*. Prentice Hall, 1 edition.

Boor, C. D. (2001). *A Practical Guide to Splines*. Springer.

Bösch, H. (2002). *Studies of the Stratospheric Iodine and Nitrogen Chemistry by Balloon-Borne DOAS Measurements and Model Calculations*. PhD thesis, University of Heidelberg.

Bösch, H., Camy-Peyret, C., Chipperfield, M., Fitzenberger, R., Harder, H., Platt, U., and Pfeilsticker, K. (2003). Upper limits of stratospheric IO and OIO inferred from center-to-limb-darkening-corrected balloon-borne solar occultation visible spectra: Implications for total gaseous iodine and stratospheric ozone. *Journal of Geophysical Research: Atmospheres (1984–2012)*, 108(D15).

Bradt, H. (2004). *Astronomy Methods: A Physical Approach to Astronomical Observations*. Cambridge University Press.

Bürki, B. and Kahle, H. (1995). Mikrowellen-Wasserdampf-Radiometer für hochgenaue Messungen mit GPS. *Géodésie et Géodynamique*, 4(95):232–240.

Carosio, A. (2001). *Fehlertheorie und Ausgleichsrechnung, Band 1.* ETH Zürich, Departement Geodätische Wissenschaften.

CAVIAR consortium (2010). New water vapour monomer linelist. `http://www.met.reading.ac.uk/caviar/data.html`.

Ceramoptec (2011). Datasheet - Optran NCC UV/WF (Silica/Silica Non Circular Core Fiber). `http://www.ceramoptec.com/filephotos/1/Optran-NCC-UVWF.pdf`.

Ciddor, P. (1996). Refractive index of air: new equations for the visible and near infrared. *Applied Optics*, 35(9):1566–1573.

Ciddor, P. and Hill, R. (1999). Refractive index of air. 2. Group index. *Applied Optics*, 38(9):1663–1667.

Dach, R., Hugentobler, U., Fridez, P., and Meindl, M., editors (2007). *Bernese GPS software version 5.0.* Astronomical Institute, University of Bern.

Daniel, J., Solomon, S., Sanders, R., Portmann, R., Miller, D., and Madsen, W. (1999). Implications for water monomer and dimer solar absorption from observations at Boulder, Colorado. *Journal of geophysical research*, 104(D14):16785–16791.

Davis, J., Herring, T., Shapiro, I., Rogers, A., and Elgered, G. (1985). Geodesy by Radio Interferometry - Effects of Atmospheric Modeling Errors on Estimates of Baseline Length. *Radio Science*, 20(6):1593–1607.

Deng, Z., Bender, M., Zus, F., Ge, M., Dick, G., Ramatschi, M., Wickert, J., Löhnert, U., and Schön, S. (2011). Validation of tropospheric slant path delays derived from single and dual frequency GPS receivers. *Radio Science*, 46(6).

Denton, B., Fields, R., and Hanley, Q. (1996). *Recent developments in scientific optical imaging.* Special publication. Royal Society of Chemistry, 1st edition.

Dick, G., Gendt, G., and Reigber, C. (2001). First experience with near real-time water vapor estimation in a German GPS network. *Journal of Atmospheric and Solar-Terrestrial Physics*, 63(12):1295–1304.

Dodson, A., Baker, H., Bürki, B., Elgered, G., Rius, A., and Rothacher, M. (1998). The Wavefront Project on Ground-Based GPS Water Vapour Estimation. In *The 2nd European Symposium on Global Navigation Satellite Systems (GNSS 98).*

Edner, H., Fredriksson, K., Sunesson, A., Svanberg, S., Uéus, L., and Wendt, W. (1987). Mobile remote sensing system for atmospheric monitoring. *Appl. Opt.*, 26(19):4330–4338.

Elgered, G. (1993). *Atmospheric Remote Sensing by Microwave Radiometry*, chapter Tropospheric Radiopath Delay from ground-based Microwave Radiometry, pages 215–258. John Wiley & Sons, 1 edition.

Elgered, G. (2013). Ground-based GPS networks for remote sensing of the atmospheric water vapour content: a review. *7th Study Conference on BALTEX June 10-14, 2013, Borgholm, Island of Öland, Sweden, (53) s. 12-13.*

Elgered, G., Davis, J., Herring, T., and Shapiro, I. (1991). Geodesy by Radio Interferometry: Water Vapor Radiometry for Estimation of the Wet Delay. *Journal of Geophysical Research: Solid Earth (1978–2012)*, 96(B4):6541–6555.

Elgered, G. and Jarlemark, P. O. (1998). Ground-based microwave radiometry and long-term observations of atmospheric water vapor. *Radio Science*, 33(3):707–717.

Encyclopedia Britannica (2012). Entry: Atmosphere. `http://www.britannica.com/EBchecked/topic/41364/atmosphere`.

Essen, L. and Froome, K. (1951). The Refractive Indices and Dielectric Constants of Air and its Principal Constituents at 24 GHz. *Proceedings of the Physical Society. Section B*, 64(10):862–875.

Fischer, J., Gamache, R., Goldman, A., Rothman, L., and Perrin, A. (2003). Total internal partition sums for molecular species in the 2000 edition of the HITRAN database. *Journal of Quantitative Spectroscopy and Radiative Transfer*, 82(1):401–412.

Florek, S. and Becker-Roß, H. (1995). High-resolution spectrometer for atomic spectrometry. *Journal of Analytical Atomic Spectrometry*, 10:145–147.

Flores, A., Ruffini, G., and Rius, A. (2000). 4D tropospheric tomography using GPS slant wet delays. In *Annales Geophysicae*, volume 18, pages 223–234. Springer.

Gamache, R., Kennedy, S., Hawkins, R., and Rothman, L. (2000). Total internal partition sums for molecules in the terrestrial atmosphere. *Journal of Molecular Structure*, 517-518:407 – 425.

Gendt, G., Dick, G., Reigber, C., Tomassini, M., LIU, Y., and Ramatschi, M. (2004). Near real time GPS water vapor monitoring for numerical weather prediction in Germany. *Journal of the Meteorological Society of Japan*, 82(1B):361–370.

Hamamatsu (2005). Datasheet: CCD area image sensor S10140/10141 series. `http://www.ccd.com/pdf/ccd_10141.pdf`.

Hamamatsu (2007). Technical Information: Characteristics and use of back-thinned TDI-CCD. `http://www.hamamatsu.com/resources/pdf/ssd/tdi-ccd_techinfo_e.pdf`.

Hamamatsu (2008). Instruction manual: Digital CCD Board Camera C9260-933-17.

Harrison, G. R., Lord, R. C., and Loofbourow, J. R. (1948). *Practical spectroscopy*. Prentice-Hall.

Held, I. and Soden, B. (2000). Water Vapor Feedback and Global Warming. *Annual Review of Energy and the Environment*, 25(1):441–475.

Hinkley, E. D., editor (1976). *Laser monitoring of the atmosphere*, volume 14 of *Topics in Applied Physics*. Springer.

Hofmann-Wellenhof, B., Lichtenegger, H., and Collins, J. (2001). *Global Positioning System: Theory and Practice*. Springer, 5th edition.

Holland, P. W. and Welsch, R. E. (1977). Robust regression using iteratively reweighted least-squares. *Communications in Statistics-Theory and Methods*, 6(9):813–827.

Holst, G. C. (1998). *CCD arrays, cameras, and displays*, volume 996. SPIE Optical Engineering Press Bellingham.

Honeywell (2005). Digital Compass Solutions HMR3200/HMR3300. `http://media.digikey.com/pdf/Data%20Sheets/Honeywell%20PDFs/HMR3200,3300.pdf`.

Huang, X. and Yung, Y. (2004). A common misunderstanding about the Voigt line profile. *Journal of the atmospheric sciences*, 61(13):1630–1632.

Humlícek, J. (1982). Optimized computation of the Voigt and complex probability functions. *Journal of Quantitative Spectroscopy and Radiative Transfer*, 27:437–444.

Hurter, F., Geiger, A., Perler, D., and Rothacher, M. (2012). Gnss water vapor monitoring in the swiss alps. In *Geoscience and Remote Sensing Symposium (IGARSS), 2012 IEEE International*, pages 1972–1975. IEEE.

Ibsen Photonics (2013). Product Sheet SNIR Spectrometer Grating: 966 l/mm for 500-1100 nm; Fused Silica Transmission Grating Technology. `http://www.ibsen.dk/ibsen/spectrometergratings/snir966gratings`.

Icron (2010a). Datasheet - USB Ranger 2224, Fiber Optic USB 2.0 Extender. `http://www.icron.com/products/usb_new/collateral/USB-Ranger-2224-datasheet.pdf`.

Icron (2010b). User Guide: USB Ranger 2224, Fiber Optic USB 2.0 Extender. `http://www.icron.com/products/usb_new/collateral/USB-Ranger-2224-userguide.pdf`.

Innovate Sensor Technology IST (2012). Datasheet: TSic 206/203/201/306/303/301. `http://www.ist-ag.com/eh/ist-ag/resource.nsf/imgref/Download_DTTSic20x_30x_E1.0.pdf/$FILE/DTTSic20x_30x_E1.0.pdf`.

Intergovernmental Panel on Climate Change (2007). *Climate Change 2007 - The Physical Science Basis: Working Group I Contribution to the Fourth Assessment Report of the IPCC*. Cambridge University Press.

Jarlemark, P. and Elgered, G. (2003). Retrieval of atmospheric water vapour using a ground-based single-channel microwave radiometer. *International Journal of Remote Sensing*, 24(19):3821–3837.

Kao, Wei-Wen, Tsai, and Chin-Lang (2006). Adaptive and learning calibration of magnetic compass. *Measurement Science and Technology*, 17(11):3073–3082.

Keutsch, F. and Saykally, R. (2001). Water clusters: Untangling the mysteries of the liquid, one molecule at a time. *Proceedings of the National Academy of Sciences of the United States of America*, 98(19):10533–10540.

Kieffer, H. and Stone, T. (2007). The spectral irradiance of the Moon. *The Astronomical Journal*, 129(6):2887.

Kämpfer, N., editor (2012). *Monitoring Atmospheric Water Vapour: Ground-Based Remote Sensing and In-situ Methods (ISSI Scientific Report Series)*. Springer, 2013 edition.

Krivova, N. and Solanki, S. (2013). Models of Solar Total and Spectral Irradiance Variability of Relevance for Climate Studies. In Lübken, F.-J., editor, *Climate and Weather of the Sun-Earth System (CAWSES)*, Springer Atmospheric Sciences, pages 19–38. Springer Netherlands.

Kruse, L. P. (2001). Spatial and Temporal Distribution of Atmospherical Water Vapor using Space Geodetic Techniques. volume 61 of *Geodätisch-geophysikalische Arbeiten in der Schweiz*. Swiss Geodetic Commission.

Lasertechnik Berlin LTB (2009). Datasheet ELIAS Spectrometers. `http://www.ltb-berlin.de/fileadmin/ltb/style/gfx/pdf/products/elias_e.pdf`.

Lawrence, M. G. (2005). The Relationship between Relative Humidity and the Dewpoint Temperature in Moist Air: A Simple Conversion and Applications. *Bulletin of the American Meteorological Society*, 86(2):225–233.

Leblanc, T., Trickl, T., and Vogelmann, H. (2012). LIDAR. In Kämpfer, N., editor, *Monitoring Atmospheric Water Vapour: Ground-Based Remote Sensing and In-situ Methods (ISSI Scientific Report Series)*, chapter 7. Springer, 2013 edition.

Leforestier, C. (2012). Infrared shifts of the water dimer from the fully flexible ab initio HBB2 potential. *Philosophical Transactions of the Royal Society A: Mathematical, Physical and Engineering Sciences*, 370(1968):2675–2690.

libnova (n.d.). libnova: Celestial Mechanics, Astrometry and Astrodynamics Library. `http://libnova.sourceforge.net`.

LOT Oriel Group (2013). Pen-Ray line sources for wavelength calibration. Retrieved February 4, 2009, from National Center for Education Statistics: `http://www.lot-qd.de/files/downloads/lightsources/eu/LQ_Pen-Ray_Line_sources_for_wavelength_calibration_eu.pdf`.

Lutz, S., Troller, M., Perler, D., Geiger, A., and Kahle, H.-G. (2010). Better Weather Prediction using GPS. *GPS World*, 21(7):40–47.

Mach, J. J. (2003). Toward Auto-Calibration of Navigation Sensors for Miniature Autonomous Underwater Vehicles. Master's thesis, Virginia Polytechnic Institute and State University, USA.

Marenco, A., Thouret, V., Nédélec, P., Smit, H., Helten, M., Kley, D., Karcher, F., Simon, P., Law, K., Pyle, J., Poschmann, G., Von Wrede, R., Hume, C., and Cook, T. (1998). Measurement of ozone and water vapor by Airbus in-service aircraft: The MOZAIC airborne program, An overview. *Journal of Geophysical Research*, 103(D19):25631–25.

Marini, J. W. (1972). Correction of satellite tracking data for an arbitrary tropospheric profile. *Radio Science*, 7(2):223–231.

MathWorks (2013). Matlab Documentation (Version 2013b): robustfit (Robust regression). `http://www.mathworks.de/de/help/stats/robustfit.html`.

Maurellis, A. and Tennyson, J. (2003). The climatic effects of water vapour. *Physics World*, pages 29–33.

Maxon Motor (2009). Bedienungsanleitung: 4-Q-DC Servoverstärker ADS 50/5. `http://test.maxonmotor.com/docsx/Download/Product/Pdf/ads50-5_de.pdf`.

McGrath, R., Semmler, T., Sweeney, C., and Wang, S. (2006). Impact of Balloon Drift Errors in Radiosonde Data on Climate Statistics. *Journal of Climate*, 19(14):3430–3442.

Mendes, V. and Langley, R. (1995). Zenith wet tropospheric delay determination using prediction models: Accuracy analysis. *Cartografia e Cadastro*, 2:41–47.

Mérienne, M., Jenouvrier, A., Hermans, C., Vandaele, A., Carleer, M., Clerbaux, C., Coheur, P., Colin, R., Fally, S., and Bach, M. (2003). Water vapor line parameters in the 13000–9250 cm^{-1} region. *Journal of Quantitative Spectroscopy and Radiative Transfer*, 82(1):99–117.

Mills, A. (1985). Heliostats, Siderostats and Coelostats - a Review of Practical Instruments for Astronomical Applications. *Journal of the British Astronomical Association*, 95:89.

NASA Earth Observatory (2012). Global maps: Cloud fraction. `http://earthobservatory.nasa.gov/GlobalMaps/view.php?d1=MODAL2_M_CLD_FR`.

National Instruments (2003). User Manual: Motion Control National Instruments 7340. `http://www.ni.com/pdf/manuals/370838a.pdf`.

National Instruments (2012). Understanding Servo Tune. `http://www.ni.com/white-paper/2923/en`.

Ngo, N. H., Tran, H., Gamache, R. R., and Hartmann, J. M. (2012). Pressure effects on water vapour lines: beyond the Voigt profile. *Philosophical Transactions of the Royal Society A: Mathematical, Physical and Engineering Sciences*, 370(1968):2495–2508.

Niell, A. (1996). Global mapping functions for the atmosphere delay at radio wavelengths. *Journal of Geophysical Research - Solid Earth*, 101(B2):3227–3246.

Niell, A., Coster, A., Solheim, F., Mendes, V., Toor, P., Langley, R., and Upham, C. (2001). Comparison of measurements of atmospheric wet delay by radiosonde, water vapor radiometer, GPS, and VLBI. *Journal of Atmospheric and Oceanic Technology*, 18(6):830–850.

NOAA (1976). US standard atmosphere, 1976. *US Government Printing Office, Washington, DC*. NOAA and NASA and USAF.

Ohtake, M., Matsunaga, T., Yokota, Y., Yamamoto, S., Ogawa, Y., Morota, T., Honda, C., Haruyama, J., Kitazato, K., Takeda, H., Iwasaki, A., Nakamura, R., Hiroi, T., Kodoma, S., and Otake, H. (2010). Deriving the absolute reflectance of lunar surface using SELENE (Kaguya) multiband imager data. *Space science reviews*, 154(1):57–77.

Palmer, C. and Loewen, E. (2005). *Diffraction Grating Handbook*. Newport, 6th edition.

Paul, H. and Fellner, W., editors (1999). *Lexikon der Optik*. Spektrum Akademischer Verlag.

Perler, D. (2012). Water Vapor Tomography using Global Navigation Satellite Systems. volume 84 of *Geodätisch-geophysikalische Arbeiten in der Schweiz*. Swiss Geodetic Commission.

Perler, D., Geiger, A., and Hurter, F. (2011). 4D GPS water vapor tomography: new parameterized approaches. *Journal of Geodesy*, 85(8):539–550.

Pfeilsticker, K., Lotter, A., Peters, C., and Bosch, H. (2003). Atmospheric detection of water dimers via near-infrared absorption. *Science*, 300(5628):2078–2080.

Photonics (2010). Ceramoptec: Noncircular Core Silica Fibers. `http://www.photonics.com/Company.aspx?CompanyID=2408&AID=41952`.

Platt, U. and Stutz, J. (2008). *Differential Optical Absorption Spectroscopy: Principles and Applications (Physics of Earth and Space Environments)*. Springer, 1 edition.

Querel, R. and Naylor, D. (2011). Lunar absorption spectrophotometer for measuring atmospheric water vapor. *Applied Optics*, 50(4):447–453.

Resch, G. and Claflin, E. (1979). Microwave radiometry as a tool to calibrate tropospheric water vapor delay. *Radio Interferometry Techniques for Geodesy, NASA Conf. Pub. 2115, Washington, D.C.*, pages 377–384.

Richner, H., editor (1999). *Grundlagen aerologischer Messungen speziell mittels der Schweizer Sonde SRS 400*, volume 61 of *Veröffentlichungen der SMA-MeteoSchweiz*. SMA-MeteoSchweiz.

Rind, D., Chiou, E., Chu, W., Oltmans, S., Lerner, J., Larsen, J., McCormick, M., and McMaster, L. (1993). Overview of the Stratospheric Aerosol and Gas Experiment II Water-vapor Observations - Method, Validation, and Data Characteristics. *Journal of Geophysical Research*, 98(D3):4835–4856.

Roedel, W. (1994). *Physik unserer Umwelt: Die Atmosphäre*. Springer.

Roper Scientific (2000). Technical Note: Etaloning in Back-Illuminated CCDs. `http://www.princetoninstruments.com/Uploads/Princeton/Documents/Library/UpdatedLibrary/Etaloning_in_Back_Illuminated_CCDs.pdf`.

Rothacher, M. (1992). Orbits of Satellite Systems in Space Geodesy. volume 46 of *Geodätisch-geophysikalische Arbeiten in der Schweiz*. Swiss Geodetic Commission.

Rothman, L., Gordon, I., Barbe, A., Benner, D., Bernath, P., Birk, M., Boudon, V., Brown, L., Campargue, A., Champion, J., Chance, K., Coudert, L., Dana, V., Devi, V., Fally, S., Flaud, J.-M., Gamache, R., Goldman, A., Jacquemart, D., Kleiner, I., Lacome, N., Lafferty, W., Mandin, J.-Y., Massie, S., Mikhailenko, S., Miller, C., Moazzen-Ahmadi, N., Naumenko, O., Nikitin, A., J., O., Perevalov, V., Perrin, A., Predoi-Cross, A., Rinsland, C., Rotger, M., Šimečková, M., Smith, M., Sung, K., Tashkun, S., Tennyson, J., Toth, R., Vandaele, A., and Vander Auwera, J. (2009). The HITRAN 2008 molecular spectroscopic database. *Journal of Quantitative Spectroscopy and Radiative Transfer*, 110(9):533–572.

Rothman, L., Jacquemart, D., Barbe, A., Chris Benner, D., Birk, M., Brown, L., Carleer, M., Chackerian Jr, C., Chance, K., Coudert, L., Dana, V., Devi, V., Flaud, J.-M., Gamache, R., Goldman, A., Hartmann, J. M., Jucks, K., Maki, A., Mandin, J.-Y., Massie, S., J., O., Perrin, A., Rinsland, C., Smith, M., Tennyson, J., Tolchenov, R., Toth, R., Vander Auwera, J., Varanasi, P., and Wagner, G. (2005). The HITRAN 2004 molecular spectroscopic database. *Journal of Quantitative Spectroscopy and Radiative Transfer*, 96(2):139–204.

Rothman, L., Rinsland, C., Goldman, A., Massie, S., Edwards, D., Flaud, J.-M., Perrin, A., Camy-Peyret, C., Dana, V., Mandin, J.-Y., Schroeder, J., McCann, A., Gamache, R., Wattson, R., Yoshino, K., Chance, K., Jucks, K., Brown, L., Nemtchinov, V., and Varanasi, P. (1998). The HITRAN molecular spectroscopic database and HAWKS (HITRAN atmospheric workstation). In *Society of Photo-Optical Instrumentation Engineers (SPIE) Conference Series*, volume 3375, pages 123–132.

Rüeger, J. (2002). Refractive index formulae for radio waves. In *Fédération Internationale des Géomètres FIG XXII International Congress*, pages 19–26.

Saastamoinen, J. (1972). Atmospheric Correction for Troposphere and Stratosphere in Radio Ranging of Satellites. In Henriksen, S., Mancini, A., and Chovitz, B., editors, *The Use of Artificial Satellites for Geodesy*, volume 15 of *Washington DC American Geophysical Union Geophysical Monograph Series*, page 247.

Savitzky, A. and Golay, M. J. (1964). Smoothing and differentiation of data by simplified least squares procedures. *Analytical chemistry*, 36(8):1627–1639.

Sawyer, R. A. (1951). *Experimental Spectroscopy*. Prentice Hall, second edition edition.

Schafer, R. W. (2011). What is a savitzky-golay filter? (lecture notes). *Signal Processing Magazine, IEEE*, 28(4):111–117.

Schödlbauer, A. (2000). *Geodätische Astronomie*. de Gruyter.

Schermaul, R., Learner, R., Newnham, D., Williams, R., Ballard, J., Zobov, N., Belmiloud, D., and Tennyson, J. (2001). The Water Vapor Spectrum in the Region 8600–15 000 cm^{-1}: Experimental and Theoretical Studies for a New Spectral Line Database: I. Laboratory Measurements. *Journal of molecular spectroscopy*, 208(1):32–42.

Schreier, F. (2009). Comments on "A Common Misunderstanding about the Voigt Line Profile". *Journal of the Atmospheric Sciences*, 66(6):1860–1864.

Seagate (2007). Datasheet: EE25.1 Series; 2.5-inch drives designed for extreme environments. `http://www.seagate.com/docs/pdf/datasheet/disc/ds_ee25.pdf`.

Seeber, G. (2003). *Satellite Geodesy - Foundations, Methods, and Applications*. Walter de Gruyter, 2 edition.

Seidel, D. (2002). Water vapor: distribution and trends. *Encyclopedia of Global Environmental Change, John Wiley & Sons, Ltd, Chichester*.

Sherwood, S., Roca, R., Weckwerth, T., and Andronova, N. (2010). Tropospheric water vapor, convection, and climate. *Reviews of Geophysics*, 48(2).

Shillings, A. J. L., Ball, S. M., Barber, M. J., Tennyson, J., and Jones, R. L. (2011). An upper limit for water dimer absorption in the 750 nm spectral region and a revised water line list. *Atmospheric Chemistry and Physics*, 11(9):4273–4287.

Sierk, B. (2001). Solar Spectrometry for Determination of Tropospheric Water Vapor. volume 62 of *Geodätisch-geophysikalische Arbeiten in der Schweiz*. Swiss Geodetic Commission.

Sierk, B., Bürki, B., Becker-Ross, H., Florek, S., Neubert, R., Kruse, L. P., and Kahle, H.-G. (1997). Tropospheric water vapor derived from solar spectrometer, radiometer, and GPS measurements. 102(B10):22411–22.

Sierk, B., Solomon, S., Daniel, J., Portmann, R., Gutman, S., Langford, A., Eubank, C., Dutton, E., and Holub, K. (2004). Field measurements of water vapor continuum absorption in the visible and near-infrared. *Journal of geophysical research*, 109(D8):D08307.

Somieski, A. (2005). Geodetic Mobile Solar Spectrometer. volume 68 of *Geodätisch-geophysikalische Arbeiten in der Schweiz*. Swiss Geodetic Commission.

Somieski, A., Bürki, B., Geiger, A., Kahle, H.-G., Pavlis, E., Becker-Ross, H., Florek, S., and Okruss, M. (2006). Tropospheric water vapor from solar spectrometry and comparison with Jason microwave radiometer measurements. *Journal of geophysical research*, 111(D9):D09104.

Somieski, A. E. (2008). *Astrogeodetic geoid and isostatic considerations in the North Aegean Sea, Greece*. PhD thesis, ETH Zürich. Diss. ETH No. 17790.

Street, J. O., Carroll, R. J., and Ruppert, D. (1988). A note on computing robust regression estimates via iteratively reweighted least squares. *The American Statistician*, 42(2):152–154.

Stremme, W., Ortega, I., and Grutter, M. (2009). Using ground-based solar and lunar infrared spectroscopy to study the diurnal trend of carbon monoxide in the Mexico City boundary layer. *Atmos. Chem. Phys*, 9:8061–8078.

Sussmann, R., Borsdorff, T., Rettinger, M., Camy-Peyret, C., Demoulin, P., Duchatelet, P., Mahieu, E., and Servais, C. (2009). Technical Note: Harmonized retrieval of column-integrated atmospheric water vapor from the FTIR network – first examples for long-term records and station trends. *Atmospheric Chemistry and Physics*, 9(22).

Sussmann, R. and Schäfer, K. (1997). Infrared spectroscopy of tropospheric trace gases: combined analysis of horizontal and vertical column abundances. *Applied optics*, 36(3):735–741.

Svanberg, S. (1994). Differential Absorption LIDAR (DIAL). In Sigrist, M., editor, *Air Monitoring by Spectroscopic Techniques*, volume 127 of *Chemical Analysis Series*, chapter 3. John Wiley & Sons, Inc., 2013 edition.

Sweedler, J., Ratzlaff, K., and Denton, M., editors (1994). *Charge-Transfer Devices in Spectroscopy*. VCH Publishers.

Tanaka, M., Brault, J., and Tennyson, J. (2002). Absorption spectrum of $H_2{}^{18}O$ in the range 12 400-14 520 cm^{-1}. *Journal of Molecular Spectroscopy*, 216(1):77–80.

Tennyson, J., Barber, M. J., and Kelly, R. E. A. (2012). An adiabatic model for calculating overtone spectra of dimers such as $(H_2O)_2$. *Royal Society of London Philosophical Transactions Series A*, 370:2656–2674.

Teunissen, P. and Kleusberg, A., editors (1998). *GPS for Geodesy*, volume 2. Springer Berlin.

Thome, K., Smith, M., Palmer, J., and Reagan, J. (1994). Three-channel solar radiometer for the determination of atmospheric columnar water vapor. *Applied optics*, 33(24):5811–5819.

Thorlabs (2012). Product Description: AC254-150-B, Near IR Achromat. `http://www.thorlabs.de/thorProduct.cfm?partNumber=AC254-150-B`.

Tolchenov, R. and Tennyson, J. (2008). Water line parameters from refitted spectra constrained by empirical upper state levels: Study of the 9 500-14 500 cm^{-1} region. *Journal of Quantitative Spectroscopy and Radiative Transfer*, 109(4):559–568.

Troller, M. (2004). GPS based Determination of the Integrated and Spatially Distributed Water Vapor in the Troposphere. volume 67 of *Geodätisch-geophysikalische Arbeiten in der Schweiz*. Swiss Geodetic Commission.

u-blox (2007). Datasheet: Antaris 4 GPS Modules. `http://www.u-blox.com/images/downloads/Product_Docs/LEA-4x_Data_Sheet%28GPS.G4-MS4-06143%29.pdf`.

United Nations Environment Programme (UNEP) (2002). *Vital Water Graphics: An Overview of the State of the World's Fresh and Marine Waters*. Stationary Office Books.

University of Michigan (2013). Control Tutorials for Matalb and Simulink: Introduction – PID Controller Design. `http://http://ctms.engin.umich.edu/CTMS/index.php?example=Introduction&section=ControlPID`.

Vaida, V., Daniel, J. S., Kjaergaard, H. G., Goss, L. M., and Tuck, A. F. (2001). Atmospheric absorption of near infrared and visible solar radiation by the hydrogen bonded water dimer. *Quarterly Journal of the Royal Meteorological Society*, 127:1627–1644.

Vey, S. (2007). *Bestimmung und Analyse des atmosphärischen Wasserdampfgehaltes aus globalen GPS-Beobachtungen einer Dekade mit besonderem Blick auf die Antarktis*. PhD thesis, Technische Universität Dresden.

Vishay (2012). Datasheet: High Precision (0.01 %/10 ppm/°C) Through Hole Thin Film Conformal Coating Sil Resistor CNS 020. `http://www.vishay.com/docs/60051/cns020.pdf`.

Vogelmann, H. (2005). *Entwicklung und Aufbau eines Hochleistungs-Wasserdampf-LIDAR-Systems auf der Zugspitze*. PhD thesis, Universität Augsburg.

Vömel, H. and Jeannet, P. (2012). Balloon-Borne Frostpoint-Hygrometry. In Kämpfer, N., editor, *Monitoring Atmospheric Water Vapour: Ground-Based Remote Sensing and In-situ Methods (ISSI Scientific Report Series)*, chapter 3. Springer, 2013 edition.

Ware, R., Carpenter, R., Güldner, J., Liljegren, J., Nehrkorn, T., Solheim, F., and Vandenberghe, F. (2003). A multichannel radiometric profiler of temperature, humidity, and cloud liquid. *Radio Science*, 38(4):8079.

Weitkamp, C. (2005). *LIDAR: range-resolved optical remote sensing of the atmosphere*, volume 102 of *Springer Series in Optical Sciences*. Springer.

Welz, B., Becker-Roß, H., Florek, S., and Heitmann, U. (2005). *High-Resolution Continuum Source AAS: The Better Way to Do Atomic Absorption Spectrometry*. Wiley-VCH, 1st edition.

Wikipedia (2013). Vierquadrantensteller — Wikipedia, the free encyclopedia. [Online; accessed 11-Februrary-2013].

Wozniak, B. and Dera, J. (2007). *Light Absorption and Absorbents in Sea Waters (Atmospheric and Oceanographic Sciences Library)*. Springer, 1st edition.

Wu, S.-C. (1979). Optimum frequencies of a passive microwave radiometer for tropospheric path-length correction. *Antennas and Propagation, IEEE Transactions on*, 27(2):233–239.

Zogg, J.-M. (2009). u-blox Tutorial: GPS - Essentials of Satellite Navigation. `http://www.u-blox.com/images/downloads/Product_Docs/GPS_Compendium(GPS-X-02007).pdf`.

A

Electronic Layout Details

A.1 DC Motor Control

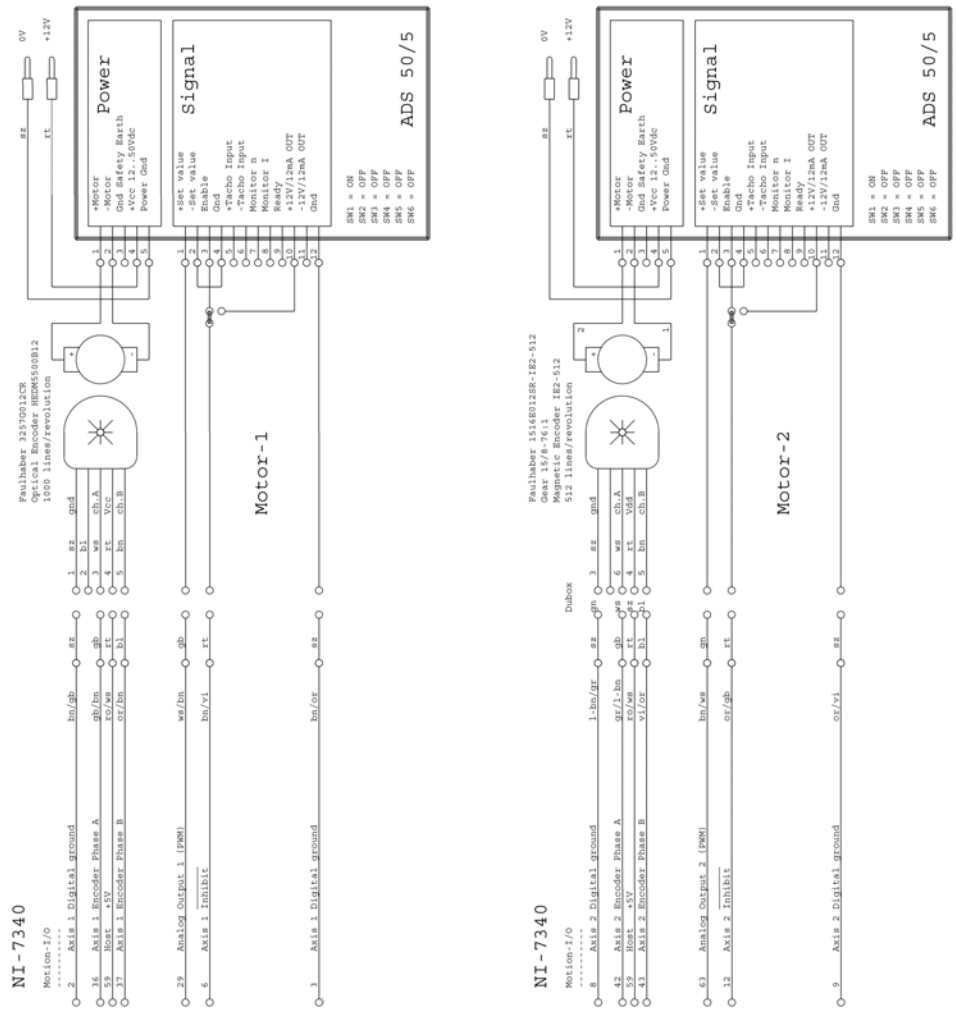

Figure A.1: Connection of the 4-quadrant servo amplifiers *Maxon AD50/5* for the control of the telescope DC-motors, with the motion control card NI-7344

A.2 Stepper Motor Control

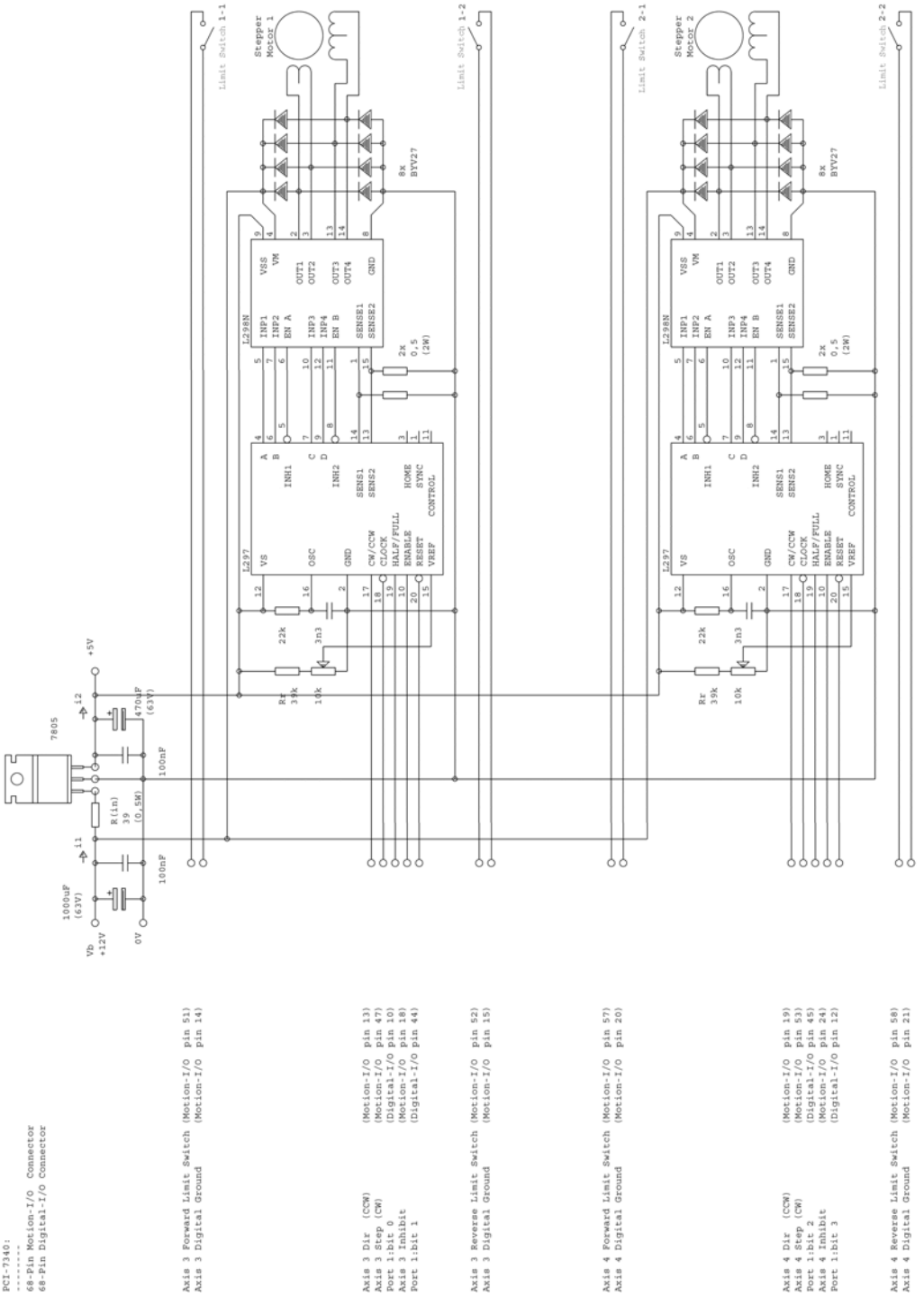

Figure A.2: Connection of the stepper motor driver units with the motion control card NI-7344. The stepper motors are used to tilt the spectrometer's folding mirror with precision screws.

A.3 Motion Control Interface

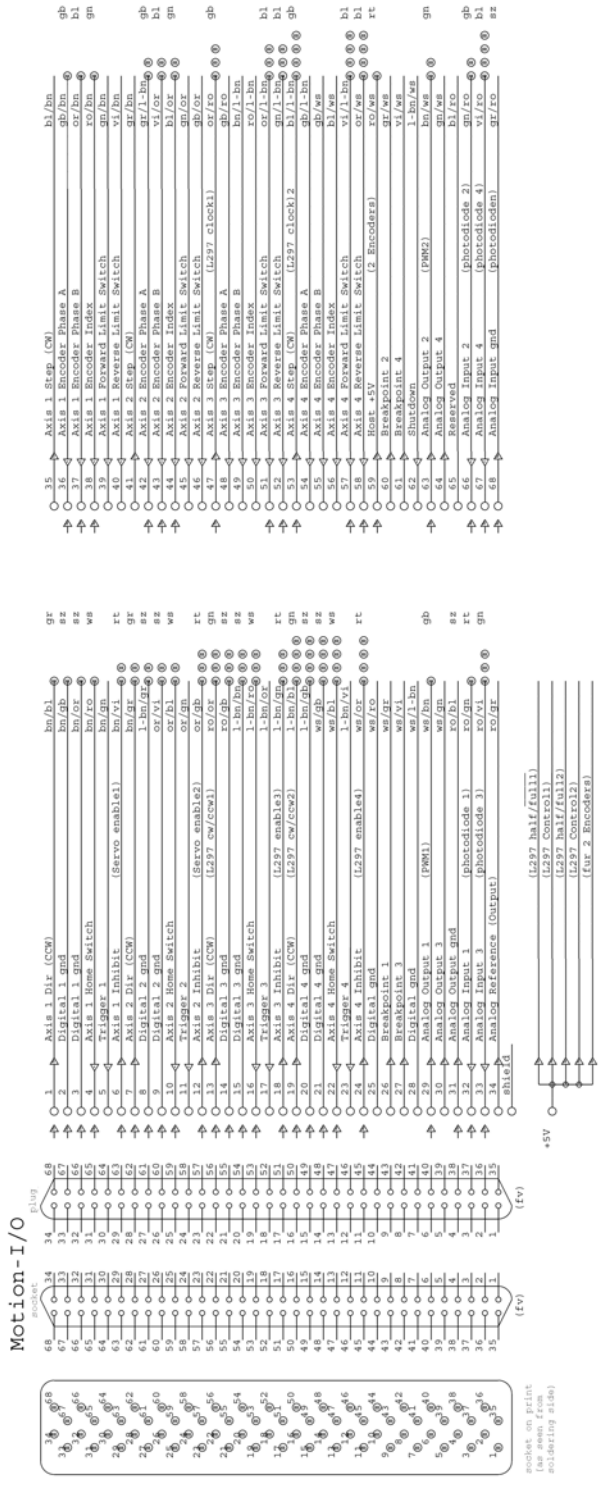

Figure A.3: Pin assignment of the interface between the motion control card and the drives of the DC and stepper motors.

A.4 Temperature Sensor

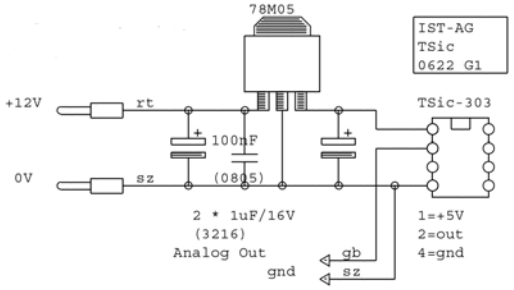

Figure A.4: Circuit diagram of the temperature monitoring set-up used inside the SOLUSAR instruments using *TSic-303* ICs by IST-AG.

A.5 Electronic Compass

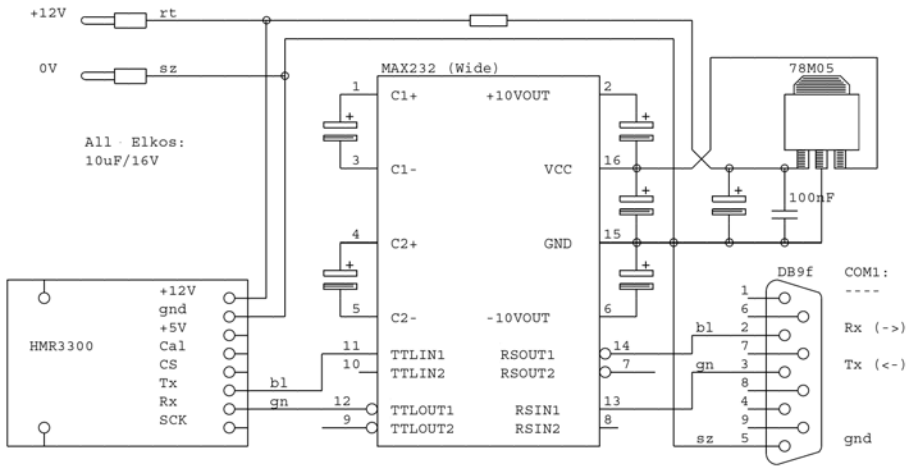

Figure A.5: Circuit board necessary for operation of the electronic compass *Honeywell HMR3300*.